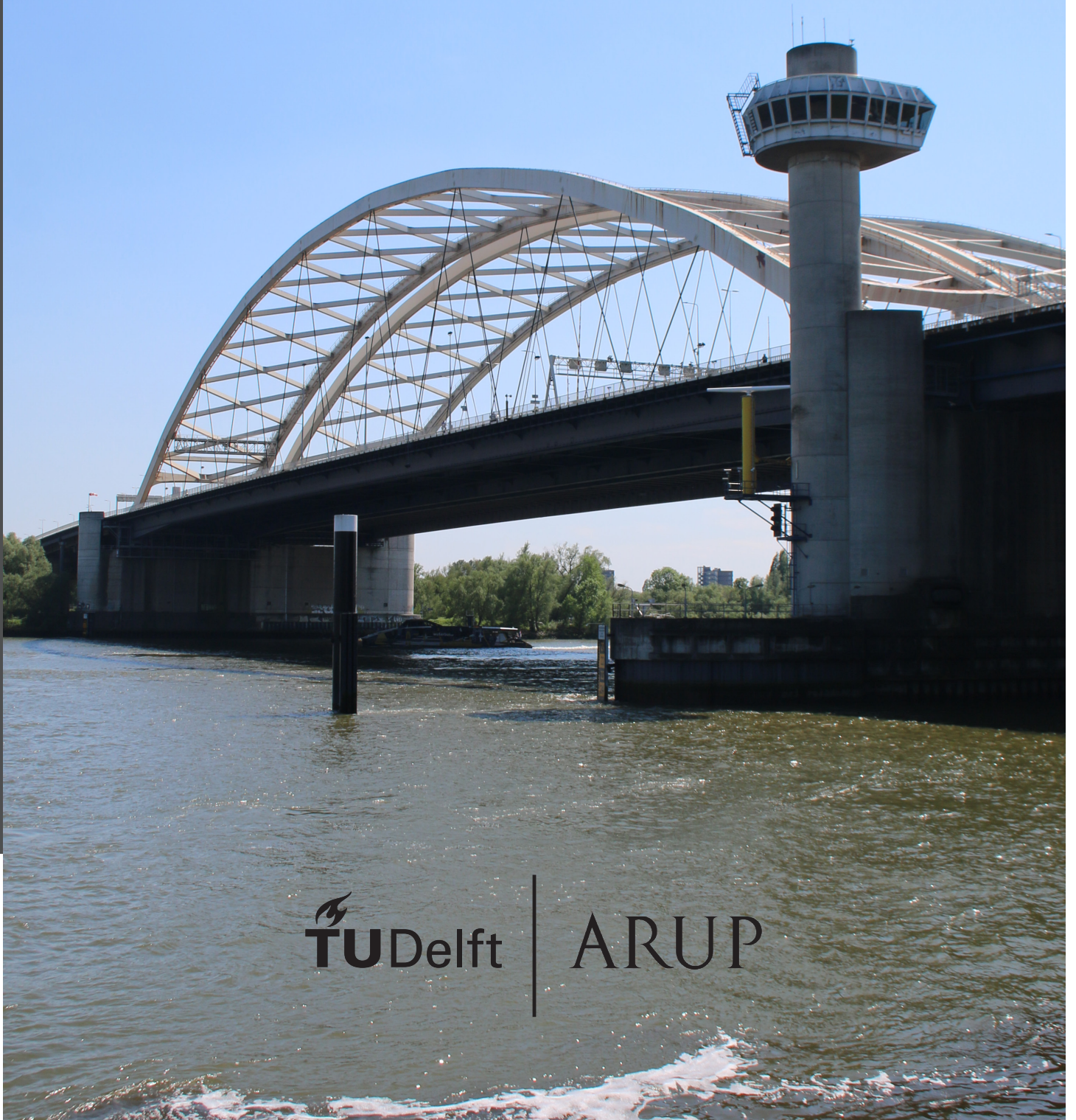# STRUCTURAL OPTIMIZATION OF STIFFENED PLATES

APPLICATION ON AN ORTHOTROPIC STEEL BRIDGE DECK
H.W. VAN DER LAAN

TUDelft | ARUP

Structural Optimization of Stiffened Plates

Application on an Orthotropic Steel Bridge Deck

by

H.W. Van der Laan

to obtain the degree of Master of Science

at the Delft University of Technology,

to be defended publicly on July 9, 2021 at 12:00.

Student number: 4486447
Project duration: September 1, 2020 – July 9, 2021
Thesis committee: Prof. dr. ir. M.A.N. Hendriks   TU Delft, chair
                              Dr. ir. P.C.J. Hoogenboom   TU Delft
                              Ir. S. Pasterkamp   TU Delft
                              R.G. Vernooij MSc. BBe.   Arup

An electronic version of this thesis is available at `http://repository.tudelft.nl/`.

TUDelft

Preface

This thesis marks the end of my master's degree in Civil Engineering at the Delft University of Technology. The last three years, I have become increasingly interested by the possibilities digitalization can provide for the structural design process. Although the civil engineering sector is often labeled as traditional, I have experienced that innovative techniques like parametric design are rapidly becoming common practice in engineering firms. For me, it feels like the use of structural optimization could be the next step forward, both to further automate the design process and to obtain improved structural designs. I hope my thesis can contribute to this development.

I could not have written this thesis on my own. Therefore, I would like to thank my colleagues at Arup, who were always ready to answer my questions. In particular, I want to thank Roel Vernooij, who has given me great suggestions for my research and introduced me to the practical side of designing orthotropic steel decks. I would also like to thank the other members of my committee, prof. dr. ir. M.A.N. Hendriks, dr. ir. P.C.J. Hoogenboom, and ir. S. Pasterkamp, who provided me with valuable and critical reviews of my work.

Finally, I want to express my gratitude to my family and friends, who have inspired and supported me at all times. I want to explicitly mention my brother Mika, who produced the cover of this report and some great figures, and Daphne, because she kept me motivated during the more difficult periods in writing this thesis.

Enjoy reading.

Dirk van der Laan
Vinkeveen, July 2021

Abstract

The orthotropic steel deck (OSD) is a deck system applied regularly in steel bridges all around the world. It consists of a steel deck plate which is stiffened by structural elements placed in two orthogonal directions. The deck plate can be used as an integral part of the structure, causing OSDs to achieve a high material efficiency and therefore low self-weight. However, this structural integration requires a large number of welded connections between the deck plate and stiffening members, which also make the system susceptible to fatigue. The fatigue evaluation of these connections is complex and time-consuming, hindering the manual optimization of orthotropic deck designs.

The use of structural optimization could be a solution for this. With *parametric optimization*, the best possible ratio between structural dimensions may be searched for automatically, while *topology optimization* could assist in finding new design concepts that could form alternatives to the traditional deck layout. This thesis investigates how these techniques could reduce the self-weight of the design of a case study (the renovated Van Brienenoord bridge) without reducing its fatigue service life. The two methods are treated in separate parts.

In the first part, considering parametric optimization, the traditional OSD concept is maintained and the values of seven selected dimensions are adjusted to obtain a design with a minimized weight. A workflow is developed in which an existing mathematical optimization solver (the artificial bee colony algorithm, a metaheuristic) is coupled to a parametric model, finite element program, and fatigue damage calculator. This enables an iterative process in which designs are generated by the solver and then evaluated in the remainder of the workflow. The information gained from the evaluation is returned to the solver and used to search for lighter designs.

In the second part, the deck remains a stiffened steel plate, but the location and orientation of stiffeners may be changed. Two possible leads for finding new structural concepts are explored. The first considers a topology optimization using the *ground structure method* as presented by Bolbotowski et al. [22], which can find the optimal orientation and size of stiffeners in a plate. This thesis evaluates the method's current applicability on steel bridge decks. The second lead interprets the results of a topology optimization made by Baandrup et al. [13]. This gives a new design concept in which the crossbeams curve directly towards the supports instead of being indirectly connected by main girders. A weight minimization using the workflow of the first part and a study of the force transfer in the deck are performed to assess the new concept's potential.

The first part showed that a 17,4 percent lighter deck structure (280 kg/m^2 instead of 339 kg/m^2) could be obtained for the case study by breaking with the general trend for designing orthotropic steel decks. The optimized design uses smaller and more rectangular troughs than commonly applied, but the largest differences are found in the deck plate thickness and stiffener spacing. For the latter, a value of 300 mm has been in use since the introduction of OSDs in the 1950's and is present in almost any bridge using an orthotropic steel deck. When fatigue issues started to appear from the 1970's onward, it was generally decided to increase the deck plate thickness. The results in this thesis strongly suggest that decreasing the stiffener spacing and trough top width is the preferred option when material efficiency is considered. A cost estimation further showed that the price of the optimized design would be comparable to that of the preliminary design that was suggested for the case study.

The topology optimization using the ground structure method showed that the optimal placement of stiffeners for a plate-like bridge deck contains two distinctive zones. Between the supports, the traditional longitudinal-transverse orientation is preferred, while the optimal direction of stiffeners in the middle of the bridge segments is arbitrary. The conventional OSD concept could be seen as optimal based on this result, but for definitive conclusions more research is needed towards a non-linear relation between cross-sectional area and resistance in the applied method. The similar support conditions of decks in other bridges make it likely that these conclusions will apply to those cases as well.

v

The optimization of the curved crossbeam concept showed the versatility of the workflow developed in the first part of this thesis, as only minor adaptations in the parametric model were needed for the application on a significantly different design. Despite the successful optimization, the potential of the new design to replace the traditional OSD concept is considered low. In its optimized form, the concept was 9,8 percent heavier and less than half as stiff as the best found result in this thesis' first part. The comparable support conditions for plate girder bridges in general again suggest similar outcomes for other cases, while a different setup of the optimization would not tackle the fundamental stiffness problem of the design. Further research towards the curved crossbeam concept as presented by Baandrup et al. [13] should therefore stick to the original application of box girder decks.

Contents

Introduction

1.1. Background information and relevance

The orthotropic steel deck (OSD) is a bridge deck system that consists of a steel plate which is stiffened by elements placed in two orthogonal directions. It is the main choice for situations where the self-weight of the deck structure is critical [31]. The system is often used in larger bridges, as for longer spans the proportion of self-weight compared to the total loads increases [57]. In the Netherlands, the system is therefore mainly found in the bridges spanning the larger rivers and canals, like in the Van Brienenoord, Galecopper, and Suurhoff bridges. Other reasons for applying OSDs may be their large strength and deformation capacity, prefabrication possibilities, and a reduced structural height [29, 31].

1.1.1. Fatigue

Despite the clear advantages, the deck system has a history with many difficulties. Numerous bridges with OSDs have suffered from fatigue problems, mainly caused by the lack of knowledge and adequate tools for fatigue analysis in the past [29], poor fabrication quality [103], and the strongly increased traffic intensity in the last 50 years [32]. The troubled history was highlighted by the large cracks found in the Van Brienenoord bascule bridge in the nineties, when the bridge had been in use for only seven years. The discovery of these fatigue cracks sparked an enormous amount of research that is still going on today.

The perfect solution has not yet been found, and it can be doubted if it exists. Newly developed refurbishment techniques and more accurate calculation methods may extend the lifetime of existing and new bridge decks, but do not mitigate the problem completely. The use of innovative materials like fiber-reinforced polymers is still in an early stage of development [32], with the first uses in small span road bridges currently emerging.

1.1.2. Implications for the design process

Meanwhile, the encountered problems cause the design process of an OSD to be mainly focused on the fatigue limit state. Checks for this limit state are very laborious, needing many evaluations of detailed finite element models with multiple moving loads. Just the analysis of these models may take multiple days to execute, while the complete design process spans over months. The time-consuming character of this procedure hinders the optimization of the design for the considered situation.

However, skipping or rushing this step may lead to unnecessary use of material and labor, resulting in higher economical and environmental costs. With the realization that the large projects OSDs are used in generally cost millions of euros and the construction industry being responsible for nearly 40 percent of global CO_2 emissions [46], this should not be acceptable.

The importance of material minimization may be even more clear when replacing damaged bridge decks. The new deck will, in general, turn out to be heavier than the original deck due to increased demands from loading. This poses a problem for the superstructure and abutments of the bridge,

which should often be maintained. The greater loads already highly utilize the capacity of the bridge superstructure, restricting the design space for the new deck. Low weight of the solution is thus critical for its success.

1.1.3. The possible role of structural optimization

Various structural optimization techniques may form a solution to this problem. Parametric optimization could (partly) automate the optimization stage of a design process, which can be especially beneficial when complex analyses like that for an OSD are needed. Additionally, topology optimization could assist in finding new structural concepts during early design phases.

The field of (mathematical) structural optimization is not new. In 1904, Michell [74] published his seminal work *The Limits of Economy of Material in Frame-structures* that already describes a form of topology optimization. Schmitt [101] coupled a mathematical solver to a finite element model to find the optimal sizes of frame members in 1960.

The majority of case studies and practical applications, however, has emerged more recently. Reasons for this may be found in the increased computational power that is now widely available, the expanded programming knowledge of present-day engineers, and the stronger acceptance of computer-aided design tools like parametric design [102]. Numerous applications in the automotive and aerospace industries can therefore be found in the last 25 years [26, 120, 121]. The civil engineering sector appeared to lag behind, but examples of practical use have been popping up in the past decade [16, 23].

1.1.4. Structural optimization of orthotropic steel decks

Although the possibilities for the structural optimization of orthotropic steel decks are clear, the applications in existing literature are very limited. The recently published doctoral dissertation of Baandrup [10] is one of the few. In the first part of the dissertation, savings of up to 14 percent in material and 17 percent in costs were achieved just by finding improved dimensions for the existing design of the Ozman Gazi bridge in Turkey.

The second part of the dissertation goes one step further and searches for new structural concepts that could replace the current orthotropic deck system. These new systems are based on the results of two topology optimization studies, and show possible reductions in self-weight of 28 and 45 percent respectively.

1.2. Problem statement

1.2.1. Differences in deck design and loading

Unfortunately, the results found by Baandrup are not directly applicable to all bridges using OSDs. The Ozman Gazi bridge's orthotropic deck is integral part of a hollow box girder, which differs from the plate girder deck present in, for example, the Van Brienenoord bridge. The box girder's increased structural height and closed cross-section causes the crossbeams (or diaphragms in this case) to be significantly stiffer than those present in plate decks. Earlier research has shown that this influences the stresses acting at the fatigue details in the deck [17].

Furthermore, these plate girder decks regularly feature the characteristic support plates (Dutch: 'kamplaten') that connect the deck to the crossbeam. Stress-relieving cut-outs around the troughs in the crossbeam or support plate (see figure 3.7) also may or may not be present. This divergent built-up of the deck comes with different detailing, which could react different to fatigue loading.

Finally, the intense use of the Dutch road network [80] means that bridges will experience a higher loading demand. Especially for structures close to the Rotterdam port area, like the Suurhoff and Van Brienenoord bridges, this has led to problems in the past. The high proportion of heavy trucks in this region's traffic enlarges the fatigue demand even further.

1.2.2. Optimization setup

Besides the consequences of the situational differences, research towards the implementation of the optimization process is also needed. The low amount of studies considering structural optimization of orthotropic decks makes that only a few possibilities have been explored.

The mentioned thesis uses a gradient-based method to solve the considered optimization problem. Although these methods can be very efficient, their performance is hindered by the presence of local optima. Other relevant studies combine a form of surrogate modeling with a genetic algorithm [122] or non-linear solver [55]. This can decrease the amount of needed finite element calculations tremendously, but the outcome of the optimization will be highly dependent on the efficacy of the used surrogate model.

Both of these problems may be amplified by the complex structural character of orthotropic decks. Their large degree of statically indeterminacy and highly non-linear stress profile around joints increases the demands on the surrogate model. It also makes the solution space highly non-convex, which is detrimental to the effectiveness of gradient-based solvers.

A second aspect that could be improved in the optimization setup regards the use of constraints. All mentioned papers limit the stresses at fatigue details, while it is fatigue damage that would be constrained in practice. Using the well-known S-N curves, these two may be interchangeable, but this requires detailed knowledge of the expected number of relevant stress cycles and influence lines in advance. When changing the design of the deck or using real traffic data, this may not be easily available.

A final improvement for practical use of structural optimization could lie in the generation of multiple design variants. Gradient-based solvers generally give only a single optimized solution, while a list of alternatives may be more valuable in practice. These can then be used for the assessment of properties that are more difficult to capture in the constraints of the optimization problem, such as manufacturability or uncertainties in new design forms.

1.2.3. Topology optimization
Baandrup's topology studies show very promising results, but practical realization of the found design cannot be expected soon. The innovative designs have the usual difficulties with the manufacturability of designs resulting from topology optimization, but these may be solved in the future by highly automated construction methods and 3D printing.

However, increased production possibilities only do not pave the road for application of the presented methods in practice. The dissertation's second study finds a new deck structure by a very precise topology optimization, solved by a letting a supercomputer with 16.000 cores run for 85 hours. This is far from accessible to be used by both other researchers and engineers in practice. An enormous increase in readily-available computational power would be needed to change this, which is not to be expected in the near future.

Despite this, there may be a solution on a much shorter term. The highly detailed structure found by Baandrup is strongly simplified to enable manufacturing and structural analysis of the design. This raises the question if the same result could also be generated by much simpler methods, making it more applicable to real world problems.

Another option could be to directly use the interpreted result for the design of other bridges. For cases without the box girder deck present in the Ozman Gazi bridge, however, the efficacy of the new design is completely unknown. The consequences of the changed structural concept should thus be explored before the new topology could be seriously considered for other deck types.

The structural principle found by the third study is not applicable to the plate girder decks that will be considered in this thesis. A significantly larger structural height would be needed for the principle to be executed, which is not available in the studied deck type.

1.3. Research questions and approach
The previous sections have outlined how structural optimization techniques can be used to save materials and costs for the complex design of an orthotropic steel deck. This thesis will further investigate the possibilities of using these procedures. A method is developed that may be used in practical design cases and the problems described in the previous section are tackled to stimulate future adoption of structural optimization in practice.

Besides being an example for future use, the application of the chosen methods enables the search for improved designs of steel bridge decks. An effort is made to give recommendations for more efficient use of material in the existing orthotropic steel deck system, and to generate ideas for new structural concepts.

To achieve these goals, it is tried to find an answer to the question:

> What is an optimized topology for a steel bridge deck - as typically found within the larger bridges in the Netherlands - to minimize its weight while maintaining its fatigue service life?

An answer is searched by applying two different structural optimization techniques on the case study of the new Van Brienenoord bridge deck (see chapter 9). This enables a comparison between the optimized deck design and the design found by more traditional methods.

The applicability of this study is not limited to finding an improved design of this bridge, however. The developed method may very well be used for cases with other global bridge dimensions, loading conditions, fatigue details, or design choices. Even new insights regarding fatigue calculations may be easily processed in the used method.

1.3.1. Part 1: Parametric optimization

The first part of this thesis will investigate the use of parametric optimization on OSDs. The structural concept of the deck will not be changed, but an effort is made to reach the current design concept's full potential by searching for a better ratio between the parameters of certain structural elements. More practically, this part could be seen as a partial automation of the optimization phase that should be present in a design process.

The term *parameters* is used here to describe the cross-sectional dimensions of, and distances between components in the deck. When members are placed further apart or closer together, components may be relocated, added, or removed. This exceeds the strict definition of size optimization (see section 5.3), where the location of members is invariable. On the other hand, the predetermined structural concept means that the design freedom usually present in topology optimization studies is not achieved. It was therefore decided to use the term *parametric optimization* to describe the scope of the study correctly.

To enable this search for improved designs, the design problem is first translated into a more mathematical optimization problem. Next, a workflow is developed that can work out this problem. During this development, the following sub-questions will be answered:

- How can the setup of the problem facilitate the generation of multiple design variants?

- How can the evaluation of damage constraints be included in the workflow?

- Which simplifications can and/or need to be made to make the optimization problem solvable within an acceptable time span?

- How do the optimized parameters compare to the original design, and what (general) recommendations may come from this?

The first and second question try to tackle the problems as mentioned in section 1.2.2. Finding an answer to these questions may increase the applicability of the method in practical design cases. The solution is mainly sought for in the setup of the optimization problem and workflow used for solving it.

As mentioned in section 1.1.2, the full fatigue analysis of orthotropic decks takes a considerable amount of time to complete. During most structural optimizations, however, some hundreds or thousands of iterations need to be made. The time needed for an analysis thus needs to be limited in order to be workable. The answer on the third sub-question should enable this. The simplifications will mostly be searched for in the finite element model and the applied loading.

The final result of the optimization could, next to showing the potential of structural optimization, be used for recommendations in future projects. This could be in the form of initial designs for traditional design projects, or starting values when using structural optimization. A comparison with deck designs generally used in practice will be made.

Not covered by the questions above, but an essential part of the workflow dealing with the optimization problem is the mathematical solver. Only a single existing algorithm is considered and the choice for one is made based on literature. This would become the artificial bee colony algorithm (section 6.2.3), a heuristic method based on the behavior of bees searching for food. To the authors knowledge, heuristics have not yet been applied to the optimization of orthotropic steel decks. The utilization of this algorithm therefore adds to the exploration of optimization methods that was mentioned in section 1.2.2. A full study of the algorithm's potential was not possible during this research (hence the lack of a dedicated sub-question), but relevant experiences will be discussed in the conclusion as well.

1.3.2. Part 2: Topology optimization
The second part of the thesis tries to improve the design even further by exploring the application of topology optimization on steel bridge decks. New structural forms are searched for or taken from existing literature. The new design will remain a stiffened steel plate, but the distribution and direction of the stiffeners may change and is no longer required to be orthogonal.

Two options will be explored in this thesis to tackle the problems stated in section 1.2.3. The first considers a topology optimization using the ground structure method, which could potentially determine the optimal orientation of stiffeners on the deck. Contrary to the highly detailed supercomputer optimization, this method can be solved on a regular computer within reasonable run times. With this, it is tried to resolve the subquestion:

- How can the ground structure method assist in finding the optimal distribution and orientation of stiffeners in a steel plate deck?

The second option focuses on the third factor stated in section 1.2.3. Here, the curved crossbeam design resulting from Baandrup et al. [13] is taken and applied on a plate deck. The new design is then optimized with the parametric optimization workflow developed in part 1 and the consequences of the new structural concept on the force transfer are analyzed. Using these two short studies, the following subquestion is tried to be answered:

- What is the potential of applying curved crossbeams in steel plate decks to reduce their mass even further than for the conventional orthotropic concept?

The word 'potential' is emphasized here. It is not intended to perform a comprehensive study of the behavior of this variant, but to asses if further research towards the application on plate decks could be of interest.

1.4. Scope
The field of structural engineering is extensive, its use in practice is still low, and fatigue analysis itself is already very complex. An all-embracing research towards practical implementation is therefore not realistic. This section outlines what is and what is not included in the scope of this thesis.

1.4.1. Design precision level
The aim is to obtain a preliminary design (VO) of the bridge deck. This means that plate thicknesses and spacing of the structural elements are determined based on loading conditions that are deemed to be governing. Based on experience at Arup, these conditions can be found in the fatigue limit state. ULS and SLS checks will be left for the detailed design (DO) phase. The detailing of welded and bolted connections (e.g. weld thicknesses) and determination of construction method is left for this phase as well. Only linear elastic calculations will be made.

1.4.2. Constructability
Constructability and repetitiveness will be implicitly considered in the first part of this thesis, as only a selection of parameters will be changed during the optimization. The fundamentals of the OSD concept will therefore remain the same and traditional construction methods will still be applicable. Design constraints in the form of upper and lower bounds on parameters may further assure this. Repetitiveness is guaranteed by considering parameters only globally (e.g. thickness of all troughs instead of one specific through).

In the second part, these demands will be somewhat loosened. A new deck system may be found that can deviate from the traditional structural principle. The focus will be more on the result that could be obtained when the current layout. Eventually, a solution is sought that could be manufacturable, albeit not necessarily with conventional methods.

1.4.3. Design space
Although implicitly stated by the title and research question, it is emphasized that the superstructure of the bridge will not be designed. Its structural system may be relevant for the deck structure, but other than that it will be assumed that it can support the deck system properly without further checks. Effects from the global behavior of the bridge will be neglected where thought to be possible. When choices for global parameters are needed, they will be taken from the existing design of the case study. Examples are the main girder stiffness and span.

The research in this thesis will only consider a deck with closed, continuous stiffeners (see figure 3.5) without the stress-relieving cut-outs around the connection between the stiffener and crossbeam (figure 3.7). Closed stiffener decks are nowadays used more often than the open stiffener deck due to their higher efficiency, while the continuous stiffeners have superior fatigue resistance compared to non-continuous stiffeners. The choice for not using the stress-relieving cut-out was taken from the case study. The applied methods, however, may be easily translated to optimize other deck forms as well.

1.4.4. Dutch practice
The application on a Dutch bridge also means that only the Dutch practice will be directly considered. Where needed, regulations from Rijkswaterstaat and Dutch Eurocode annexes will be used. When knowledge from experience is used, this will mainly come from bridges found in the Netherlands. Examples of these may be the fatigue details that are deemed to be governing for design, which may differ from the ones found in relevant papers.

1.5. Structure
The remainder of this thesis is subdivided into five segments, all comprised of multiple chapters. The first segment discusses the literature review performed prior to this research. This starts with chapter 2 covering the fundamentals of fatigue in materials, followed by the basics of orthotropic steel decks in chapter 3. This introduces the structural concept with its advantages and sketches a historic overview from its initial use up to the current state-of-the art. Chapter 4 explains the most important factors for the design of OSDs today, which is governed by the fatigue phenomenon as explained in chapter 2.

The remaining four chapters of the literature review focus on structural optimization. Starting in chapter 5, the topic is introduced by discussing the available forms and their use, presenting the general mathematical formulation, and giving a historic overview of its development. Chapter 6 follows with a more thorough discussion of two strategies available for solving such an optimization problem: convex and heuristic programming. Chapter 7 then lists several methods for topology optimization that could be used on steel plate decks. Literature that has already used these methods or other forms of structural optimization for the improvement of OSDs are finally discussed in chapter 8.

The second segment contains the setup and results of the first part of this research, which applied parametric optimization. Chapter 9 first shortly introduces the case study of the Van Brienenoord bridge and compares its design with similar bridges. Chapter 10 gathers the necessary elements to formulate the optimization problem that will be solved in this part of the thesis. The parametric model used for this is then thoroughly discussed in chapter 11 and compared to the results of the Van Brienenoord bridge's preliminary design in chapter 12. The remaining elements and an overview of the workflow developed for the parametric optimization follow in chapter 13. The results of the case study's eventual optimization are presented in chapter 14 and verified in chapter 15.

The third segment has two chapters that each discuss one of the possible applications of topology optimization. Chapter 16 covers the results of the layout optimization using the ground structure method, while chapter 17 presents the study regarding the implementation of curved crossbeams.

Finally, the fourth segment contains the conclusions and recommendations in chapters 18 and 19 respectively. The appendices are gathered in the fifth segment.

I

Literature Review

<div style="text-align: right">

2

Fatigue

</div>

Fatigue is the weakening of materials resulting from cyclic loading. It is caused by progressive damage of the material under repeated stress changes that can even occur at stress levels far below the yield point. Given enough time, the accumulation of damage can lead to complete fracture of the structural member. Orthotropic steel decks are vulnerable to fatigue problems, resulting in a focus on the Fatigue Limit State in the design phase. Therefore, a proper understanding of the fatigue phenomenon is essential when designing steel decks. A practical introduction is given here, covering the most important aspects during the design phase.

First, the origin and development of fatigue damage are discussed, which also explains why welded joints are particularly vulnerable to fatigue damage. Then, the common practice to determine the fatigue resistance of structural elements is presented. The chapter concludes with an explanation of the necessary steps for fatigue life analysis in design.

2.1. Fatigue process

The fatigue phenomenon in materials became known due to the rise of steam engines and heavy machinery during the Industrial Revolution in the nineteenth century. Although it was observed that the many load cycles to which the material in these devices was exposed to led to fractures that would not occur at a single load cycle of the same magnitude, the cause of this problem remained largely unknown [99]. The lack of knowledge resulted in frequent accidents across railway, aerospace, and civil engineering industries, often with great loss of life [24, 85].

Since then, a massive amount of research has been put into the subject. Large steps have been taken towards better understanding, but fairly recent incidents like the high speed train crash near Eschede (Germany) in 1998 [85] and the problems with the second Van Brienenoord bridge in 1997 (see section 3.2.3) show that fatigue problems are still not completely solved.

One of the largest difficulties is that the process behind fatigue damage starts long before visible cracks in the material occur. During most of the fatigue life of a structural member, damage can only be seen using a microscope. This crack initiation period ends once cracks deviate from their nucleation site and their growth is no longer dependent on microscopic material properties [100]. As can be seen in the scheme of figure 2.1, cracks then grow further in the crack growth period until final failure.
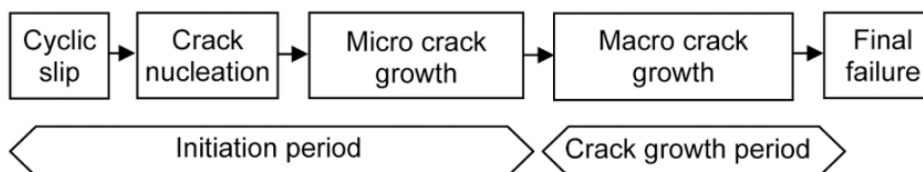
Figure 2.1: Schematic overview of different phases in the process leading to fatigue failure [100].

2.1.1. Initiation of fatigue

In the crack initiation period, microcracks form at shear slip locations. These can occur at the surface of the material, or at impurities or inclusions inside the material [75, 85]. The slip locations experience small local plastic deformations, leading to local strain hardening and new material becoming exposed to the environment. The strain hardening is not completely reversible and causes parallel slip planes to also experience strain hardening when the stress direction is reversed. The exposure of new material to the environment causes a small oxide layer to cover the new surface [100]. These phenomena combined lead to the formation of slip bands where microcracks can nucleate. The process is visualized in figure 2.2.
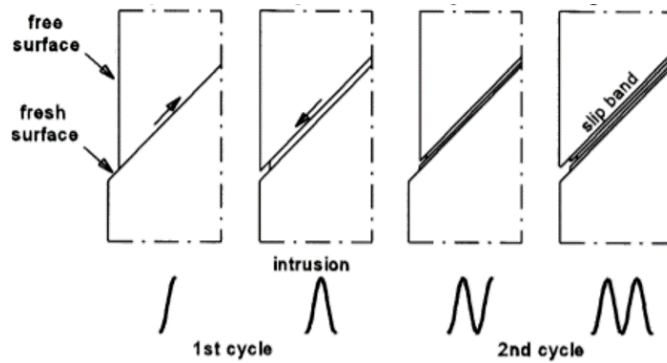
Figure 2.2: Crack nucleation by the formation of slip bands at the surface of the material [100].

2.1.2. Crack growth

The microcracks lead to stress concentrations in the material, activating more slip planes. During each loading cycle, strain hardening occurs along these planes, which causes the deformation to be partly permanent [24, 100]. The microcrack grows a little larger with every stress reversal (figure 2.3a), eventually becoming a macroscopic crack. Although a quantitative boundary between the crack initiation and growth phase is difficult to give, the crack growth period can be said to have started once the crack growth rate no longer depends on the local material properties of its nucleation site [100].

Despite the slip bands often forming at a 45° angle with the surface due to their shear stress origin, the direction of crack growth will generally diverge from this and grow perpendicular to the principle tensile stress direction (figure 2.3) [75, 85]. When the crack advances deeper into the material, the stress concentrations around the crack tip become larger, increasing its growth rate. This self-reinforcing mechanism causes damage to accumulate ever faster [24, 100].
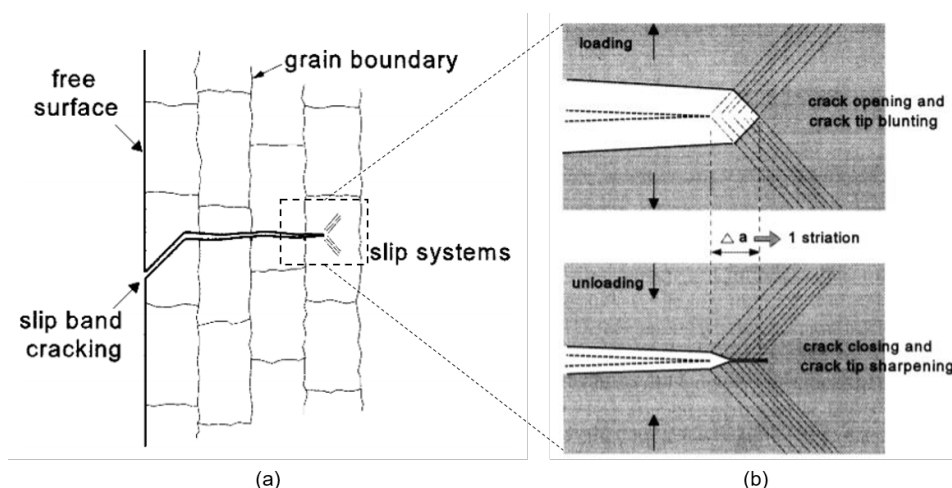
Figure 2.3: Example of a typical crack growth pattern for cracks initiated at the material surface (a) and a visualization of crack growth in a single load cycle (b) [100].

2.1.3. Final failure

Fatigue cracks in structural elements will reduce the cross-section that can withstand (tensile) stresses. When the remaining cross-section becomes too small to bear the applied load, the element will fail. Fatigue fractures have a very distinct failure surface, visible in figure 2.4. The failure surface clearly shows the origin of the fatigue crack and its propagation through the cross-section from the so-called *beach marks* or *striations*. Beach marks can be compared to the growth rings found in trees; they give information on the loading history of the element, just like growth rings show the change in environmental conditions during the tree's life. Wide bands correspond to large loads that resulted in heavy damage, while smaller loads leave narrower marks [24, 73].

As can be seen in the photo on the right of figure 2.4, the beach marks are not present on a part of the failure surface. This part was the remaining cross-section when complete failure occurred. Depending on the ductility of the material and failure load characteristics, it can show plastic deformation, which is never present in the fatigue zone.
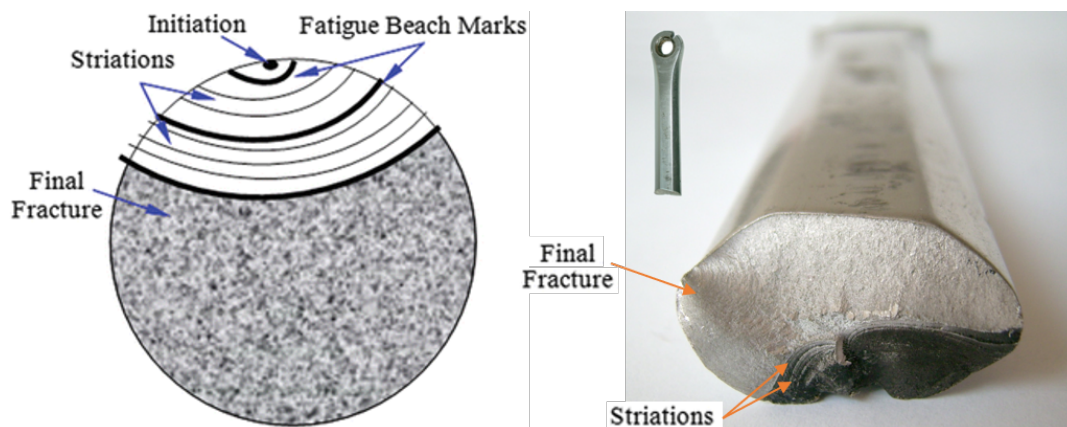
Figure 2.4: Schematic drawing (left, [83]) and photo of a fatigue failure surface (right, adapted from [69]). The different zones in the failure surface are labeled.

2.1.4. Vulnerability of welded joints

For structural members without any imperfections, the crack initiation phase covers the largest part of its fatigue life. However, defects, inclusions, or imperfections in the material shorten this phase considerably. This is caused by the larger dimensions of microcracks forming at these locations. Macroscopic defects can even result in the complete absence of the crack initiation phase, shortening the fatigue life of the member tremendously [100].

All of these promoters of crack forming apply to welded joints [66]. Welding processes leave small discontinuities in the form of impurities and inclusions, and cause residual stresses in the weld and the material around it. Furthermore, welds often have a rough profile and relatively sharp corners can be present between the structural elements. The differences in material properties between the welds and parent material also lead to abrupt changes in stiffness. These factors all lead to stress concentrations in and around the weld.

The absence of the crack initiation phase is therefore often observed in welded joints, causing them to have a much lower fatigue strength than the steel members they connect. Consequently, fatigue damage in steel structures containing welds will almost certainly start in the welded joints [65]. Other likely origins of fatigue cracks may be holes of rivets or bolts, which are also prone to material imperfections and stress concentrations.

2.2. Fatigue resistance

The fatigue resistance of structural elements is determined by laboratory tests, where test specimens are subjected to alternating loads. In general, constant amplitude cycles are used and the number of cycles until failure is counted. This is done for different stress levels and the results are plotted in a graph. A line can be fitted through these results for the prediction of the fatigue life of similar structural members. For design purposes, the characteristic value can be taken by shifting the mean by two standard deviations to obtain a survival probability of 97,7 percent [52]. An example of fatigue test results and a shift of the mean value is given in figure 2.5.
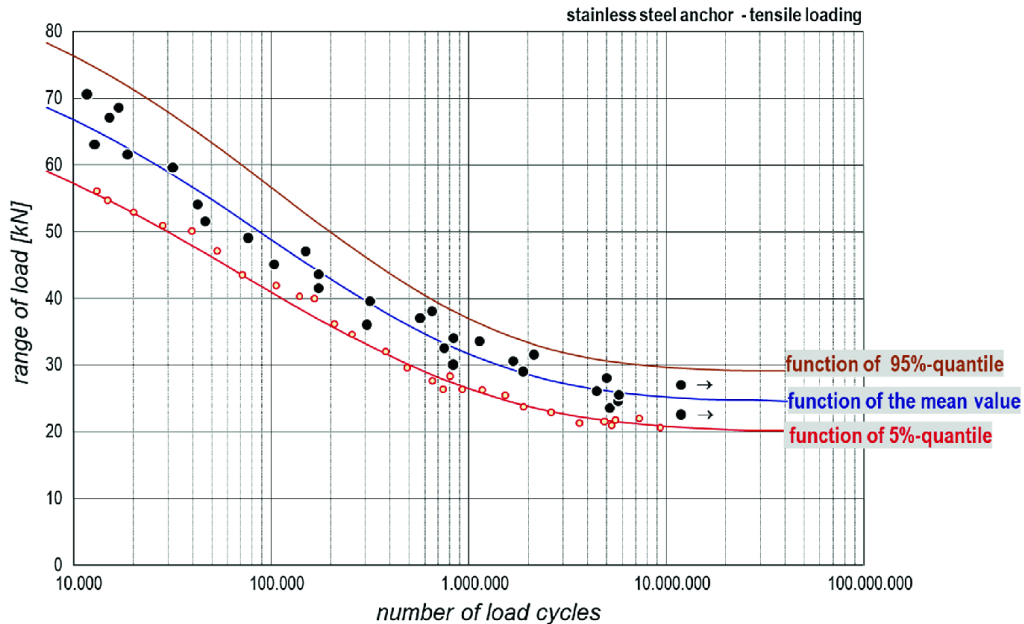
Figure 2.5: Example of fatigue test results: stress range plotted against number of cycles until failure on a logarithmic scale. The scatter in results is used to estimate the 5 and 95 percent quantiles [21].

2.2.1. S-N curves

The relation between the magnitude of the stress ranges $|\Delta\sigma|$ and the number of cycles N until failure found in laboratory tests is approximately linear on a log-log scale. The lower bound curves of test results are therefore linearized to form the so-called S-N curves, visible in figure 2.6. The relation described by these curves has the form of:

$$N = \frac{C}{\Delta\sigma^m} \tag{2.1}$$

where m depends on the value of the stress range. C depends on the joint geometry, which will be discussed in section 2.3.1. The variable value of m is used to capture the stronger influence of larger stress variations on the fatigue life of a structural element. m is equal to the slope of of the S-N curve when plotted on the log-log scale (figure 2.6). As the figure shows, EN 1993-1-9 [3] distinguishes three regions in the S-N curves for normal stresses:

1. $1 \times 10^4 \geq N \geq 5 \times 10^6$ cycles: $m = 3$. For large stress variations, a change in stress will have a strong influence on the fatigue life.

2. $5 \times 10^6 \geq N \geq 1 \times 10^8$ cycles: $m = 5$. For less stressed elements, the influence of a change in the stress range is smaller.

3. $N \geq 1 \times 10^8$ cycles: $m = \infty$. Infinite life: for joints for which the stress ranges do not exceed a certain limit, the fatigue damage may be neglected according to the Eurocode. This value is referred to as the cut-off limit.
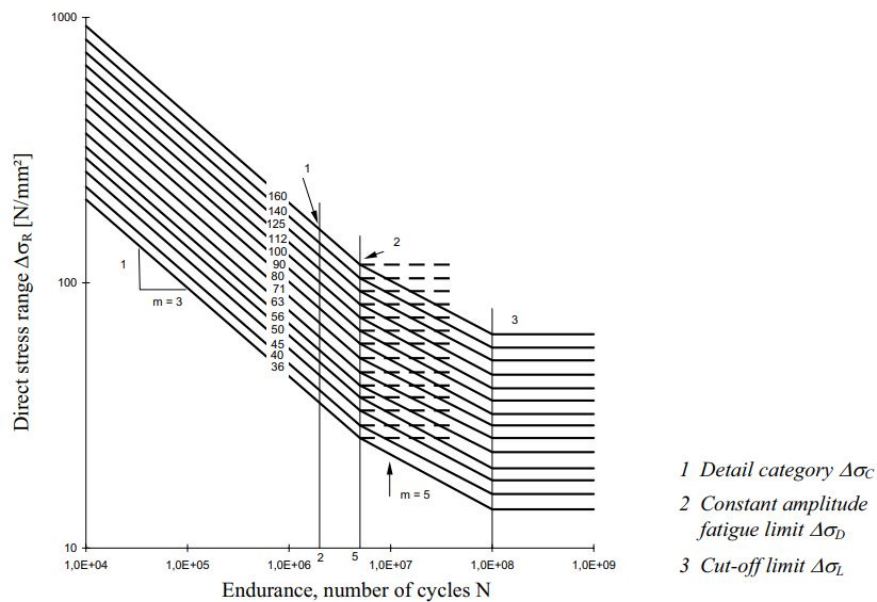
Figure 2.6: S-N curves for normal stresses as given in NEN-EN 1993-1-9. The stress range is plotted against the amount of expected cycles until failure. The numbers in the graph represent the detail category it belongs to, corresponding to the stress range for which the expected fatigue life consists of 2 million stress cycles [3].

The exact locations of the 'knee point', where the value of m is changed from 3 to 5, and the cut-off limit are somewhat arbitrary. The International institute of welding uses, deviant from the Eurocode, values of $N = 10^7$ and $N = 10^9$ for the knee point and cut-off limit respectively [52]. It may even be argued that a true cut-off limit does not exist [85], and a value of $m = 22$ would be more accurate for small values of stress ranges [52].

2.3. Fatigue life analysis in design

As mentioned in section 2.1.4, fatigue damage in steel structures will often start at welded joints. Fatigue calculations in design will therefore focus on the fatigue resistance of these joints. In short, a fatigue calculation consists of the following steps:

1. Determine the detail category of the joint.

2. Calculate the stresses in the joint.

3. Extract stress ranges from the stress history.

4. Calculate the fatigue damage.

The result of such a calculation is a number comparable to the well-known unity check and should thus be smaller than 1. The different steps will be elaborated in the coming subsections. An important step for fatigue analysis that was purposely left out is the determination of loading. The content of this step is thought to be more specific to the application. The determination of loading for orthotropic steel decks is therefore covered in section 4.4.

2.3.1. Detail categories

When the causes of fatigue damage are considered (section 2.1.4), it is not surprising that the joint geometry has a strong influence on its fatigue life. Tests have been performed on different types of joints to determine their resistance, after which they are organized in 'detail classes'. A detail class is represented by a number that corresponds to the stress range for which joints from this category are expected to survive 2×10^6 load cycles. This determines the value of C in equation 2.1 and thus which curve of figure 2.6 should be used. Detail categories for widely used joints are given in NEN-EN 1993-1-9 and 1993-2 [1, 3].

2.3.2. Calculation of stresses

There are multiple methods available for the calculation of stresses in the joint, differing from each other by their level of detail. Which method to choose depends on the complexity and accuracy that is desired. The complexity of the analysis may influence the previously discussed detail category of the joint. When these detail categories are determined by laboratory research, the influence of many possible variables is included, such as:

- Stress concentrations due to the joint itself

- Stress concentrations due to the weld geometry

- Expected weld imperfections

- Loading direction

- Residual stresses

- Metallurgical conditions

- The welding process

The codes that describe the detail categories should be generally applicable and these effects are thus mostly considered in a conservative way. More accurate methods are able to capture some of the influences in the analysis, disposing the need to include them in the fatigue curves. The use of a more complex analysis methods may therefore come with the benefit of a higher detail category for a joint, which can lead to more economical designs. On the other hand, it will increase the time needed for design and engineering. Using complex methods for all joints in a structure, even those that are unlikely to be governing, can then also prove to be inefficient.

Four methods for the calculation of stresses in welded joints will be discussed here, taken from Hobbacher [52]. The first three methods are also to be found in ECCS publication N° 105 ([39], as presented by Kolstein [66]). The methods are in order of complexity and accuracy, starting with the least complex and accurate method. The use of stress intensity factors is a somewhat odd one among these, as it is mostly used to find the stress patterns around cracks. However, as the crack initiation phase is practically absent in welded joints, it can also be used to asses their fatigue life.

- Nominal stress: As the least complex method, the nominal stress method only considers the global layout of the structure. Dimensions and shape of the structural members are taken into account, but stress concentrations due to the joint itself are not. These, and the other effects as summed up before, should all be included in the fatigue resistance curves. The stresses in the members can be calculated by ordinary mechanics theories.

- Structural hot spot stress: The hot spot stress does include the local stress concentrations caused by the joint. Only the effects of the weld itself are not taken into account. This method is preferred over the nominal stress method when the stress distribution is uncertain due to complex geometry of the joint. The hot spot stress can be calculated by extrapolating the stress at two points at a distance from the joint (figure 2.7). The stresses at these points can be determined by a Finite Element Analysis or by measurements. Multiple types of extrapolating the stresses are possible.

- Effective notch stress: The effective notch stress goes one step further and also takes the effect of the weld geometry into account. Joints are modeled including the welds. Stresses can be calculated using parametric formula, diagrams, or FEA. This method can only be used for the assessment of fatigue failure starting at the weld root or toe. Additional checks should be done for the parent material using either of the previous methods. The effective notch stress can be especially helpful in the comparison between different weld geometries.

- Stress intensity factors: Stress intensity factors are based on fracture mechanics, which describe the behavior of cracks or imperfections and the material around them. Usually, the nominal or hot spot stress approach is used to calculate the stresses at a location as if the crack or imperfection was not present. This stress is then adjusted by multiple functions that correct the stress state for the effects of the crack to end up with a stress intensity factor K. The correction functions for many situations can be found in literature (e.g. Broek (1982) [24]).
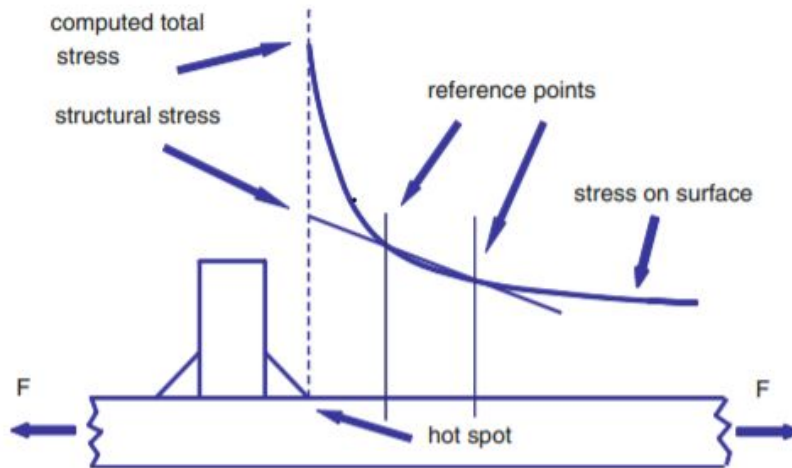
Figure 2.7: Explanation of the determination of the hot spot stress at a weld toe. The calculated or measured stress at two reference points is extrapolated to the location of interest [52].

2.3.3. Extracting stress ranges from stress history: cycle counting

Contrary to idealized set-ups like laboratory tests where constant amplitude tests are mostly used, real-life structures are often subject to irregular stresses of variable amplitude. The determination of a stress cycle in a highly irregular stress history can be less trivial than it may seem. Two methods to overcome this problem are the *rainflow* and *reservoir* counting method. Both give similar results for welded joints [52]. Figure 2.8 illustrates the reservoir method, which is easier to use when counting by hand [65]. The rainflow method is more suitable when using a computer to analyze long stress histories.
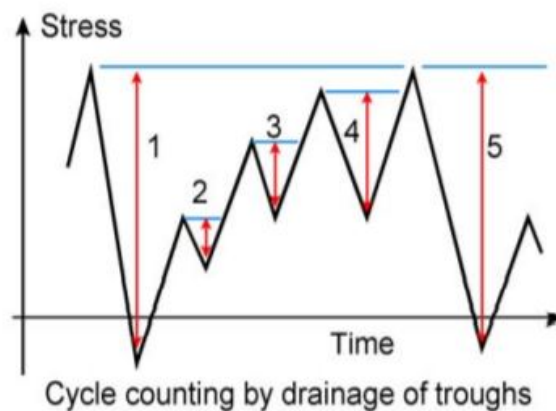
Figure 2.8: Illustration of reservoir counting. Each number in the figure represents a cycle with the stress range shown by the red arrow next to it [52].

2.3.4. Damage calculation: Palmgren-Miner

The problem of having variable amplitude load does not stop once the stress cycles are extracted from the stress history. The stress ranges of different magnitudes cannot be directly summed up and compared to a fatigue life found in codes, as these only give the expected number of cycles withstood for a constant stress range. To overcome this, the Palmgren-Miner rule is generally used. This rule assumes that each stress cycle causes some damage related to the number of cycles that can be withstood for a stress cycle of that magnitude. In formula:

$$D = \sum \frac{n_i}{N_i} \leq 1 \tag{2.2}$$

Where:

D : The expected damage during the service life of the structure

n_i : The number of load cycles of a certain stress range $|\Delta\sigma_i|$

N_i : The number of load cycles leading to failure for the same stress range $|\Delta\sigma_i|$ see figure 2.2
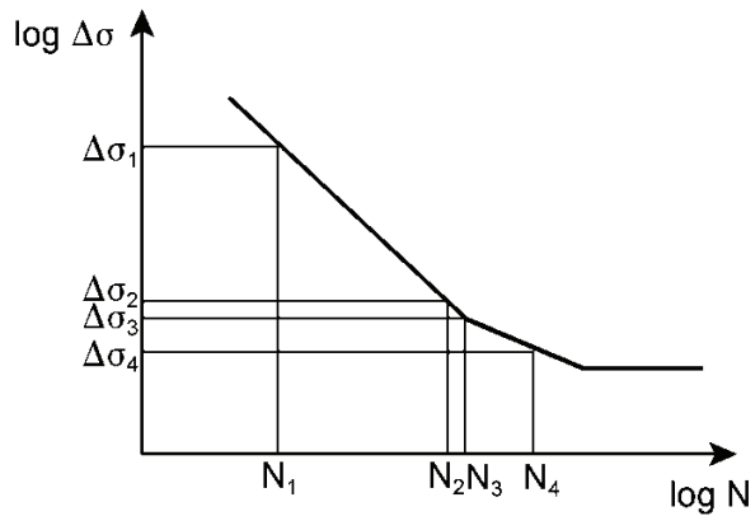
Figure 2.9: Determining N_i corresponding to a known σ_i from an S-N curve when using the Palmgren-Miner rule (equation 2.2) [3].

The Palmgren-Miner rule does not consider the loading sequence, which could lead to erroneous, non-conservative results. A proper safety factor should therefore always be used when applying the Palmgren-Miner rule [14].

3

Introduction to Orthotropic Steel Decks

This chapter will give an introduction to the origins of and developments towards the current orthotropic steel decks. After a summary of the concept and its main advantages, the history of the deck system will be discussed. The chapter then ends with a short discussion of innovations that fall outside of the main scope of this thesis. The primary goal of this approach is to familiarize the reader with the orthotropic steel deck system, its past and present problems, and what is done to mitigate these.

3.1. Concept and advantages

Orthotropic steel decks are built up from a steel plate which is stiffened by steel elements in two orthogonal directions. Stiffened steel plates are used in many fields of engineering, with applications found in the aerospace, maritime and civil engineering industry. For bridge decks, the stiffeners are usually executed as transverse *crossbeams* and smaller longitudinal *ribs* or *troughs* (figure 3.1). This clear distinction between elements in the deck construction results in different stiffness properties in perpendicular directions, and thus the reaction of the deck system may be called orthogonal-anisotropic, which abbreviates to *orthotropic* [6].
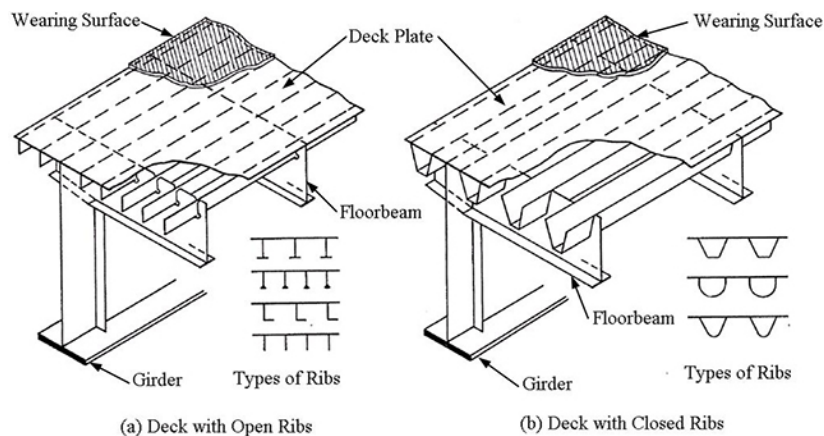
Figure 3.1: Common built up of an orthotropic steel deck. [29].

The main advantage of the orthotropic steel deck system, or OSD in short, is its low weight compared to comparable bridge deck systems [31]. This low weight is realized by efficient use of the available material, as the deck plate is used to support the traffic loads and acts as the upper flange of the main girders, crossbeams, and longitudinal stiffeners. Integral behaviour of deck plate and stiffeners requires rigid connections, which is accomplished by welding. Other advantages of OSD systems are its large strength and deformation capacity, ease of construction due to prefabrication, and reduced structural height [29, 31]. A service life of 100 years is possible when properly designed.

17

These advantages make it that orthotropic steel decks are applied in large numbers all around the world. The low weight of OSDs is especially beneficial for long span bridges, as more than 90 percent of the loads on these can come from the self-weight of the structure [57]. For the longest span bridges in existence, the OSD system is therefore even the most applied deck system [31]. Famous bridges as the Golden Gate bridge, the Millau Viaduct and the Akashi Kaikyo (currently the longest spanning bridge of the world) all have orthotropic steel decks. In the Netherlands, the deck system is often found in the bridges spanning the large rivers and canals, such as the Van Brienenoord bridge in Rotterdam and Galecopper bridge in Utrecht.

3.2. History of Orthotropic Steel Decks
3.2.1. Early developments
The first developments towards an orthotropic steel deck can be found in the 1930s in the United States and Germany. In the US, the *battledeck floor* was used for the first time in 1932 on the Salt River Bridge in Michigan [31]. The deck system, visible in figure 3.2, got its name as it was considered to be as strong as a battleship [29] and was built up from longitudinal I-shaped beams that were welded to a steel deck plate. The I-beams were in turn supported by crossbeams that were attached to main girders on the sides of the bridge deck. The deck was not yet an integral part of the crossbeams and main girders.
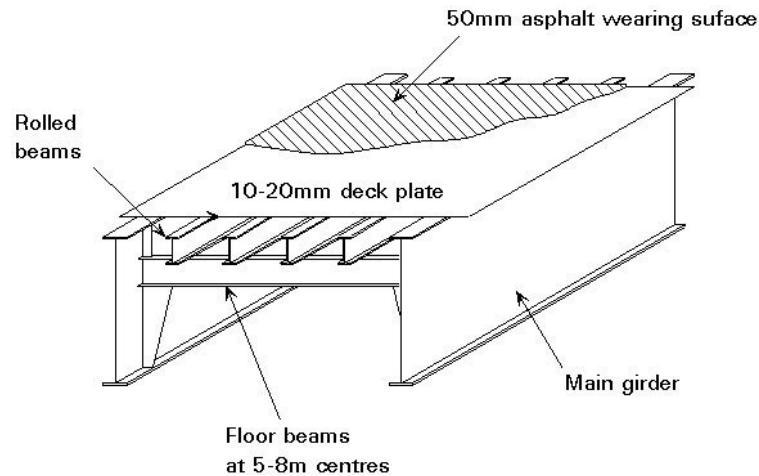
Figure 3.2: Conceptual built-up of a Battledeck floor as used in the 1930's in the USA, an early predecessor of the OSD [40].

Around the same time, German engineers used a similar system to build the bridge near Kirchheim/Teck in the Autobahn. The relatively short span of 17,5 meters was directly spanned by I-beams that were welded to the deck (figure 3.3). The same type of I-beams were also used in transverse direction. The center-to-center distance of these transverse beams was twice the distance of the longitudinal distance, resulting in an orthogonal-anisotropic plate construction. For longer spans, it was realized that a system with a division in function between primary and secondary beams would be necessary to give an economical design. However, this would result in complex stress patterns from a combination of local loads and global force transfer, with which no experience was present at that time. The large amount of welding necessary for this type of decks presented another problem, as welding was a time-consuming process under harsh conditions. Research was started to improve the economy of this type of decks, but was delayed by World War II [81].
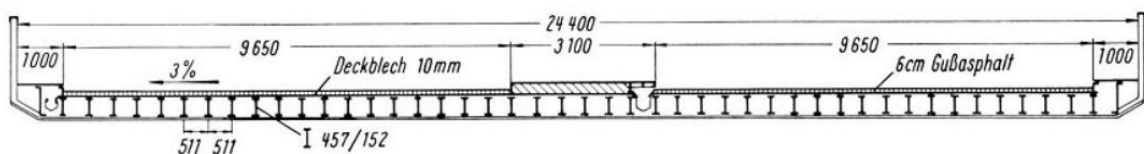
Figure 3.3: Cross section of the deck of the Autobahn bridge near Kirchheim/Teck, built before WOII [81]. The bridge was the first having an orthogonal-anisotropic deck plate construction and would form an important step towards the current OSD concept.

The aftermath of the war in Germany accelerated the developments towards the orthotropic deck systems we know today. Multiple long span bridges needed to be rebuilt with a shortage of steel [6]. Developments in theoretic work made better estimation of stress states possible and the war had caused strong developments in welding technique [81]. This first led to the application of steel decks in movable bridges, but was later extended to regular bridges as well. A milestone was the Kurpfalzbrücke in Mannheim, which was completed in 1950 (figure 3.4). This bridge was the first in which the deck was an integral part of the main girders, and thus the first using the modern concept of an OSD [81]. More would quickly follow, with already more than 40 bridges in Germany using an orthotropic steel deck in 1960 and several more in other countries [6].
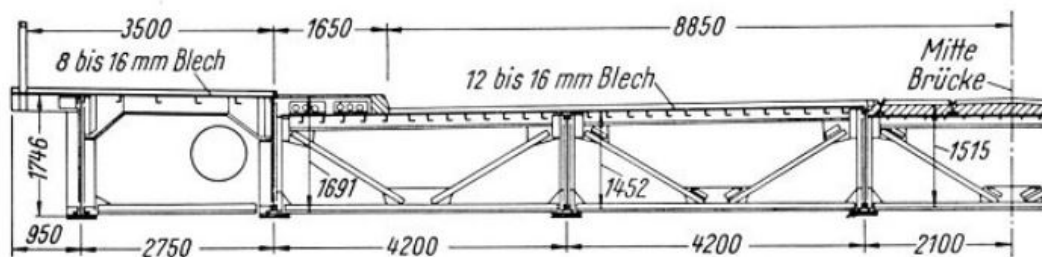
Figure 3.4: Cross-section of the deck of the Kurpfalzbrücke near Mannheim, built in 1950. Its integration of the deck plate in the main construction would make the bridge deck the first modern OSD [81].

3.2.2. Stiffener types

The first orthotropic bridge decks and its predecessors used open longitudinal stiffeners, such as the I-beams of the battle deck system and the bridge near Kirchheim/Teck, or the L-shaped stiffeners of the Kurpfalzbrücke. Other forms of open stiffeners can be seen on the left side of figure 3.1 and consist of bulb stiffeners and regular flat plate stiffeners. The open ribs have negligible torsional resistance, causing only small load transfer over the deck in transverse direction. Closed ribs, having a much higher torsional rigidity, were therefore introduced in 1954 in the bridge crossing the river Rhine between Duisburg-Ruhrort and Homberg, Germany [81].

The lateral load transfer possible with closed ribs makes the deck system more efficient and can result in an even lighter structure. Figure 3.1 shows that, just as with open ribs, multiple forms of closed ribs are possible, varying from trapezium and V-shaped to semicircular. Other advantages of closed ribs are the decreased amount of welding and painting necessary due to the inaccessibility of the inside of the rib. Conversely, this inaccessibility causes the joint between closed rib splices and between closed rib and crossbeam to be more complex. Their torsional rigidity also causes secondary stresses and deformation in the ribs and joints, making them more susceptible to fatigue [116].

3.2.3. Fatigue problems

In the years after their introduction in Germany, the improved efficiency of closed rib decks made them to be the main choice for highway bridges. In 1971, however, fatigue damage was observed in the Severn Bridge in the United Kingdom, after being in use for only five years [93]. More bridges showing fatigue damage would soon follow, such as the Sinntal and Haseltal bridges in Germany [115]. All three bridges were opened in the 1960s, when the fatigue phenomenon was known, but not expected to occur in highway bridges [93]. This had resulted in the design of joints that were not suited for fatigue loading. Damages like on these bridges can be prevented by the use of continuous stiffening ribs, instead of fitting them between crossbeams (figure 3.5), and providing maximum penetration of the welds connecting the ribs to the crossbeams and deck [115]. Both are now recommended in the Eurocode and have become common practice [1].

The fatigue problems did not stop after these alterations, however. The continuous closed ribs caused large stress concentrations in the crossbeam web due to out of plane deformation by the forced rotation of the ribs (figure 3.6). It was tried to solve this by introducing a cut-out or cope hole in the crossbeam web at the bottom of the connection with the closed rib. A bulkhead was later added within the closed rib to prevent peak stresses caused by the large hole in the crossbeam web (see left side of figure 3.7).
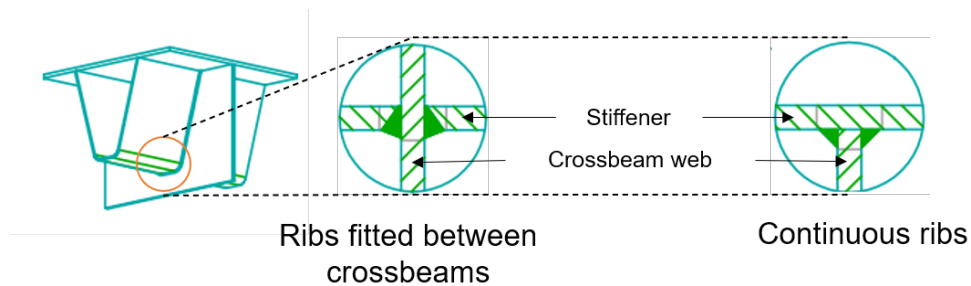
Figure 3.5: Comparison of rib to crossbeam detail for ribs fitted between the crossbeams and continuous ribs. Edited from [67].

Nevertheless, the fatigue resistance of the structure was not improved. Heavy cracking occurred in the bulkhead and at the rib web just below the edge of the cut-out. Engineering intuition had failed to find working solutions for this complex problem. Finite element analysis and experiments in the early 2000's led to better solutions, introducing a smooth transition between the cut-out and the rib and removing the bulk head (right side of figure 3.7) [29].
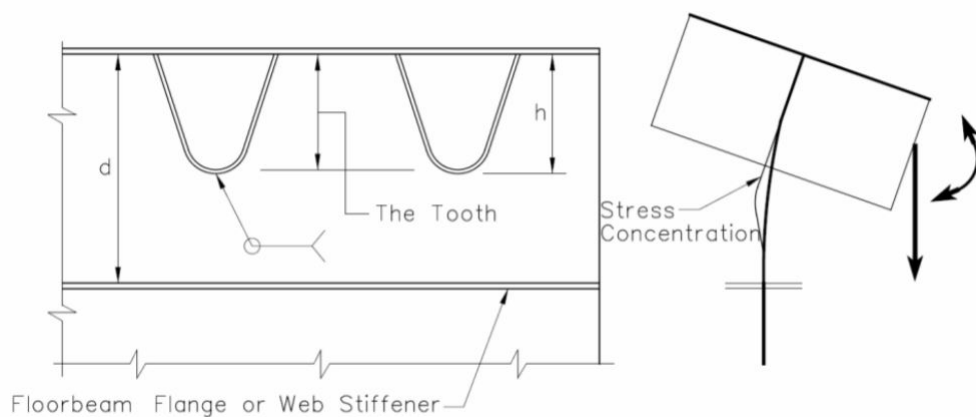
Figure 3.6: Rotation of troughs leading to out of plane deformation of and stress concentration in the crossbeam web [29].
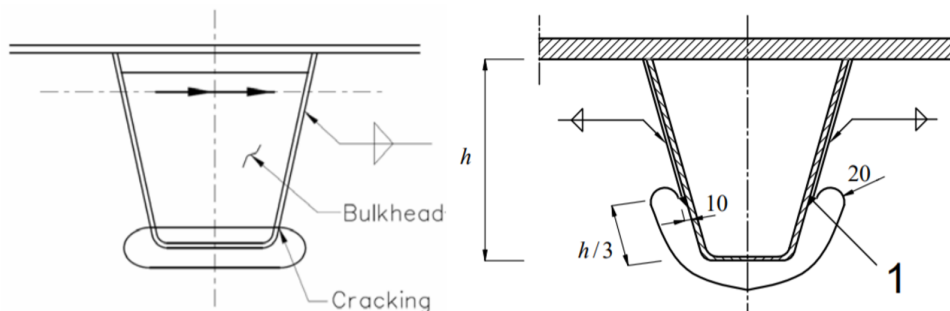
Figure 3.7: Early version of a cut-out and bulkhead on the left [29] compared to a newer versions of the cut-out on the right [1]. The bulkhead is left out and the shape of the cut-out is different in newer OSDs.

More problems occurred in 1997, when serious fatigue damage was found at the Van Brienenoord bascule bridge in Rotterdam after only 7 years of service life. Cracks of up to 700 mm length were found at the connection between the trough and deck near the crossbeams (figure 3.8), seriously compromising the safety of the passing traffic [93]. This type of crack was not observed before and stimulated more research towards fatigue damage in orthotropic steel bridge decks. At the location of the crack, the large difference in stiffness between the unsupported deck above the trough and rigid crossbeam to through connection causes a large stress concentration in the deck [116]. The resulting crack starts at the bottom side of the deck, inside the closed rib, making it impossible to spot during visual inspection.

Detection using more advanced techniques like ultrasonic testing can find these cracks before they propagate to the surface, but this requires the removal of surfacing [93]. Besides being very costly, the regular inspections may thus be very obstructive to traffic.
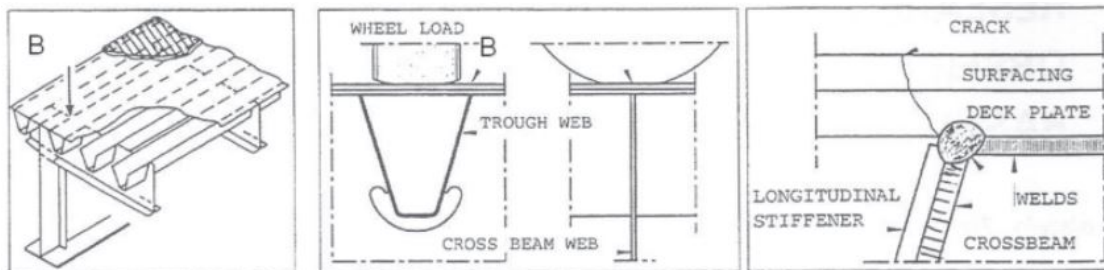
Figure 3.8: Location of cracks found in the Van Brienenoord bridge in 1997: in the deck plate at the connection with the trough, near the intersection of the crossbeam [93].

Other than the cracks found in the Severn, Sinntal and Haseltal bridges, cracks in the Van Brienenoord bridges were not avoided by the improvement of joints. Instead, the thickness of the deck plate for the replacement deck system was increased from 12 mm to a thickness varying between 18 and 28 mm. The Dutch National Annex of the EN 1993-2, covering steel bridges, currently recommends a minimum deck plate thickness of 18 or 22 mm for bridges in main roads, depending on the applied surfacing on the deck [2]. Increasing the thickness of the deck plate significantly decreases the stresses at fatigue-sensitive locations [76], but comes at the cost of a larger self-weight of the deck. This is not compensated by the possibility for less or lighter ribs, as the deck plate is responsible for more than half of the weight of the total deck system in a typical configuration [17].

Although the larger self-weight is a disadvantage in most situations, it may be especially problematic in the renovation of damaged bridge decks. The existing superstructure should preferably be maintained, but is designed for the lighter existing bridge deck, while at the same time the live load has often increased during the bridge's lifetime. Limiting the self-weight of the new deck system can therefore be crucial for its success.

3.2.4. Refurbishment techniques
The unexpected fast deterioration of bridges with OSD systems brought the need for lightweight techniques to considerably extend the lifetime of the damaged decks. The fatigue damage of the Van Brienenoord bridge started research towards the use of Reinforced High Performance Concrete (RHPC) as an overlay of the steel deck plate [58]. Inspiration came from the large difference in performance between the fixed and bascule part of the Van Brienenoord bridge. The latter showed much more fatigue damage, while the only difference between the two bridge decks was the presence of a mastic asphalt layer between the deck plate and wearing surface on the fixed bridge, which was not used for the bascule bridge.

The Caland bridge in the port area of Rotterdam was the first bridge where the RHPC strengthening was applied [58]. The 50 mm mastic asphalt layer was replaced by a layer of 50 mm reinforced high performance concrete, which has a much higher stiffness. The stiffer concrete layer spreads the traffic loads better and can generate composite action with the steel deck if a proper connection between the steel and concrete is ensured. The refurbishment of the bridge was done within a few days and proved the potential of the method. Strain measurements on the bridge showed a reduction of stresses of 80 percent in the deck plate, and 60 percent in the deck-to-rib joint.

Another option to strengthen the damaged deck is to install an additional steel plate on top of the existing deck plate. This can be done using a thin epoxy or a thicker polyurethane adhesive layer to bond the two steel plates. The bond between the steel plates generates so-called 'sandwich' action, where the two plates work together to increase the bending stiffness en reduce the stresses in the deck. Testing showed both systems are viable strengthening options [32, 41]. The sandwich plate system, using the thicker polyurethane (PU) core, has already been applied in a pilot project in the Krefeld Schönwasserpark bridge in the German Autobahn. Experimental results showing a large reduction of stresses in the deck plate were confirmed by tests during this pilot project.

3.3. Parallel innovations for OSDs

Despite this thesis' focus on the structural optimization of OSDs, it can be useful to be aware of other efforts to improve the system. Two innovative subjects that have received significant attention are computational analysis based on fracture mechanics and the use of new materials like fiber-reinforced polymers. Their status is shortly discussed here. Innovation of the design by structural optimization is separately discussed in chapter 8.

3.3.1. Computational fracture mechanics

The fatigue problems encountered at various bridges in the Netherlands were overlooked by researchers in the past [116]. It illustrates the difficulties in the fatigue assessment of structures. Possible improvements are still sought, for which one of the options can be found in the use of fracture mechanics. Finite element calculations using fracture mechanics can incorporate crack propagation into the analysis to give a better estimate of the (remaining) fatigue life of a structure [31]. The strong interest in the subject recently can be found in the papers by Nagy et al. and Wu et al. [77, 117], and the extensive amount of recent Master theses at the TU Delft treating this subject (e.g. [48, 111]).

When using fracture mechanics, special attention can be given to the effects of the loading sequence and residual stresses in the structure. The current Eurocode neglects these factors, but the paper by Nagy et al. [77] shows that these can have a considerable effect on the expected service life of bridge decks. Using more accurate methods that include these effects can prevent the overestimation of dimensions in structures [31].

3.3.2. New materials

Parallel to the efforts regarding the improvement of the orthotropic bridge deck concept, a continuous search towards alternatives has been going on. One of the most promising options has been the application of fiber reinforced polymers (FRP) for bridge decks. FRPs offer a high strength-to-weight ratio, enabling lightweight solutions for bridge decks [109]. Applications in The Netherlands are abundant in footbridges, but use of FRPs in road bridges is scarce [32]. The Nelson Mandela bridge in Alkmaar, The Netherlands, is one of these applications. Opened in 2016, its 22,5 meter span meant the bridge was the largest road bridge made of FRP in the world [94]. The bridge shows the possibilities of the material, but also the early stage of development of the application of FRP in road bridges.

Another option for a lightweight bridge deck was suggested by De Corte in 2011 [32]. His proposal can be described as a composite steel-concrete sandwich plate. Similar to the steel-polymer sandwich plate described in section 3.2.4, two outer steel plates cover an intermediate concrete layer that should transfer shear loads between the plates (figure 3.9). The lack of welds in the structure is claimed to make the system better resistant to fatigue problems, which is proven in a later study [33]. However, in this later study, it is also mentioned that the self-weight of the system is expected to be higher than that of a traditional OSD. In situations where the the mass of the deck structure is highly critical, such as renovations or long span bridges, this will thus not be a viable option.
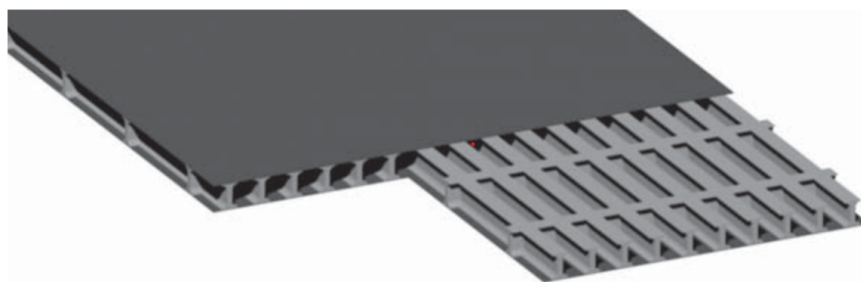
Figure 3.9: Steel-concrete sandwich plate, an alternative to an OSD as suggested by De Corte [32].

4

Design of Orthotropic Steel Decks

This chapter will give an overview of the necessary steps for the preliminary design of an orthotropic steel deck. First, the limit states considered by the Eurocode for OSDs will be shortly explained. As the fatigue limit state is almost always governing, the remainder of the chapter will not further discuss the serviceability and ultimate limit state. Section 4.2 will give an overview of the fatigue analysis of an OSD. The sections following it will discuss the necessary input and important aspects in more detail. The chapter ends with a summary. The general part of the fatigue calculation (framed in orange in figure 4.1) was already discussed in chapter 2 and will not be treated here.

4.1. Relevance of the limit states for OSDs in the Eurocode

As illustrated in the previous chapter, fatigue plays a major role in the service life of orthotropic steel bridge decks. It can be expected that this is also present in the design methodology of such systems, which indeed mainly focuses on the fatigue limit state of joints. Conversely, testing has proved that the large ductility of OSD systems results in an enormous reserve strength capacity, making the ultimate limit state unlikely to be governing for design [29].

The serviceability limit state (SLS) consists of the usual limits on deflection to prevent loss of clearance height and water discharge, dynamic amplifications, and cracking of surfacing. Annex C of EN 1993-2 gives recommendations for the thickness of the deck plate and the stiffness of the longitudinal stiffeners to realize this. The deformation limits are supplemented with some stress limits in certain elements to prevent excessive yielding leading to permanent deformations. Finally, ease of maintenance and repairability is also mentioned in the SLS [1].

For the fatigue limit state, which is most likely to be governing, EN 1993-1-9 [3] describes two strategies for design: the safe life and the damage tolerant method. The safe life method is the more conservative of the two. A design using this method should ensure that the structure will fulfill its function during its service life without the need of regular inspections. This can be done by making sure that stresses at fatigue-sensitive locations are always below the cut-off limit of fatigue damage. For many situations, this will result in very uneconomical designs. The damage tolerant approach may then be adopted, which accepts the possibility of cracks appearing in the structure during its service life. This approach is only possible when regular inspections are done and enough redundancy is present in the structure.

4.2. Outline fatigue analysis of an OSD

Figure 4.1 shows a flowchart of a fatigue analysis based on the preliminary design of the Van Brieneno-ord bridge deck renovation. The essential steps of a general fatigue calculation were already given in section 2.3, and can be recognized in the bottom part of figure 4.1. As can further be seen, the asphalt stiffness, load model, and fatigue detail category are needed as input for the calculation. These will therefore be further discussed in this section. Special details of the finite element analysis are also treated.

Calculation steps   Input

```
┌──────────────────────────┐                 ┌──────────────────────────────┐
│ Center trucks at assumed │                 │ Determine variation of asphalt│
│ worst position           │                 │ stiffnesses due to temperature│
└──────────────────────────┘                 └──────────────────────────────┘

┌──────────────────────────┐                 ┌──────────────────────────────┐
│ Determine transverse     │                 │ Determine load model and axle │
│ position of wheel loads  │                 │ types                         │
│ within a lane            │                 └──────────────────────────────┘
└──────────────────────────┘
                                             ┌──────────────────────────────┐
┌──────────────────────────┐                 │ Transverse wheel position     │
│ Run FEA with 3 axle types│                 │ distribution                  │
│ tracking across model.   │                 └──────────────────────────────┘
│ Repeat for each of 5     │
│ weave positions and 6    │                 ┌──────────────────────────────┐
│ temperatures             │                 │ Number of trucks expected     │
└──────────────────────────┘                 └──────────────────────────────┘

┌──────────────────────────┐                 ┌──────────────────────────────┐
│ Combine axle results to  │                 │ Probability of multiple trucks│
│ find results for all     │                 │ passing at once               │
│ possible truck passages  │                 └──────────────────────────────┘
└──────────────────────────┘

┌──────────────────────────┐
│ Retrieve stress history  │
│ for fatigue sensitive    │
│ locations from results   │
└──────────────────────────┘

┌──────────────────────────┐
│ Extract stress ranges    │
└──────────────────────────┘

┌──────────────────────────┐
│ Combine stress ranges and│
│ calculate the number of  │
│ expected cycles for all  │
│ resulting stress ranges  │
└──────────────────────────┘

┌──────────────────────────┐                 ┌──────────────────────────────┐
│ Calculate the expected   │                 │ Determine detail category     │
│ damage with the Palmgren-│                 └──────────────────────────────┘
│ Miner rule               │
└──────────────────────────┘
```

FE Analysis · Load Model · Fatigue calculation

Figure 4.1: Flowchart of a fatigue analysis of an OSD (based on the preliminary design of the renovation of the Van Brienenoord bridge [8]).

Notable in figure 4.1 is the block representing the FE Analysis, as it shows one of the reasons why the computational demand of a fatigue analysis may quickly become large. The load model to be used considers three different axle types, that should be placed at five different transverse positions on the deck and tracked across the deck (see section 4.4). The results in a great amount of load cases, each of which should be solved for a model with a different asphalt stiffness (see section 4.3). A simple calculation reveals that this already gives 90 possible permutations that should be solved in the FEA, which increases even further when the longitudinal positions needed for tracking the load over the deck are included. A detailed fatigue analysis of an OSD can therefore need well over 1000 load cases.

4.3. Asphalt stiffness

According to EN 1991-2 [4], the effect of the wearing surface may be integrated in the structural calculation by spreading local loads under an angle of 45° to the center of the deck plate. However, this is often a non-conservative assumption when the wearing course consists of asphalt (see also appendix A). The stiffness of asphalt depends on its temperature, as can be seen in figure 4.2. Especially for warmer conditions, a spread of 45° will not occur in the asphalt and will thus give too optimistic results.

When a more accurate analysis is needed, the asphalt layers may be modeled by volume elements. The temperature dependent stiffness of the asphalt layers should be accounted for in the model. Rijkswaterstaat prescribes to consider six different stiffnesses of the asphalt layer, which should be based on the temperatures on the x-axis of figure 4.3 and the temperature-stiffness relation of the used material (e.g. figure 4.2). The six models that are obtained this way should each be combined with the different wheel types and load positions as described in the previous section.
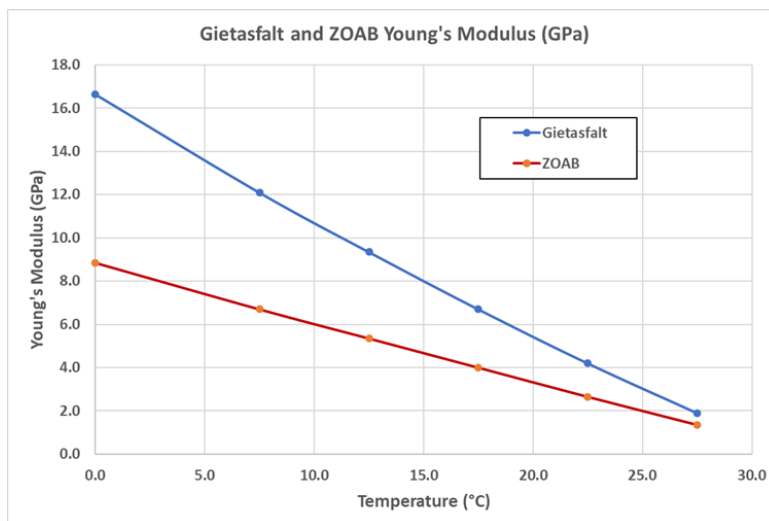
Figure 4.2: Young's modulus of mastic asphalt and ZOAB layers for different temperatures. Taken from [8], based on [88].

The asphalt temperatures of figure 4.2 are not equally likely to occur. This should be accounted for during the cycle counting in the fatigue analysis. The amount of trucks that is to be expected for each temperature can be calculated by using the total expected amount of trucks (see table 4.1 and section 4.4) and the proportion of trucks for each temperature as found in figure 4.2.
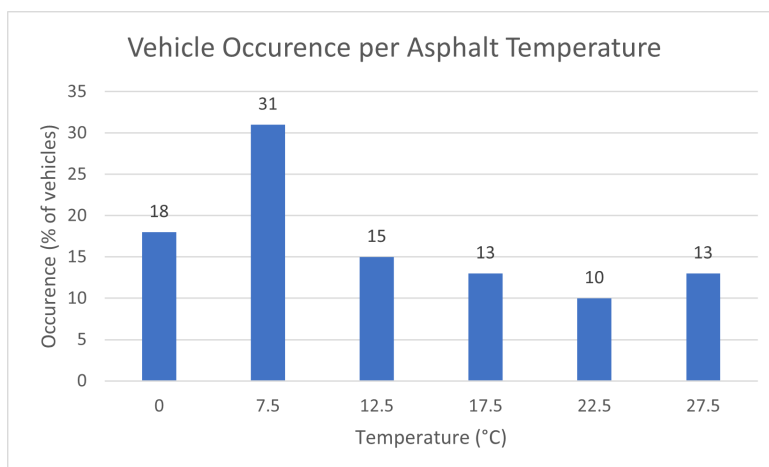
Figure 4.3: Percentage of total trucks expected to pass a bridge at different asphalt temperatures according to [88].

The volume elements can also be used to account for possible composite action between the steel deck and layers on top of it. However, it should be checked to which extend this effect is expected to occur in the deck. Membranes are often used between the different layers, preventing the generation of shear forces necessary for composite action. A conservative approach may therefore be justified, where the cooperation between the wearing courses and the deck is completely neglected [8].

4.4. Load models

The relevant load models for the design of bridges are found in EN 1991-2 [4] and its national annex [5]. Different loading schemes are used for the ultimate and serviceability limit state on the one hand, and the Fatigue Limit State on the other hand. The loading schemes of the ULS and SLS consist of four load models, which represent the actions from regular cargo trucks and passenger vehicles (LM1), dynamical effects of traffic on deep beams (LM2), extraordinary vehicles (LM3), and large crowds (LM4). As mentioned in section 4.1, the ULS and SLS limit states are rarely governing for the design of orthotropic steel decks. These load models will therefore not be discussed in more detail here.

For fatigue loading, EN 1991-2 [4] gives five load models. Other than the load models for the ULS and SLS, only one of these should be adopted for testing. The models do not differ from each other in types of loading, but in complexity and conservatism. Load models 1 and 2 check if the service life of a structure may be seen as infinite. Load models 3 and 4 both test the fatigue life, where model 3 uses only one vehicle and model 4 a set of equivalent trucks. The Dutch national annex [5] splits load model 4 into 4a and 4b. 4a should be used when materials are used for which only the stress range is of interest for fatigue damage (e.g. steel), while 4b should be used when the magnitude of the stress contributes as well (e.g. concrete). Model 5 uses measured traffic data to estimate the fatigue life of the structure. The higher numbered models have a greater complexity, but a lower level of conservatism.

The ROK ('Richtlijnen Ontwerp Kunstwerken' - Translation: 'Guidance for Design of Civil Works') [89], published by Rijkswaterstaat, prescribes that load model 4a must be used for steel bridges in the Netherlands. Model 5 may be used when this is explicitly stated in the contract with Rijkswaterstaat. Model 4a consists of a set of five equivalent cargo trucks, shown in table 4.2. The wheel types described in the last column can be found in table 4.3. At the moment of writing, an updated version of the ROK is worked on, which prescribes to limit the length of the wheel imprint to 220 mm [88].

As can be seen in the fourth to sixth column of table 4.2, the distribution of the trucks depends on the type of traffic crossing the bridge. Traffic covering larger distances will in general consist of heavier trucks. Together with the number of expected trucks found in table 4.1, the expected number of each truck type can be calculated. The number of expected trucks depends on the type of road the bridge is part of. The Dutch national annex [5] prescribes that the 'Long distance' traffic type (Lange afstand in table 4.2) should be combined with traffic category 1 of table 4.1. The 'Medium distance' (Middellange afstand) should be combined with categories 2 and 3, and the 'Local traffic' type is valid for category 4.

	Traffic categories	N_{obs} per year and per slow lane
1	Roads and motorways with 2 or more lanes per direction with high flow rates of lorries	$2,0 \times 10^6$
2	Roads and motorways with medium flow rates of lorries	$0,5 \times 10^6$
3	Main roads with low flow rates of lorries	$0,125 \times 10^6$
4	Local roads with low flow rates of lorries	$0,05 \times 10^6$

Table 4.1: Truck numbers for different types of roads [4].

Finally, the lateral placement of the loads on the bridge deck should be determined. It is to be assumed that the (theoretic) driving lanes can be present anywhere on the bridge deck. The most unfavorable position should therefore be chosen. For local checks, a lateral spread of loading position can be included to distribute the effects of the loads. Figure 4.4 shows this spread, which is often referred to as the *weave*, and the frequency of the positions that should be used.
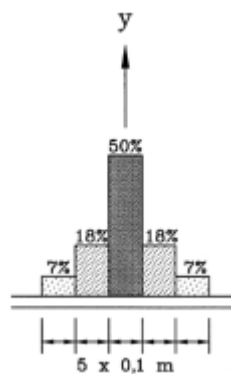
Figure 4.4: Lateral weave of the axis of the vehicle that should be applied. The percentages indicate the proportion of total trucks that is to be expected at each position [4].

Type voertuig		Verkeerstype				
Afbeelding van de vrachtwagen	Afstand tussen de assen m	Gelijkwaardige aslast kN	Lange afstand % [a]	Middellange afstand % [a]	Lokaal verkeer % [a]	Wiel-type
	4,5	70 130	20,0	50,0	80,0	A B
	4,20 1,30	70 120 120	5,0	5,0	5,0	A B B
	3,20 5,20 1,30 1,30	70 150 90 90 90	40,0	20,0	5,0	A B C C C
	3,40 6,00 1,80	70 140 90 90	25,0	15,0	5,0	A B C C
	4,80 3,60 4,40 1,30	70 130 90 80 80	10,0	10,0	5,0	A B C C C
[a] Percentage vrachtwagens.						

Table 4.2: Trucks used in Load Model 4a of the Dutch national annex to NEN-EN 1991-2 [5].
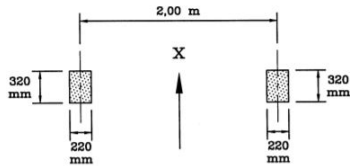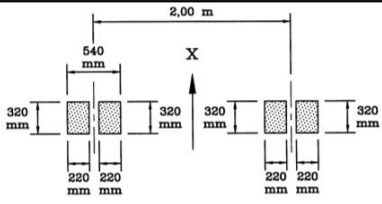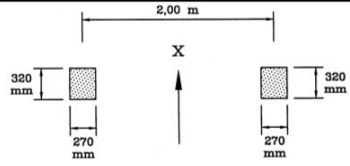
WHEEL/ AXLE TYPE	GEOMETRICAL DEFINITION
A	
B	
C	

Table 4.3: Wheel types as found in NEN-EN 1991-2 [4]. The future version of the ROK advises to use a wheel length of 220 mm for all types instead of the 320 mm given here [88].

4.5. Critical joints

Eurocode 3 part 2: Steel Bridges [1] states that all structural elements should be checked for possible fatigue damage. The deck plate, crossbeams, longitudinal stiffeners, and connection between the crossbeams and longitudinal stiffeners are explicitly mentioned. However, as discussed in section 2.1.4, fatigue cracks in steel structures will almost certainly start at welded joints. The Eurocode therefore identifies five critical zones in the decks which are likely to be governing:

1. Deck plate subject to longitudinal stresses at fillet welds in transverse direction (e.g. deck-to-crossbeam joint).

2. Deck plate subject to longitudinal stresses at welded connections between the longitudinal stiffeners and deck plate.

3. Closed stiffener at the connection with the crossbeam.

4. Butt weld at the (transverse) splice between longitudinal stiffeners, including base plates. The deck plate is also vulnerable at this location.

5. Free edges of cut-outs in crossbeam webs at the bottom side of the longitudinal stiffeners.

These zones are also visible in figure 4.5. The figure also highlights the butt welds at the deck plate splices as a critical zone. The paper by Yan [119] - where the figure is taken from - identifies this as a fatigue sensitive joint with a short fatigue life compared to the other evaluated joints visible in the picture. The deck-to-crossbeam and deck-crossbeam-rib joint were not considered in Yan's paper but are critical zones according to the Eurocode, and were therefore added to the figure.

For decks featuring continuous ribs, the deck-crossbeam-rib joint can be considered as a special case where critical zones 1 and 2 meet. This is also the location of the cracks in the Van Brienenoord bridge (compare figure 3.8), and thus proven to be a location of interest. Decks with ribs fitted between the crossbeams are less sensitive to fatigue damage at this location.
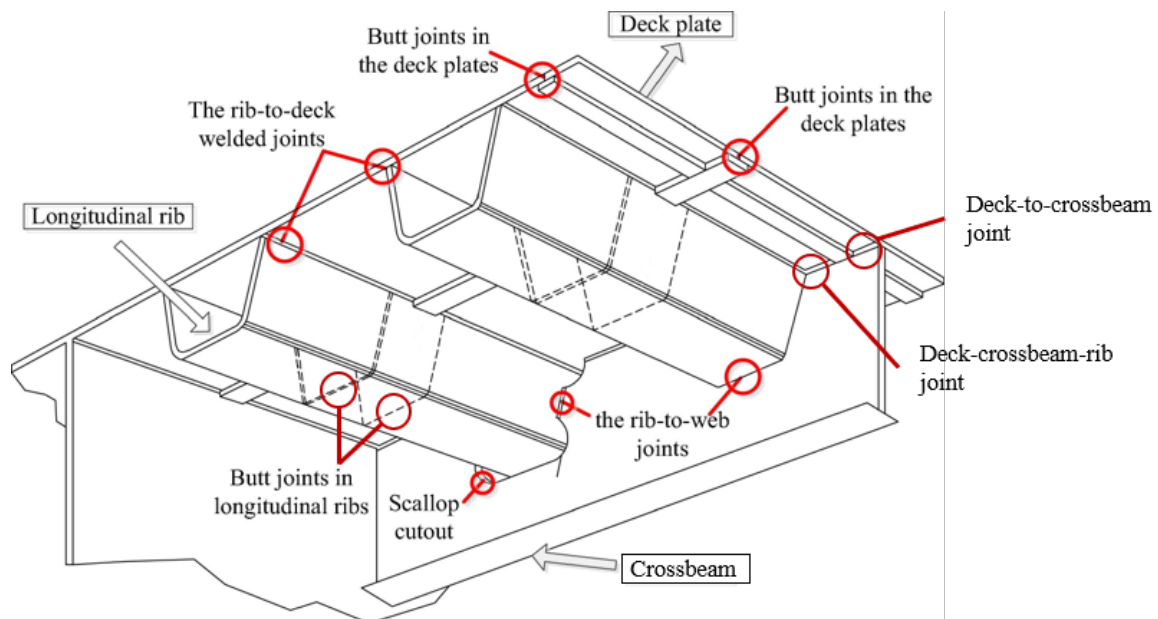
Figure 4.5: Critical zones for fatigue in an OSD with closed and continuous stiffeners [119] (edited).

4.6. Finite element modeling

As described in section 3.2.1, the development of theoretical work made more accurate calculations of stress states in orthotropic decks possible. However, the geometry of fatigue details is often too complicated to determine the stress state around it by analytical methods [79], and parametric formulas are rarely available [52]. Nowadays, finite element analysis is thus essential in the design of orthotropic steel decks.

Yet, even with FEA, the calculation of nominal stresses at many fatigue details is far from trivial [79]. For these fatigue details, the hot-spot stress (see section 2.3.2) is therefore used to determine the governing stresses. Finite element analysis for the hot-spot stress requires choices in the modeling of joints and meshing of structural members. Recommendations from literature are presented here.

4.6.1. Element types

Fatigue details in orthotropic decks may be modeled using shell or volume elements. Shell elements are to be modeled in the center of the respective plate, and attached plates should be connected at the intersection of mid planes. Welds at connections can be modeled by using thicker elements at weld locations (see figure 4.6), inclined elements, or rigid links. This is especially relevant when multiple discontinuities are present close to each other, although solid elements may give more accurate results in these cases [79]. The new ROK [88], meant to give recommendations for the analysis of OSDs and still under development at Rijkswaterstaat, prescribes to model all welds in the deck by using thicker elements at weld locations.

When solid elements are preferred, these may be used in a single layer over the thickness of the plate. Quadratic elements with reduced integration are sufficient and perform well. Linear elements may be prone to shear locking, while using multiple element layers over the thickness would enable a non-linear stress peak to form around the weld. This would have to be accounted for, as excluding the stress peak from the results is the main goal of the hot-spot stress approach [52, 79].

4.6.2. Mesh size and extrapolation

In Niemi [79], a distinction is made between type a and type b hot-spots. The mesh and extrapolation method of type a hot-spots is dependent on the thickness of the member, while for type b it is not. This division is based on the presence of out-of-plane bending at type a hot-spots, which is negligible for type b. No mention of such a distinction is made in the future version of the ROK [88]. The out-of-plane bending present in almost all fatigue-sensitive details could be the cause of this. Only type a details will therefore be discussed further.

Also according to Niemi, a relatively coarse mesh with an element size equal to the member thickness may be used in combination with quadratic elements. Stresses then need to be extracted from the center of an element at 0,5 and 1,5 times the thickness of the member. The ROK, on the other hand, prescribes to use a finer mesh with linear elements smaller than half of the thickness of the member. The location of stress extraction for the extrapolation is the same.

It should be noted, however, that the location of the stress extraction and extrapolation does depend whether the welds are modeled or not. If these are neglected, the distances should be measured from the intersection of the members. The extrapolation should also be performed towards this junction. When the welds are modeled (e.g. by rigid or thicker elements) the reference point moves to the weld edge [79] (see figure 4.6).
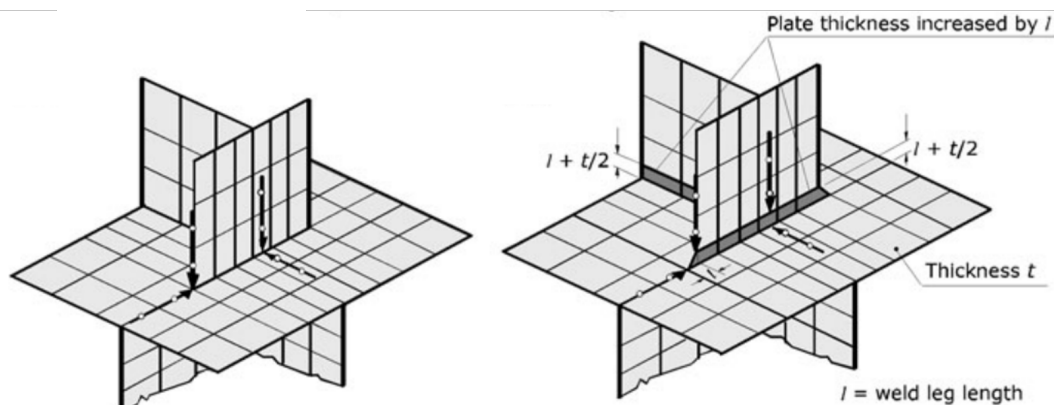
Figure 4.6: Examples of relatively coarse meshes for shell elements. In the left figure, the effects of the weld are neglected, while on the right, these are included by using thicker elements. The extrapolations for the hot-spot stress are indicated with arrows and nodes [79].

4.7. Summary

This chapter discussed the essential elements of the analyses needed for a preliminary design of an orthotropic steel deck. These will form the basis for the choices that will be made in the remainder of this thesis.

Summarized, a preliminary design should check a set of critical welds for the expected fatigue damage. The ultimate and serviceability limit state are unlikely to be governing for the design of the deck.

Nowadays, fatigue damages are generally calculated using finite element analysis due to the complex stress state around the joints. The applied loading consists of a set of five equivalent cargo trucks (table 4.2) having three different axles (table 4.3). Bridges in highways are subjected to two million trucks per year, distributed over the equivalent truck types as given in table 4.2. The loads should move over the deck and the worst possible transverse location should be assumed. For local checks, the transverse position of some trucks may be slightly shifted to soften the effect of stress concentrations (figure 4.4).

For the execution of the finite element model and the implementation of the asphalt layers, deviant recommendations can be found in literature. Suggestions for element types and mesh sizes vary and multiple options are given for the modeling of welds. The Eurocode furthermore allows the spread of wheel loads trough the asphalt layers under an angle of 45°, while newer recommendations from Rijkswaterstaat prescribe to model the asphalt layers with volume elements. Final choices for these factors will be discussed later in this thesis, mostly in chapter 11.

As a whole, this chapter also illustrated the complexity and large computational demand of fatigue analysis for OSDs. It was shown that, for a complete analysis, a considerable amount of load cases needs to be evaluated for a highly detailed finite element model. The run times needed for this are substantial and reducing these is a major focus of the next part in this thesis. Chapters 11 and 13 discuss the most important strategies therein.

Introduction to Structural Optimization

This chapter will give an introduction to the mathematical approach of structural optimization (SO). It will form a basis for understanding the optimization problems that will be stated further on in this thesis.

Firstly, the concept of structural optimization is defined and its possible uses within a design process are explored. The next section presents the mathematical form in which structural optimization problems are usually encountered. It also introduces some terms that are important for optimization problems in general. The third section states the traditional three forms that are often distinguished in SO: sizing, shape and topology optimization, and adds the description of a fourth: parametric optimization. The chapter concludes with a historical overview of the developments within the field of structural optimization.

5.1. Definition and use

For a definition of structural optimization, a quote from Christensen and Klarbring [28] is used:

> "Structural optimization is the subject of making an assemblage of materials sustain loads in the best way."

It can be argued that this addresses the fundamental core of any (structural) engineering problem, as any decent design will be intended to perform its function in the best possible way. The field of structural optimization, however, approaches the problem in a more mathematical manner.

This approach does lead to an immediate problem, since not all functionalities and demands tied to a structure can be effectively captured in mathematical sense. Clear examples are aesthetics and social influences of the structure. It is therefore useful to identify the role of this mathematical sense of structural optimization in a common design process, which Kirsch [64] divides into the following four steps:

1. Analysis: The start of each design should be to identify the function of the structure. This gives a set of demands and constraints the design should satisfy, which are supplemented by requirements from stakeholders.

2. Conceptual design: Based on the analysis made in the previous step, the designer forms an idea for the structural system to be used. A first solution based on this system is suggested.

3. Optimization: The suggested solution is elaborated and possible improvements are made within the constraints from earlier steps.

4. Evaluation and detailing: The results of the optimization step are checked for the requirements from the first step, and a decision to accept or decline the design. When the design is accepted, a further detailing can be done. When the design is declined, a return the either of the previous steps can be made.

Structural optimization can be used in the conceptual design phase to bring inspiration for possible solutions to the problem. Especially for unique or complex designs, computational optimization tools can be valuable. Engineering judgment and intuition will not always provide adequate answers to these problems, as was seen in the example of the cut-out form in orthotropic bridge decks explained in section 3.2.3.

The described approach to the optimization step is traditionally of iterative nature, usually adopting a trial-and-error tactic. A design is suggested and tested, then altered based on intuition and experience, and tested again. A more mathematical approach could automate this process, potentially leading to better designs in a shorter time span [28].

5.2. Mathematical formulation

For structural applications, an optimization problem has the form of [28]:

$$
\text{SO} \begin{cases} \text{minimize} & f(x,y) \text{ with respect to } x \text{ and } y \\[1em] \text{subject to} & \begin{cases} \text{design constraint on } x \\ \text{behavioral constraint on } y \\ \text{equilibrium constraint} \end{cases} \end{cases}
$$

Where:

- $f(x,y)$ is the objective function, expressing the quantity that should be optimized. In structural design problems, this can for example be cost, weight, displacement, or number of nodes.

- x portrays the design variables. These variables are to be chosen by the designer or the algorithm and can be changed to find an optimal design. Examples in structural engineering may be cross-sectional dimensions, orientation of elements, or material choice.

- y forms the state variable, describing the structural response of a given design x. Quantities like displacement, stresses, and strains may be found in y.

x and y can be functions or vectors in this set-up. Design constraints narrow the possible values of design variables, such as minimum or maximum values for cross-sectional dimensions. Behavioral constraints limit the values of state variables. Natural examples may be a limit on maximum stress or deflection of the structure. Both constraints are often presented as $g_i(x,y) \leq 0$. As the finite element method is generally used in structural optimization, the equilibrium constraint generally has the form of $\mathbf{K}(x)\mathbf{u} = \mathbf{f}(x)$, but differential equations can be used as well. The dependence of the stiffness matrix and force vector on the design is clear from the "(x)" that appear in the equation. All of these combined, the formulation looks like:

$$
\begin{aligned} \min_{x,y} \quad & f(x,y) \\ \text{s.t.} \quad & \mathbf{K}(x)\mathbf{u} = \mathbf{f}(x) \\ & g_i(x,y) \leq 0 \end{aligned} \tag{5.1}
$$

5.3. Forms of structural optimization

The field of structural optimization is often divided in three categories, depending on the freedom of the design variable x:

- Sizing optimization finds the best possible dimensions for the elements of a given design. It does not alter the design itself, so the efficacy of the result depends on the initial design. Therefore, it is most useful in the *Optimization* step depicted in section 5.1.

- Shape optimization focuses on the boundary of a given design. The shape of the design domain boundary is optimized for the given goal. No new boundaries can be formed in this method, which hampers its practicality. The greater freedom of the method's result makes that it can be used in the *Conceptual design* phase of section 5.1, but use can also be found in the *Optimization* phase.

- Topology optimization gives even more design freedom. The topology (literal Greek translation: *Location study*) of a structure contains all information about boundaries, connectivity, and location of holes within the structure. The great freedom of result makes this optimization type be the most effective of the three for the *Conceptual design* phase (section 5.1). As a true topology optimization procedure only determines whether material is present or not at a certain location [28] and complex forms may be obtained, it can be necessary to interpret the design or apply a sizing optimization to come to a further optimized and manufacturable solution.

The differences between the results from the three methods are visualized by an example in figure 5.1.
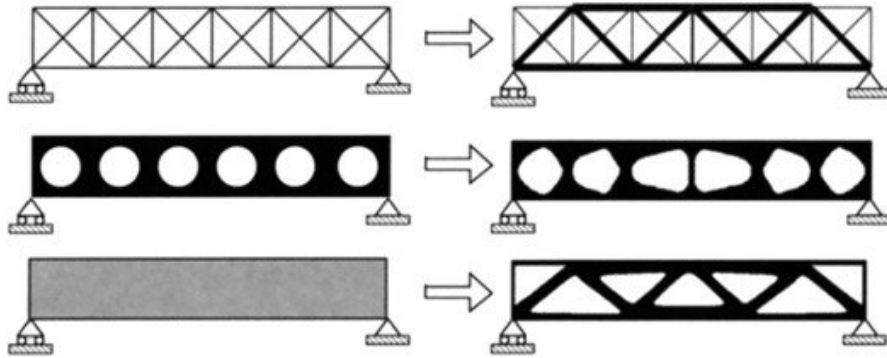
Figure 5.1: Visual explanation of the differences in results between the three forms of structural optimization. From top to bottom, these are size, shape, and topology optimization [19].

From the conceptual description and visual results as in figure 5.1, shape and topology optimization seem to be similar, with topology optimization being more generic. The implementation of the methods is completely different, however. The opposite applies to the link between size and topology optimization; conceptually these are very different, but in the execution both methods show many similarities [28].

Figure 5.2 tries to explain the contrast between the implementation of the methods on a free body diagram. Size and topology work inside the given domain Ω, while shape optimization works on the boundary Γ_h of this domain. The difference between size and topology optimization lies in the values subdomains of Ω can take. When size is considered, any dimension larger than zero is allowed. Topology only allows the presence of either material or no material at a point; often indicated by a 0 for a void, or a 1 for material. Multiple methods for topology optimization loosen this strict discrete ordering though. The well-known SIMP method, for example, approximates the discrete void-material relation with a continuous function. This will be discussed in more depth in the next chapter.
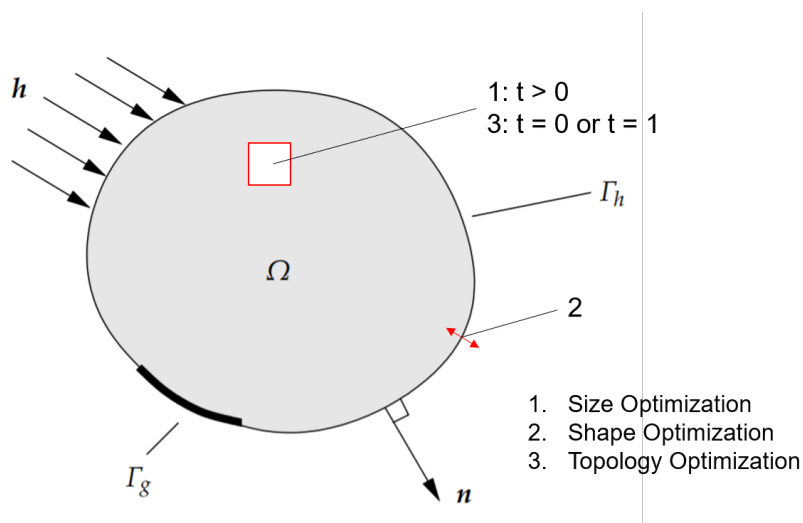
Figure 5.2: Differences between the three forms of structural optimization when applied to a free body. Edited from [114].

5.3.1. Parametric optimization

Besides these three often distinguished forms of structural optimization, a fourth term may be encountered in literature and this thesis: parametric optimization. Although a sharp definition was not found, it is generally used for problems where it is tried to find the best possible values for the parameters that define a design. That is, the design concept itself is not changed, but for example material grades, member thicknesses, and center-to-center distances may be altered.

Finding the optimal ratio of parameters within a certain design makes this type of problems similar in nature to size optimization. However, altering the placement of members exceeds the strict definition of this structural optimization form. On the other hand, the design freedom of topology optimization is not obtained, as the design concept is predetermined. Figure 5.3 tries to explain the form again with a visual example.

This difficulty of proper classification into one of the three classes necessitates the use of the term *parametric optimization* to accurately describe the method used in this thesis. Determination of its placement in a design process is less problematic; as the design concept needs to be determined beforehand, it is most useful in the *Optimization* phase as described in section 5.1.
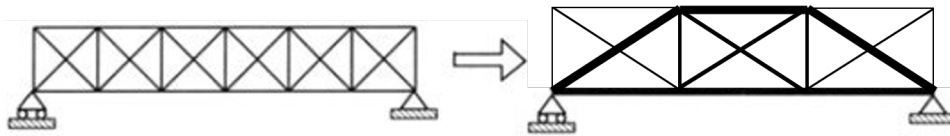
Figure 5.3: Visual explanation of parametric optimization. It can be seen that sizes of and distances between members may vary, but the result is still the same structural concept: a truss with two diagonals per bay.

5.4. Historical context of Structural Optimization

An overview of developments within the field of structural optimization is given in this section. This is in the first place meant to place the current state of the subject into a timely perspective. Secondly, it states the problems some methods experienced in early stages, explaining why the general acceptance of these methods proved to be difficult. The section is split in analytical and numerical methods for clarity. As the origins of the former are older, it is treated first.

5.4.1. Analytical methods

The origins of the field of mathematical structural optimization are generally attributed to the Australian mechanical engineer Michell. In 1904, he published his paper *The Limits of Economy of Material in Frame-structures* [74], in which he presents an analytical solution for the optimal layout of truss structures. The paper concludes that for general cases, optimal frames consist of a system of infinitely many orthogonal bars that remains orthogonal after deformation. The absolute values of the strains are equal in all bars in these type of frames. Examples of structures following this requirement are given in figure 5.4.
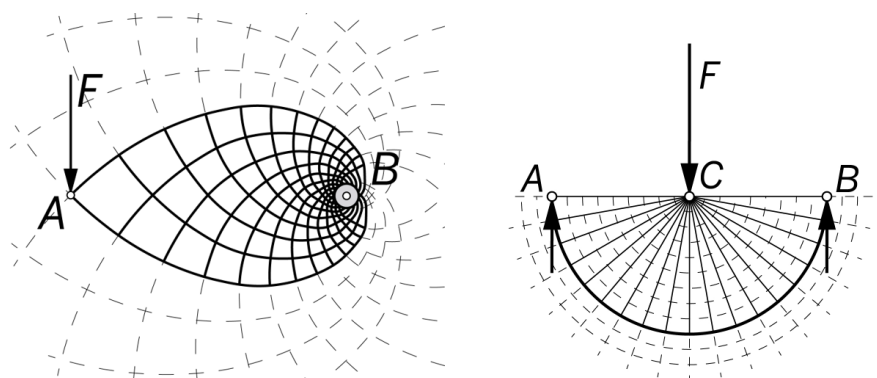
Figure 5.4: Michell cantilever and cartwheel. Taken from [71, 72], which were based on the original work by Michell [74].

The work of Michell inspired others to search for analytical conditions that would indicate an optimal structure. During the 1950's and 60's various of these optimality criteria (OC) were found based on plasticity theory. The work of Prager is most notable therein, coming to a general optimality criterion for plastic design in 1968 in a collaboration with Shield [86]. For more complex structures, these OC could be implemented in numerical methods as well, involving an iterative procedure to come to a (near-)optimal structure.

Where Michell's and Prager's work mainly focused on structures loaded in-plane, Rozvany treated discrete structures loaded out-of-plane. These structures, also called *beam grids* or *grillages*, were treated in a series of papers published from the 1970's onward [95, 96]. Using the Prager-Shield optimality criterion, it is stated that in an optimal grillage the principle curvatures κ_1 and κ_2 have the same direction as the principle moments M_1 and M_2 respectively. The optimal structure consists of infinitely many beams, similar to the Michell trusses.

The papers showed that in any out-of-plane loaded structure five zones may be identified that determine the optimal orientation of the beam grid. These zones are visually represented by the symbols found in figure 5.5. R^+, R^-, and R^{+-}-zones have fixed optimal beam orientations that follow the principle moments. For R^{++} and R^{--}-zones the orientations are arbitrary [96]. Figure 5.6 shows an example for two fundamental cases.

Figure 5.5: Symbols representing the five optimal zones in a beam grid as proposed by Rozvany [95].
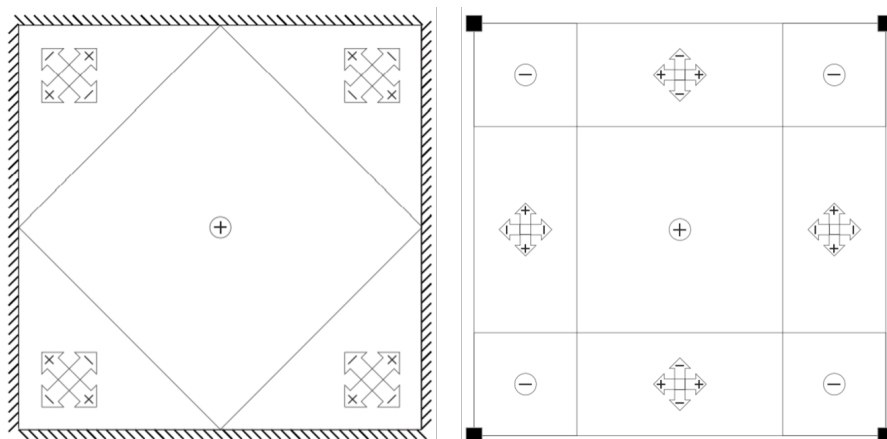
Figure 5.6: Examples of the described zones (figure 5.5) for a uniformly loaded plate; simply supported at all edges (left) or clamped at the corners (right) [22]. The arrows show the optimal beam orientation in each zone. In a zone symbolized with a circle, the optimal orientation is undetermined.

5.4.2. Numerical methods
In 1960, Schmit [101] presented a method coupling the - at the time - quite new Finite Element Method to a non-linear mathematical solver. This concept would form the basis of most modern structural optimization techniques. Schmit already saw his method to partly replace the iterative design process as described in section 5.1. It would, however, take some time until numerical optimization following his approach would be really embraced. Reasons for this were named to be the novelty of the required FE method, which was only just gaining acceptance, and the lack of knowledge of mathematical programming methods in engineering researchers [102].

In 1964, Dorn et al. [38] proposed the *ground structure method* to find the optimal layout of truss structures. This method uses a set of joints connected by potential members. The method comes to the optimal form of the structure by eliminating inefficient elements from this ground structure (see figure

5.7). The fact that elements can be deleted makes that this method can be seen as one of the first true topological optimization methods, resulting in more design freedom. Unfortunately, the number of potential members grows quickly with an increasing number of joints, requiring large computational efforts for practical applications. Computers of that time could not provide these efforts, meaning that Dorn's ground structure approach would follow the same fate as Schmit's proposal for quite some time.
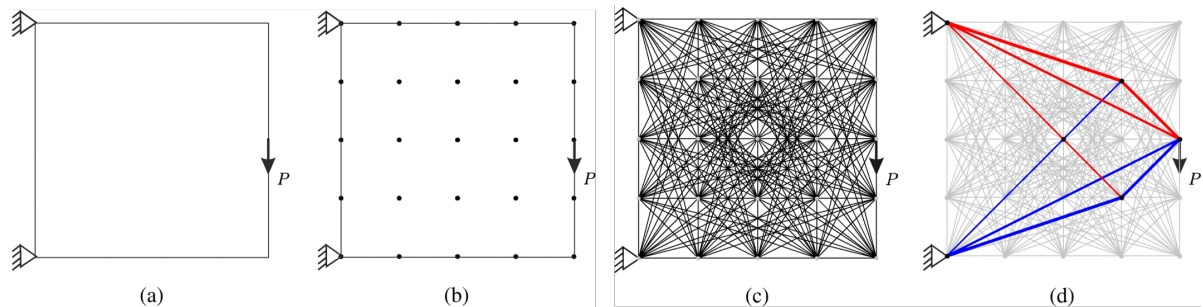
Figure 5.7: Illustration of the steps taken in the ground structure method. A domain with load and supporting conditions (a) is discretized with a grid of nodes (b), which are connected to each other to form the characteristic *ground structure* (c). During the optimization, a number of members from this ground structure is selected to obtain the most efficient structure possible (d) [51]. These steps are more elaborately treated in section 7.2.1.

The years following these publications, some progress was made using the numerical implementation of the previously mentioned Optimality Criteria, but a real breakthrough came with the seminal work of Bendsøe and Kikuchi in 1988 [18]. Their paper speaks of a *homogenization method* that could improve the shape optimization algorithms that were studied intensely in the period prior to its publication, but would turn out to form the start of the now so-called *SIMP* method. This FEM-based method made the topology optimization of 2D and 3D continua possible (figure 5.8), making it one most popular method for topology optimization today. It will be discussed in more detail in section 7.1.1.
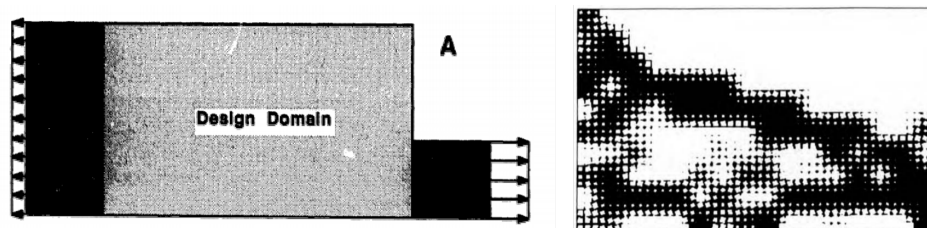
Figure 5.8: An example of a design situation and the optimal structure (in black) found for it using the new method by Bensøe and Kikuchi [18].

Shortly after, in 1992, Xie and Steven [118] followed with another nowadays popular method for topology optimization of continuum structures: Evolutionary Structural Optimization, or ESO in short. The idea of the method is simple: a Finite Element calculation is performed and afterwards the least stressed elements are removed from the structure. It makes no use of any gradients and is therefore completely *heuristic* (see section 6.2 for an explanation of this term). ESO was quickly picked up by the research community and developed further, of which a result was the Bidirectional Evolutionary Structural Optimization (BESO). ESO and BESO are futher discussed in section 7.1.2.

The success of ESO showed the potential of heuristic methods for topology optimization. Application of other heuristic methods would follow from the 2000's onward, like Genetic Algorithms, Particle Swarm, and Ant Colony search. The independence of gradients for heuristic methods means that these methods can handle discrete values of design variables, which can be beneficial in design problems. This is further discussed in section 6.2.

Another development in the 2000's was made by Gilbert and Tyas [45]. They altered Dorn's traditional ground structure method to feature a 'member adding' scheme. By starting large problems with an only partly connected ground structure, the necessary computational time is significantly reduced . It made the analysis of much larger structures possible and scientific interest in the method seems to have been returned. Results of this research can be read in section 7.2.1.

6

Solving strategies for general optimization problems

The previous chapter introduced the types of structural optimization and its general mathematical formulation. To complete the set-up, a strategy for solving the problem needs to be chosen. A wide range of options is available for this in existing literature and new possibilities are still found. When choosing a solution strategy, the convexity of the problem is important to consider. The applicability of the solution strategy heavily depends on this property, as well as the certainty of the found result.

When a problem is found to be convex, it enables highly efficient solution procedures and guarantees to find a global optimum. Unfortunately, many - if not most - structural optimization problems turn out to be non-convex. This poses a problem for the traditional convex solvers, as these are likely to get stuck in local optima. Heuristic methods are one of the possible solutions for this problem.

Section 6.1 will first discuss the concept of convexity in more detail, and present arguably the most simple way of solving an optimization problem: linear programming. Understanding of this method helps in the basic insight of mathematical optimization in general and some structural optimization techniques in particular. It is encountered in, for example, the ground structure method of section 7.2.1. The section also shortly describes the general idea behind some other convex programming methods.

Section 6.2 describes another category of solvers: heuristic methods. Although these methods lack theoretical mathematical proof, they are often capable of finding good solutions to very complex problems. A short description of their advantages is given, and some examples of heuristic methods are presented. The section ends with a comparison between these.

6.1. Convex programming
As mentioned in the introduction of this chapter, it is essential to understand the concept of *convexity* when studying a structural optimization problem. It may determine the choice for a solution procedure and how valuable the found optimum is.

The criterion for convexity is given as [28]: *"A set $S \subset \mathbb{R}^n$ is convex if for all $x_1, x_2 \in S$ and all $\lambda \in (0,1)$, it holds that:"*

$$\lambda x_1 + (1-\lambda)x_2 \in S \tag{6.1}$$

This means that any point on the line connecting two arbitrary points of the set, should also be part of the set. The visual explanation of figure 6.1 may clarify this.

Convexity is applicable to the objective function and constraints of an optimization problem. When both are convex, the total problem may be called convex. Convex problems have the desirable property that any local optimum is guaranteed to be the global optimum as well. This makes the search for a solution to the problem easier and more reliable.

Figure 6.1: Comparison between a convex set (left), and a non-convex or *concave* set (right) [28].

Unfortunately, the majority of practical applications of structural optimization problems is non-convex or *concave*. Optimization algorithms may consequently find local optima that can be very inefficient compared to the global optimum. The found solution for concave problems is often dependent on the initial values of the variables. It is therefore recommendable to repeat the analysis with different initial values to verify the result. Using methods that are less susceptible to local optima may reduce the risk of ending in one as well, but finding the true global optimum is never guaranteed. Sigmund [105] therefore recommends that one should be wary with claims considering an *optimal* structure. It may be better to refer to the solution as *optimized*, unless global optimality has been explicitly proven.

6.1.1. Linear programming

For convex problems with a linear objective function and only linear constraints, linear programming (or LP) algorithms may very efficiently find the optimal solution. Their efficiency partly comes from a beneficial property of LP problems: the optimal value will always be found at a corner point [110].

This can be seen when figure 6.2 is considered. The constraint functions determine a region P in which feasible solutions are found. For an arbitrarily chosen value, the objective function can be drawn in the figure by a straight line. Lower (or higher) values of the objective function $f(x,y)$ can be found by moving perpendicular to the direction of this line. It is easily visible in the figure that the optimal value that still lies in the feasible region will be at a corner point.
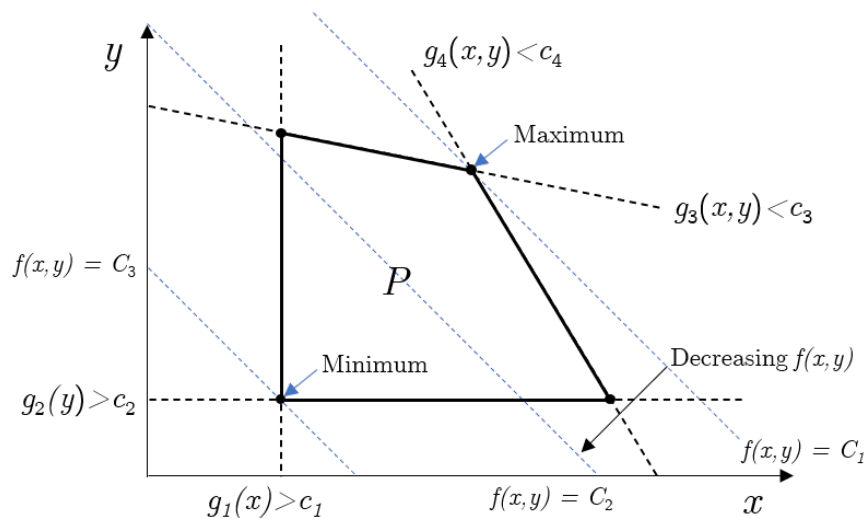
Figure 6.2: Graphical representation of a two dimensional linear programming problem. Four constraint functions g_i bound the feasible region P. A certain value of the objective function $f(x,y)$ will always produce straight lines in the figure. When this value is increased or decreased, the optimal quantity will be found at a corner point.

Practical LP problems will generally have more than two dimensions and at multitude of constraints. Computational solvers are therefore preferred over the graphical method presented here. The simplex method is one these. This algorithm starts at the origin and then moves along the edges of the feasible region in the direction of the strongest increase in the objective function. At each corner, this direction is computed again and the direction is changed. Once a corner is reached where no improvement of the objective function can be found, the optimal value is reached [110].

6.1.2. Other convex programming methods

When one of the objective or constraint functions is nonlinear, direct application of LP solvers is not possible. A large range of options is then still available to be used, such as the steepest ascent method (if the problem is unconstrained), sequential quadratic programming, convex linearization (CONLIN), or the method of moving asymptotes (MMA).

A complete description of each method would far overshoot the goal of this literature review. Some more in depth information for application of these methods was found in Christensen and Klarbring [28] and Taha [110]. The former also gives a general description of the workflow of this type of methods when applied to structural optimization problems, which is given below:

1. Start with an initial design.

2. Perform an FE analysis to calculate the displacement vector.

3. Evaluate the objective function, the constraint function, and their gradients for the given design.

4. Approximate the the true problem by an explicit and convex optimization problem at the current design.

5. Solve the approximated problem with one of the mentioned algorithms to give a new design.

6. Return to step 2, unless a stopping criterion is met.

Step 3 in this workflow involves the computation of gradients of the objective and constraint function. The calculation of these derivatives make targeted search of better designs possible and give these type of methods their name of *gradient-based* methods. Their direct exploration of the design space makes these algorithms generally converge in a relatively low amount of iterations, but the computation of gradients may become costly when the number of design variables or constraints increases. In other situations, algebraic calculation of the derivatives may not be possible, and approximation using finite differences could be needed. For the application intended in these thesis, both of these difficulties apply, and thus the use of gradient-based methods is probably less suited. Heuristic methods can then be a better option, which will be discussed in the next section.

6.2. Heuristic programming

The word *heuristic* comes from the Greek word *heurisko*, meaning *I find* or *I discover*. The split meaning of *finding* and *discovering* embodies the nature of heuristic methods well, as these encompass practical methods that do not guarantee to find a optimal solution to the problem, but are able to discover a sufficient approximation by systematic search of the design space. Heuristic methods are actually well-established in engineering practice; standard approaches like rules of thumb and trial-and-error are heuristic as well.

Heuristic methods can also be used in structural optimization to overcome some of the drawbacks of traditional gradient-based methods when optimizing large and highly nonlinear practical engineering problems. The general idea of heuristic methods is to generate some possible solutions to the problem and compute their performance. This information is then used to search for better solutions. As for all procedures, this comes with the usual advantages and disadvantages, which are summarized below.

Advantages:

- Easy to implement as no gradients are needed.

- Can handle discrete design variables.

- The chance of being trapped in a local minima is smaller then for gradient based methods due to global search of design space.

Disadvantages:

- It is not guaranteed that an optimum is found, as the end result will be partly random.

- The randomized search may be highly inefficient compared to gradient based methods due to the high number of necessary evaluations.

The number of heuristic methods available for structural engineering is extensive and a comprehensive description of these does not fit within the scope of this thesis. Four algorithms are discussed here: genetic algorithms, particle swarm optimization, artificial bee colony, and tabu search. This is mainly meant to give an illustration about these methods and improve the understanding of heuristic methods in general. A more detailed description of heuristic methods for structural optimization and many references to applications was found in Hare et al. [49].

6.2.1. Genetic algorithms

The development of genetic algorithms was inspired by the natural selection phenomenon found in nature. Design variables of the optimization problem are called *genes* and a complete set of design variables is called a *chromosome*. The process is started by forming an initial *population* of *individuals* (possible solutions) that is often randomly generated. The *fitness* of the individuals is then evaluated by computing the value of the objective function that was realized.

The next step is to apply the selection principle on the initial population. Individuals from the population are randomly selected, where individuals with a higher fitness value have a higher chance of being chosen. The selected individuals become the *parents* for the new generation that will be created. The chromosomes of these parents are combined to form new sets of design variables. To increase diversity in the new solutions, a small number of genes in the generated population is then *mutated* (randomly changed to a different value). The second generation population is then finished.

For this second population, the fitness value can again be calculated and the complete procedure can be repeated. The process is terminated when the fitness values of new generations do not significantly differ from their parent generations, a value of the objective function is reached, or if a maximum amount of generations is reached. An overview of the complete process is given in figure 6.3.
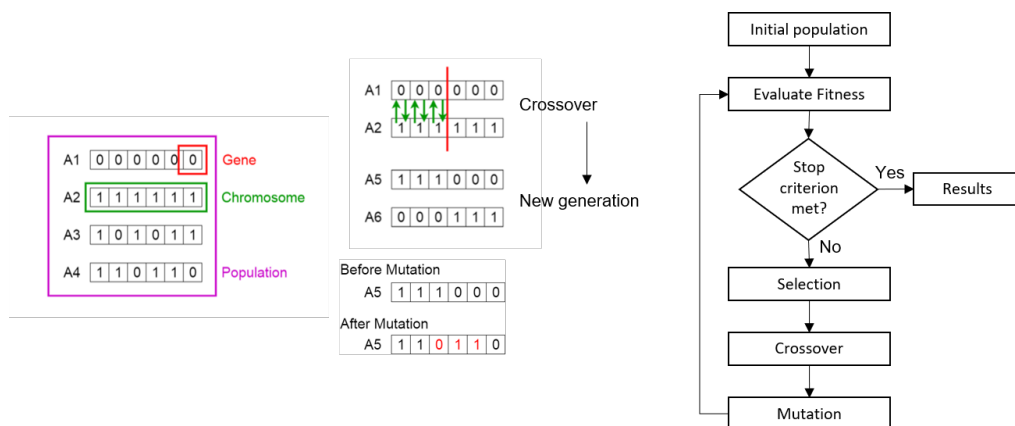
Figure 6.3: Visualization of the process and some terms of the genetic algorithm. Edited from [70].

The random nature of the process means that the population sizes need to be large enough to find useful results. Many evaluations of finite element models may be needed for structural optimization problems, which can become problematic for larger structures where the FEA takes a substantial amount of time. Another difficulty may be found in the dependence on initial values and the parameters of the evolutionary process. Examples of these parameters are the selection method and mutation ratio. Kallassy and Marcelin [60] illustrate that a wrong choice of these parameters may have a very detrimental effect on the results. The paper also shows a large amount of iterations necessary for a relatively simple problem.

6.2.2. Particle swarm optimization

Particle swarm optimization belongs, just like genetic algorithms, to the group of evolutionary algorithms. It is inspired by the evolutionary advantage of sharing information between members of a swarm. Just like the genetic algorithm, the method starts by generating an initial set of designs, now called *particles*. The objective function is evaluated for the particles and the best result is stored. The next position of the particle is then generated by [84]:

$$x_{k+1}^i = x_k^i + v_{k+1}^i \Delta t \tag{6.2}$$

$$v_{k+1}^i = w v_k^i + c_1 r_1 \frac{p^i - x_k^i}{\Delta t} + c_2 r_2 \frac{p^g - x_k^i}{\Delta t} \tag{6.3}$$

where:

$x_k^i = $ the position of particle i in iteration k

$v_k^i = $ the velocity of particle i in iteration k

$w = $ the inertia weight, controls the exploration ability

$c_1 = $ cognitive parameter, determines the influence of the best found position of the particle

$c_2 = $ social parameter, determines the influence of the globally best found position

$r_1; r_2 = $ randomly generated values between 0 and 1

$\Delta t = $ the time interval covered per iteration, usually set to 1

$p^i = $ the best found position of particle i

$p^g = $ the globally best found position

The objective function for the new particle is then evaluated again. If a new particle finds a better solution than was found until then, it replaces the earlier best found solution p^i or p^g. This process is repeated until a stop criterion is met. Stopping criteria may be a maximum number of iterations, a stable best found solution, or a certain value of the objective function.

Although the search strategy of particle swarm algorithms differ significantly from genetic algorithms, their main advantages and disadvantages are the same. During each iteration, the design described by each particle needs to be evaluated, which results in many FE calculations for structural optimization. Most of the studies comparing particle swarm to genetic algorithms seem to prefer the first [44, 84], but other recommendations can be found as well [27].

6.2.3. Artificial bee colony

The artificial bee colony algorithm is the most recent of the here discussed algorithms, being proposed by Karabuga in 2005 [61, 62]. It was inspired by honey bees' search for food and the share of information between members of the colony. In this, it shares some similarities with the described genetic algorithm and particle swarm optimization. All were inspired by processes in nature and have multiple *individuals* that are present in a single iteration of the algorithm. The determination of next possible design alternative differs, however.

The process of the algorithm (figure 6.4) starts by dividing the *colony*, or number of design variants considered in a single iteration, in *employed bees* and *onlooker bees*. The employed bees all have a dedicated *food source* (design variant) whose performance they check. Based on the results from these employed bees, a probability is assigned to each food source by [62]:

$$p_i = \frac{f(x_i)}{\sum_{n=1}^{N} f(x_n)} \tag{6.4}$$

in which f is the objective function, N the number of food sources included in the current optimization, and x_i the food source considered. This probability is then used to distribute the waiting onlooker bees over the investigated food sources and as such, better performing design variants will get more attention.

A sent onlooker bee will choose a new food source close by the assigned one and assess its performance. If the performance is better than that of the earlier assigned food source, the new variant replaces it in the collective memory of the colony. When all onlooker bees have had their turn, the employed bees are again sent to their (updated) dedicated food sources and also choose a new variant in the neighborhood. The cycle then repeats itself.

Both the onlooker and employed bees choose new food sources based on the equation [62]:

$$v_{ij} = x_{ij} + \phi_{ij}(x_{ij} - x_{kj})$$
(6.5)

where the index k selects a random other employed bee and the index j a random design variable. ϕ_{ij} is a random number between -1 and 1. The final term in the equation causes the area of search to decrease when food sources get closer together. The initial global search thus slowly transforms to a more local search when the algorithm progresses.

Besides the number of employed and onlooker bees and the usual stopping criterion, the value of the *limit* needs to be chosen. This limit determines how many failed attempts to find better variants are allowed before a food source is abandoned. It is then assumed that the respective food source is the best in its region and further checks are of no use. When this happens, the dedicated employed bee belonging to the food source becomes a *scout bee* and will be randomly assigned to a new and unexplored design variant.

6.2.4. Tabu search

The tabu search algorithm is different from the previously presented methods as it does not consider multiple entities that represent design alternatives during a single iteration. Instead, a single variant is considered and the neighborhood of that variant is explored. This means that design variables are slightly changed and their performance is evaluated. The next design variant is chosen from the computed variants. This can be done by selecting the one with the best performance or at random.

Before continuing to the next iteration, the current design is stored in the *tabu list*. This list contains variants towards which a future step is not allowed. The variant is remembered on this list for a pre-determined amount of iterations: the so-called *tenure period*. The prevention of moving to previous locations makes the escape of local optima possible [110].

The tenure period and definition of the neighborhood are parameters that need to be chosen for this solution scheme. Tabu search is generally used for constrained problems with discrete variables [49].

6.3. Conclusions

Although the methods presented in this chapter are only a fraction of the true amount of available methods, its shows the great variety of possibilities for solving a structural optimization problem. The more traditional gradient based methods have the strong advantages of speed and convergence when the right conditions apply, but can be very much hindered by the presence of local minima or the difficult calculations of derivatives. As both of these disadvantages are expected to be present in the intended application for this thesis, their use is uncertain.

The application of heuristic methods may therefore be preferred. This is, however, only the first part of the complete choice. The number of heuristic methods is extensive, and many have been applied to structural optimization problems. A large number of studies can also be found that compares the performance of different algorithms for academic examples (e.g. [7, 20, 27, 44, 63, 82, 84, 107]), but definitive conclusions are hard to draw as used examples and applied algorithms often differ [49, 108]. The often needed calibration of algorithms using tuning parameters further hinders proper comparison.

Despite this difficulty, a choice will have to be made for a method to be used to solve the optimization problem. The final decision for an algorithm will be made and motivated in section 10.1. Although a definitive conclusion for a best strategy may not be possible, trends can be found in the listed comparative studies. Genetic algorithms, for example, were only once found to be the preferred choice when only compared to particle swarm optimization [27]. The latter is also only sporadically found to be the favored approach [49], but its performance may be improved by one of the many alternative algorithms that have been derived from it [63]. Tabu search was occasionally found to outperform the other algorithms [7, 49]. The artificial bee colony algorithm has been applied less often, probably due to its more recent introduction compared to the other three. In the papers it was considered, it has been performing well consistently [20, 49, 107].
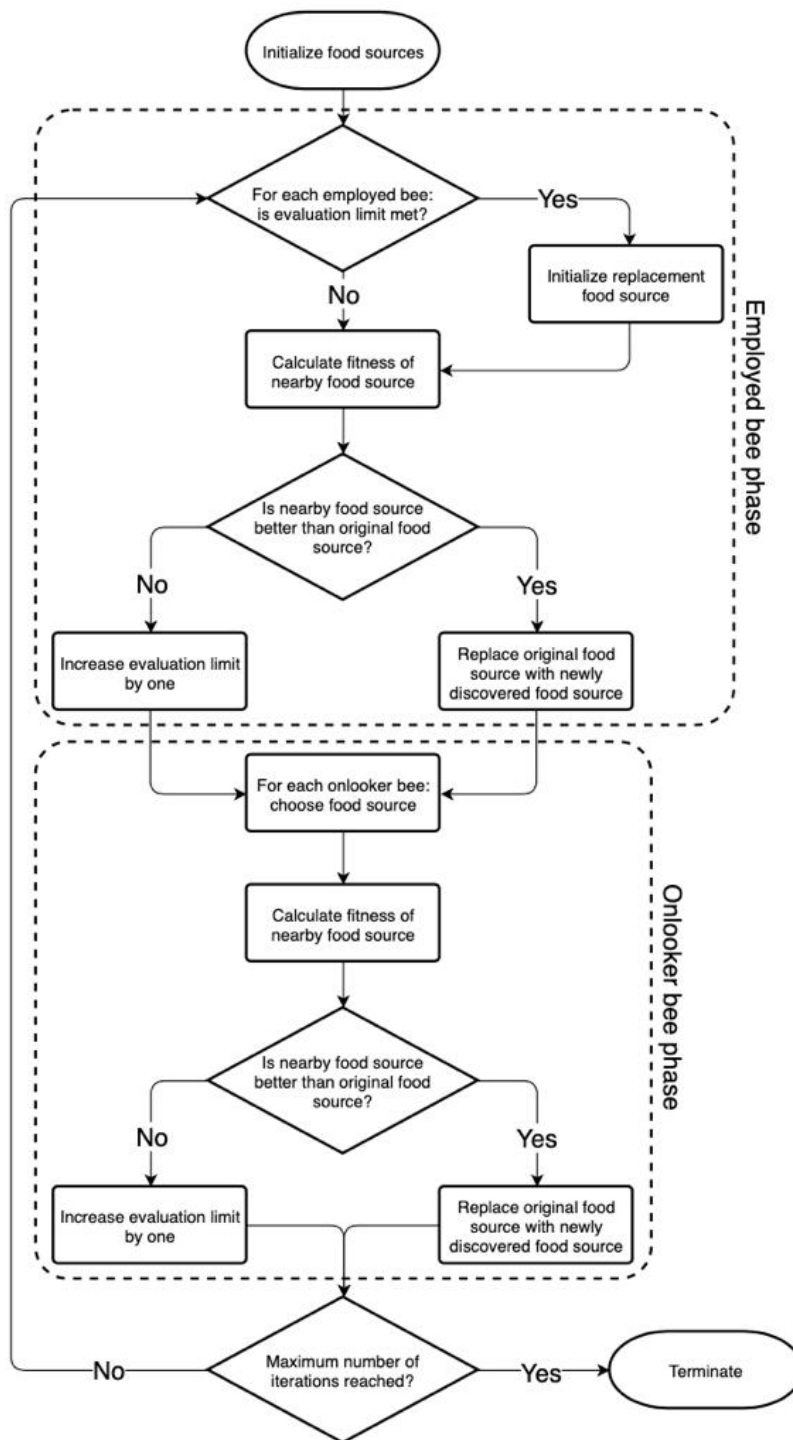
Figure 6.4: Diagram illustrating the workflow of the artificial bee colony algorithm [20].

<div style="text-align: right; font-size: 3em;">7</div>

Methods for Topology Optimization of stiffened plates

In chapter 5, several methods for topology optimization (TO) were introduced and a short overview of their history was given. In this section, these methods are further elaborated and similar methods are compared to each other. It is meant to give a basic understanding of the principles behind these methods, with the intention to make an educated decision for which to use further on in this thesis.

A division into two classes of structures is made: continuum and discrete element structures. The topology optimization methods developed for these two classes are generally quite different. TO for continuum structures is treated in section 7.1, methods aimed at discrete element structures in section 7.2.

7.1. Topological optimization of continuum structures

The two most popular topology optimization methods, SIMP and ESO/BESO, were introduced in section 5.4.2. Both methods apply to structures modeled as a *continuum* (plural: *continua*); that is, they fully occupy the design space. This is opposite to the methods that use discrete elements, such as the truss structures in section 7.2.

This section discusses the concept of these methods in more detail and compares them. The most important problems these methods encounter during implementation are also covered, including tactics to mitigate them. The section concludes with a summary of other similar methods and why these were not further considered in this thesis.

7.1.1. SIMP

Solid Isotropic Material with Penalization, or SIMP, is a strategy to mitigate the complications that come with the discrete parameter problem that true topology optimization is. Mentioned in section 5.3, strict TO gives a design result that only dictates whether material is present at a certain point or not, and thus forms a discrete 0-1 problem. Gradient-based mathematical solvers (see section 6.1) have a very hard time solving these type of problems.

SIMP solves this by effectively converting the topology optimization problem into a sizing problem where the density of material throughout the structure is optimized. The relative density $\rho(x)$ at a certain location determines the effective stiffness at that location and can take any value between and including 0 and 1. However, to steer the result towards an eventual 0-1 solution, intermediate densities are penalized. This is usually done by applying an exponent p to the density when calculating the stiffness of at a point in the domain [19]:

$$E^{eff}(x) = \rho(x)^p E^0, \quad p > 1$$
$$\int_\Omega \rho(x)d\Omega \leq V; \qquad 0 \leq \rho(x) \leq 1, \quad x \in \Omega \tag{7.1}$$

where E^0 is the unaffected Young's modulus of the material, E^{eff} the effective stiffness, and V an upper limit to the volume fraction of the resulting design. The power function for the effective stiffness makes the use of intermediate densities in the structure inefficient, as their volume contribution is high compared to the obtained stiffness (figure 7.1). Experience has proven that a value of $p \geq 3$ is recommended [19].
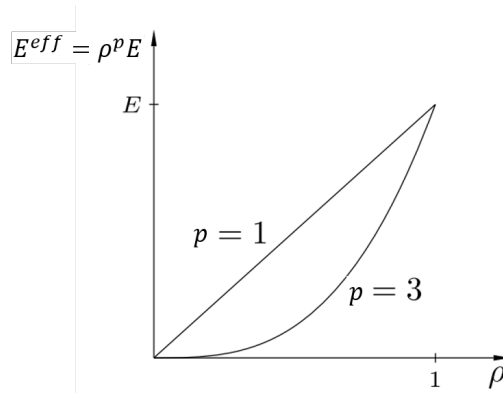
Figure 7.1: Effective stiffness - density plot. A higher value of p will diminish the effective stiffness of elements with intermediate density values. Edited from [28] .

SIMP is almost always used in combination with the Finite Element method to discretize the design domain and calculate the reaction of the structure. The elements are given individual density values, which are the design variables during optimization. To do this, the influence of the stiffness of an element on the objective function is calculated in a step called sensitivity analysis. Using these gradients, mathematical algorithms like those treated in section 6.1 can iteratively find the optimal design.

Difficulties and solutions
The described procedure makes SIMP an effective and efficient method for TO, but it still has some difficulties. Some of these and their solutions will be described below.

When densities reach 0, elements without stiffness will be present in the FE formulation, resulting in a singular stiffness matrix. This is avoided by adopting a minimum value for the density. A value of $10^{-3} \cdot E_0$ is often used for this [19].

A downside of the penalization of equation 7.1 is that it will always give a non-convex problem, even if the original problem is convex. Adopting the SIMP method therefore means risking to end up in a local optimum. The continuation method was introduced to diminish this problem: by starting a SIMP analysis with $p = 1$ and gradually increasing its value during the iterations, the solution tends to stay close to the global optimum [97].

Another problem for SIMP, and TO for continua in general, is the non-existence of an applicable solution. The most optimal structure will consist of a microstructure with as much holes as possible, which will not be isotropic anymore and thus does not fit the original design description. The tendency to form microstructures creates a problem of mesh-dependency, as a finer Finite Element mesh will allow more holes to form in the structure (see figure 7.2). This is undesired; a mesh-refinement should result in clearer material-void boundaries, not a different structure [19].

Multiple solutions have been developed for this problem, but the most generally used is based on the filtering of sensitivities. In this approach, the design sensitivity of an element is related to that of neighboring elements. This prevents the formation of structural elements smaller then a given threshold.

Next to mesh-independency, filtering gives two additional advantages: the prevention of checkerboard patterns and increased manufacturability. An example of a checkerboard pattern can be seen in figure 7.2. It is a result of the FE discretization that overestimates the stiffness of such a pattern. Using higher order elements can also prevent the formation of checkerboard patterns. The manufacturability of solutions is increased when a filtering scheme is used, as a lower limit on the dimensions of structural parts can be given.
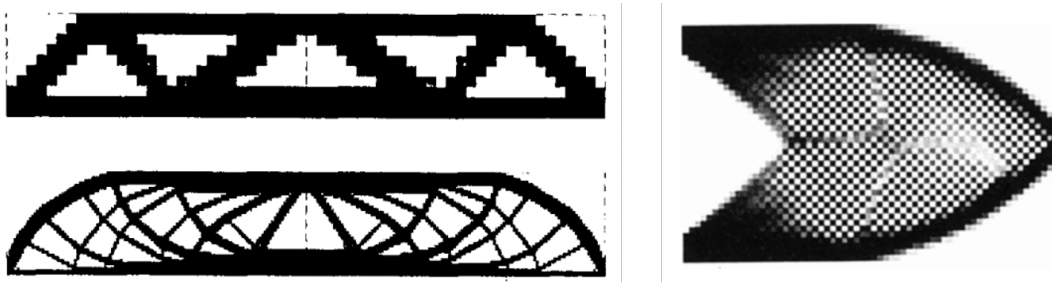
Figure 7.2: Two types of problems encountered in unfiltered SIMP: mesh-dependency (left) [104], resulting a different structure when a finer mesh is used (top to bottom), and checkerboard patterns (right) [35].

7.1.2. ESO/BESO

Evolutionary Structural Optimization or ESO is an iterative and heuristic method aimed at improving the performance of a structure. The method is described by Huang and Xie [56] as to be "*based on the simple concept of gradually removing inefficient material from a structure*". Like the SIMP method elaborated above, ESO is almost exclusively used in combination with the finite element method. An improved design is searched for by iteratively removing elements from the FE model that comply to a certain condition. This condition is generally based on the stress level of an element or its influence on the stiffness of the structure (the sensitivity).

In contrary to SIMP, traditional ESO does consider the original discrete 0-1 problem formed by topology optimization. Furthermore, it does not make use of mathematical solvers for the optimization problem. The updating of the structural layout is purely based on the chosen removal condition. The process behind ESO can then be summarized as [56]:

1. Apply a fine mesh of finite elements to discretize the structure.

2. Perform a finite element analysis on the discretization. If necessary, this is followed by a sensitivity analysis.

3. Remove elements according to the specified condition.

4. Update the removal condition for the next iteration.

5. Return to step 2 and repeat until a desired solution is obtained.

Clear from this scheme is that elements are only removed and can not be returned once they are discarded. The amount of elements during the iteration process is thus gradually reduced, also lowering the amount of computational effort necessary for later finite element analyses. As a consequence, the speed of iterations increases during the evolutionary process.

Although the permanent removal of elements saves computational time, it can restrict the performance of the final solution. Elements that are removed in early iteration can be beneficial to the structural performance when the design has significantly changed. The Bi-directional Evolutionary Structural Optimization (BESO) was developed to tackle this problem. BESO does not permanently delete elements from the analysis, but has the option to reintroduce removed elements. To accomplish this, the sensitivity of removed elements is estimated using the sensitivities of neighboring elements. This is done in a similar way as the filtering schemes of the SIMP method. When the return of an earlier removed element has a significant positive effect on the compliance, it can be reintroduced in step 3 of the procedure described above.

Criticism, Difficulties and solutions

As with SIMP, no true solution is available for the discrete continuum topology optimization problem. This results in the same mesh-dependency problem as described in section 7.1.1 and visible in figure 7.2 for ESO. When linear elements are used for the FE discretization, checkerboards can also occur (also described in section 7.1.1 and visible in figure 7.2). The use of a filtering scheme can again prevent these types of problems. The BESO method already uses this filter for the reintroduction of elements, and is thus not sensitive to these problems.

Criticism of the ESO and BESO approaches is often aimed at their heuristic nature. The absence of mathematical basis of the method means that convergence or finding even a local optimum is not guaranteed. Rozvany [97] furthermore states that its efficiency is in general worse than for SIMP and shows that the method can break down for certain layouts of problems.

Rozvany's comments on the evolutionary methods led to further research towards improvements of convergence and the breakdown for certain problems. Convergence can be improved by averaging the sensitivity values over iterations, reducing large fluctuations of the solution. To prevent non-optimal solutions for certain problems, a mesh refinement can sometimes be applied. Another option can be to apply a material interpolation scheme similar to that of SIMP (equation 7.1) for removed *void* elements. These elements are no longer excluded from the FE analysis, but given a very small minimum thickness. When the value of p is chosen large enough, the effective stiffness of the void elements will be negligible. This implementation of BESO is named the soft-kill method, opposed to the original hard-kill method.

While this solution does still not guarantee the solution to be globally optimal, it is more stable than the original BESO procedure. However, this comes at the cost of computational efficiency, as void elements have to be included in the analysis. Huang and Xie [56] therefore still advise the use of the original hard-kill BESO method, and back their claim by an example showing that the results for both are very close, while the hard-kill BESO is faster.

7.1.3. SIMP compared to ESO/BESO

The scientific community seems to be divided over which of the two methods is to be preferred for the topological optimization of continua. Advocates of SIMP point at the better theoretical basis, convergence, and stability of the method [97], while those supporting ESO/BESO refer to the simplicity, decent results and efficiency for applications of these methods [56].

More recently, however, a different view was presented by Sigmund and Maute [106]. In this comparative review, the authors state that the differences between the modern implementation of the two methods are minimal. The earlier mentioned soft-kill BESO even uses the material interpolation scheme of SIMP and both use the same filtering techniques. Furthermore, hard-kill BESO can be interpreted as having a material interpolation scheme like that of SIMP (equation 7.1) with the value of p going to infinity. When p is chosen large enough, variations in it will generally not influence the results of the optimization [56]. Sigmund and Maute even go as far as to call BESO methods "*discrete SIMP approaches*" [106].

7.1.4. Other methods

Other methods that are possibly suited for the topology optimization of continua are the use of topological derivatives, the level-set method, or phase field approaches. Topological derivatives try to predict the influence of the introduction of a hole at a certain location in the design domain, and use this to generate new holes. The bubble method was a predecessor of this approach.

The level-set method uses a scalar field determined by the level-set function to describe the shape of the design domain. The level-set function is then updated by a partial differential equation, most often the Hamilton-Jacobi equation. Originally, this is a shape optimization method, but it can be transformed into a topological optimization method by introducing terms into the differential equation used to update the level-set function. Phase field approaches also use a partial differential equation, but directly update the density variables. These two methods appear to be in an earlier stage of development than ESO/BESO and SIMP.

The differences in results between the methods mentioned in this section turn out to be small, and just like for ESO/BESO, the practical implementation is eventually very similar to SIMP methods. Studies comparing the convergence or efficiency are scarce of even absent, such that making meaningful statements about which method to prefer is hard [106]. This combined with the less available documentation on these methods led to the decision to not further include these methods into the scope of this research.

7.2. Topological optimization of discrete element structures

The previous section introduced the topological optimization of continuous structure. A point of strong focus in these methods lies on obtaining clear 0-1 solutions to be able to manufacture the solution. A logical solution for this problem could be to search for methods that give solutions containing only discrete elements. Such a method would also be the logical choice when optimizing the layout of structures consisting of beam-like elements, like trusses or beam grids. The *ground structure method* initially developed by Dorn [38], and improved by Gilbert and Tyas [45] tries to tackle this problem. The *adaptive growth technique* proposed by Ding and Yamazaki [36] can be seen as an alternative purely focused on plate stiffeners.

7.2.1. Ground structure method

The ground structure method starts by discretizing a design domain with loads and boundary conditions into a grid of nodes (figure 7.3a and b). These nodes are connected to each other by potential structural members, creating the characteristic *ground structure* (figure 7.3c). The optimization step consists of finding the areas of the members that correspond to a minimum volume structure capable of resisting the applied loads (figure 7.3d). In mathematical form, the problem can be presented as [51]:

$$
\begin{aligned}
\min_{\mathbf{a},\mathbf{q}} \quad & V = \mathbf{1}^T \mathbf{a} \\
\text{s.t.} \quad & \mathbf{B}\mathbf{q} = \mathbf{f} \\
& \mathbf{q} \geq -\sigma^- \mathbf{a} \\
& \mathbf{q} \leq \sigma^+ \mathbf{a} \\
& \mathbf{a} \geq \mathbf{0}
\end{aligned}
\tag{7.2}
$$

Where:

V = the structural volume

$\mathbf{1} = [l_1, l_2, ..., l_m]^T$ is a vector containing the length of the members

$\mathbf{a} = [a_1, a_2, ..., a_m]^T$ is a vector containing the cross-sectional area of the members

$\mathbf{B}$ = an equilibrium matrix related to the directions of the members and the nature of the problem

$\mathbf{q}$ = the vector containing the member forces

$\mathbf{f}$ = the vector containing the external forces

σ^- = the compressive strength of the material

σ^+ = the tensile strength of the material

| (a) | (b) | (c) | (d) |
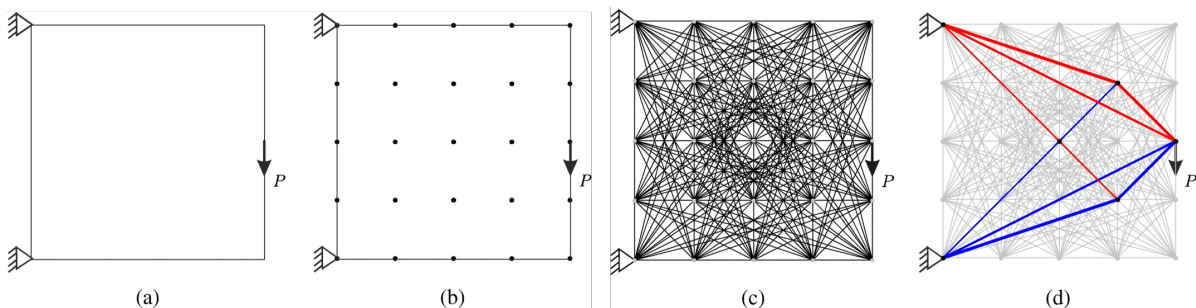
Figure 7.3: An illustration of the steps taken in the ground structure method. A domain with load and supporting conditions (a) is discretized with a grid of nodes (b), which are connected to each other to form the characteristic *ground structure* (c). During the optimization, the a number of members from this ground structure is selected to obtain the most efficient structure possible (d) [51]. This figure is a copy of figure 5.7.

Multiple load cases can be considered by substituting q and f for q^k and f^k, with $k = 1,2,...,p$ representing the load cases that should be included. When joint costs need to be included, this can be done by adding a term s to entries of the $\mathbf{1}$-vector. Inclusion of joint costs can considerably simplify the layout resulting of the structure [51].

Figure 7.3 shows that even for a small number of nodes the number of possible beams is already substantial. When the number of nodes increases, the number of possible members - and thus the number of equations in the problem - quickly explodes. This limits the size of the problems that can be solved when the original version of the ground structure method is used. Gilbert and Tyas [45] developed a *member adding* scheme that solved this problem.

The improved process starts with a small subset of members, and other members can be gradually added to this set. This process is repeated until all potential members satisfy the constraint:

$$\epsilon_i = \sum_{k=1}^{p} \frac{\max(\sigma^+ \mathbf{B}_i^T \mathbf{u}_i^k; -\sigma^- \mathbf{B}_i^T \mathbf{u}_i^k)}{l_i} \leq 1 \tag{7.3}$$

where the subscript i indicates the potential member, and the vector $\mathbf{u_i^k}$ contains the virtual displacement of nodes connected to member i. The eventual process can be seen in figure 7.4. The primal problem is the original ground structure problem stated in equation 7.2, which can be solved using various mathematical solvers. In most applications, the problem is a linear programming problem (see section 6.1.1) and can thus be solved very efficiently.
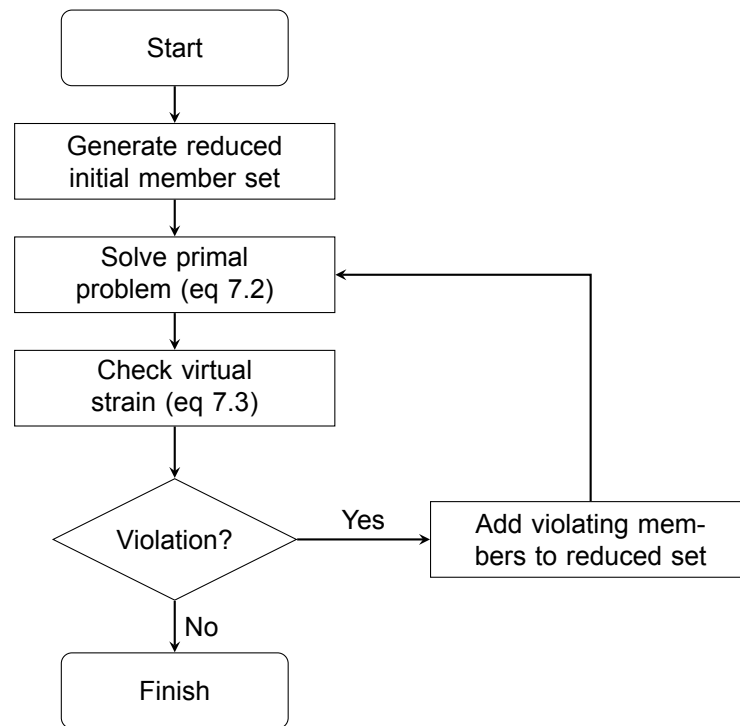
Figure 7.4: Flowchart of the ground structure method including the member adding scheme. Based on [51].

7.2.2. Adaptive growth technique

The adaptive growth technique was inspired by the growth and branching pattern found in trees. It tries to mimic the natural process where branches grow in a way that enhances the global performance of the system. For plants, this may be the availability of sunlight or water, while for structures it may be maximization of stiffness or buckling load [36].

The technique starts by setting up a base plate and ground structure of stiffeners (see the left of figure 7.5). The plate is modeled using triangular or quadrilateral plate elements, while the stiffeners are represented by beam elements. The nodes of the plate and beam elements are connected to provide interaction between the two. The right side of figure 7.5 illustrates the configuration of this connection. As the plate is located on the neutral axis of the stiffener, no influence from the Steiner rule is obtained.
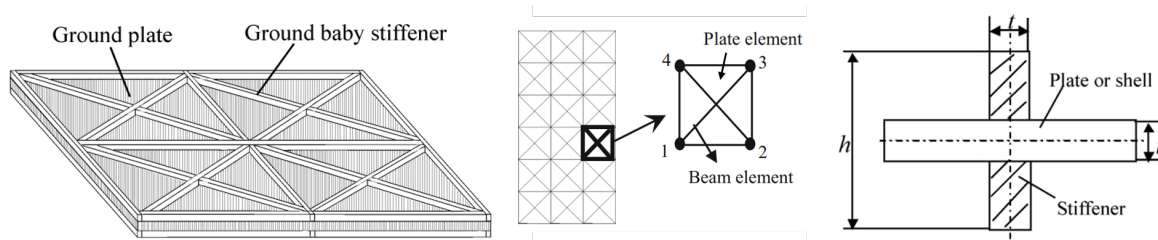
Figure 7.5: Illustration of several key concepts for the adaptive growth technique. Visible is the ground structure of a plate with possible stiffener locations (left), the connection between plate and beam elements (middle), and the arrangement of the stiffeners relative to the plate (right) [36].

After the ground structure is set up, the *seeds* from where the branches may start to grow are appointed. The last step before the optimization may start is the determination of the volume constraint and A_{branch}, which determines the area stiffeners must have before new branches may grow from their ends. The set of stiffeners this applies to is called P_{branch}. Only the area of stiffeners connected to a seed or a branch in this set can increase.

The iterative process then start with a finite element analysis, followed by a sensitivity analysis to determine the influence of increasing the area of the active stiffeners. The most effective stiffeners are selected and enlarged. If their cross-sectional area then exceeds A_{branch}, they are included in P_{branch} and new branches may sprout from their ends. After all active stiffeners are considered, a new FEA is performed and the process is repeated until the volume constraint is reached. The complete procedure is captured by the flowchart of figure 7.7.

The seed positions should be carefully chosen, as the outcome of the process is heavily dependent on it. This is illustrated by figure 7.6, which also serves as an example of the results of the adaptive growth technique. The ground structure requires the same amount of attention, as it determines the possible positions of stiffeners.
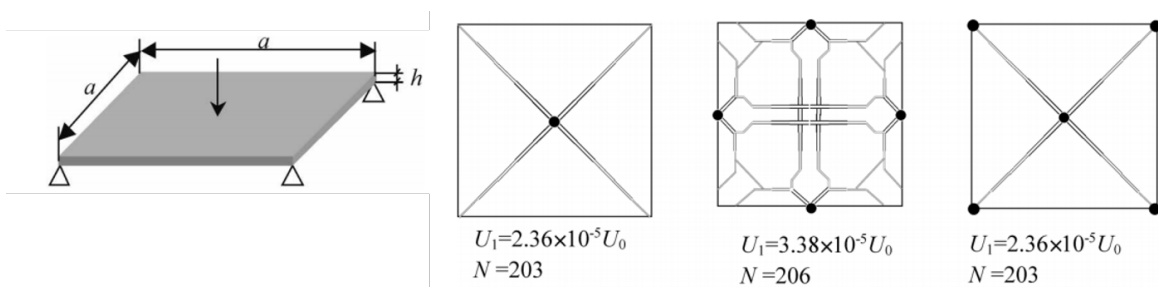
Figure 7.6: Results for the optimized stiffener placement found by the adaptive growth technique. As can be seen on the right of the figure, different seed positions may lead to different layouts [36].

Indications of run times of the method are not given in Ding and Yamazaki [36] and Dong et al. [37]. Ding and Yamazaki claim the method may be more efficient than continuum based methods, as those require many finite elements to capture the distribution of the narrow stiffeners well. However, the analyses made in Dong et al. show that many iterations (over 400) are made before a result is obtained. It should be noted that this was for a buckling analysis and not for a regular compliance minimization, but does show that the algorithm may cost a long time to run.

7.2.3. Comparison Ground structure method and Adaptive growth technique
Strong similarities between the ground structure method and adaptive growth technique are found in the use of discrete elements and a ground structure of beam elements that may change their cross-sectional area. It could even be argued that the branching algorithm is an alternative way for the *member adding* scheme to decrease the amount of possible stiffeners and limit the computational effort. Differences are present in the plastic approach of the ground structure method contrary to the elastic FE analysis made in the adaptive growth technique. The latter also incorporates the effect of the plate between the stiffeners.
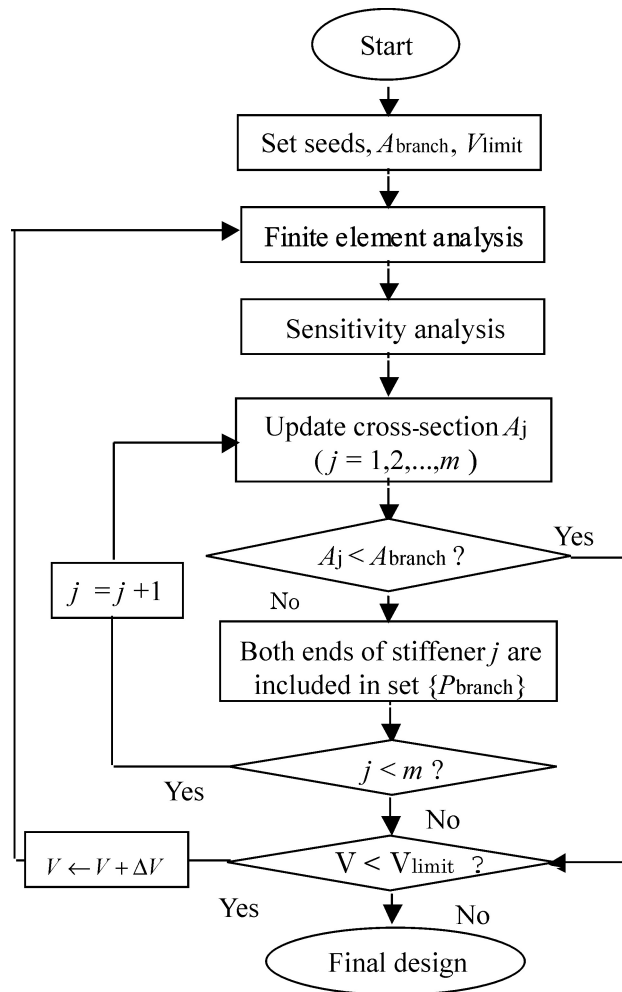
Figure 7.7: Flowchart of the adaptive growth technique [36].

8
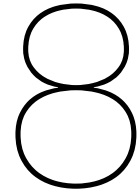
Relevant Applications of Structural Optimization

The previous chapters gave an introduction to orthotropic steel decks and structural optimization. The goal of this thesis is to combine these subjects. This chapter will explore some publications that have already done this or could be relevant to it.

The first section will cover three publications that treat the parametric optimization of orthotropic steel decks. As mentioned in section 5.3.1, parametric optimization only optimizes structural dimensions and leaves the design concept unaltered. The second part of this chapter deals with applications of topology optimization on steel bridge decks, which do search for new structural concepts. These applications appear to be very scarce, as only the PhD work of Baandrup [10] was found. The third and final section covers a more theoretical application of structural optimization, which can be useful to check results from automated algorithms.

8.1. Parametric optimization of orthotropic steel decks

Parametric optimization aims at finding the optimal values for structural dimensions in a given design (see section 5.3.1), which could be seen as the fundamental problem in structural engineering. Although it is thus not a new field of research, the current increasing computational capabilities do open up new possibilities to be explored. Finite element calculations can (partly) substitute costly and time-consuming experiments, making it much easier to investigate the effects of changing parameters on structural behavior. Fettahoglu [43] uses this to formulate recommendations about the ratios of several geometrical properties of OSDs.

Although this method can result in improved rules of thumb, the current possibilities of parametric optimization stretch further. This is shown by Baandrup et al. [11], who couples an FE-model to a mathematical algorithm (sequential quadratic programming, see section 6.1.2) to search for improved dimensions. Huang et al. [55] and Zhuang et al. [122] take a different approach and both use a form of surrogate modeling to estimate the results of a finite element analysis. The obtained proxy model is then coupled to a non-linear solver and genetic algorithm respectively to find the optimized parameters for the design. These approaches can be used to automate the optimization phase often found in a design process, and thus similar methods can result in a more efficient structure as well as a reduction of engineering workload.

The paper by Baandrup mentioned above simultaneously optimizes ten parameters, while Huang and Zhuang consider eight parameters at once. Although this is necessary to find true optimal solutions, the complex relation between the design parameters and resulting structural behavior makes it often impossible to do without the use of computational algorithms [11]. Usage of such methods when searching for true optimum designs of complex structures is therefore claimed to be almost inevitable.

8.1.1. Used methods

Baandrup et al. [11] use two different objectives in the optimizations: weight and price minimization. A fatigue constraint was implemented in the form of a maximum stress for three fatigue-sensitive details that were deemed to be governing. The maximum stress for each detail was determined such that the eventual fatigue damage for the joint would be acceptable when the constraint is satisfied. The deflection criterion consisted of a maximum difference of deflection between adjacent crossbeams. All optimization parameters were bounded by minimum and maximum values within which the solution was expected. The optimization framework used finite difference gradients computed in a Matlab script that was coupled to the FE model in Abaqus. Initial values were varied, but no deviations in the results were found. Nevertheless, this does not guarantee global optimality.

Huang et al. [55] start by forming a *response surface*. This surface describes the relation between the structural parameters of interest and the design variables. It is constructed by analyzing 120 models with different values for the design variables. Explicit functions describing the influence of the variables on the structural parameters are obtained, which are then used in the optimization step. Multiple optimizations objectives are considered in the paper, including steel, pavement and system height minimization. Constraints were present in the form of maximum pavement stresses, deflection criteria, and the maximum stress in three fatigue sensitive joints. This stress was set to 30 MPa for all joints in accordance with the Chinese regulations.

Zhuang et al. [122] first train a neural network to predict the outcome of a fatigue analysis based on the values of four parameters. This is done by performing a set of training fatigue analyses in which the parameters are varied. After these analyses, it is claimed that the neural network can predict stress ranges in welds within a five percent error. The second step in the optimization process is to use a genetic algorithm to find optimized values for the structural dimensions. The objective for the optimization is the minimization of stress ranges at three fatigue-sensitive joints. Constraints, number of iterations and parameters used for the genetic algorithm are not reported.

Table 8.1 gives an overview of the design variables that were used in the mentioned papers. The large differences in used variables and design constraints make a fair comparison between the results of the various papers difficult.

Design variable	Baandrup et al. [11]	Huang et al. [55]	Zhuang et al. [122]
Deck plate thickness	5-20 mm	12-20 mm	12-18 mm
Pavement layer(s) thickness		20-40 mm	
Pavement layer(s) stiffness		4-17 GPa	
Crossbeam ctc distance	4170-6250 mm	2400-3600 mm	
Crossbeam height	500-1500 mm		
Crossbeam web thickness	5-20 mm	10-20 mm	
Crossbeam flange width	50-500 mm		
Crossbeam flange thickness	5-20 mm		
Through height	100-600 mm		260-320 mm
Through thickness	5-15 mm	6-14 mm	6-12 mm
Through width top	200-400 mm		280-340 mm
Through width bottom	50-300 mm		

Table 8.1: Design variables and their allowed ranges used in the three considered papers.

8.1.2. Results

The research by Baandrup [11] shows a possible weight saving of 13,8 percent and a price saving of 16,7 percent for the case study of the Osman Gazi bridge in Turkey. It was, however, noted that these results did not comply to the recommendations in EN 1993-2 annex C regarding the minimum plate thickness and combined stiffness of the deck plate and ribs. Baandrup claims that this stiffness requirement can be seen as very strict, since the calculated deflection of the crossbeams was still small in the FE-models when the requirement was disregarded. The maximum savings in weight and price were 5,8 and 8,7 percent respectively when all Eurocode recommendations were fulfilled.

Huang's paper does not apply the results on a case study, but focuses on the used method. The results differ strongly depending on the optimization objective. The optimized design variables often reach their upper or lower bound, indicating that shifted design constraints could improve the design further. The work of Zhuang reports only minor changes of the parameters compared to the initial values that were based on the design of the Taizhou Yangtze River bridge.

8.2. Topology optimization of orthotropic steel decks

As mentioned in the introduction of this chapter, examples of topology optimization applied to orthotropic steel decks are scarce. To the authors knowledge, only the doctoral work of Baandrup [10] applies topology optimization to find better solutions for the design of OSDs.

This section covers two papers of Baandrup et al. that treat topology optimization for orthotropic steel decks. The first does this by applying a very fine, density-based TO, while the second uses the ground structure method to find a new deck structure with discrete elements. The other paper in the dissertation (chronologically the first) covers parametric optimization and was already treated in the previous section.

8.2.1. Density-based topology optimization

A first innovative concept can be found in the second paper [13] of Baandrup's dissertation. Here, a new design for the case study of the Osman Gazi bridge is made after a highly detailed topology optimization study. The design features curved crossbeams that bend towards the cable supports, and is supposed to better facilitate the natural flow of forces towards the supporting cables (see figure 8.1).
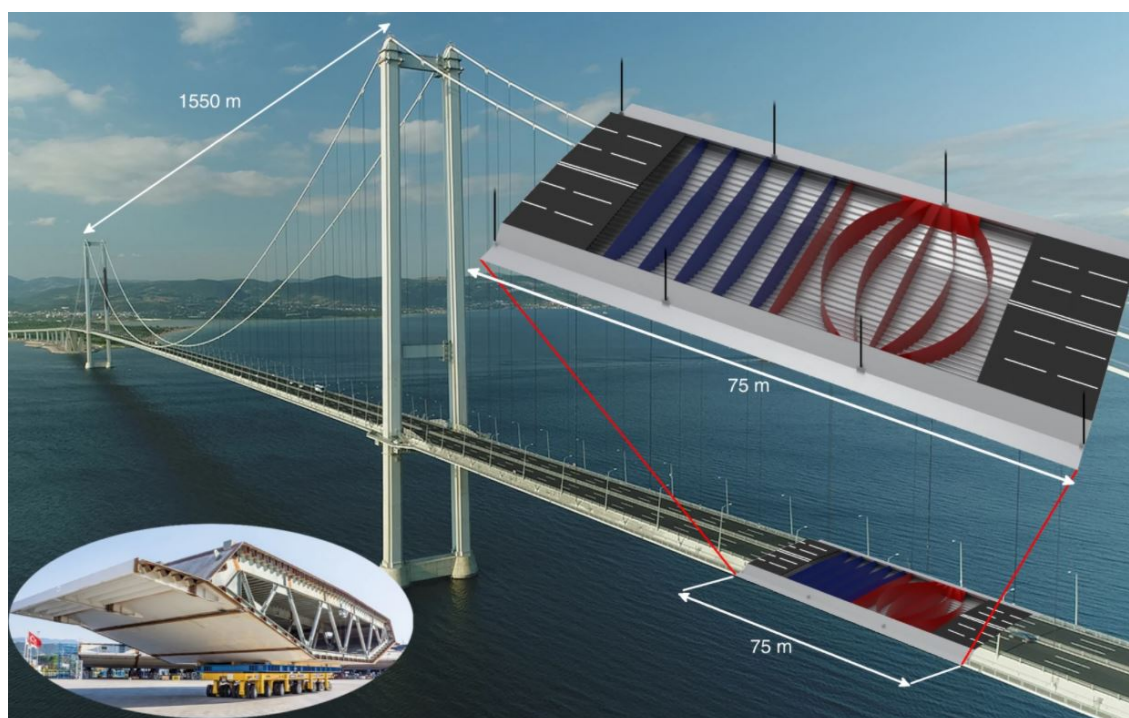
Figure 8.1: The new design concept for the Ozman Gazi bridge deck as presented in Baandrup et al. [13]. The new curved crossbeams (in red) are compared to the traditional straight crossbeams (in blue). In the bottom left, a photo of a bridge deck section is shown.

The curved diaphragms were inspired by the patterns found after a giga-scale topology optimization step. Only the inside of a box girder was considered, so the pavement layer and outer skin panels were not altered. This design domain was divided into 2,1 billion elements, resulting in an element size of approximately 17 mm. A SIMP scheme (section 7.1.1) is then adopted with a volume constraint of 3 percent of the total volume of the structure. The loading of the structure contained twelve global load cases, applying section forces to the ends of the girder, and two local load cases that consisted of a distributed load on part of the deck surface. Fatigue loading was thus not considered.
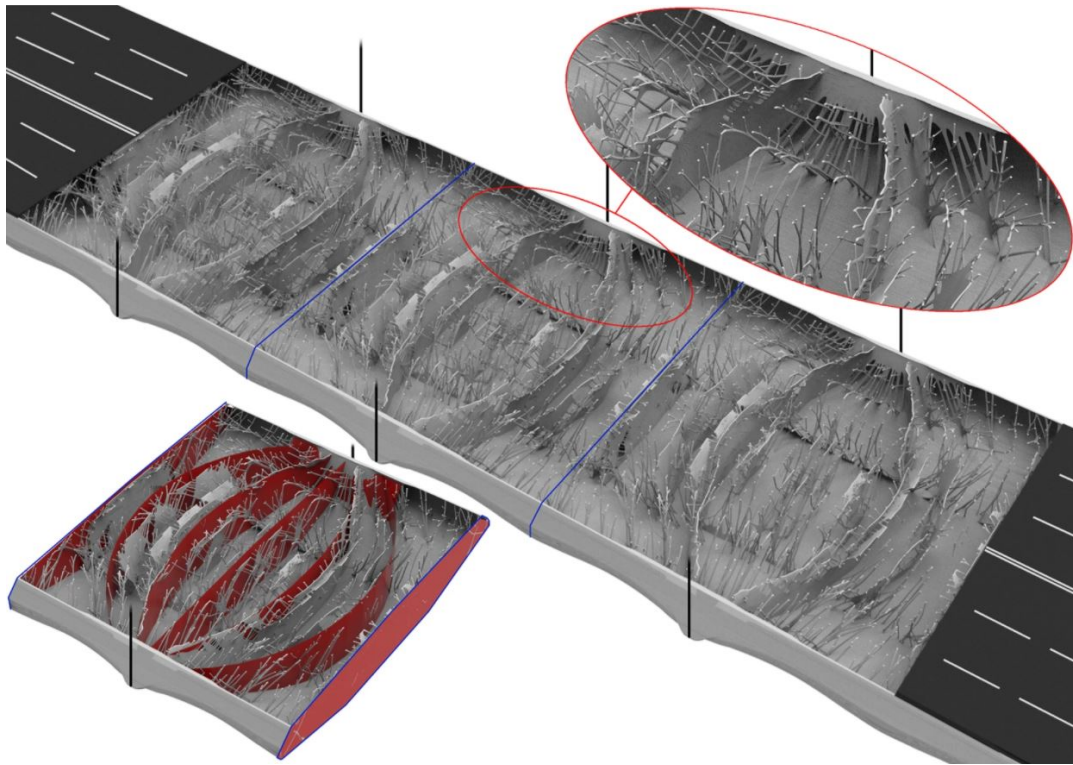
Figure 8.2: The result of the fine topology optimization and the interpreted design (in red) used in Baandrup et al. [13].

The optimization problem was then solved by a supercomputer with 16.000 cores running 85 hours. The resulting structure, visible in figure 8.2, is highly detailed, but practically impossible to make or analyze. Its main characteristics were therefore used for the interpreted design that was already shown in figure 8.1. The new design was then optimized by the parametric optimization algorithm developed in the earlier mentioned paper by Baandrup [11], which was discussed in section 8.1. The potential weight savings of the deck were claimed to be 28,4 percent, against a maximum of 13,8 percent for the parametric optimization of the classic OSD concept.

8.2.2. Truss based topology optimization

The second new alternative for an orthotropic box girder was presented in Baandrup's last dissertation paper [12]. The same case study of the Ozman Gazi bridge girder was considered. This time, a truss-like inner structure is obtained that connects the upper and lower skin plates (figure 8.3). The top plate supporting the pavement was changed from the orthotropic steel deck to an isotropic plate that should be able to span three meters. A sandwich plate of some sort is suggested, but the precise realization is left outside of the scope.

The ground structure method (section 7.2.1) was used to find the three-dimensional truss structure. 6.665 possible elements were used in the ground structure, which filled the complete interior of the box girder. Just like for the SIMP-based optimization, the outer skin plates and pavement layer were not part of the design domain, and the same fourteen load cases were used. The objective function considered minimization of the total volume of the truss elements, while the constraints consisted of maximum stress values and local and global stability considerations. Run times required for the analysis were not reported.

The total weight of the proposed girder design is claimed to be 54,7 percent lower than the original design of the Osman Gazi bridge. Depending on the necessary equivalent deck plate thickness, this could turn out to be between 35 and 63 percent. Next to the weight reduction from the thinner deck plate, the truss structure would reduce the material needed in the diaphragms and bottom plate of the deck. Construction costs were not considered.
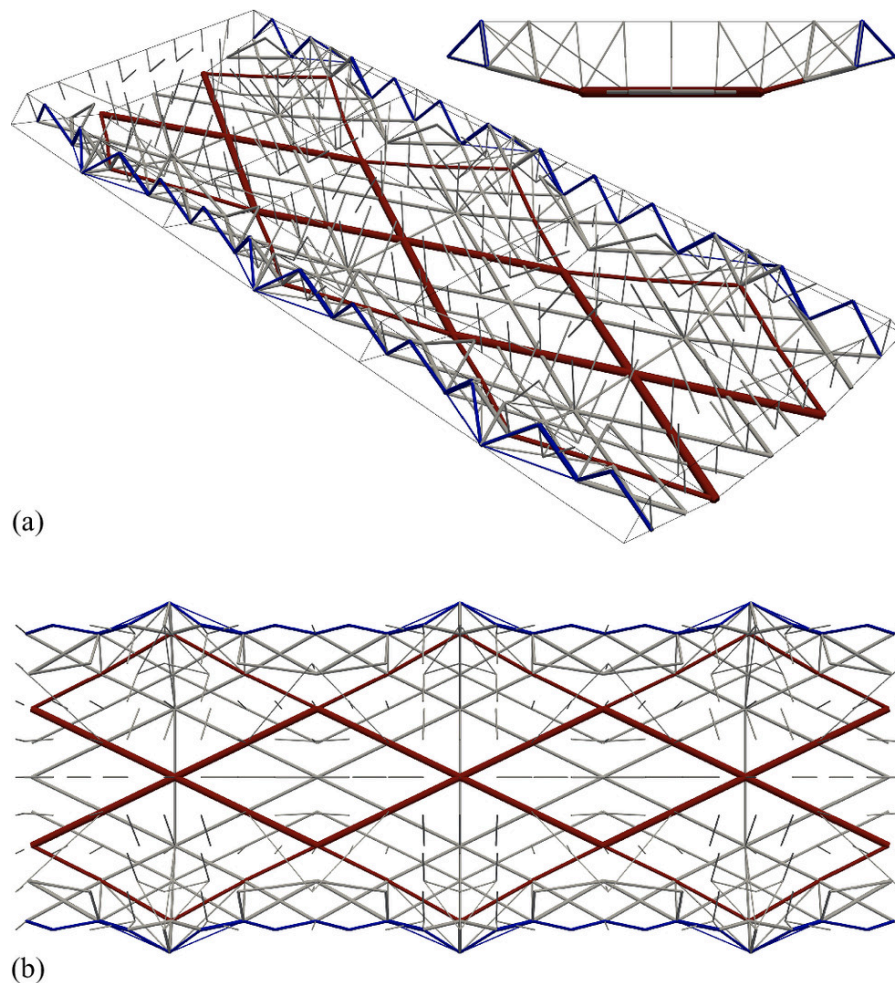
Figure 8.3: The optimized truss structure found by Baandrup et al. [12] for the Ozman Gazi bridge girder.

8.2.3. Critical review of the topology optimizations

An important first point of criticism on the two proposed solutions is the lack of any fatigue checks made for the designs. The first paper states that the authors expect that fatigue will not be a larger issue than in the conventional OSD concept, as the average Von Mises stresses in the optimized design have decreased for the considered load cases. While this could indicate a more efficient load transfer, it does not guarantee that the structural response to local wheel loads has improved. Neither of the papers considered load cases containing wheel loads.

Another point of criticism of the first paper applies to the interpretation of the design. It seems to be overkill to let a supercomputer run 85 hours to find a highly detailed design, only to convert it to a simple concept using seven plain diaphragms per section. A lot of features of the detailed design are neglected, like arches and branching patterns (see figure 8.1). It raises the question if a similar design could have been made by simpler procedures, making it much more accessible for use in practice.

The fine optimal structure was better captured by the truss optimization procedure, leading to larger weight savings. However, the result can only be seen as preliminary, as the concept for the deck structure was not yet considered. Verification studies of the assumptions regarding the deck structure are necessary to strengthen the credibility of the promised savings.

Still, the papers show the possibilities of topology optimization in civil engineering practice. The expected weight savings are substantial, justifying further investigation of applications for TO in civil engineering. Although the found solutions are often complex, future use of added manufacturing and robotized construction processes could be able to build them.

8.3. Theoretically optimal orthogonal beam grids

Despite the large potential of automatic structural optimization techniques, their results should always be critically evaluated. Insights gained from theoretical studies may be especially valuable to do this.

In this context, the article by Hoogenboom [54] is interesting to mention. The article elaborates on the theoretical optimal ratio for the spacing of subsequent orders of beams in a grid. A situation was considered where a beam grid spans the space between two walls, as visualized by figure 8.4.
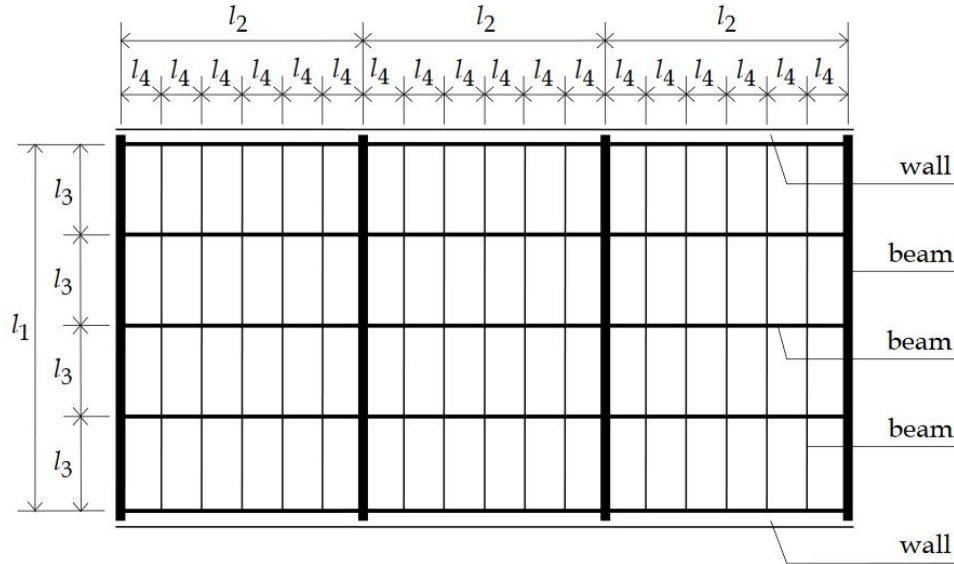
Figure 8.4: The grid of beams studied by Hoogenboom [54]. An area spanning between two walls is supported by beams of different orders forming an orthogonal grid.

An elastic distribution of forces and stresses is assumed and the beam height is related to its width using an aspect ratio that is the same for all elements in the grid. A universal maximum allowable stress is assigned as constraint. The derivative of the total beam volume V to the beam length l_i is then set to zero and solved, leading to an optimal ratio for the spacing of consecutive beam orders:

$$l_{i+1} = 64 \frac{l_i^5}{l_{i-1}^4} \quad \text{for} \quad i = 2 \text{ to } i = m - 1 \tag{8.1}$$

With this expression, the optimal spacing for the next, smaller beam order can be calculated from the spacing used in the two previous, larger beam orders. For the other way around, the equation can be rewritten to:

$$\frac{l_i}{l_{i-1}} = \left(\frac{1}{64} \frac{l_{i+1}}{l_i} \right)^{1/4} \tag{8.2}$$

which can be used to start with the smallest beam spacing and then calculate the larger ones. For any positive starting value, this sequence will converge to $\frac{1}{4}$ very quickly. It is therefore concluded that the optimal spacing of every next order of beams is a fourth of the spacing of the current order of beams, i.e. $l_{i+1} = \frac{1}{4} l_i$.

This same results were found when continuous instead of simply supported beams were used. Although treating an orthotropic deck as a beam grid is a simplification, it may be interesting to compare the current practice or the results from an optimization step with this found ratio.

8.4. Conclusion: Current state of the art

From the applications of structural optimization of orthotropic steel decks presented in this chapter, it can be concluded that the subject is still in an early stage of development. The very few papers that investigate the subject suggest that significant reductions in material and costs may be achieved, but also leave questions unanswered.

In the parametric optimizations, only a limited amount of options has been explored. The methods, parameters, and results presented in the studies vary, making a proper comparison hard to perform. Further research could give more insights regarding the proper use of optimization algorithms, design variables, and design constraints.

All papers simplify the necessary fatigue analysis to limit the run times of the analysis, either by considering only a limited number of load cases or using surrogate modeling. Although these tactics could give accurate results, they should be at least be verified by a full fatigue analysis of the optimization result. This, however, appears to be lacking at all three papers and the feasibility of the found variants is therefore uncertain. The difference in design between the investigated decks and those often found in the Netherlands amplifies this problem further for utilization of the results in Dutch practice.

Applications of topology optimization are even more scarce, as only two articles coming from the same author were found. These articles find new structural principles with potentially very large material savings, but a great amount of research still needs to be done before practical adoption becomes realistic. Besides the apparent difficulties for manufacturing, some significant engineering problems remain in the form of fatigue checks and the design of structural detailing.

Furthermore, an effort should be made to make topology optimization of orthotropic bridge decks in practice more accessible. Although Baandrup's highly detailed supercomputer optimization shows an intriguing result, it is of little use for most practical applications. The strongly simplified design that is interpreted from this reveals this as well. Still, the found design and savings are admirable, and it may be interesting to see if similar reductions can be achieved using better available methods.

Finally, it may be interesting to see if results found by optimization algorithms show similarities to theoretically optimal values. The presented paper by Hoogenboom could be valuable for this.

II
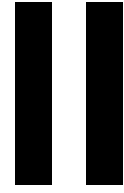
Parametric Optimization

<div align="right">

9

</div>

Case study introduction:
The new Van Brienenoord west bridge

This chapter will give a short introduction of the case study that will be considered in this thesis. First, some general information about the existing Van Brienenoord bridges will be given. Then, the future plans for the renewal of the bridge structure are presented and the new design of the deck structure is discussed. Finally, the main design parameters for the new Van Brienenoord bridge are summarized and compared to those of other Dutch bridges.

9.1. General information

The Van Brienenoord bridge spans the Nieuwe Maas on the east side of Rotterdam for the A16 to cross. It consists of an eastern and a western part, each featuring a tied-arch and bascule bridge. The construction of the eastern bridge was completed in 1965, followed by the western bridge in 1990. The newer western bridge has a different deck structure than the older eastern part. As discussed in section 3.2.3, the bascule section in the newer bridge experienced heavy fatigue cracking after only seven years of service life.

Figure 9.1: The Van Brienenoord bridge, seen from the north bank of the Nieuwe Maas.

The 295 meter span of the Van Brienenoord bridge western arch makes it the longest spanning bridge in the Netherlands [78]. The eastern bridge's span is with 287 meters a little shorter. Besides its impressive length, the bridge is also one of the busiest bridges found in the Netherlands, with 230.000 vehicles crossing daily over six lanes in both directions and 120.000 ships passing the bridge yearly [87]. This high traffic intensity is caused by the critical location of the bridge within the ring of Rotterdam and its span over a major shipping route (figure 9.2).
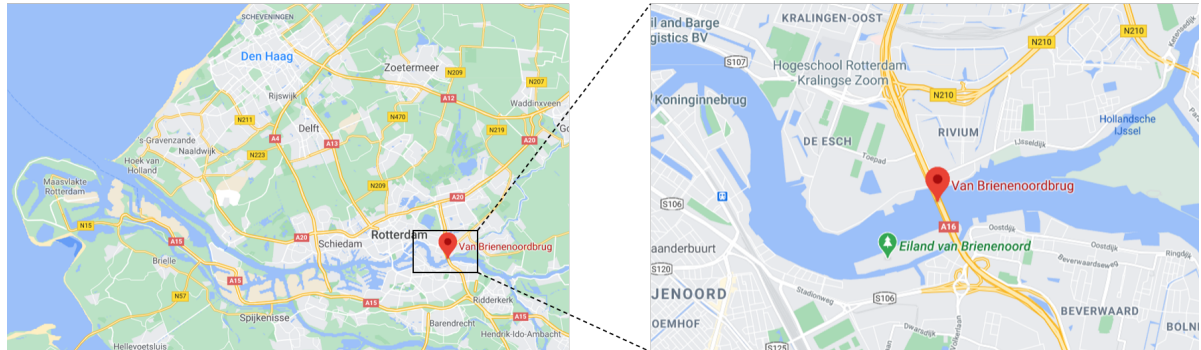
Figure 9.2: Location of the Van Brienenoord bridge [47].

9.2. Renewal

As for most older bridges in the Netherlands, the Van Brienenoord bridge suffers from the significant increase in traffic intensity and truck loading since its commissioning. The ministry of infrastructure has therefore ordered for a renewal of the existing bridge structure to ensure the safety and flow of traffic in the future.

For this renewal, a new arch bridge will be built at a yard and transported over water to the bridge site. There, it will replace the current western bridge arch, which will be transported back to the yard to be renovated. When this renovation is complete, the modernized bridge will be returned to site to replace the current eastern bridge. Preparations and tendering is still ongoing, and the first replacement is planned for the summer of 2025. By the end of 2027, the renewal should be completed.

9.2.1. New deck design

The design of the orthotropic deck of the new eastern and western bridge will be equal. The 29 m wide deck will have a continuous trough system with a 24 mm deck plate, 8 mm trapezoidal troughs, and 16 mm thick support plates (Dutch: *kamplaten*). No cut-out will be present around the trough in these support plates. The crossbeams and main girders of the existing western bridge will be reused in the renovation, predetermining the crossbeam spacing for the new deck. A stiffener spacing deviating from the traditional 300 mm was not considered. Figure 9.3 contains a schematic overview of the new design for the deck.
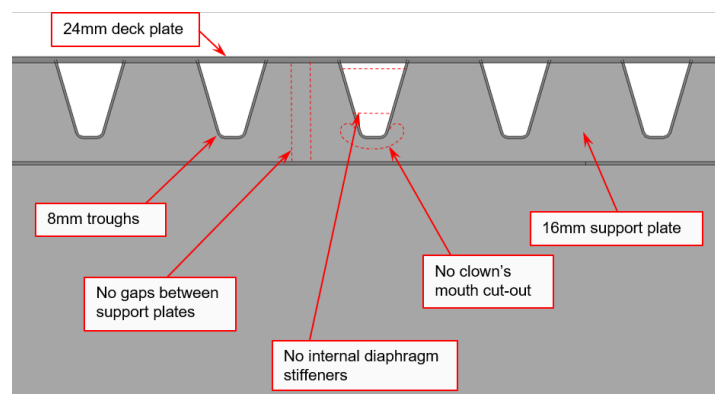
Figure 9.3: Schematic structure of the new Van Brienenoord deck [8].

9.2.2. Design parameters

An overview of parameters for the new design is given in table 9.1 below. To put the chosen values into perspective, the values of some other bridges are presented as well. The tables produced here can help to determine which are most interesting to integrate in the optimization that will be performed.

Parameter (mm)	New VBB	New SH	2nd VBB	2nd GC	1st GC	Ewijk
Year of opening	2025	2021	1990	1976	1971	1971
Bridge type	Tied-arch	Tied-arch	Tied-arch	C-S	C-S	C-S
Deck type	Plate	Plate	Plate	Plate	Plate	Box
Span (m)	300	200	300	180	180	270
Deck width (m)	29,0	13,4	29,0	34,6	34,6	37,1
Deck plate:						
thickness	24	20	12	10	10	10
Crossbeam:						
maximum span	25800	13400	25800	6000	6800	n/a
center-to-center	3645	3100	3645	3333	3333	5000
t. flange width	200	n/a	200	n/a	n/a	n/a
t. flange thickness	14	n/a	14	n/a	n/a	n/a
web height	1000	1280	1000	800	800	3476
web thickness	12	12	12	10	10	8
b. flange width	400	350	400	300	300	n/a
b. flange thickness	30	25	30	18	18	n/a
Kamplaten:						
height	425	n/a	425	n/a	n/a	510
thickness	16	n/a	12	n/a	n/a	10
width	2400	n/a	2300	n/a	n/a	2300
spacing	0	n/a	100	n/a	n/a	100
Cut-out style	None	Complex	Complex	Simple	None	Simple
Troughs:						
center-to-center	600	600	600	600	600	600
height	325	300	325	275	250	350
width upper side	300	300	300	300	300	302
width bottom side	105	180	105	135	R = 110	92
thickness	8	7	6	6	6	6

Table 9.1: General and design parameters of the new Van Brienenoord deck compared to some other bridges in the Netherlands. Values in mm, unless stated otherwise. Contrary to the plate girder deck of the other bridges, the Bridge near Ewijk has a box girder deck. This explains the much larger (and variable) crossbeam height and missing other dimensions. The R in front of the 1st GC's trough bottom width indicates the radius of the semi-circular bottom of the trough (a rib like the third closed rib of figure 3.1 was used instead of the more usual trapezoidal shape).
VBB = Van Brienenoord bridge, SH = Suurhoff, GC = Galecopper, Ewijk = Bridge near Ewijk, C-S = Cable-stayed, n/a = not applicable. Sources: New VBB: [8]. New SH: [98]. 2nd VBB: [92]. 2nd GC: [90]. 1st GC: [91]. Ewijk: [34, 53].

10

Optimization problem formulation

This chapter will set-up the optimization problem that will be solved in the remainder of this part of the thesis. The necessary elements as introduced in section 5.2 will all be treated: first the optimization algorithm to be used, then the intended objective function, followed by the parameters functioning as design variables, and finally presenting the adopted behavioral constraints. The chapter closes with an overview of the optimization problem.

10.1. Optimization algorithm

The optimization problem will be solved by using the *artificial bee colony* algorithm, which was already treated in section 6.2.3. The choice for this algorithm was first of all made because of the good results that it showed in comparative studies [20, 49, 107].

Secondly, the artificial bee colony algorithm evaluates multiple design variants during a single iteration of the process. These variants are independent of each other and can thus be used to generate various design alternatives in a single run. Besides, the independence of the variants could be used in future applications to distribute the workload over multiple computers, servers, or cores. This could strongly decrease the time needed for the optimization.

Thirdly, the method only accepts better results to be remembered. This so-called *elitism* property can be very favorable for problems where the calculation of the objective function is computationally cheap, but the evaluation of the constraints is not. Structural optimization problems almost always belong to this category, as the needed finite element analysis usually forms by far the largest part of the computational demand. The neglecting of worse variants makes it possible to skip the costly calculation of constraint compliance if the objective value of a design alternative will never be better than the current one. Cao et al. [25] showed that this can reduce the time required for a structural optimization tremendously.

Finally, the artificial bee colony algorithm needs significantly less tuning parameters than most other swarm-based heuristics. Besides the usual population size and stopping criterion, which are present in all methods of this category, only a value for the so-called *limit* needs to be chosen. This can be beneficial to find good results quickly.

10.2. Objective function

The objective of the optimization will be the minimization of normalized mass of the deck structure. The choice for weight minimization over price minimization was first of all made as mass is "*a clear and unambiguous measure*" [11], that does not depend on the time and place the bridge deck is built in. The result of a costs minimization will heavily depend on the price ratio between material and labor, which can change overnight, making it harder to formulate general recommendations. It is underlined that a comparison between a design optimized for costs and a design optimized for mass can be interesting, which can be recommended for future research.

Expressed in a formula, making use of the symbols of table 10.1, figure 11.5, and 11.6, the objective function is defined as:

$$f_{obj}(x) = m_{total} + f_{pen}(x) = (V_d + V_{stiff} + V_{cb+sp} - V_{gap}) * \rho_{steel} + f_{pen}(x) \tag{10.1}$$

$$V_d = t_d \tag{10.2}$$

$$V_{stiff} = \frac{\left(2 * \sqrt{h_{stiff}^2 + \left(\frac{1}{2}(a_{stiff} - b_{stiff})\right)^2} + b_{stiff}\right) * t_{stiff}}{2 * a_{stiff}} \tag{10.3}$$

$$V_{cb+sp} = \frac{h_{sp} * t_{sp} + h_{cb,w} * t_{cb,w} + w_{cb,tf} * t_{cb,tf} + w_{cb,bf} * t_{cb,bf}}{ctc_{cb}} \tag{10.4}$$

$$V_{gap} = \frac{\frac{1}{2}(a_{stiff} + b_{stiff}) * h_{stiff} * t_{sp}}{2 * a_{stiff} * ctc_{cb}} \tag{10.5}$$

The considered mass will be per squared meter of bridge deck. The symbols V and w and subscripts tf, bf, and gap were not used in table 10.1 (as they are not design variables) and represent volume (per square meter), width, top flange, bottom flange, and the gap in the support plate for passing of the stiffener respectively. A value of 7850 kg/m³ will be used for the density of steel. The effect of the rounding of the troughs on the calculated weight is neglected. $f_{pen}(x)$ is the penalty function to include the constraints and will be discussed in section 10.4.2.

10.3. Design variables
As table 9.1 shows, the global structure of an orthotropic bridge deck generally has a substantial amount of parameters that may be altered to optimize the design for the considered case. The bridges presented in the table already show a great spread in the values used for these parameters, indicating the large design space available to an orthotropic deck. From the parameters that are applicable to the Van Brienenoord bridge, a motivated choice is made here for which parameters to include in the optimization.

10.3.1. Deck
The most striking difference in dimensions between the bridges of table 9.1 is the applied deck plate thickness, which has (more than) doubled for the new Van Brienenoord design compared to the bridges built in the past. The thin deck plates in these bridges are the main source of the fatigue problems that were discussed in section 3, explaining the large increase in thickness in current practice. The extensive influence of the deck plate on the performance of the complete deck and its great influence on the weight of the structure [17] makes it a design variable that must be included in the optimization.

10.3.2. Crossbeams
A second variable that has a large influence on the structural behavior of the deck can be found in the center-to-center distance of the crossbeams, as it affects the shape of the influence lines used for the stress range calculations and determines the span of the troughs. A relation between the span and center-to-center distance of the crossbeams is not visible from the data of these bridges, which would be expected when considering the optimal ratio of spans of successive beam orders as found by Hoogenboom [54] (see section 8.3). An explanation for this could be found in the connection the crossbeam center-to-center distance has with the segmentation of the deck and the global bridge layout.

Still, investigating if savings can be found when varying this parameter may be interesting, especially when comparing the values found in table 9.1 with the optimized values found by the papers presented in section 8.1. Both papers considering the center-to-center distance of the crossbeams suggest a larger spacing may be beneficial [11, 55].

Furthermore, the relation with the segmentation and global bridge layout often requires the choice for a crossbeam spacing to be made in an early stage. An automated optimization tool or general recommendations may be especially helpful in making a choice in this phase.

Although the deflection of the crossbeams has an effect on the stress at fatigue details [17], the stiffness of the crossbeams will not be considered as a design variable. Having more design variables will increase the size of the design space and therefore the computational demand of the optimization problem. In addition, it is expected that the deck plate and rib design will have a stronger influence on the structural performance of the deck, as their effect on the stresses in fatigue details is more direct. Future applications may include the dimensions determining the stiffness of the crossbeam to possibly enable even larger weight reductions than presented here.

10.3.3. Support plates
The most influential parameter of the support plate will be its thickness. It will both influence the stress range present in the plate and the detail category valid for its fatigue performance. The new design for the Van Brienenoord deck uses a relatively large support plate thickness, and it may be interesting to investigate the effects this has.

The height of the support plate could be relevant for the efficiency of the deck, mostly because it determines the distance between the bottom of the troughs and the top flange of the crossbeam. To properly optimize relation, however, the dimensions of the crossbeams should be included as variables as well. Moreover, the height of the support plate is also tied to the level of the deck plate, which cannot be changed easily in a bridge renovation. This dimension was therefore not included as design variable.

The width and spacing of the support plates will not be considered as well. A choice for these is thought to be mostly based on demands from fabrication, not fatigue performance.

10.3.4. Troughs
Troughs in orthotropic steel decks share a remarkable similarity: their center-to-center distance is almost always equal to 600 mm (see table 9.1). This is not only true for orthotropic decks found in the Netherlands, but for most of the orthotropic decks in other countries as well [29]. The same holds for the width on the top side of the troughs, which is almost always set to 300 mm, leaving the same space in between them.

Both dimensions have been the preferred option since the earliest OSDs were built in the 1950's [6] and, considering figure 3-4 from the US Department of Transport's design manual [29] and table 9.1, only few bridges deviate from this. No examples of recent bridges with a center-to-center distance (significantly) below 600 mm were found. The mentioned design manual explains this by stating that the currently used trough width and spacing *have proven to be cost effective and have performed well* [29]. With the fatigue problems recently found in a significant amount of Dutch bridges, this statement may be debated. Most illustrating for this is the fatigue damage found on the second Van Brienenoord bridge in the nineties (section 3.2.3), which can be directly linked to the top width of the troughs.

Furthermore, the parametric study done by Fettahoglu [43] shows that a smaller rib spacing will lead to smaller stresses in the structure (figure 10.1). The deck plate is explicitly mentioned herein as having lower stresses, which is promising for the deck-crossbeam-rib joint. Remarkable is the local minimum in the displacement to rib spacing graph around a value of 300 mm. It is also found in the relation between the rib spacing and the longitudinal stresses in the deck plate (figure 10.2) and could be a reason that the rib spacing is not often changed. After all, a small decrease in rib spacing may, initially, lead to higher stresses and displacements. A larger decrease will still give lower deflections and stresses, however.

The strong similarities present in the spacing and top width of the troughs are not found in their bottom halves. A multitude of shapes can be found, each with an extensive variety in bottom widths and/or
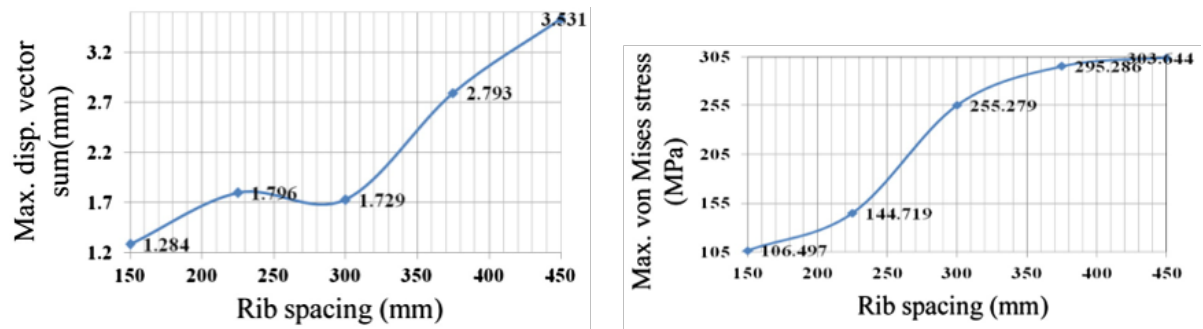
Figure 10.1: Relations between deflection and rib spacing, and maximum Von Mises stress and rib spacing as found by Fetta-hoglu [43].
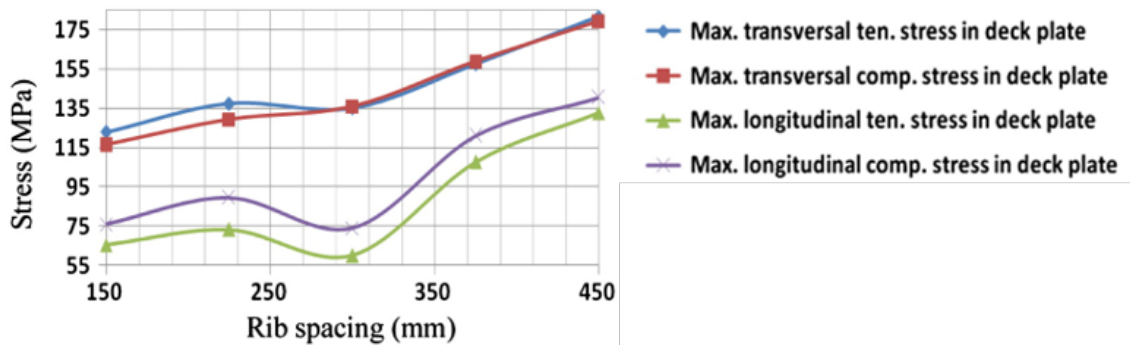
Figure 10.2: Deck plate stresses to rib spacing, as found by Fettahoglu [43].

corner radii. The trapezoidal trough is the most common type of closed rib, but even within this class many varieties exist. Comparing the dimensions in the previously mentioned tables, no relation at all is found between the width at the top, width at the bottom and the total height of the rib.

A second study by Fettahoglu [42] shows that shallower trough bottom leads to lower stresses in the crossbeam and somewhat lower stresses in the rib itself. Stresses in the deck plate increase when the bottom width is decreased. The deflections of the deck plate show a parabolic distribution when the bottom width increases, with a minimum at a trough wall angle around 75°. The diversity in reactions of these structural responses underlines the complex behavior of the orthotropic deck. More clarity regarding optimized trough ratios may be very valuable and thus the height and bottom width of the troughs will be added to the optimization as a design variables.

The final parameter that will be considered as a design variable will be the thickness of the troughs. Although increasing the trough height will always be a more economic option for increasing the stiffness of troughs, the trough thickness has a direct effect on the stresses in all governing fatigue details.

10.3.5. Overview and design constraints

The previous subsections motivated the choice for the design variables that will be added to the optimization. These are summarized below in table 10.1. To keep the outcome manufacturable and prevent second order effects such as plate buckling, the values the variables may take on are constrained.

These constraints are mostly based on recommendations found in EN 1993-2 and its Dutch national annex [1, 2]. Only for the thickness of the troughs, a smaller value is allowed than advised in the codes. This way, it is intended to investigate the possibility of using lighter troughs that are spaced closer together. The constraints for parameters for which the codes do not give recommendations were determined by seeking values that are often used in existing bridge structures, and then slightly extending the found range. The presented constraints are the eventually chosen values. Preliminary constraints were re-evaluated after some optimizations had been made and extended where needed. When an analysis used different values, these are presented at the respective section.

Parameter	Symbol	Lower bound	Upper bound	Increment	Unit
Deck plate:					
thickness	t_d	10	30	1	mm
Crossbeam:					
center-to-center	ctc_{cb}	2000	6500	5	mm
Support plate:					
thickness	t_{sp}	8	20	1	mm
Troughs:					
height	h_{stiff}	100	400	5	mm
width upper side	a_{stiff}	100	400	5	mm
width bottom side	b_{stiff}	0.3	1.0		a_{stiff}
thickness	t_{stiff}	4	10	1	mm

Table 10.1: Parameters to be used as design variables in the optimization and their allowed ranges. The spacing between the troughs will be equal to the width on the upper side. The increment column is only applicable when discrete parameters are used and indicates the base to which the variables are rounded.

10.4. Behavioral constraints

To complete the optimization problem, the behavioral constraints on the deck need to be defined. These consist of fatigue damage constraints at four selected fatigue details.

10.4.1. Fatigue details

In section 4.5, the for fatigue critical joints found within an orthotropic were discussed. Figure 4.5 shows that approximately ten connections need to be checked for fatigue in a regular orthotropic deck. The exact amount of checks depends on the design choices made, like the use of a cut-out or the application of open or closed stiffeners.

In this thesis, the amount of connections that is checked during the optimization will initially be reduced to three. The choice for these is made based on the preliminary design of the Van Brienenoord bridge. Herein, the three selected connections turned out to have significantly higher damage values than the other checked details. It is therefore expected that these three joints will be governing in the design made in this thesis as well. Additional checks should be performed in a follow-up study to verify this assumption.

The three selected connections are the rib-to-deck joint at the crossbeam intersection, the rib-to-support plate joint, and the splice between troughs of different deck sections. For the connection between the rib and support plate, a check will be done for both elements in the connection. As such, the number of checked connections is three, but the number of considered fatigue details is four. The details are shown in figures 10.3 and 10.4.
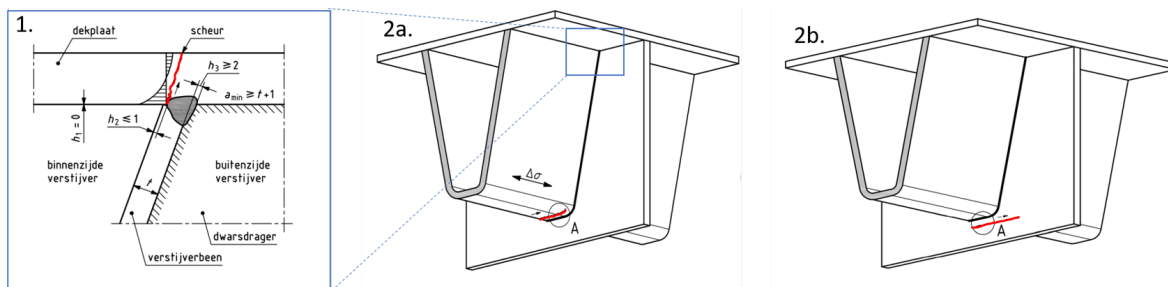
Figure 10.3: The first three fatigue details that will be considered in the optimization, located in the deck-to-rib joint at the crossbeam intersection (detail 1) and the rib-to-support plate connection. For the latter, both the rib (detail 2a) and the support plate (detail 2b) are checked for fatigue damage. The red lines indicate the approximate location of the expected fatigue crack. [2] (edited).
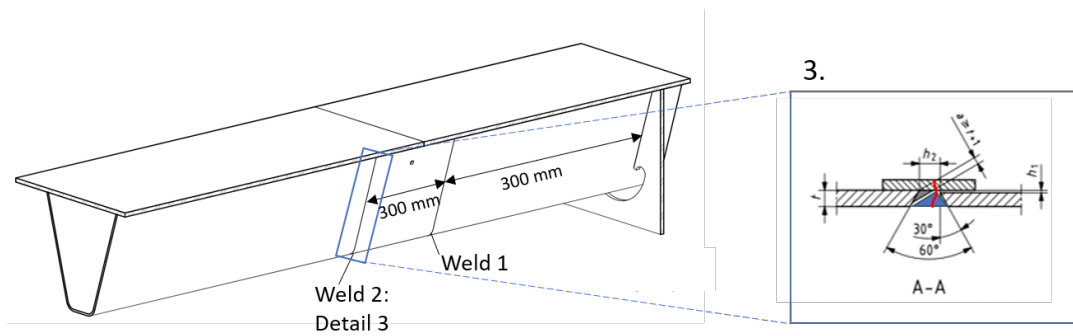
Figure 10.4: The third fatigue detail that will be considered in the optimization: the splice between two trough sections. Only the second weld is considered, as it is most likely governing. The connection is formed by a butt weld with backing strip (figure on the right). The blue triangle represents the weld material that will be deposited and the red line indicates an approximate fatigue crack location. Cracking is most likely to occur on the bottom side of the trough [2].

Table 10.2 gives an overview of the detail categories belonging to the selected details. It also presents the damage constraints that are applied to the details. For the rib splice, this constraint is chosen to be 0,8. This somewhat lower constraint is applied as the calibration of appendix D showed that the stresses at this detail are slightly underestimated by the modeling simplifications that were made (see chapter 11). The reduced damage constraint assures that a more detailed analysis will still result in a damage below 1,0. For the other details, the modeling simplifications mostly have conservative effects. An accurate calculation is thus expected to result in less damage and the maximum acceptable damage is therefore set to 1,0.

	Fatigue detail	Crack location	Detail category	Damage constraint
1	rib-to-deck at crossbeam	deck inside rib	see table 10.3	1,0
2a	rib to support plate	rib	140	1,0
2b	rib to support plate	support plate	100	1,0
3	rib splice	rib	100	0,8

Table 10.2: Overview of stress constraints for the fatigue details.

Thickness deck plate	Detail category	$N_{knee\ point}$	$N_{cut-off}$
≥18 mm	200	20 million	300 million
16 mm	188	25 million	200 million
≤14 mm	167	30 million	100 million

Table 10.3: Detail categories rib-to-deck at crossbeam joint [88]. The assumption is implicitly made that the thickness of the deck plate is always a multiple of 2. This thesis will use the data for 16 mm for any thickness between 14 and 18 mm.

10.4.2. Implementation of behavioral constraints: Penalty function

Heuristic algorithms like the artificial bee colony are not directly applicable to constrained optimization problems. Most often, this is solved by adding a penalty term to the objective function. This penalty term decreases the performance of a variant that does not comply to the given constraints. When chosen properly, this should make the calculated performance of unfeasible variants worse enough to not show up in the final solution.

The precise implementation of the penalty function has many options, such as static, dynamic, adaptive, and death penalty functions [59]. Here, a static penalty function will be adopted. The static character of this function means that it does not change over the course of the optimization.

The choice for the eventual penalty function was made after the preliminary optimizations given in appendix F. This appendix also explored the use of dynamical penalty functions (used in e.g. Kaveh [63] and Sonmez [107]), but these performed worse than the simple static function presented here. The increasing penalization caused early convergence to a local optima and often prevented variants with only little damage to be accepted in later stages. Only a few members of the population would ever find feasible results, which decreases the efficiency of the algorithm.

The used static function was based on the one used by (among others) Alberdi and Khandelwal [7], namely:

$$f_{penalty}(x) = \alpha * \sum_{i=1}^{4} \delta_i \tag{10.6}$$

With:

$$\delta_i = \begin{cases} 0 & \text{if } \quad \frac{d_i}{D_i} \le 0 \\ \frac{d_i}{D_i} - 1 & \text{if } \quad \frac{d_i}{D_i} > 0 \end{cases} \tag{10.7}$$

Where d_i is the damage of the ith fatigue detail and D_i the damage constraint there as given in table 10.2. α can be tuned for higher or lower penalization and was chosen as 100. This value was found partly due to an error in the fatigue analyses made in appendix F, which used an α of 1. The error caused the found damages to be a factor 100 too high, but did give satisfactory results. After the error was corrected, the value of α was increased to 100 to get a similar behavior of the penalty function.

Finally, the penalty function will not be multiplied with the objective function, as the earlier cited papers do, but simply added. This is done to prevent excessive values of the objective function that would prevent global exploration of the search space. Contrary to stresses in truss members, which is what the mentioned researches used as constraints, the damage at fatigue details may quickly reach very high values due to its high sensitivity to stress changes. Multiplying the weight of a variant with these large numbers may lead to excessive penalization. This would essentially rule out such a design, while a small adjustment could potentially reduce the damage from strongly. By only adding the computed penalty function, these design alternatives are given a chance to be properly investigated.

10.5. Overview

This chapter elaborated on the choices that were made to set-up the optimization problem. The most important points are summarized here.

- The artificial bee colony algorithm will be used to solve the optimization problem.

- The objective of the optimization will be the minimization of normalized mass. The formulas to calculate this are given in equations 10.2 to 10.5.

- Seven dimensions were chosen as design variables: the thickness of the deck plate, the center-to-center distance of the crossbeams, the thickness of the support plate, and the height, top width, bottom width and thickness of the troughs. These variables were chosen as they were expected to have the largest effect of the performance of the deck structure. Table 10.1 gives an overview.

- Four behavioral constraints are applied to the problem, all setting a limit on the expected damage at selected fatigue details. These were chosen based on the preliminary design of the Van Brienenoord bridge, in which the details were found to be governing for the design of the deck.

- The constraints are implemented in the problem by adding a penalty function to the objective function, executed as a summation of the damages at the fatigue details that is multiplied by 100 and added to the mass of a design variant.

In mathematical form, the problem can be presented as:

$$\begin{aligned} \text{minimize} \quad & f(x) = m_{total} \\ \text{subject to} \quad & \begin{cases} g_i(x) \le 0 & i = 1, .., 4 \\ K(x)u = \mathrm{f}(x) \end{cases} \end{aligned} \tag{10.8}$$

With:

$$g_i(x) = \frac{d_i}{D_i} - 1 \leq 0 \tag{10.9}$$

Where d_i is the fatigue damage and D_i the damage constraint at detail i, which can be found in table 10.2. When the constraints are included in the problem through the penalty function, the final problem to be solved becomes:

$$\text{minimize} \quad f(x) = m_{total} + f_{penalty}(x)$$

$$\text{subject to} \quad K(x)u = \mathrm{f}(x) \tag{10.10}$$

With:

$$f_{penalty}(x) = \alpha \sum_{i=1}^{4} \delta_i \tag{10.11}$$

$$\delta_i = \begin{cases} 0 & \text{if} \quad \frac{d_i}{D_i} \leq 0 \\ \frac{d_i}{D_i} - 1 & \text{if} \quad \frac{d_i}{D_i} > 0 \end{cases} \tag{10.12}$$

Description of parametric model

This chapter will give a description of the finite element model that is used in the optimization. Choices that were made during the setup of the model are presented and motivated.

The optimization problem set up in the previous chapter will need more than a thousand iterations for a proper solution to be found. It is therefore of great importance to limit the time needed for the fatigue analysis. The sensitivity of fatigue, on the other hand, also requires the result to be very precise. Hence, a constant balance between accuracy and required analysis time had to be taken into account during the development of the parametric model. This has led to simplifications in the modeling where possible. The assumptions that come with these are tested in the appendices A, C, and D.

First, the global layout of the model with dimensions will be given. Second, the levels of model detailing are discussed, followed by a more elaborate description of the model per structural component. Finally, some general model information and a summary of the model is given.

11.1. General layout and dimensions

The used finite element model consists of a segment of the bridge deck that is present between two cable supports (see figure 11.1). The deck plate, crossbeams and troughs have been modeled over the full width and length of this segment. The main girders are extended by one segment at each side.
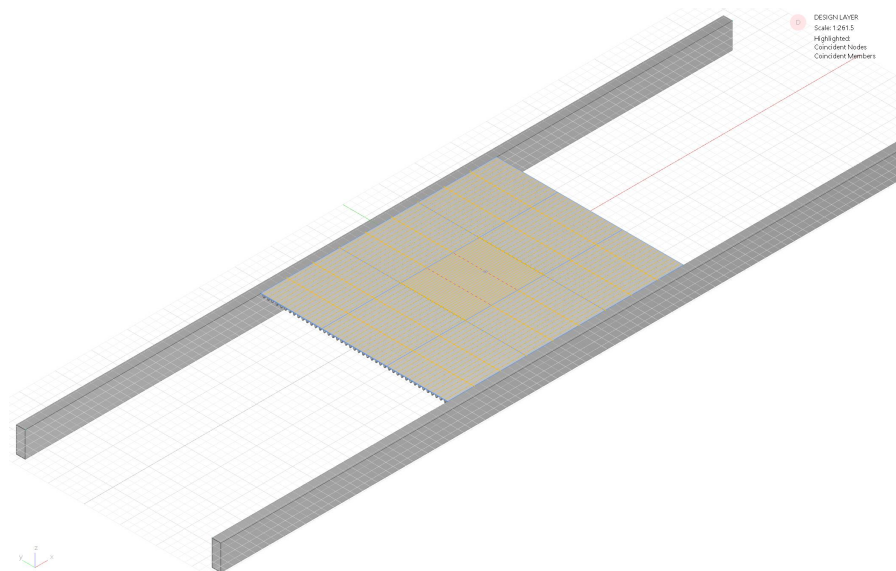
Figure 11.1: A 3D view of the parametric finite element model.

The length and width of the segment are constant during the optimization and are taken from the case study. For the Van Brienenoord bridge, these correspond to 32,8 m and 26 m respectively. The total length of the main girders thus becomes 98,4 m, with four evenly distributed supports per main girder. The support at the far left end of the top main girder is pinned, while the support on the distant right of the bottom main girder is supported in global y- and z-direction (see figure 11.2). The remaining supports are only supported in global z-direction.
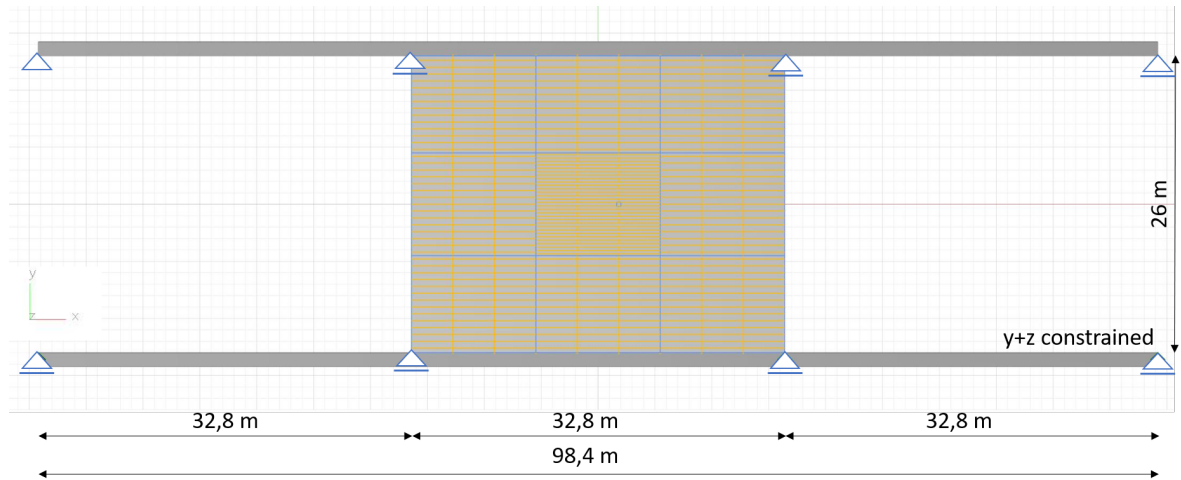
Figure 11.2: Top view of the parametric model, including length and width dimensions of the bridge. The support points are labeled. The top left is simply supported, while the bottom right has a constraints on displacements in y- and z-direction. The remaining supports only restrict displacement in z-direction.

11.2. Levels of finite element model detailing

As mentioned in the introduction of this chapter, a balance between accuracy and required analysis time was sought when developing the parametric model. An important tactic for this was the utilization of different detail levels in the finite element model (figure 11.3). This way, a precise model with a fine mesh can be used where necessary, while more crude modeling with a coarser mesh can be used where possible.
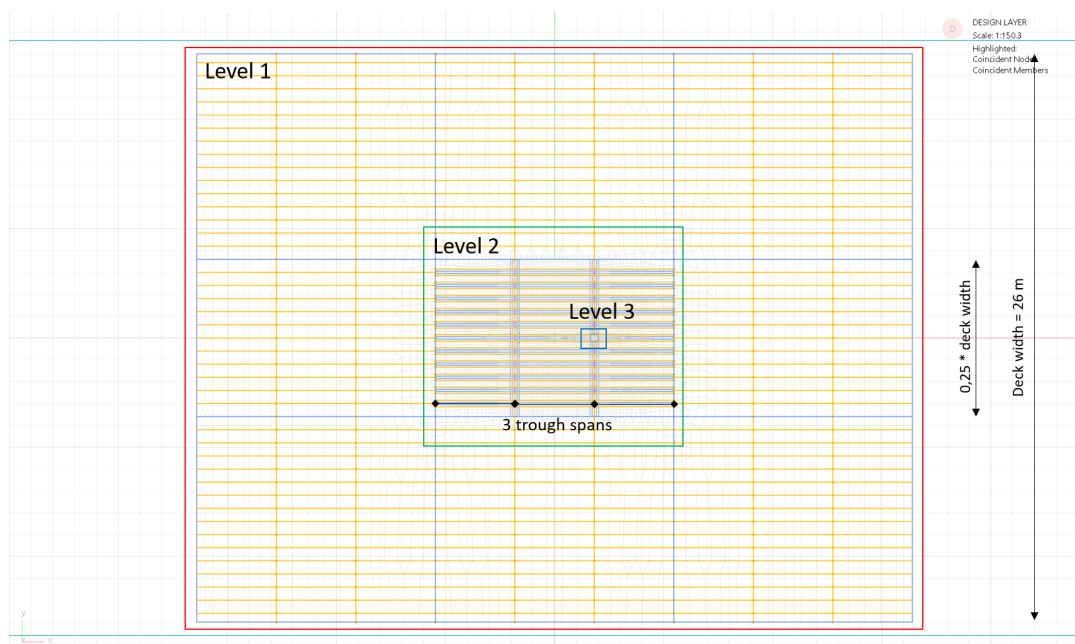
Figure 11.3: Location of detail levels within the deck. The used dimensions of detail level 2 are indicated.

The outer area of the modeled deck can be considered as *level 1*, where the crossbeams and troughs are modeled using beam elements and the deck plate is represented by shell elements with a coarse mesh. Due to the necessary connection between the deck plate and troughs, this comes down to a mesh size equal to the center-to-center distance of the latter. The mesh size of the beam elements serving as the troughs and crossbeams follows this.

The mid area of the deck can be seen as *level 2*, having the crossbeams and troughs completely modeled with shell elements. It is assumed that this will be necessary to predict the local effects that come from the wheel loading on the deck. For example, the out of plane bending of part of the crossbeams and the effects of having an unsupported deck part within a trough can only be captured when two or three dimensional elements are used. To generate a uniform mesh, the target mesh size is set to the dimension of the top width of the troughs. The hole in the crossbeam for the passing of the trough is present, but the rounding in the corners of the troughs are neglected.

The area around the fatigue details of interest can be named *level 3*. Here, the mesh size is chosen small enough such that fatigue stresses can be calculated with enough precision. Recommendations from literature for this were already discussed in section 4.6, while a small study regarding the effects at detail 2a is given in appendix E. The rounding of the troughs is also modeled in this area to avoid stress peaks around corners and the gap in the support plate for the passage of the trough follows this form. At plate intersections, a single row of elements with a higher thickness is present to incorporate the larger local stiffness caused by the welds. A more detailed description of used dimensions and mesh sizes is given in the respective subsection further in this chapter.

The sizes of detail level 2 and 3 were determined in a short analysis comparing the effects of the various sizes of these areas on the calculated stresses at fatigue details. This analysis is fully presented in appendix D. The appendix shows that the influence of only partly modeling the structural members on the stresses at the fatigue details is relatively minor and in most cases a conservative approach. Only the stress at the trough splice (fatigue detail 3 from section 10.4.1) is slightly underestimated. This was accounted for in the fatigue damage constraint for this detail as given in section 10.4.1.

Based on the described analysis, modeling level 2 was chosen to be a quarter of the width of the deck and incorporate three trough spans in the length of the deck (see figure 11.3). Level 3 has a length of 1,2 times and a width of 2,0 times the top width of the trough (see figure 11.8 and figure 11.9). Initially, a value of 1,2 was chosen for the width of the area as well, but this would sometimes give problems with the elements for detail 2b. For variants with a relative large bottom width, these elements would then partly fall outside of detail level 3.

11.3. Modeling description and dimensions per component

This section describes the modeling per component of the deck structure. Distinguished are the main girders, crossbeams, troughs, and deck plate. The section finalizes with an explanation why the asphalt was not modeled, and what has been done to include its effects in the analysis.

11.3.1. Main girders

As shown in the previous section, the main girders are modeled for one additional segment at each side of the bridge segment of interest. All supports are modeled as hinged point supports (see figure 11.2). This underestimates the stiffness of at the end points, but the effect of this is assumed to be negligible for the local fatigue stresses.

The dimensions of the main girder are taken from the case study, as the design of it is outside of the scope of this thesis. This gives a rectangular hollow section with an inner height of 3500 mm and an inner width of 1200 mm. The thickness of the web is 16 mm, of the top flange 20 mm, and of the bottom flange 24 mm. For simplicity, the thickness of the top and bottom flanges is averaged to 22 mm. These dimensions are visualized in figure 11.4.

The main girders have been completely modeled with beam elements. As can be seen from the position of the supports in figures 11.2 and 11.4, the elements have been given an offset towards the upper corner on the side of the deck. This way, the crossbeams can be modeled using their actual length and do not need to be extended towards the center of the main girder.
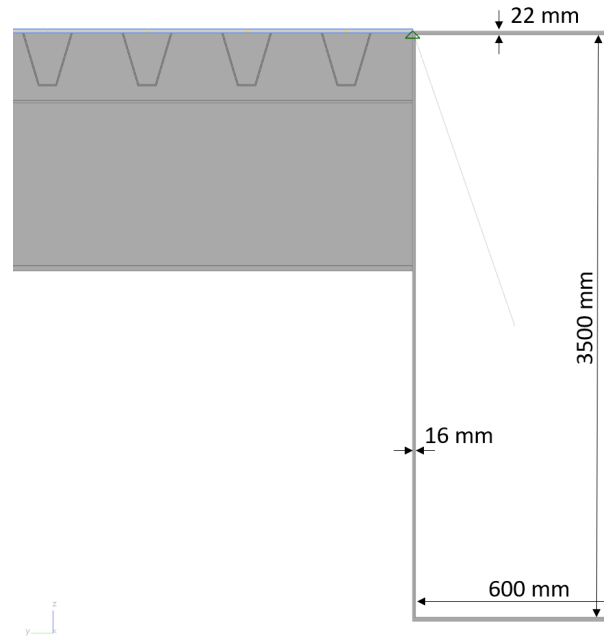
Figure 11.4: Cross-section of a main girder with dimensions as used in the FE model.

11.3.2. Crossbeams and support plate

The crossbeams of the Van Brienenoord bridge have a 1000 mm high and 12 mm thick web connecting a relatively small 200 x 14 mm top flange to the heavier 400 x 30 mm bottom flange. On top of the crossbeam, a 425 mm high support plate ensures the attachment to the deck plate and troughs. In the new design of the bridge, no gaps are present between the support plate. Naturally, these are not modeled. The dimensions are shown in figure 11.5.

As section 11.2 and figure 11.3 introduced, the FE model has different detail levels. Crossbeams that fully lie within level 1 of these are modeled by beam elements over their entire length. Two crossbeams fall partly within level 2 and are modeled by shell elements in that region, and beam elements around. The connection between the shell and beam part is provided by a pinned rigid constraint. This couples the degrees of freedom of the nodes at the end of the crossbeam to the end node of the beam element according to:

$$u_{node} = T u_{beamend} \tag{11.1}$$

$$
\begin{bmatrix} u_{x,n} \\ u_{y,n} \\ u_{z,n} \\ \varphi_{xx,n} \\ \varphi_{yy,n} \\ \varphi_{zz,n} \end{bmatrix} = \begin{bmatrix} 1 & & & & z & -y \\ & 1 & & -z & & x \\ & & 1 & y & -x & \\ & & & & & \\ & & & & & \\ & & & & & \end{bmatrix} \begin{bmatrix} u_{x,b} \\ u_{y,b} \\ u_{z,b} \\ \varphi_{xx,b} \\ \varphi_{yy,b} \\ \varphi_{zz,b} \end{bmatrix} \tag{11.2}
$$

With this formulation, the influence of local rotation of plate elements is not transferred to the beam elements. The effect of this on the global behavior is assumed to be small. Therefore, when the transition of plate to beam elements is far enough from the fatigue details, the influence on the measured stresses is assumed to be negligible.

Like the beam elements from the main girder, the crossbeam beam elements are given an offset from their centroid. The complete section, including support plate, is represented by elements that are placed at the centerplane of the deck plate.
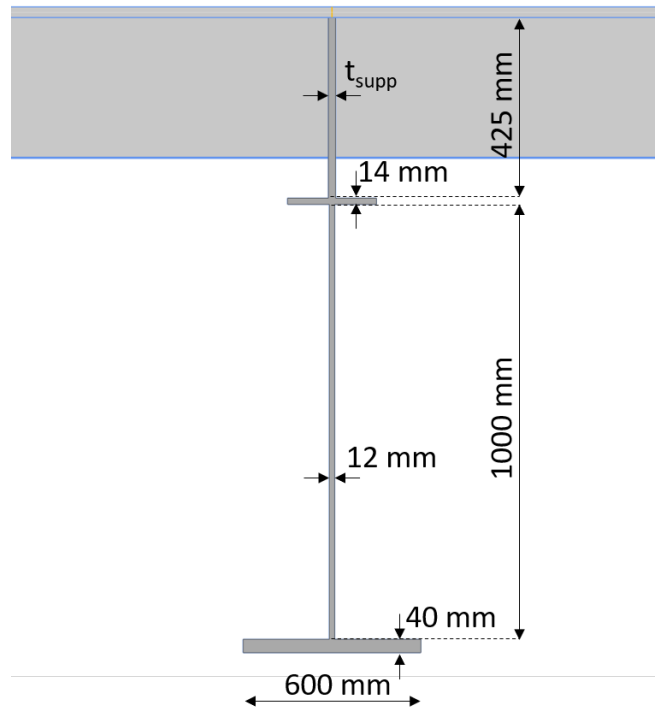
Figure 11.5: Cross-section of the crossbeams and support plate including dimensions.

11.3.3. Troughs

All dimensions of the troughs are selected as design variables (see section 10.3.4). Figure 11.6 shows these as used in the model.
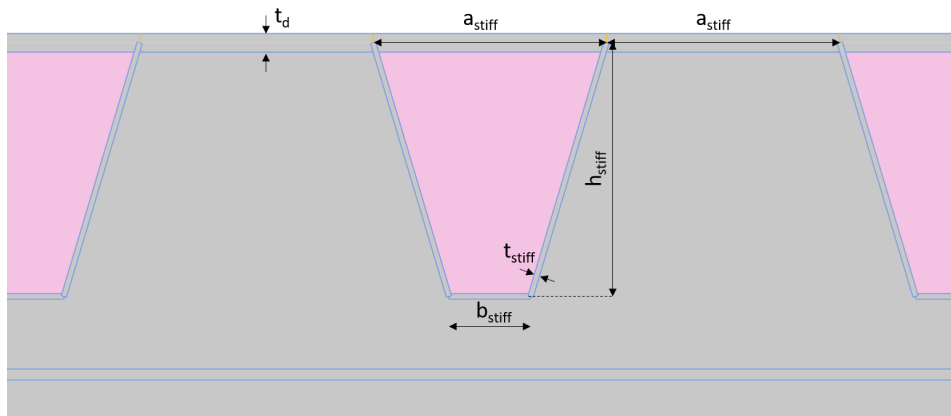
Figure 11.6: Cross-section of a trough including the definition for the design variables of table 10.1. The pink area indicates a hole in the crossbeam.

Some troughs in the model cross multiple design levels and are thus modeled partly by beam elements and partly by plate elements. The rigid constraint of equation 11.1 is again used to connect the two parts.

Where plate elements are used for the troughs, the gap for their passage in the crossbeam is modeled as well. This is indicated by the pink area in figure 11.6. The rounding of the troughs is neglected for design level 2. Only at level 3 the rounding is modeled, as it requires a very fine mesh. Applying this in a large area would greatly increase the computational demand of the model.

11.3.4. Level 3 model area and stress extraction

Three of the four fatigue details of interest (detail 1, 2a, and 2b) are at the crossbeam-trough intersection. To accurately capture the stress state in this region, a very fine mesh needs to be used. This has been applied on a small part of the deck plate, trough, and support plate around the intersection (figure 11.7).
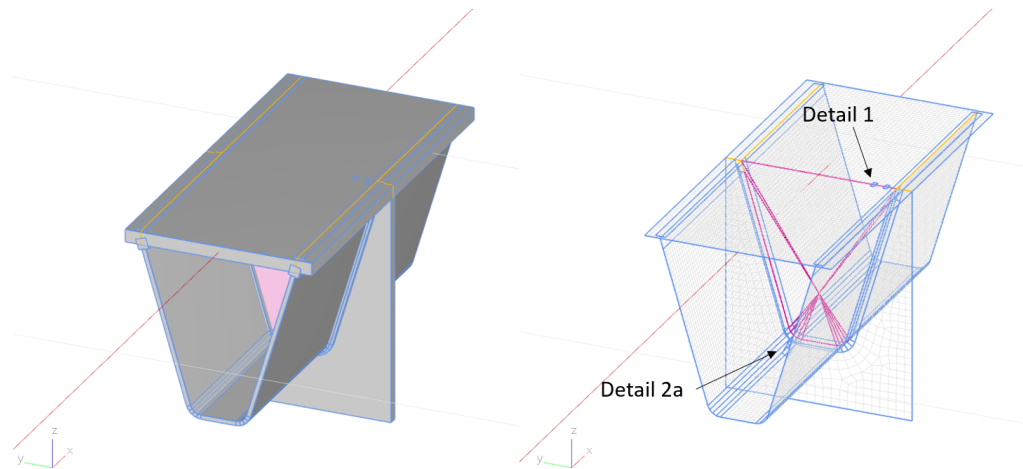
Figure 11.7: A 3D-view of the detailed area around a trough to crossbeam connection. A very fine mesh of approximately the thickness of the trough has been used and the rounding at the bottom of the trough is modeled.

The rounding of the trough has been modeled by dividing the curved part into four straight lines. The used radius of 25 mm is the same as found in the second Van Brienenoord bridge and is constant during the optimization (see figure 11.8).
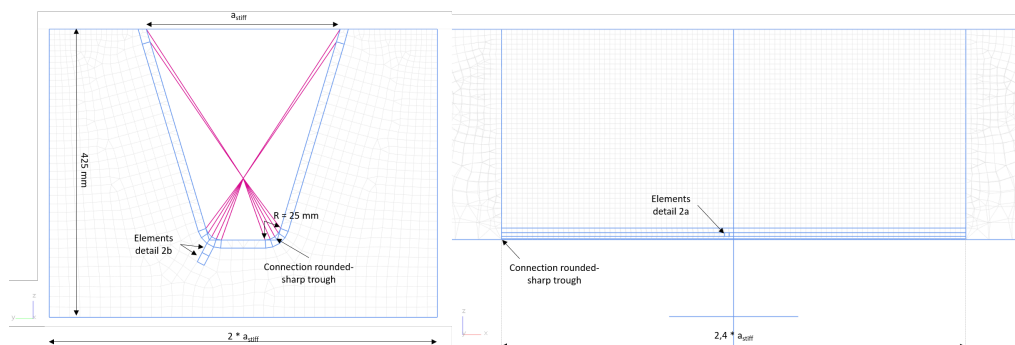
Figure 11.8: Cross-section along the y-axis (left) and x-axis (right) of the detailed area including dimensions. The full height of the support plate is included in the detailed area. The division of the trough into four straight parts and the connection to the non-rounded trough is visible in the left figure. The elements from which the stresses for details 2a and 2b are taken are indicated.

The corners of the rounded and non-rounded troughs do not connect to each other (see dotted lines in figure 11.8). This is solved by connecting the nodes in the rounded area to the corner node of the non-rounded trough by a relation like that presented in equation 11.1. This will give a strong stress concentration in the non-rounded trough and could result in a locally lower stiffness. However, as the respective area is small, it is assumed that the resulting inaccuracy is negligible. Checks of the found stress pattern further showed that the disturbed region is very limited.

The hot spot stress approach (see section 2.3.2) is used to determine the acting fatigue stresses in this area. The reference points for the stresses are located at 0,5 and 1,5 times the thickness of the structural member, following the recommendations discussed in section 4.6. In these, it is advised to use at least two elements in between the plate intersections and point of extraction, or to use quadratic elements. Both are undesirable considering computational demand. Appendix E shows that the gain in precision is small when literature would be followed.

Therefore, the elements used for the stress extraction are first located at the desired location and the finite element program then meshes the area around these. The elements are located such that their midpoints coincide with the desired reference points. The target mesh size for the complete detail level 3 area is equal to the size of the parts used in the rounding of the troughs. This measure was chosen universally to generate a uniform mesh, as triangular elements are undesired around the reference points for the hot spot stress [88]. Furthermore, the chosen design constraints and dimensions for the trough rounding cause the length of the elements therein to range between 6-10 mm. The allowed values for the thickness of the troughs, which require the smallest mesh size according to the mentioned recommendations, are of the same order.

The described approach mostly results in one element between the element modeling the weld (see section 11.3.5) and the element including the first reference point. Between the elements containing the reference points, again one element is usually present. In some cases, however, this would give very narrow elements for which the stiffness is not properly estimated. When this threatens to occur, the size of the elements used for the stress extraction are enlarged and no elements are present between them and the weld element. This can, for example, be seen in figure 11.9, where the elements for detail 1 are not connected, but those for detail 2a are. The thickness of the respective structural member is used for the mesh size when connected elements are used.

As two centered elements would not match with the present junction with the crossbeam, the members for detail 1 are doubled to keep a regular mesh. The stresses from the midpoint of both elements are averaged to find the stress at the desired position. The maximum stress found this way is slightly smaller than the true maximum at the correct position, but relative differences were found to be less than one percent for the studies that were done in appendix C.

Section 15.2 revealed that the location of largest stress reversal is uncertain for detail 2a. For the preliminary design of the Van Brienenoord bridge, this was at the side of the loaded trough leg, but the results of the first optimization run proved different. The stresses for detail 2a are therefore measured in both roundings of the trough, as can be seen in figure 11.9.
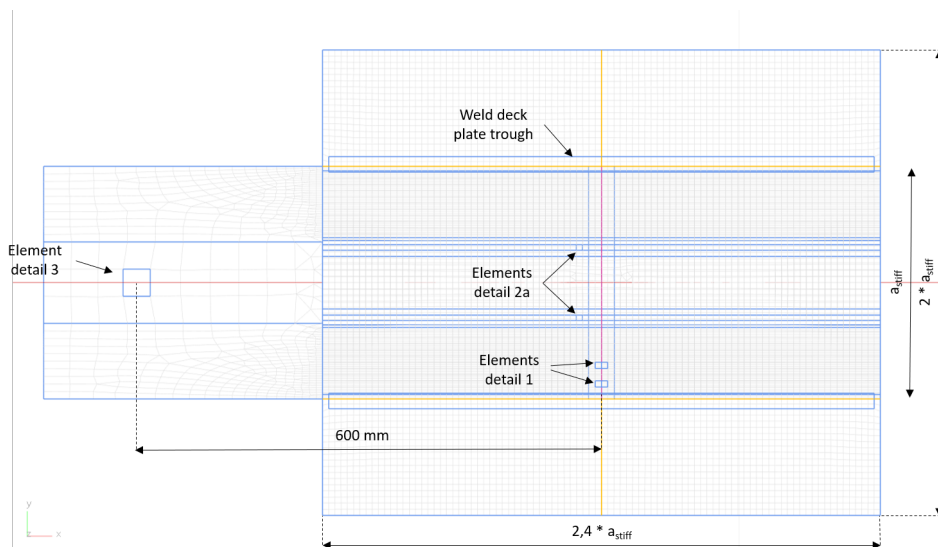
Figure 11.9: Top view of the detailed area and trough splice location including dimensions. The location of visible elements used for the stresses at fatigue details are indicated. The deck plate-trough weld is shown as well.

11.3.5. Weld modeling

Also visible in figure 11.9 are rows of elements around joints to model the additional local stiffness of the welds. For the analyses made in appendices A up to D, these were not included, as their influence on the stresses was thought to be small and recommendations in literature leave the option open to exclude the welds from the analysis (see section 4.6). When this latter method is adopted, however, the elements used for the hot spot stress extrapolation lie closer to the plate intersection. Appendix E showed that this leads to very high stresses and thus also to considerable damages.

Test runs of the optimization without the welds modeled resulted in no feasible designs. A viable design was found when all parameters were manually set to the most advantageous values (highest thicknesses, smallest spans, etc.), but this resulted in a deck with a mass of over 500 kg/m^2. Considering the preliminary design of the Van Brienenoord bridge [8] found a deck with a self-weight of 339 kg/m^2, this amount of material is unlikely to be actually necessary for feasible designs. The welds were therefore incorporated for all optimization runs.

These welds are modeled by the application of thicker elements at plate intersections, as suggested by Niemi [79]. The value of the additional thickness was based on the new ROK [88]. The determination of these is given in figure 11.10. The value of h_3 and h_4 is equal to the thickness of the trough. The throat thickness a of the weld is chosen to be equal to 6 mm. The welds at the support plate-deck plate intersections are neglected, as their influence on the stresses at fatigue details is considered to be small. At the intersection between the deck plate, trough and support plate, the larger thickness calculated from the trough-deck plate intersection is used.

Support plate - Trough   Trough - Deck plate
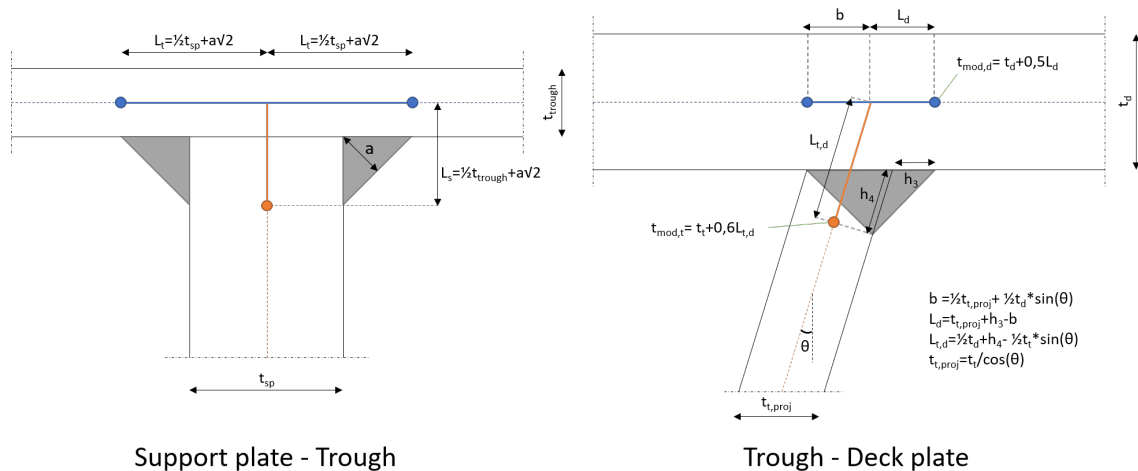
Figure 11.10: Schematic representation of the method used for modeling the welds at the support plate-trough and trough-deck plate intersections. The thick blue and orange lines portray the elements in the FEM model with an increased thickness, while regular elements are placed at the corresponding dotted lines. The formulas for calculating the modified element thickness are present as well, taken from the ROK [88].

11.3.6. Trough splice
The trough splice is the only considered fatigue detail for which the nominal stress is sufficient for the damage calculation. As such, only one element is necessary for it in the finite element model. Figure 11.9 visualizes its position relative to the level 3 model area.

The center of the element is placed at 600 mm from the crossbeam. The optimal position of the trough splice is investigated in appendix B, where it is found that a placement as close as possible to the crossbeam results in the smallest stress range. Due to constraints regarding manufacturability, this comes down to a governing weld at the indicated position. Figure 10.4 showed an overview of a trough splice with the governing weld.

11.3.7. Asphalt
Although the future recommendations regarding the modeling of orthotropic steel decks for fatigue damage calculation prescribe to include the asphalt layers in the analysis (see section 4.3), these are not modeled in this thesis. The reason for this is twofold.

Firstly, because the addition of 3D elements to the model would greatly increase its computational demand. The low thickness of an asphalt layer (70 mm) would require a small element size, while the width and length of layer would need to be large enough to properly account for the load spread. An asphalt model as used in section A.1 would double the amount of elements when added to the orthotropic deck model as presented in this chapter.

Secondly, because the implementation of 3D elements in GSA (the used finite element program) is still in development. The element type can be used, but meshing needs to be done mostly manually or should be fully scripted. The former poses a problem in the intended workflow, while the latter would be too time-consuming to do during this thesis' research.

It was therefore decided to fall back on the current recommendations found in the Eurocode, which prescribe to disperse the load under an angle of 45° through the asphalt layers and further exclude it from the analysis. However, section 4.3 already spoke of the doubt regarding this 45° spread. Appendix A therefore investigated the spread that occurs in an asphalt layer similar to that found on the new Van Brienenoord for two cases: when rigidly supported and when placed on an orthotropic bridge model. In both cases, it was found that a spread of 45° is mostly not achieved at higher asphalt temperatures.

The remainder of this thesis will therefore work with with an angle of dispersal trough the asphalt of 35°, which was the lower bound found in the analysis of appendix A. This is considered a conservative assumption, as literature suggests that including the asphalt layers in the analysis has a positive influence on the determined fatigue life [112, 113].

As using 3D elements is currently not a viable option in the intended workflow and methods to properly integrate the effect of temperature in the load dispersal of the asphalt are lacking, it is furthermore decided to disregard the effects of asphalt temperature in this research for now. The assumption of a single angle of stress dispersal is considered conservative, and may decrease the optimality of the structure. This could be improved in future studies once proper simplifications for the asphalt layer are found or the use of 3D elements becomes feasible. On the other hand, indications are present that a (very) large part of the total fatigue damage in an orthotropic deck occurs at higher temperatures, at which the influence of the asphalt is lower [30, 68, 112]. This could reduce the differences with more accurate analyses that do integrate the effect of asphalt temperature.

11.4. Loading

Besides the size of the needed finite element model, a significant part of the computational demand of the analysis comes from the large amount of load cases. A full check of an orthotropic steel deck would require wheel loads to be centered in at least three locations: in the middle of a trough, above a trough leg and in between two troughs [88]. A quick analysis already revealed that for the latter the stresses at the considered fatigue details are significantly lower than for the other two. This load position is therefore not expected to be governing and not included in further studies.

In addition to the center positions, section 4.4 already showed that three wheel types have to be considered and five lateral weaves must be applied per central position. These wheel loads should then all travel along the deck with enough steps to accurately capture the stress peak they cause. All combined, a full fatigue check could therefore need well over a thousand load cases.

Considering all load cases during the optimization is thus not considered feasible, as analysis times would become far too large. The load will therefore only be applied on the position for which the largest stress is expected. This will then be used to scale a predetermined influence line that can then be used in the damage calculation.

A short analysis was made on the model as presented in this chapter to determine the load position resulting in the largest stress at each fatigue detail. Appendix C presents the complete methods and results of this study. Here, only the expected worst positions are presented in table 11.1, as this is the loading scheme that will be used in the optimization.

The table shows that for some load cases, multiple wheel types are present in the same row. For these cases, a single wheel type may be used to estimate the stress for all types. One of the things that came from the analysis in appendix C was that in all cases, wheel type C may be conservatively approximated by wheel type A. The influence lines at all fatigue details show close similarities between the two wheel types, where the smaller A type always results in slightly higher peak values. Secondly, the stress at detail 1 appeared to be completely independent on the used wheel type. When the load completely covers the free spanning deck plate above the gap in the support plate, only the applied pressure is of interest. Loads applied next to the trough legs, outside of the gap in the support plate, have no influence on the stress at detail 1.

Fatigue detail	Center position	Wheel type	Position relative to trough span
Detail 1	Middle of trough	A/B/C	0,0
Detail 2a	Above trough leg	A/C	0,16
	Above trough leg	B	0,23
Detail 2b	Above trough leg	A/C	0,13
	Above trough leg	B	0,19
Detail 3	Middle of trough	A/C	Above trough splice
	Middle of trough	B	Above trough splice

Table 11.1: Second proposal for load positions to use, ordered per corresponding fatigue detail and wheel type. These positions can be used when scaling of a known influence line is to be used. Multiple wheel types in the same row would be possible to predict using a single load. This table is a copy of table C.2.

The lateral weaves prescribed by the Eurocode load model (figure 4.4) are not used during the optimization. Incorporating these in the finite element analysis would require five times as many load cases, increasing the calculation time tremendously. This simplification is conservative and will result in heavier decks. Future research could improve the method and thus the derived designs. The great number of trucks and high sensitivity of fatigue damage, however, will likely mean that the effect is small. Tables 14.6 and 15.2 illustrate this well: only a slight exceedance of the cut-off limit will already result in damages that are just within the set constraints. When the lateral weaves would be considered, the allowed increase in stress would thus be minimal.

In appendices A up to E, a single wheel load was used in each load case. This was mainly done for convenience, as the influence of loads placed at a distance from the fatigue details was thought to be small. A quick check, however, revealed that the maximum stress at fatigue detail 1 does increase when both wheels of the axis are considered. This effect is mainly caused by an increased normal force in the deck plate due to the additional wheel load. The remainder of this thesis will therefore consider the complete axis as presented in section 4.4 and accompanying figure 4.3. The length of the wheel imprint will be set to 220 mm, as advised by the new ROK [88]. The highest stresses were obtained when the second wheel load was placed at the opposite side of detail 1, and at the adjacent side of details 2a and 2b. The location of the second wheel load is irrelevant for detail 3 due to its symmetric placement.

11.5. General model information

The parametric FE model only uses linear shape functions, which comes down to two-noded beam elements, and three- or four-noded shell elements. The latter consist of as much quadrilateral elements as possible and use the GSA-default MITC formulation, giving three translational and rotational degrees of freedom per node. Shear deformation was ignored for the beam elements representing the troughs and crossbeams. The shear deformation is included for the main girders, although it is expected that its effect is negligible. Details of the element formulations can be found in the theory description of GSA [9].

The simplification of the asphalt layer means that the all modeled members are made of steel. A value of 200 GPa was used for the Young's modulus, while the Poisson's ratio was set to 0,3. Only linear elastic calculations are performed

11.6. Summary

This section explained the modeling choices that were made for the parametric model. This section will give an overview of these.

- The model of the deck covers a single bridge section, with the main girders extending one section on each side. The main girders are supported in vertical direction where hangers would be present.

- Three modeling levels were adopted to find a balance between accuracy and computational demand. Level 1 used beam elements for the troughs and crossbeams and shell elements for the deck plate. Level 2 is fully modeled in shell elements. Level 3 adds welds and the trough rounding to level 2 and uses a finer mesh. Table 11.2 gives an overview of this.

- The effect of the welds is modeled by using locally thicker elements.

- Fatigue stresses are extracted from predetermined locations based on hot spot stress extrapolation. These locations were found to be governing in many situations, but need to be verified for the result of an optimization (which is done in chapter 15).

- The trough splice is positioned at 600 mm from the crossbeam. This choice is based on the analysis in appendix B and manufacturability constraints.

- The asphalt is incorporated in the analysis only by the use of a 35° load dispersion through its thickness. Implementation of 3D elements to model the asphalt layers and include its temperature dependent stiffness was found to be unfeasible. Appendix A explains why in more detail.

- The number of load cases during the optimization is limited to seven. In these seven load cases, the load is placed at positions where the maximum occurring stress is expected. This value is then used to scale a predetermined influence line that can be used in the damage calculation.

- All elements in the finite element model use linear interpolation functions. Only linear elastic analyses are made.

Level	Component	Element type	Element size
1	Deck plate	2D-Shell	$2 * a_{stiff}$
	Crossbeam	1D-Beam	$2 * a_{stiff}$
	Trough	1D-Beam	$2 * a_{stiff}$
	Main girders	1D-Beam	$2 * a_{stiff}$
2	Deck plate	2D-Shell	a_{stiff}
	Crossbeam	2D-Shell	a_{stiff}
	Trough	2D-Shell	a_{stiff}
3	Deck plate	2D-Shell	$d_{el,rounding}$ t_d
	Support plate	2D-Shell	$d_{el,rounding}$ t_{sp}
	Trough	2D-Shell	$d_{el,rounding}$

$$d_{el,rounding} = \frac{R}{4} * \arctan\left(\frac{h_{stiff}}{a_{stiff} - b_{stiff}}\right) \qquad (11.3)$$

Table 11.2: Overview of the element types and sizes used in the different modeling levels. The meaning of the symbols can be found in table 10.1. $d_{el,rounding}$ is the dimension of an element in the rounding of the troughs, calculated by equation 11.3. When multiple element sizes are given, the used one depends on the situation. With certain parameters, using the length of the elements in the trough rounding prohibits the proper placement of the elements for stress extraction. When the elements of extraction are placed adjacent to each other, the second value is used.

12

Comparison between parametric model and Van Brienenoord design model

In chapter 9, the case study of the Van Brienenoord bridge was introduced. Chapter 11 described the parametric model that is used in the optimizations presented further in this chapter. Some modeling choices made there deviate from that made in the preliminary design of the Van Brienenoord bridge as made by Arup [8] and thus some variations in results may be expected. This chapter evaluates how large these differences are.

Besides this evaluation, a short note will be made on some of the limitations that were present on the design freedom of the Van Brienenoord case. These should be taken into account when a comparison is made between the results coming from the optimization and the traditional design process.

The first section will explain the deviating choices in modeling. Then, the restraints on the design freedom for the preliminary design will be discussed. Next, the calculated damages from both models are compared. The chapter ends with a conclusion about the expected accuracy and level of conservatism of the parametric model.

12.1. Differences in modeling
Although the initial application of the parametric model is the same as for the finite element model used in the preliminary design of the Van Brienenoord bridge, differences between the two were still present. This was mainly caused by the tactics applied to reduce the computational demand of the parametric model. Updated recommendations and non-reported values in the preliminary design also gave variations in the two analyses.

The first difference in between the two models lies in the modeling levels. Both the parametric model of this thesis and the preliminary design use three detail levels, but their range and interpretation is different:

- Modeling level 1 in the preliminary design is present at adjacent bridge segments and uses beam elements for the crossbeams and main girders. The troughs are neglected here.

- Level 2 covers almost the entire bridge segment where the fatigue details are located. All structural elements are represented by shell elements. The gaps for the passage of the troughs are modeled.

- Detail level 3 has a length of approximately one trough span and is placed such that the crossbeam-trough intersection is around a third in longitudinal direction. In this area, all welds are represented by thicker elements, including those in the deck-support plate and support plate-top flange connections that were left out in the parametric model.

A second divergence can be found in the integration of the asphalt layers in the model. In the parametric model, the asphalt layers are only accounted for by a 35° dispersion of the load over their thickness. Section 11.3.7 explained why this was done. The preliminary design of the Van Brienenoord modeled a 30 mm thick mastic asphalt and a 35 mm thick ZOAB layer with solid elements. The influence of the temperature was incorporated by changing the stiffness of these elements as was described in section 4.3. The dimensions also mean that the total thickness of the wearing courses is less than half of the thickness used for the asphalt layers in this thesis.

A third difference is present in the loading. In this thesis, the simultaneous presence of multiple trucks on the bridge is ignored. The preliminary design does consider this and studies the effects of different methods of combining stress profiles of individual trucks. The differences in resulting damage appear to be very small, suggesting that the assumption made in this thesis is justified.

A fourth discrepancy concerns the use of the detail categories. The preliminary design of the Van Brienenoord bridge used different values than were presented earlier in this thesis (see table 12.1). As illustrated in the literature review of this thesis, the fatigue life of orthotropic decks is still a very active subject of research. The categories used in both the design as in this thesis are based on research that is ongoing and changes in insights may have occurred in the meantime. The results of the parametric model will also be checked with the 'old' detail categories to enable a fair comparison.

	Detail 1	Detail 2a	Detail 2b	Detail 3
Old detail category	167 (no cut-off)	125	80	100
New detail category	200 (table 10.3)	140	100	100

Table 12.1: The old and new detail categories used for the comparison. For detail 1 the cut-off limit was removed for the preliminary design. In the new situation, a modified SN-curve is used, which can be found in table 10.3.

A fifth and last change regards the material factor γ_{Mf}. This thesis will use a value of 1,15 for this, opposed to the 1,25 used in the design. Again, both values will be considered for a fair comparison.

Finally, some assumed values are not explicitly mentioned in the preliminary design report that was available for this thesis. This applies mostly to the dimensions of the welds. The values used for what is indicated as R in figure 11.8 and a, h_3, and h_4 in figure 11.10 are not given in the report. The length of the elements used for the modeling of the welds (L_d, L_s, L_d, and $L_{t,d}$) is not given either.

12.2. Limitations on design freedom of the preliminary design
The design made by Arup for the Van Brienenoord bridge contains a considerable effort to find the best solution for the given case. However, this was subjected to some constraints that the study in this thesis is not. These should be mentioned to draw fair conclusions about the potential of structural optimization for similar cases.

The first constraint came from the reuse of the existing superstructure. This prohibits modification of the center-to-center distance of the crossbeams, which has a significant influence on the performance of the deck. The stresses at most fatigue details are dependent on this parameter and could only be decreased by enlarging the deck plate thickness or trough dimensions.

The second restriction was placed on the trough top width and spacing. As discussed in section 10.3.4, these are both almost exclusively chosen to be 300 mm. Initiative was present to investigate the possibility of using narrower troughs combined with a thinner deck plate, but this was skipped due to restricted available time. The large influence of the deck plate on the total mass of the structure makes that this could prevent better solutions to be found.

12.3. Comparison of found damages
The results of the found damages from the different models is presented in table 12.2. The loading of the parametric model consisted of 101 load cases. Their spacing was obtained by squaring an equally spaced array of numbers from -1 to 1 (apart from the sign) and multiplying this with the crossbeam spacing. The weaves as found in figure 4.4 were used as well.

Case	γ_{Mf}	Damage			
		Detail 1	Detail 2a	Detail 2b	Detail 3
Preliminary design	1.25	0.82	0.89	0.31	2.04
Parametric model, old DC	1.25	0.21	0.61	3.34	0.00
Parametric model, new DC	1.15	0.00	0.00	0.15	0.00

Table 12.2: Comparison between damages found in the preliminary design of the Van Brienenoord bridge and the parametric model. Equal parameters are used where possible. Differences in modeling were discussed in section 12.1. DC = Detail Categories. The differences between the old and new DC were shown in table 12.1.

The table shows that the parametric model gives a conservative estimation for the damage of detail 2b compared to the preliminary design, but the damages found at the other details are somewhat lower. The disregard of the asphalt layers could be a reason for the former. At lower temperatures, the asphalt layers of the preliminary design spread the load better, giving lower total damages.

On the other hand, the thinner asphalt layers in the preliminary design may also be responsible for the higher damages found in detail 1 and 2a. Appendix A showed that the load above the gap in the crossbeam is very sensitive to the asphalt stiffness, which is very relevant to detail 1. The low damages in both cases indicate that the stresses only slightly exceed the cut-off limit. A marginally more concentrated load at higher asphalt temperatures might thus be enough to cause a significant increases in the damage.

A second reason may be the fact that the passage of overtaking trucks is not considered in the parametric model. A quick check of influence of loads placed at two meters from the detail area in lateral direction revealed that the stresses at details 1 and 3 could somewhat increase because of these. The effect on details 2a and 2b was opposite to the experienced stresses and would thus likely not lead to higher damages.

Other explanations for the deviating values may be found in the modeling simplifications made in the parametric model or the method used in the preliminary design. For the former, appendix D showed that the stress at detail 3 is somewhat underestimated. The last option regards a possible inaccurate estimation in the preliminary design. That is, the reported value was approximated by using a 'stress factor' that was based on a single load case, not a full analysis.

At first glance, the differences found in table 12.2 may seem quite large. It should be realized, however, that small changes in stress values will have large consequences for the calculated damage. The presence of the cut-off limit plays a considerable role herein. When the extrapolated stress falls just below it, the damage will be zero. A slight exceedance immediately gives a significant damage due to the 200 million trucks passing the bridge in its lifetime. As the cut-off in the old situation is equal to 100 million cycles, exceeding the corresponding stress value will very quickly lead to damages above 1.

This effect is somewhat softened by the use of weaves and different temperatures of the asphalt layer. These decrease the number of trucks for a given case significantly, meaning that an exceedance of the cut-off limit in one does not directly lead to unacceptable damages.

The parametric model, however, does not use the temperature distribution (see section 11.3.7 and appendix A), but makes an assumption for the load spread that likely corresponds most to that found at higher asphalt temperatures. This can skew the resulting damages, something that could be happening at detail 2b.

Using the new detail categories and lower material factor decreases the computed damages strongly, setting the damage at detail 1 and 2a to zero and reducing the damage at detail 2b with a factor of more than twenty. The new categories are all higher than those used in the design of the Van Brienenoord bridge and combined with the lower material factor this gives a significantly higher cut-off limit. The maximum stresses at detail 1 and 2a consequently fall below the new limit, giving a far lower damage.

12.4. Conclusions

The reported damages of table 12.2 show that the parametric model of chapter 11 gives a reasonable approximation for the expected fatigue life of most details. The numeric values in the table may appear as if the differences between the models are significant, but this can for a large part be attributed to the large number of expected vehicles relative to the cut-off limit. A small change in the stress may then have considerable consequences for the calculated damage.

When these numbers are to be expected, it may even be questioned whether its use is appropriate, considering that the choice for a cut-off limit is somewhat arbitrary ([52, 85], see section 2.2.1). The preliminary design of the Van Brienenoord bridge also shows that the removal of the cut-off limit can more than double the calculated damage. The new categories for detail 1 already reflect this realization. It could be interesting to investigate the effect of similar measures for the other details in future research.

The differences in the asphalt layers are most likely also a strong factor in the differences in results. The disregard of the temperature dependent stiffness could lead to the higher damages of detail 2b. On the other hand, the thinner asphalt layers in the preliminary design could also be the reason for the higher damages at detail 1. The stresses at this detail are particularly sensitive to changes in the asphalt layers, as was shown in appendix A.

A final possibility could be that the use of different values for certain dimensions gives divergent damages. The values for R in figure 11.8 and a, h_3, and h_4 in figure 11.10 were not known and could thus not be copied. A different value for the rounding radius would almost certainly be of influence of the damages at detail 2a, which is located there.

No damage was found for detail 3, which was not expected based on the preliminary design. Explanations may possibly be found in the thicker asphalt layer, modeling choices or the preliminary design itself. In all cases, the results for this detail should be verified with extra care after the optimization.

Although the lower damages of the parametric model are explainable, it can not be said with certainty that the parametric model gives conservative results. During the optimization, however, the lateral weaves will be neglected. It is expected that this gives enough overcapacity to let the model pass possibly stricter follow-up analyses as well.

13

Workflow

Chapter 10 formulated the optimization problem that is to be solved in this thesis and elaborated on the choice for the artificial bee colony algorithm to solve it. Chapter 11 then presented the finite element model that is used in the analysis to determine the stresses for a geometry. This chapter explains their role in the workflow of the optimization and discusses the steps that have not yet been treated.

The first section visualizes the workflow and gives a summary of the important steps. The next sections provide more information on the two steps that have not been treated in the previous chapters: the scaling of the reference influence lines and the calculation of fatigue damages.

13.1. Overview

The optimizations start with the artificial bee colony algorithm, which was treated in section 6.2.3 and visualized in figure 6.4. Only the calculation of the performance (*fitness*) of a design variant (*food source*) needs to be filled in for an application of the algorithm. This part is treated in this chapter. The remainder of the artificial bee colony algorithm's workflow was already treated in the dedicated subsection.

For each considered design, the algorithm generates a set of variables between zero and one. These represent a design variant, from which the mass is calculated. If this variant could be an improvement to the stored variant, the variables are passed on to a script that generates the parametric model. The script translates the variables to the dimensions of the design variables and creates the geometry and loading for the respective variant.

These are then used to create a finite element model in GSA (Arup's in-house FE program) through its API. GSA meshes the model and starts an analysis. The analysis results in the stress peaks that are expected for each fatigue detail. These peaks are used in a third Python script to scale a set of reference influence lines that were determined prior to the optimization.

The scaling of the references leads to an estimation for the full influence lines for the considered design variant. These are used as input for a fatigue tool, which calculates the expected damage at each fatigue detail. The calculated damages are, together with the earlier computed mass of the design, returned to the optimization algorithm to finally asses the performance of the design.

13.2. Scaling of influence lines

The stresses for the considered fatigue details are extracted from the FE model by the using the predetermined elements that were discussed in section 11.3.4. For each of these elements, the absolute maximum value of the stress component perpendicular to the weld is taken and compared to the absolute maximum of the reference, which was determined before the optimization. The ratio that is obtained this way is used to scale the complete reference influence line.
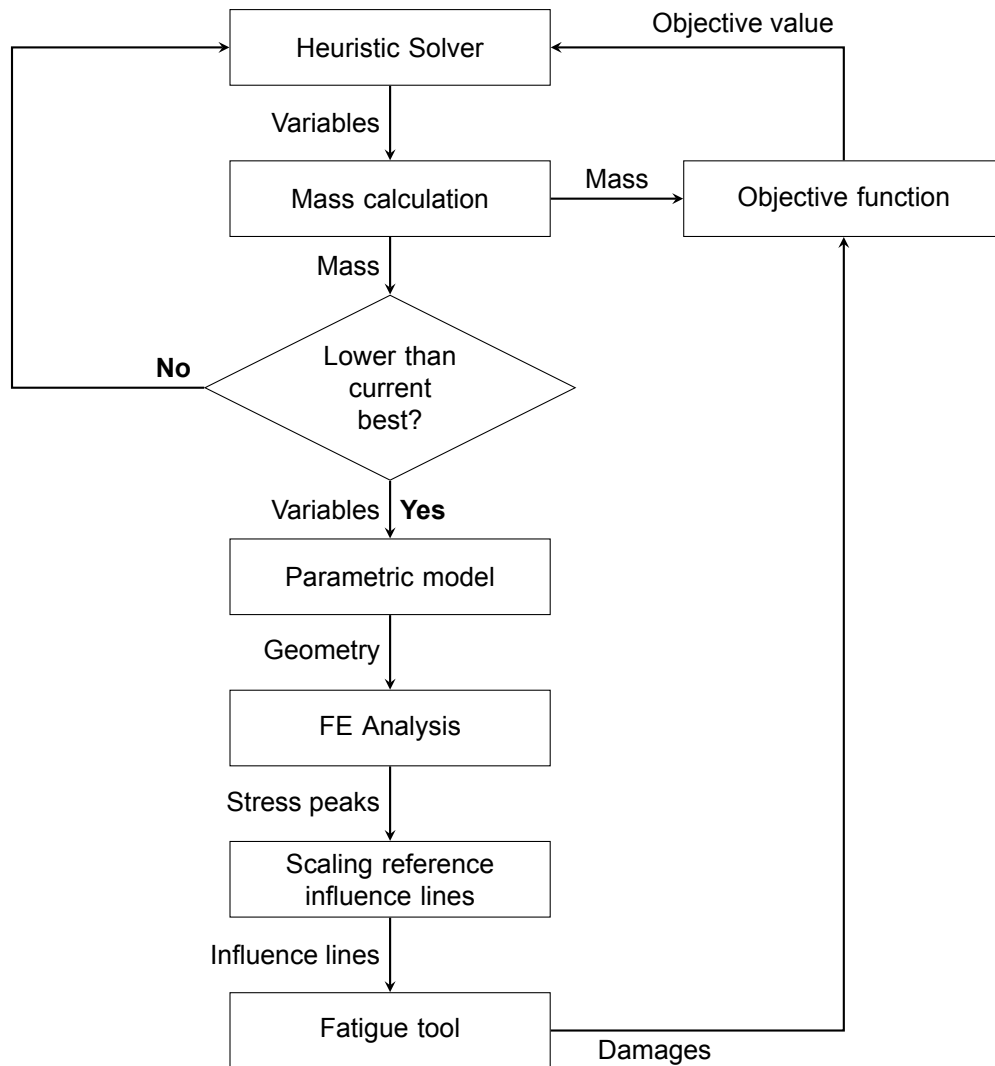
Figure 13.1: A visualization of the workflow that is used during the optimization to determine the performance of a generated design variant. The blocks describe certain processes, while the arrows indicate information that is shared between these.

This results in an estimated influence line for the stresses at each element, for each wheel type (see figure 4.3). Wheel type C is not used in the loading as presented in table 11.1. The scale factor for wheel type C is assumed to be equal to that of wheel type A, after the two wheel types gave very similar results in appendix C. Their references were determined independently, however, and thus their estimated influence lines will be different as well. Eventually, this process thus gives twelve influence lines: one for the three wheel types at each of the four fatigue details.

13.3. Fatigue calculation

The fatigue damage calculation is done with the fatigue tool that was developed at Arup. This combines the influence lines of the wheel types into an influence lines for each of the five trucks prescribed by EN 1991-2NB [5] in fatigue load model 4a. These can also be found in figure 4.2.

The tool then extracts the stress cycles from these combined influence lines using the rainflow method (see section 2.3.3). Combining these with the expected number of trucks and their distribution, the total amount of stress reversals can be determined. The Van Brienenoord bridge belongs to one of the heaviest loaded bridges in the Netherlands and therefore the maximum number of two million trucks is expected per year (table 4.1). Its position in a highway dictates that the distribution for 'long distance' ('lange afstand' in figure 4.2) should be used.

14

Parametric Optimization Results

This chapter will present the outcome of the optimizations that have been done based on the setup presented in chapters 10, 11, and 13. The first already mentioned that some choices in therein can be rather arbitrary. Multiple penalty functions and values for the *limit* parameter were therefore used and analyzed in appendix F. The results of this appendix were used for the selection of the parameters in this chapter.

Multiple runs are needed to truly asses the performance of the algorithm, as it partly relies on chance. A full statistical analysis is not possible during the limited time available for this thesis, but the differences between the runs can be used for a tentative conclusion about the reliability of the current setup.

Three analyses were made, differing slightly in setup. A mistake in the input of the damage calculation made that the first analysis essentially used the cut-off limit of the SN-curves as stress constraints. Nonetheless, this analysis still produced some fairly light and feasible designs and is therefore still presented here.

After the results from the first analysis were evaluated, it was seen that the quite some parameters reached their design constraints. These were therefore enlarged for the second. The third analysis used discrete instead of continuous variables, as this would be much more applicable in practical designs.

14.1. Analysis 1: Continuous parameters 1

The partial dependence on chance of the artificial bee colony algorithm requires multiple runs of the algorithm to give more credibility to the results. The first full analysis therefore used three consecutive runs with a large number of maximum evaluations (relative to the preliminary runs) to enlarge the likelihood of obtaining relevant results. Based on the preliminary runs in appendix F, the values of table 14.1 were used:

Penalty function	Population size	Limit	Evaluations	Parameter type
$\sum_{i=1}^{4} \delta_i$	30	30	1500	Continuous

Table 14.1: Optimization setup choices for the first complete run. δ_i is the damage at detail i.

As the introduction of this chapter mentioned, this first analysis used slightly different design constraint than were presented in chapter 10. These are presented in table 14.2 and include a smaller upper bound for the deck plate, a narrower range for the crossbeam spacing, and stricter constraints for the trough height and top width.

Table 14.3 shows the best performing design variants found in each run. The differences between the resulting parameters are remarkable. The center-to-center distance of the crossbeams, thickness of the support plate, and top width of the stiffeners show (approximately) repeating values for run 1 and 3, but all other found values are unique.

Parameter	Symbol	Lower bound	Upper bound	Unit
Deck plate:				
thickness	t_d	10	24	mm
Crossbeam:				
center-to-center	ctc_{cb}	2500	5500	mm
Support plate:				
thickness	t_{sp}	8	20	mm
Troughs:				
height	h_{stiff}	140	380	mm
width upper side	a_{stiff}	140	380	mm
width bottom side	b_{stiff}	0.3	1.0	a_{stiff}
thickness	t_{stiff}	4	10	mm

Table 14.2: Parameters used as design variables in the first full optimization analysis and their allowed ranges. The spacing between the troughs will be equal to the width on the upper side.

run	t_d	ctc_{cb}	t_{sp}	h_{stiff}	a_{stiff}	b_{stiff}	t_{stiff}	mass (kg/m^2)
VBB PD	24,0	3645	16	325	300	105	8,00	339
1	17,9	4010	15,1	272	140	79,8	6,29	313
2	14,5	2960	10,0	209	178	169	8,86	308
3	13,2	4070	15,1	183	140	106	9,30	289

Table 14.3: Optimized results from the first full analysis and the preliminary design of the Van Brienenoord bridge. All values except mass are in mm. All values are rounded to have 3 significant digits in this table.

Still, some trends can be found in the results when compared to the preliminary design of the Van Brienenoord bridge. The largest change occurs in the top width of the troughs a_{stiff}, which decreases strongly in all cases. For run 1 and 3, the value even reaches the lower bound. This is combined with a thinner deck plate and a smaller height in all cases. The ratio between the top width and bottom width of the stiffeners increases as well, leading to more rectangular cross-sections of the troughs.

The diversity in results continues in the minimized mass. The first run gives a reduction of 7,67 percent compared to the Van Brienenoord design, while the third more than doubles this saving with 14,7 percent.

Due to the use of randomness in the artificial bee colony algorithm, some variety in results is unavoidable. The spread of table 14.3, however, is considerable and an effort should be made to decrease it. It could be that the design space has a great number of local minima and the presented run 1 and 2 find one that is less optimal. When only considering the artificial bee colony algorithm, possible ways to reduce this may be increasing the population size or maximum number of evaluations.

A second cause may be found in the incomplete convergence of the algorithm. This could mainly be an explanation for the difference between the result from run 1 and 3, as these also show some strong similarities. The further increase of the limit could prevent design variants from being abandoned too soon. Another option could be to use a gradient based solver after a run of the artificial bee colony algorithm, which would guarantee to find at least a local minimum. This will not be investigated in this thesis further due to time restrictions.

The damage at all fatigue details of the resulting variants was equal to zero, which is not surprising considering the mistake causing heavy penalties even for designs with only a little fatigue damage. The result of run 3 was analyzed more thoroughly in chapter 15 to check whether the assumptions that were made during the optimization are correct. This did not lead to an exceedance of constraints and thus the design is considered to be feasible.

14.2. Analysis 2: Continuous parameters 2
The second analysis again uses three runs to increase the certainty of the results. The penalty function of the first analysis had to be modified. The error in the fatigue calculation made sure that any occurring damages would already penalize the objective function severely, but these are all 100 times smaller

in the new situation. The old penalty function, however, did perform well. It was therefore chosen to multiply the damages with 100, resulting in a very similar penalty function as in analysis 1. The difference is that the function now only penalizes when damages exceed one instead of when stresses exceed the cut-off limit.

The maximum number of evaluations was increased to 2500. It is hoped that this will reduce the differences between the results of various runs, as was the case in analysis 1. Table 14.4 gives an overview of the complete setup.

Penalty function	Population size	Limit	Evaluations	Parameter type
$100 * \sum_{i=1}^{4} \delta_i$	30	30	2500	Continuous

Table 14.4: Optimization setup choices for the second complete analysis. δ_i is the damage at detail i. A factor 100 was added to the penalty function to get approximately the same behavior as in analysis 1 after correcting the mistake. The number of evaluations was increased.

Besides the slight changes in the setup of the algorithm, some changes were made to the design constraints as well. The first analysis showed that some parameters often reached these, thus indicating that improved options could be found with looser boundaries. The new limits were already included in table 10.1. The previous section showed the old limits in table 14.2.

14.2.1. Best resulting variants

The outcome of the analysis is presented in table 14.5. Compared to the results of analysis 1, the deviations in the optimized parameters have reduced significantly. The minimized mass only differs by 6 kg and the parameters found in run 1 and 3 are very similar. Although the number of runs is still too little to draw definitive conclusions, these observations do suggest that at least some convergence has occurred during the optimization.

run	t_d	ctc_{cb}	t_{sp}	h_{stiff}	a_{stiff}	b_{stiff}	t_{stiff}	mass (kg/m^2)
VBB PD	24,0	3645	16,0	325	300	105	8,00	339
1	10,0	3140	10,5	264	101	62,0	5,83	288
2	14,3	2890	10,2	229	166	166	6,36	287
3	10,0	3260	14,3	259	111	68,7	6,13	282

Table 14.5: Optimized results from the second full analysis and the preliminary design of the Van Brienenoord bridge. All values except mass are in mm. All values are rounded to have 3 significant digits in this table.

Similar to the first analysis, the runs all give a result with a much smaller top width of the stiffeners, enabling a very thin deck plate. The stiffeners again have a reduced height and relatively wider bottom. The thickness of the troughs now also shows more cohesion: all runs give an optimized value of around 6 mm. The preferred center-to-center distance of the crossbeams appears to be quite close to that used in the Van Brienenoord bridge, as all runs give a result near 3500 mm.

The largest difference between the results of the first and third run can be found in the thickness of the support plate. The latter uses a higher value for this, but the final mass is still lower. It can be that the thicker support plate facilitates the slightly larger center-to-center distance of the crossbeams and top width of the troughs, leading to a lower self-weight. Overall, however, the two designs are very similar.

The variant resulting from the second run can be viewed as truly different. A more than 4 mm thicker deck plate is used combined with wider, but slightly shallower troughs. The bottom width of the trough is equal to the top width, leading to an almost square-shaped cross-section.

Contrary to the results of analysis 1, the designs found in analysis 2 can have acceptable damages. Table 14.6 shows the values that were calculated during the optimization. It can be seen that, although low damages were tolerated, run 1 still resulted in a variant with no damage for any detail. This suggests that a the mass could have been reduced even further. The damages found in the other runs hint that the proposed solutions come close to the (presumably) local optimum. The damage for detail 3 in the third run is even equal to the set constraint.

| | Damage at | | | |
Run	Detail 1	Detail 2a	Detail 2b	Detail 3
1	0,00	0,00	0,00	0,00
2	0,00	0,00	0,85	0,00
3	0,00	0,88	0,00	0,80

Table 14.6: Damages found for the best found design alternatives in analysis 2 during the optimization run.

The progression of the best found variant per iteration is plotted in figure 14.1. The long plateau present in the graph of run 3 strengthens the suggestion that the number of evaluations was chosen large enough for this run. The figure also illustrates the random character of the algorithm, as all runs show a completely different path over the iterations. The shorter flat part of run 1 could indicate that more evaluations could have led to improved solutions.
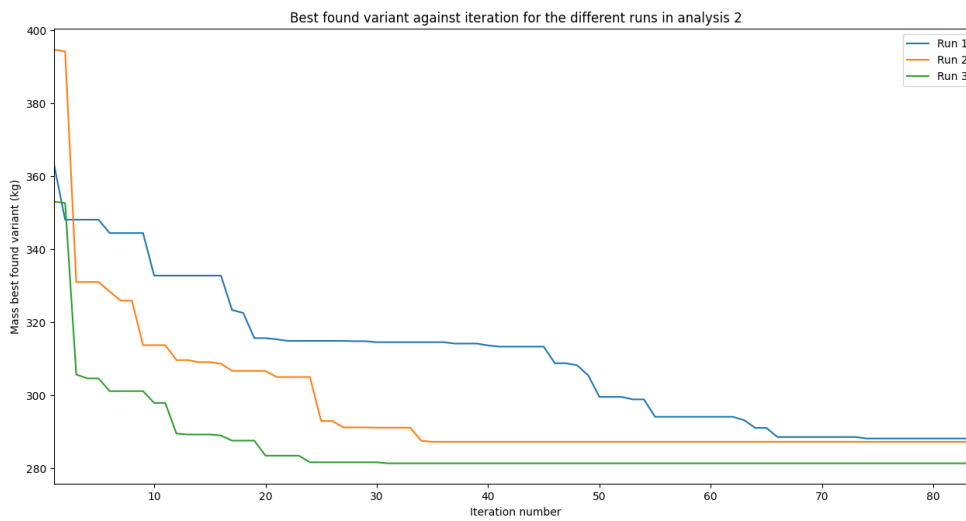
Figure 14.1: Mass of the best found design alternative plotted against the iteration number for the three runs made in analysis 2. An iteration refers to a cycle of the full artificial bee colony algorithm and is thus equal to 30 evaluations.

14.2.2. Results from other food sources
The variance in results is undesirable in the minimized variant, but can be beneficial when multiple design alternatives are sought. The results of the different food sources can also be used. Table 14.7 illustrates this by showing the best variant found by three other employed bees. Interesting to see is the wide range of possible designs, of which some also have a quite economical mass.

run	t_d	ctc_{cb}	t_{sp}	h_{stiff}	a_{stiff}	b_{stiff}	t_{stiff}	mass (kg)
1	14,7	3090	10,8	265	142	136	5,69	310
1	13,7	2360	8,64	323	151	72,6	5,67	310
1	21,7	4330	14,5	234	192	176	6,45	312
2	10,0	4610	17,5	213	100	52,9	9,45	313
2	18,1	2940	10,3	263	200	111	7,48	317
2	21,2	4460	12,5	153	145	145	7,95	318
3	12,0	3800	12,6	143	111	95,2	10,0	294
3	13,2	4010	11,9	196	100	67,9	7,63	302
3	12,1	3030	10,9	296	107	32,0	5,90	310

Table 14.7: The three lightest designs found in each run by other employed bees than the one that eventually found the best result. All values except mass are in mm. All values are rounded to have 3 significant digits in this table.

Also notable is that the height and bottom width of the stiffeners and thickness of the support plate have parameters all over their possible range, while for the others faint trends can be seen. First of all, decks with a thickness of more than 22 mm are not present. These decks are very heavy and rarely result in economical designs. Further inspection of the more than 4000 results generated in the complete first analysis showed that the lowest mass of a design with a deck thickness of more than 22 mm turned out to be 322 kg, considerably more than the variants presented in table 14.5 and 14.7.

Center-to-center distances of the crossbeams of more than five meters are not present as well. The complete set of results does show design variants with these values, but most of them are unfeasible. Particularly detail 2a and 2b appear to be problematic for this. Many of the respective variants turn out to be unfeasible due to unacceptable damages at these to locations. The extra material needed to prevent this is not compensated by the larger spacing of the crossbeams, as the lowest feasible mass found with a center-to-center distance of more than 5 m was again 322 kg.

A third parameter with a clear preference is the top width of the stiffeners. In both tables no values of more than 200 mm appear, while the standard in practice is 300 mm. A great number of variants with wider troughs were analyzed, but again many were found to be unfeasible. Remarkably, this was not only due to high damages at detail 1 (the deck plate at the trough-crossbeam intersection). All four details are highly influenced by the top width of the troughs. This does not benefit the minimized mass. When only variants with a top width of 300 mm of more are considered, the lightest feasible design was found to be 340 kg, which is close to the Van Brienenoord preliminary design.

The final observation, for the thickness of the troughs, may be the most clear. Values of less than 5 mm rarely result in feasible designs and the best found variant with acceptable damages still had a mass of 377 kg. The lower bound for this design constraint could therefore be confidently increased to 5 mm.

It is recognized that these results are influenced by certain modeling choices, global parameters, and design constraints on other parameters. To make definite conclusions, a more specific setup should be made, investigating the influence of a particular upper or lower bound in more detail. The results do, however, give strong suggestions for where the minimized mass of the deck structure should be sought. Therefore, they can be used as starting point for further research or for first estimates of future optimizations in practice.

14.2.3. Computational performance

The large number of necessary finite element calculation makes that the the total procedure takes a considerable amount of time to complete. For the runs of the current analysis, this was between 20 and 22 hours. All analyses were done on a HP Elitebook 840 G3 with an Intel i7-6600 CPU and 16 GB memory running Windows 10. Table 14.8 presents more detailed computational times per run.

Run	Evaluations	Time	Skipped FEA	Performed FEA	Avg. Time Eval.
1	2500	22 h, 00 min	955	1545	51,2 s
2	2500	20 h, 44 min	983	1517	49,2 s
3	2500	20 h, 29 min	1002	1498	49,2 s

Table 14.8: Run times and evaluation information on the three runs made during analysis 2. The total time needed was rounded on minutes. Finite element analyses may be skipped when the objective function will never give an improved value for a certain parameter (see section 10.1). The last column reports the average time required for a single evaluation in which the FEA and fatigue damage calculation were carried out.

The strong influence of skipping some finite element calculation is also visible in the table. This is done when a generated design alternative cannot possibly be better than the best found solution at a certain food source. Around 40 percent of the finite element and fatigue calculations can be skipped this way. This decreases the total computational time by approximately the same amount, as the time spent on the other parts in the workflow (running the artificial bee colony algorithm and creating the parametric model in Python) is negligible compared to the total time of an evaluation.

14.3. Analysis 3: Discrete parameters

The third analysis used the same setup as the second, but the variables produced by the artificial bee colony algorithm are rounded before the mass and damage calculations. Table 10.1 contains the base to which each parameter is rounded. Table 14.9 gives an overview of the setup.

Penalty function	Population size	Limit	Evaluations	Parameter type
$100 * \sum_{i=1}^{4} \delta_i$	30	30	2500	Discrete

Table 14.9: Optimization setup choices for the second complete analysis. δ_i is the damage at detail i. The third analysis uses the same setup as the second, apart from the use of discrete parameters.

14.3.1. Best resulting variants

Three runs were again performed with the settings of table 14.9. The design with the best value of the objective function in each run is shown in table 14.10. The lowest mass found in the three runs differs more than in the results of the previous analysis, but less than in the first. Run 1 found the lightest design, which is with 280 kg/m^2 slightly lower than the best alternative in analysis 2.

run	t_d	ctc_{cb}	t_{sp}	h_{stiff}	a_{stiff}	b_{stiff}	t_{stiff}	mass (kg/m^2)
VBB PD	24	3645	16	325	300	105	8	339
1	12	3500	13	175	125	110	8	280
2	10	3350	13	300	105	50	6	296
3	15	4010	13	215	175	105	9	288

Table 14.10: Optimized results from the third full analysis and the preliminary design of the Van Brienenoord bridge. All values except mass are in mm. The discrete nature of the parameters makes rounding unnecessary.

The design for which that mass is achieved, however, is quite different. The new design uses a thicker deck plate, support plate, and stiffener, but compensates the extra weight from this with a larger cross-beam spacing and lower and wider troughs. Similar to the result of analysis 1, the relatively large bottom width makes the cross-section of the troughs almost rectangular.

The three results combined suggest that the relative similarity of the results of table 14.5 may be a coincidence. Apart from the equal thickness of the support plates, the results do not give any consensus about the best possible dimensions to be used in a design. This could be caused by the algorithm not having the opportunity to properly converge or a possible strong non-convex character of the design space.

Despite this, the most important trends that were found in the previous analyses are still visible: the top width of the stiffeners is much lower, decreasing the span of the deck plate strongly and therefore enabling it to be much thinner. The height of the troughs is also decreased, while the bottom width is larger compared to the top width.

Table 14.11 contains the damages calculated for the three variants during the optimization. The best variant of each run comes very close to the damage constraint of a detail or exceeds it by a small amount (the damage constraint of detail 3 is 0,8; see table 10.2). It shows that, even though a heuristic algorithm is used, the boundaries of a feasibility can be approximated with great accuracy. The slight exceedance of the damage at detail 3 is not directly problematic, as the precise value of the damages could change in the verification in the next chapter.

		Damage at		
Run	Detail 1	Detail 2a	Detail 2b	Detail 3
1	0,00	0,00	0,00	0,82
2	0,00	0,00	0,97	0,00
3	0,00	0,00	0,99	0,00

Table 14.11: Damages calculated during the optimization run for the best found design alternatives in analysis 3.

In figure 14.2, the best found result is plotted against the iteration number of the optimization. The results of each run appear to be stable for a large number of iterations. This suggests that the number of evaluations was appropriate, even though the results do not converge. It strengthens the hypothesis that performing multiple runs of the algorithm is more efficient than increasing the number of evaluations.
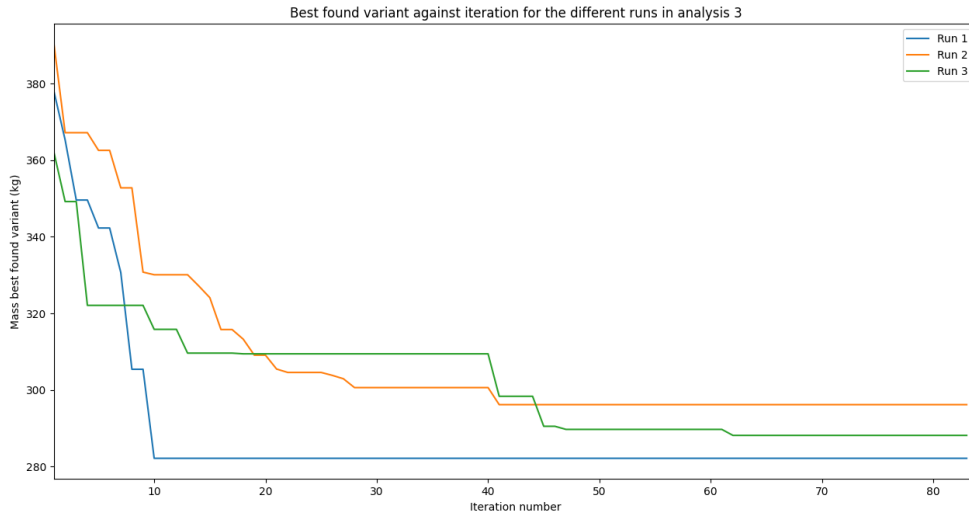
Figure 14.2: Mass of the best found design alternative plotted against the iteration number for the three runs made in analysis 2. An iteration refers to a cycle of the full artificial bee colony algorithm and is thus equal to 30 evaluations.

14.3.2. Results from other food sources
Similar to in analysis 2, the results from the other food sources in table 14.12 show a large variety with some designs having a quite economical mass. This again confirms the suitability of the other food source results as potential design alternatives.

run	t_d	ctc_{cb}	t_{sp}	h_{stiff}	a_{stiff}	b_{stiff}	t_{stiff}	mass (kg)
1	18	4275	14	250	200	95	9	306
1	20	3475	11	195	195	165	8	315
1	18	2860	13	305	195	140	6	315
2	16	3380	10	195	180	135	9	298
2	15	2560	13	200	170	170	7	304
2	14	2950	10	310	145	75	6	304
3	18	3085	11	250	195	190	6	300
3	12	4810	17	275	130	95	8	306
3	13	3670	11	185	120	60	10	309

Table 14.12: The three lightest designs found in each run by other employed bees than the one that eventually found the best result. All values except mass are in mm.

Like the best found result in each run, the table does not show a particular design that performs the best overall. The same general trends for efficient designs are present as discussed in the previous subsection. The observations of the second analysis regarding constraint are confirmed as well: deck thicknesses of more than 22 mm appear uneconomical, center-to-center distances of the crossbeam rarely exceed 5 m, trough top widths are mostly below 200 mm, and a trough thickness of less than 5,5 mm seldom leads to feasible results.

14.3.3. Computational performance

Table 14.13 shows that the run times of the third analyses come close to that of analysis 2. The first run was somewhat quicker, possibly due to less use of the computer for other processes. The third run of the optimization was interrupted twice, making the run times unreliable.

Run	Evaluations	Time	Skipped FEA	Performed FEA	Avg. Time Eval.
1	2500	19 h, 02 min	1014	1486	46,2 s
2	2500	21 h, 15 min	940	1560	49,0 s
3	2500	-	691	1809	-

Table 14.13: Run times and evaluation information on the three runs made during analysis 3. The total time needed was rounded on minutes. Run 3 was interrupted twice and its run time was therefore not representative.

Notable is the much smaller number of skipped finite element calculation for the third run. This is surprising, as the condition for skipping this part of the analysis was altered for this last run. Since then, it should also disregard the analysis if the mass of the newly generated variant is equal to the remembered best variant of the respective food source. This can occur if the change of the continuous variable in the artificial bee colony algorithm is not large enough to induce an alteration of the rounded discrete value. In previous analyses, the chance of generating two decks of equal mass was negligible and thus the condition was chosen to be a simple 'less than'.

The fact that the broadened condition led to less skipping will be further investigated. In principle, skipping equal variants should bring the total run time of the optimization down.

It may be needed to increase the value of the limit parameter as well for future runs of discrete parameters, because the discovery of an improved solution is expected to occur less often when more evaluations are skipped.

14.4. Comparison with results from literature

Chapter 8 mentioned a number of papers that considered applications of structural optimization relevant to orthotropic steel decks. A comparison between the results of these applications and this chapter is made here.

14.4.1. Theoretically optimal orthogonal beam grids

Firstly, the ratio between the crossbeam span and its center-to-center distance can be compared to the optimal ratio of 1/4 as found by Hoogenboom [54]. Considering the 26 m span of the crossbeams, their expected optimal center-to-center distance would be 6,5 m. It was already mentioned in the observations of analysis 2, however, that a crossbeam spacing of more than 5 m did generally not lead to economical designs.

The ratio of the center-to-center distance of the crossbeams to the trough spacing does not come close to the given ratio either. For the optimized designs of all three analyses, this value is approximately equal to 1/29.

A reason for this difference may lie in the stress concentrations that occur around the fatigue details in an orthotropic deck. A second explanation may be that the orthotropic bridge deck may need more orders of stiffening elements to enable the successive spans to have a ratio of 1/4. Requiring a reasonable span of the deck plate, the 26 m wide bridge would then need 4 orders of stiffeners; placed at 6500, 1625, 406, and 102 mm apart.

14.4.2. Parametric optimization

The comparison of the resulting parameters of the in table 14.14 shows that similar papers report vastly different values. Consensus can only be found in the deck thickness and support plate thickness, albeit to a small degree. The center-to-center distance found by Huang, that comes close to the values found in the three analyses made here, is not representative, as it is a reached design constraint. The optimized value with more design freedom may be completely different and in most practical applications this value will not be limited to only 3600 mm.

Paper	t_d	ctc_{cb}	t_{sp}	h_{stiff}	a_{stiff}	b_{stiff}	t_{stiff}
Baandrup [11]	12,3	5760	14,6	311	250	154	4
Huang [55]	12	3600	14	-	-	-	6
Zhuang [122]	13,5	-	-	286	292	-	6,17
Analysis 1	13,2	4070	15,1	183	140	106	9,30
Analysis 2	10,0	3260	14,3	259	111	68,7	6,13
Analysis 3	12	3530	13	175	125	110	8

Table 14.14: Comparison between the results of different studies applying various versions of a parametric optimization on an orthotropic steel deck and the best result from each of the three analyses made here. The values that were left out were not used as design variable in the given paper. For the paper by Baandrup, the values from *Case 8*, with the most design freedom, were used. For the paper by Huang, this was the optimization for minimized steel weight.

The found differences are well explainable, as the built-up, global bridge parameters, and considered fatigue details vary. The effect of this can be easily seen when, for instance, Baandrup's results are compared to any of the analyses of this thesis. The most striking feature in the former are the very thin troughs combined with a large center-to-center distance of the crossbeams. This is possible due to the lack of fatigue details considered in the troughs. A similar configuration would almost certainly give unacceptable damages in the trough splice when it would be considered in the setup of this thesis.

14.4.3. Comparison with existing bridges

Table 14.15 compares the solutions of the three analyses with the design of existing and future bridges. These were earlier presented in table 9.1. It again confirms the break of the results of this chapter with the current trend to increase the thickness of the deck plate while keeping the top width of the troughs intact. The (generally) lower height and relatively larger bottom width of the stiffeners are visible as well.

Bridge	t_d	ctc_{cb}	t_{sp}	h_{stiff}	a_{stiff}	b_{stiff}	t_{stiff}
Ewijk	10	5000	10	350	302	105	6
1st GC	10	3333	10	250	300	110	6
2nd GC	10	3333	10	275	300	135	6
2nd VBB	12	3645	12	325	300	105	6
New SH	20	3100	12	300	300	180	7
New VBB	24	3645	16	325	300	105	8
Analysis 1	13,2	4070	15,1	183	140	106	9,30
Analysis 2	10,0	3260	14,3	259	111	68,7	6,13
Analysis 3	12	3530	13	175	125	110	8

Table 14.15: Comparison between the results of the three analyses and the values used in the design of existing and future bridges. The complete set, including the source, of the latter is found in table 9.1. If a bridge did not have a support plate, the thickness of the crossbeam web was used. The local behavior of these is then similar. The order of the bridge designs is in chronological order, with the oldest at the top. (VBB = Van Brienenoord bridge, SH = Suurhoff, GC = Galecopper, Ewijk = Bridge near Ewijk).

14.5. Cost calculation

Although minimization of costs was not the explicit goal in the optimization, it can be valuable for the use in practice to estimate the price of the structure. Here, a rough cost calculation will therefore be made for the lightest variant found in this chapter: the result of analysis 3. The outcome of the calculation for the resulting designs of analysis 1 and 2 is also reported, but not further elaborated. Estimations for weld and material expenses were taken from two different sources to decrease the effect of uncertainties.

The first source is the paper describing the parametric optimization of Baandrup et al. [11], which was based on values provided by experienced bridge engineers. For the structural members, this consisted of a separate price per kilogram for the deck plate, troughs, and crossbeams. These prices included machining costs. For the welds, a distinction was made between automatic and manual welding. Costs were again given per kilogram.

The second source was an estimation based on experience at Arup and only gives a price per kilogram for welds and material. No distinction is thus made for automatic and manual welding or different structural components. As can be seen from table 14.16, the costs from this estimation are somewhat higher. This can be partly explained by the fact that these also include an addition for the conservation and installation of the material. Other reasons may be increased steel prices or regional differences.

(€/kg)	Baandrup et al. [11]	Arup experience
Deck plate	1,3	5
Crossbeam	1,5	5
Troughs	1,6	5
Automatic welding	333	140
Manual welding	95,2	140

Table 14.16: Estimation for the prices of material used for the structural members and the welds that connect them. Two different sources were used to decrease uncertainties in the result. All values are in €/kg.

The volumes of the structural members can be calculated using the equations 10.2 up to 10.5. With figures 10.4 and 11.10, the cross-sectional area of the welds in the structure may be computed. h_3 and h_4 were already given to be equal to the thickness of the trough, while h_2 is chosen as 10 mm according to [88]. The throat thickness of the welds a was set to 6 mm and the butt weld for the deck splices is assumed to have an average width w_{weld} of 4 mm. The cross-sectional area of the welds can then be expressed with:

$$
\begin{aligned}
A_{w,sp} &= a^2 \\
A_{w,stiff-d} &= t_{stiff}^2 \\
A_{w,d-splice} &= t_d * w_{weld} \\
A_{w,stiff-splice} &= t_{stiff} * (h_2 + t_{stiff} * \sin(30°))
\end{aligned}
\tag{14.1}
$$

$A_{w,sp}$ is the cross-sectional area of all welds connected to the support plate, $A_{w,stiff-d}$ of the weld connecting the stiffeners to the deck plate (which is slightly approximated), $A_{w,d-splice}$ of the deck splice weld, and $A_{w,stiff-splice}$ of the trough splice weld. Using these formulas, the area of each weld was calculated in table 14.17 together with the respective length of the weld. These combined give the mass of the welds that can be used to estimate the costs of the design variants.

	Preliminary design		Optimized design	
	Area (mm^2)	Length (mm/m^2)	Area (mm^2)	Length (mm/m^2)
Longitudinal deck splice	96	400	48	400
Transverse deck splice	96	55	48	57
Deck plate-trough	64	3333	64	8000
Deck plate-support plate	36	274	36	286
Support plate-crossbeam	36	549	36	571
Support plate-trough	36	717	36	1052
Trough splice	120	72	120	105

Table 14.17: Calculation of weld lengths and cross-sectional areas for the optimized design resulting from the third analysis and the preliminary design of the Van Brienenoord bridge. These values are used for the calculation of the mass of the welds in tables 14.18 and 14.19. The area of the welds was calculated using equation 14.1

Table 14.18 shows that the optimized design is expected to be 14,3 percent more expensive. The cost of the deck plate-trough connections has more than doubled due to the increased number of troughs. As the troughs in this design have equal thickness, the area of the weld cannot be decreased. The higher weld costs of this connection are partly compensated by the cheaper deck splices and lower material costs, but the large contribution of the deck plate-trough plate makes that this is not enough to obtain a cheaper variant.

The values based on experience at Arup give a considerably smaller difference in the costs of the two variants. Table 14.19 shows that the optimized variant is only 1,4 percent more expensive than the

	Price (€/kg)	Preliminary design		Optimized design	
		Mass (kg)	Costs (€)	Mass (kg)	Costs (€)
Material:					
Deck plate	1,3	188,4	244,92	94,2	122,46
Crossbeam	1,5	57,7	86,58	60,1	90,16
Support plate	1,5	10,9	16,30	10,0	14,99
Trough	1,6	82,0	131,23	115,6	185,01
Subtotal material		339,0	**€ 479,02**	279,9	**€ 412,63**
Welding:					
Longitudinal deck splice	333,0	0,301	100,38	0,151	50,19
Transverse deck splice	333,0	0,041	13,77	0,022	7,17
Deck plate-trough	95,2	1,675	159,43	4,019	382,63
Deck plate-support plate	95,2	0,078	7,38	0,081	7,69
Support plate-crossbeam	333,0	0,155	51,64	0,161	53,77
Support plate-trough	95,2	0,203	19,28	0,297	28,31
Trough splice	333,0	0,068	22,48	0,099	33,00
Subtotal welding		2,520	**€ 374,35**	4,830	**€ 562,76**
Total			**€ 853,38**		**€ 975,39**

Table 14.18: Cost calculation for the optimized design resulting from the third analysis and the preliminary design of the Van Brienenoord bridge, using the values as estimated by Baandrup et al. [11]. Mass and costs are calculated per m^2 of deck.

	Price (€/kg)	Preliminary design		Optimized design	
		Mass (kg)	Costs (€)	Mass (kg)	Costs (€)
Material	5	339	1695,00	280	1400,00
Welds	140	2,52	353,13	4,83	676,83
Total			**€ 2048,13**		**€ 2076,83**

Table 14.19: Cost calculation for the optimized design resulting from the third analysis and the preliminary design of the Van Brienenoord bridge, using the values as estimated based on experience at Arup. Mass and costs are calculated per m^2 of deck.

preliminary Van Brienenoord design. The welding costs again almost double, but the relatively higher material costs make that this is almost fully compensated by the lower mass of the structural members.

Similar calculations were performed for the results of analysis 1 and 2. This resulted in a price of €1054,06 and €2225,51 for the design of analysis 1 according to the values of Baandrup and Arup respectively. For analysis 2, costs of €869,51 and €1919,97 were found. Even though the latter has an even smaller trough spacing than the result of analysis 3, it is thus expected to be cheaper. This is mostly caused by the thinner troughs, which decrease the area of the deck plate-trough weld considerably. The costs of the second analysis' result also come very close to that of the preliminary design when Baandrup's values are used and are even lower when the prices from Arup are considered.

14.6. Conclusions

The results presented in this chapter show that the optimization problem as set up in chapter 10 can find design alternatives that are significantly lighter than the deck structure that was composed for the preliminary design of the Van Brienenoord bridge. The lowest mass found during the optimization was 280 kg/m^2, found in run 1 of analysis 3. This corresponds to a saving of 57 kg/m^2 compared to the 339 kg/m^2 of the preliminary design, giving a 17,4 percent reduction. Not all of this reduction can be attributed to the potential of structural optimization, as chapter 12 explained that the change of detail categories and design restrictions on the preliminary design will have enabled lighter designs to be found as well.

The optimized design's trough cross-section is illustrated by figure 14.3. The results of the other two analyses and the preliminary design of the Van Brienenoord bridge are also shown for comparison. Table 14.15 gives the full set of optimized variables for all of these cases.
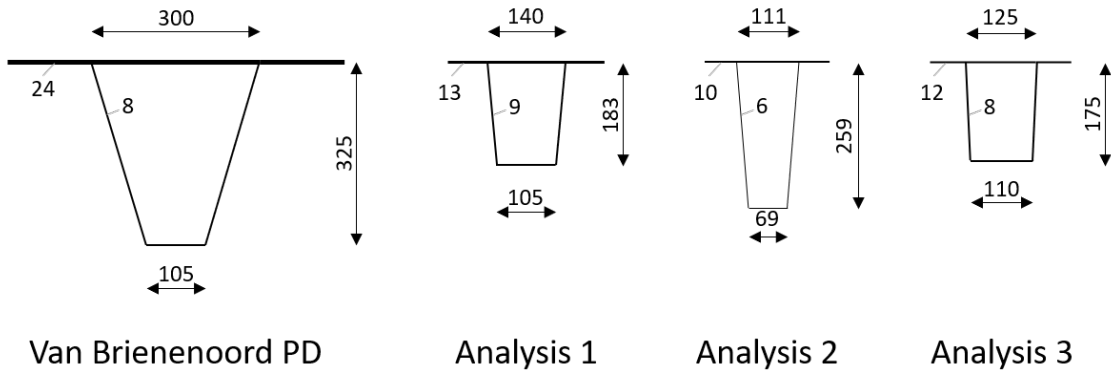
Figure 14.3: Comparison of trough cross-sections used in the Van Brienenoord preliminary design and the results of the three analyses. The use of a thinner deck plates and lower, narrower troughs is easily identified.

14.6.1. Variance in results

The partly random character of the artificial bee colony algorithm expressed itself clearly in the deviating results in the analyses. Multiple runs with the same setup never resulted in the same solution, although they did come close in some cases. Some variation will be inevitable when using heuristics, but it would be beneficial to reduce this to a degree such that satisfactory results can be found in a limited number of runs.

Besides the nature of the used algorithm, the character of the design space may also be responsible for the spread in the outcome. The many different designs that use a completely different ratio of parameters while having competing masses strongly suggest that the design space of the optimization problem is highly non-convex. Appendix G studies this further and proves the concave character of the design space.

Increasing the population size has not been tried yet and could be a solution for both of these problems. Having more completely different design alternatives being worked out should increase the chance that one of those finds the 'right' local peak. This may decrease the variety in results between different runs. Another option can be to increase the maximum number of evaluations. When figures 14.1 and 14.2 are considered, however, it may be more efficient to simply run the algorithm twice instead of doubling the amount of evaluations.

Although the variety of results is undesirable for the best found result, it is valuable for the generation of design alternatives. Even when the divergence of the solution would be decreased, the results found at other food sources can be used for this. These proved to give economical designs with truly different ratios of parameters in all three analyses.

14.6.2. Recommendations for improved designs

Formulating strict recommendations about the optimal form of an orthotropic deck are hard to formulate with the current outcomes. The vastly different optimized options do not give clear ratios that should lead to a single 'best' design. Moreover, the non-convex design space would make it impossible to identify the optimal design, even if it was to be found.

Despite this uncertainty, some general trends that can be used for recommendations are clear in all found results. All economical designs feature a strongly decreased top width of the troughs, which enables a much thinner deck plate to be applied. This is combined with lower heights and relatively larger bottom widths of the troughs. Figure 14.3 illustrates this by comparing the results of the three analyses with the Van Brienenoord design. Evident design constraints were found in deck plate thicknesses of more than 22 mm, crossbeam center-to-center distances of more than 5 m, and trough top widths of more than 200 mm, which never resulted in economical designs. Trough thicknesses of less than 5,5 mm were rarely feasible.

14.6.3. Algorithm performance

Although no comparison with alternatives are made, the results suggest that the artificial bee colony algorithm performs well for the considered optimization problem. Its *elitism* property enables a strong reduction of needed finite element analyses and the use of a vast number of bees leads to proper design alternatives. This swarm-based nature can also reduce run times even more in future applications.

The good performance of the algorithm is further represented by the close approach of the damages to the constraints. In all runs of both analysis 2 and 3, the calculated damage for at least one detail was less than fifteen percent off from the respective damage constraint. Run 3 of analysis 2 even reached the constraint, while run 3 of analysis 3 came within one percent. Given the high sensitivity of fatigue damage and random character of the solver, this does reinforce the potential of heuristics.

14.6.4. Continuous or discrete parameters

The analyses using discrete and continuous parameters resulted in decks of approximately equal mass. Although more runs should be made using both to give more certainty to these conclusions, it can be said that the use of discrete parameters does not hamper the algorithm in finding optimized solutions. Discrete parameters would therefore always be preferred for practical purposes, as results would come closer to the actual design. This leads to better optimized designs and less manual checks after an optimization.

Besides, the use of discrete parameters could also save time in the optimization. The algorithm will then only focus on changes in the configuration that matter for practical use. A change of, for instance, 0,1 mm in the thickness of a structural member is not of any interest in practice, but could occur when using continuous parameters.

Surprisingly, this effect was not observed in run 3 of analysis 3. Where more skipped FE calculations were expected, less were reported. This requires more research.

14.6.5. Further reduction of run times

The subsections in analyses 2 and 3 treating the computational performance of the workflow show that a complete run takes around 19 to 22 hours. While this is certainly long, it is considered acceptable compared to the duration of a general design process of an orthotropic deck. Fatigue analyses performed during this may take a similar amount of time.

Still, the workability of the method may be improved if it is sped up. A significant improvement would already be possible by an enhanced coupling between the parametric model in Python and GSA. In the current setup, GSA needs to be opened and closed for every situation. Moreover, the creation of the model and loads uses the old API of GSA, which is rather slow. A reduction of more than five seconds per evaluation would be possible in this part alone, leading to a potential reduction in run time of more than ten percent.

Even larger savings may be achieved when the workload is spread over multiple cores or servers. The independence of a single bee's choice for a food source makes that the calculations needed in a phase of the algorithm could be easily distributed. A division over two cores or servers could already enable the current setup to be solved in a night, three could do this within a work day.

14.6.6. Cost calculation

Although the objective of the optimization was minimization of mass, the effect of the new design on the costs of the deck were estimated using rules of thumb from two sources. This showed that the lightest design that resulted from the optimizations is likely to be somewhat more expensive than the suggested preliminary design. Depending on the values used, this would come down to a 1,4 or 14,3 percent difference in costs.

Despite the slightly increased costs of the deck itself, the lighter design may still lead to a cheaper structure when the complete bridge is considered. The significant weight reductions may enable the crossbeams, main girders, superstructure, and abutments to be executed lighter, which can give considerable reductions in costs. Furthermore, the lighter deck may also lead to reductions in costs that were not yet considered in the calculations made here, such as transportation costs and reduced weld throat thicknesses.

In addition, the calculations underline the potential of an optimization where minimization of costs is the objective. The costs of the result of analysis 2 were already found to be very competitive or even lower compared to the preliminary design. This was mainly caused by the thinner troughs, which gave a significant reduction in weld volume for the deck plate-trough connection. Integration costs in the objective function may include these kind of relations in the optimization and therefore give considerable reductions in costs.

15

Verification of results

This chapter aims to verify the feasibility of the designs resulting from the analyses of the previous chapter. As this process is quite time-consuming, only the best performing variant of each analysis is treated.

The focus of the verification lies on the influence of simplifications that were made during the optimization. All design variants are checked for possible underestimations at at least three points. These are explained in the first section. The remaining sections each treat an optimized design.

15.1. Points of attention during verification

The simplified analysis made during the optimization could underestimate the stresses at the fatigue details in three possible ways:

- The true influence line of the stresses is non-conservatively approximated by the scaled reference. This does not only regard to the stress peak that occurs, but to the complete course of the influence line. This was seen in section F.1.

- The maximum stress reversal occurring at a detail is not located at the expected location.

- The simplified modeling introduces errors in the analysis results. Appendix D showed that this mainly considers detail 3. Errors at other locations are expected to be conservative.

The design proposals coming from the previous chapter are therefore checked for these three points to verify their feasibility. For the first point, the number of load cases is increased to 606: all three wheel types travel over two trough spans in the deck in 101 load steps, centered once at the middle of the trough and once above a trough leg. The results from this are again combined to find the influence line for the passing of each of the trucks from table 4.2.

The second point is checked by comparing the maximum stress occurring at the elements used for extraction and other elements surrounding the respective fatigue detail. It is recognized that this is not a completely safe method: the difference in the stress reversal could be larger than the difference in the peak stress. For elements in close proximity, however, this difference is assumed to be small. A more thorough check is made when larger stress peaks are found at some distance of the extraction elements.

The third point is checked by increasing the length of the level 3 modeling area in a new finite element model. Appendix D showed that the shorter length of the detailed area introduces the largest error in the stresses at the trough splice. The length of detail level 3 is increased to 5,5 times the trough center-to-center distance (or 11 times the trough top width) as this is expected to diminish the error almost completely (see figure D.8). A new analysis is made with all wheels traveling in 101 steps over two trough spans in the deck, only centered above the middle of the trough. Loads positioned above the trough leg are not expected to be governing for this detail.

Besides the verifications for the assumptions made during the optimizations, the finite element models were also validated on more general aspects. This includes comparison with analytical results and computation of the difference between total loads and reactions. For the latter, it was found that the difference for the five significant digits given by the finite element program was zero in all cases.

Eventually, there may be other factors contributing to non-conservative results. The limited width of the detailed area, choices in mesh sizes, and modeling simplifications in the troughs, crossbeams, main girders, and supports can be named as such. Appendices D and E suggest that their influence is limited, however.

External aspects may also play a role. For example, the correct use of detail categories and the hot-spot stress method for orthotropic steel decks is still subject of ongoing research. New insights may label currently found designs unfeasible, but these cannot possibly be taken into account already.

15.2. Result analysis 1

The lightest resulting variant of analysis 1 was obtained in run 3 and has a mass of 289 kg/m^2, 14,7 percent less than the reference design of the Van Brienenoord bridge. The complete overview of parameters can be found in table 14.3.

15.2.1. Increased number of load cases

The damage at none of the details in this variant was influenced by the more accurate determination of the influence line. All damages were still determined to be zero. Chapter 12 already mentioned the influence of the cut-off limit and very large number of trucks that passes the bridge. On top of that, the input of this analysis contained a mistake that caused the calculated damages to be a factor 100 too high. This made that the damage constraints at the details are essentially stress constraints that could not exceed the cut-off limit. Table 15.1 compares the maximum stress ranges at each detail found during the optimization with the stress range found with the increased number of load cases and the cut-off limit.

Case	Detail 1	Detail 2a	Detail 2b	Detail 3
Simplified	42,6	42,1	34,7	34,8
Detailed	41,8	38,4	31,5	32,5
Cut-off	46,5	49,3	35,1	35,1

Table 15.1: Comparison between the maximum stress range obtained during the optimization run and from a more detailed analysis. The cut-off limit is listed as well to visualize how close the designs come to the constraints. All values are given in MPa.

The table shows that the simplified determination of the influence line leads to a conservative estimate for the stress range at all details. A comparison between the simplified results and the cut-off limit also reveals that the estimated stresses at detail 2b and 3 come very close to the constraint. Keeping the high sensitivity of local stresses in mind, it is unlikely that the heuristic algorithm would have been capable of truly reaching these. A secondary, gradient-based algorithm would be better suited for this. This is only useful when the secondary stage would also involve an improved estimate of the influence line. For practical purposes however, this small improvement is insignificant or even unwanted in preliminary stages.

15.2.2. Check of neighboring elements

For detail 1, the location of the maximum stress reversal is very predictable. The stress concentration is caused by the presence of the crossbeam and the maximum stress is occurs near its intersection with the trough. Visual inspection revealed that the stresses at the considered elements were considerably higher than for neighboring elements. No further checks were therefore deemed necessary.

Detail 2a, at the bottom of the trough, is less predictable. This is proven by the contour plot of figure 15.1. The general expectation is that the maximum stress occurs at the side of the trough above which the load is centered, but this case contradicts that. The highest value of the stress here occurred on the exact opposite side of the elements used for extraction. Here, an extrapolated value of 26,6 MPa is found, compared to the 20,6 MPa in the highlighted elements.
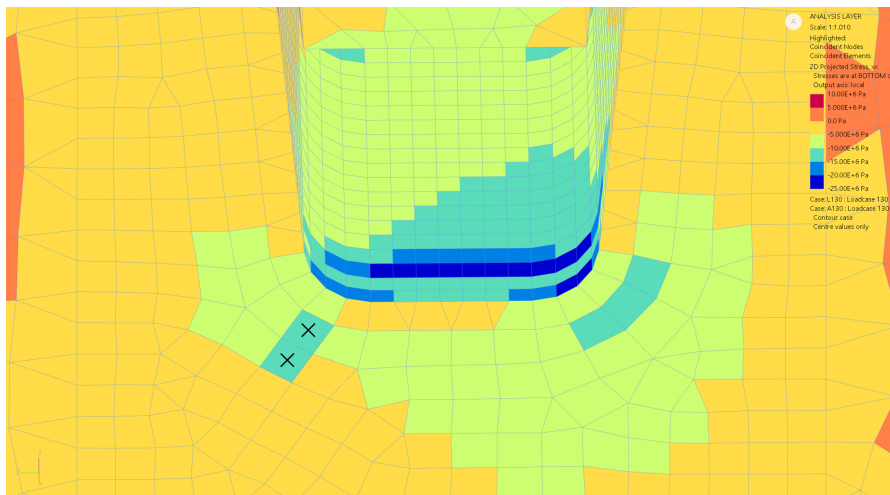
Figure 15.1: Contour plot of the stresses in local x-direction at the bottom of the element, around the trough-support plate connection. The elements used during the optimization to extract the stresses are marked with a cross and have deviating local axes. Wheel load A is centered above the trough leg on the left side of the figure, in the governing longitudinal position for the marked elements. Only the stresses in the center of the elements are used, hence the discontinuous patterns.

The large difference in stress peak required an additional fatigue check for the new location. This did, however, not lead to a violation of the damage constraint. The newly found location experiences a maximum stress range of 48,9 MPa, which is just below the cut-off limit of 49,3 MPa. The estimated value of 42,1 MPa is no longer conservative. More elements to extract the stress from are needed in the trough close to the support plate to be safe in future cases.

Visual inspection of the contour plots at detail 2b (figure 15.2) shows that the predicted location of largest stresses comes very close to the true one. As the local direction would need to be changed for every element to obtain the stress perpendicular to the weld, the minimum principle stress was used to determine this. Inspection of the direction of the principle stresses at the elements revealed that the difference between these is small. The element adjacent to the highlighted element showed a slightly higher stress, but the difference (<0,25 MPa) is negligible.
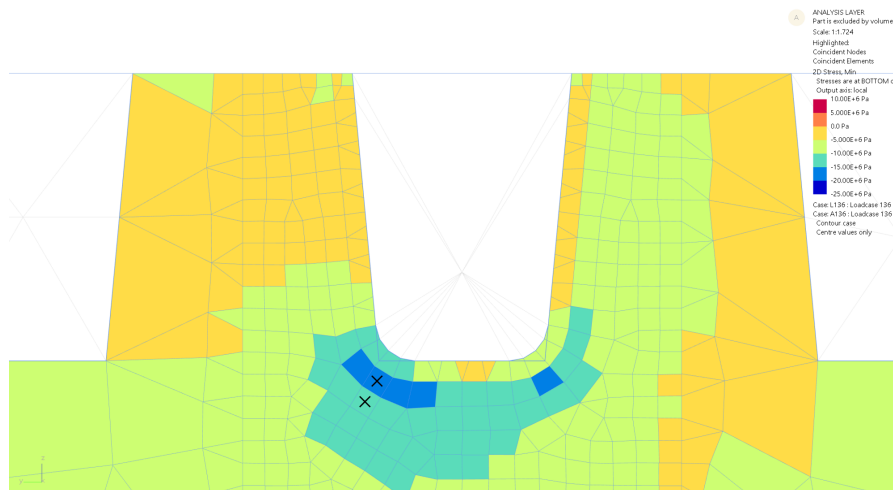

Figure 15.2: Contour plot of the minimal principle stresses at the bottom of the element around the trough-support plate connection. The elements used during the optimization to extract the stresses are marked with a cross. Wheel load A is centered above the trough leg on the left side of the figure. The longitudinal position is chosen such that the maximum stress is obtained in the highlighted elements. Only the stresses in the center of the elements are used, hence the discontinuous patterns.

The absence of sharp corners and other irregularities near detail 3 cause the stress profile around this joint to be gradual and predictable. The differences between the stresses at the considered location and at elements around it were less than 0,2 MPa, which is thought to be negligible.

15.2.3. Increased size of detail area

The maximum stress at the trough splice was found to be 20,8 MPa, both during the optimization as when the amount of load cases was increased. The approximation of the influence line thus appears to be very accurate. When the length of the detail area is increased, however, the maximum stress increases to 22,7 MPa. The rounded trough may have a slightly lower bending resistance, leading to an increase in stresses at the bottom.

This increase is also seen in the maximum stress range. The model containing a larger detail area gave a stress range of 34,3 MPa, which is larger than the 32,5 MPa found with the smaller detail area. The scaled influence line still finds a greater value (34,8 MPa) and is thus conservative. The final stress does not violate the constraint.

15.2.4. Conclusion verification 1

Even after the more detailed analyses made in this section, the stresses at no fatigue detail exceed the cut-off limit. All damages are therefore equal to zero.

The analysis further confirmed the conservative character of the scaled influence lines. The extraction of the maximum stress in the trough rounding (detail 2a) does need some further attention, as the obtained value during the optimization was not the maximum. The eventually calculated value still satisfied the constraints, however.

15.3. Result analysis 2

The best performing variant of analysis 2 was found in its third run and has a mass of 282 kg/m^2. Compared to the 339 kg/m^2 of the Van Brienenoord deck, this is a 16,8 percent reduction. Table 14.5 contains the complete set of parameters that determines this design.

15.3.1. Increased number of load cases

The increased number of load cases did not lead to an increase of the damages at the fatigue details, but all decreased to zero. Table 15.2 explains this. The conservative character of using the scaled reference influence lines makes that the maximum stress ranges at detail 2a and detail 3 are decreased. This way, they fall below the cut-off limit and no damage is expected to occur.

Case	Detail 1	Detail 2a	Detail 2b	Detail 3
Simplified	43,1	50,8	31,7	35,3
Detailed	43,0	43,7	31,5	31,8
Cut-off	46,5	49,3	35,1	35,1

Table 15.2: Comparison between the maximum stress range obtained during run 3 in the second optimization analysis and from a more detailed analysis. The cut-off limit is listed as well to explain the reduction of the damages to zero. All values are given in MPa.

The stress values in the table show the very accurate estimation of the stresses at detail 1 and 2b, while the stresses at detail 2a and 3 are overestimated by sixteen and eleven percent respectively. This implies that the design could be improved even further, as the two restricting constraints during the optimization are lifted. Reducing the thickness of the troughs would be most promising, as both constraints applied to details that are located there.

For detail 2a, the error could be caused by the current approach in the fatigue analysis during the optimization. The two measuring points for this detail (see figure 11.9) use the same influence line, which is scaled bases on the highest stress found at either of the locations. The largest stress for this variant occurs in the detail at the opposite side of the second load, while the reference line is based on the detail at the same side of the load. Naturally, this can induce an error.

Further inspection of the influence lines obtained during the optimization and with the increased number of load cases revealed that the overestimation of the stress range mostly comes from the second half of the influence line. This corresponds to the load being placed on the span adjacent to the one in which detail 2a and 3 are located. In the preliminary run 4 of appendix F, the opposite was obtained and a more conservative reference influence line was adopted. Approximating the second part of the

influence line by scaling a reference thus proves to be difficult. A load scheme that determines both the value of the primary and secondary peak could be adopted when more precision is desired. The first proposal of appendix C already had this goal, but would come at the cost of significantly larger computation times.

Another option could be to start a secondary stage after the optimization using the artificial bee colony algorithm has ended. The reference influence line should then be updated to better represent the obtained variant. A new optimization can then be set up to push the design to the edge, possibly also involving a more detailed analysis using the influence of weaves. Application of gradient-based solvers may be better suited for this, as they can likely approach the constraints more efficiently than the random search of heuristic methods.

15.3.2. Check of neighboring elements
A check similar to that done for the result in analysis 1 was made for the design alternative from analysis 2. The stress pattern around the trough-support plate intersection turned out to be very similar to that presented in figures 15.1 and 15.2. The maximum stress in the trough again occurred at the opposite side of where the second wheel load was placed (the right side of figure 15.1). This posed no problem, as after the previous verification an additional stress extraction point was implemented for this location. The maximum stress range here was already used in table 15.2.

The check of neighboring elements to detail 2b also proved similar to that made in the previous section. The principle stresses were highest around the corner of the trough, in the area where the measuring points are situated. The element besides the used element showed a slightly higher stress (approximately 0,5 MPa), but this will not affect the calculated damages.

15.3.3. Increased length of detail area
The length of the detail area for this final check was increased to six times the center-to-center distance of the troughs (666 mm on each side of the crossbeam) instead of the 5,5 times mentioned in section 15.1. This was done to properly include the trough splice in the detailed area.

Again, the maximum stress range increased due to the lengthening of modeling level 3. The more accurate model resulted in a reversal of 34,7 MPa, which is 9,1 percent higher than the 31,8 MPa found with the same number of load cases and a smaller detailed area. This is difference is slightly higher than expected based on appendix D, but the stress range obtained in the simplified analysis is still larger. The more precise value does also not exceed the cut-off limit and no damage is thus expected.

15.3.4. Conclusion verification 2
The more detailed analyses made in this section showed that the simplified analysis made during the optimization was conservative in all cases. The latter reported some damage in details 2a and 3, but the stresses here were reduced to below the cut-off limit in the more precise analyses. This made all expected damages to be equal to zero and the design variant thus feasible.

The estimation of the maximum stress range at detail 1 and 2b based on the simplified analysis proved to be very accurate. At detail 3, the same was found when the increase due to the longer detailed modeling area is accounted for. Only the stress estimation at detail 2a is overestimated too much and could be improved in future research.

15.4. Result analysis 3
Analysis 3 found a design with a mass of 280 kg/m^2 in its first run, making it the most successful of the studies made in this thesis. The 59 kg/m^2 reduction is equal to 17,4 percent of the preliminary design's original mass. The set of parameters used for this design is presented in table 14.10.

15.4.1. Increased number of load cases
Like in the previous two more detailed analyses, damages were found to be lower than computed in the simplified calculation during the optimization. All stresses were again reduced to below the cut-off limit and thus no damages were expected at any fatigue detail. Table 15.3 summarizes this.

Case	Detail 1	Detail 2a	Detail 2b	Detail 3
Simplified	39,1	48,1	34,9	35,4
Detailed	38,0	47,3	31,3	33,0
Cut-off	46,5	49,3	35,1	35,1

Table 15.3: Comparison between the maximum stress range obtained for the design during the optimization and resulting from a more detailed analysis. The cut-off limit is listed as well to explain the reduction of the damages to zero. All values are given in MPa.

The table also shows that the differences between the simplified and detailed analyses are again relatively small. Most notable is that the stresses for detail 2a are much better estimated than in analysis 2, where it could be seen as overconservative. It could be that the thicker troughs used in this design show more similar behavior to the design that was found during the first preliminary run (see appendix F), from which the reference influence lines were taken.

15.4.2. Check of neighboring elements
Comparable to analysis 2, the check of neighboring elements did not lead to significant changes in stress peaks. Differences were of the order of 0,5 MPa and would thus not lead to unacceptable damages when the values of table 15.3 are considered.

15.4.3. Increased length of detail area
The final check of the design again increased the stresses at the trough splice. The largest cycle was found to be 36,1 MPa, fourteen percent higher than the 31,8 MPa from table 15.3. The damage corresponding to this value was calculated to be 0,91. This makes the design feasible, albeit just.

15.4.4. Comparison with analytical results
An extra check of the finite element results is made by a comparison to analytical methods that are given in the Dutch national annex to EN 1993-2 [2]. The first considers the deck plate-trough connection at the crossing with the support plate, which is represented by detail 1 in this thesis. The detail is simplified to a beam that is fixed on both ends and loaded by a uniformly distributed load.

The distributed load q_{wheel} resulting from the axle load Q_k with wheel type A is calculated by:

$$
\begin{aligned}
q_{wheel} &= \frac{Q_k}{2 * (b_{wheel} + 2 * \tan(\theta_{spread}) * t_{asphalt}) * (l_{wheel} + 2 * \tan(\theta_{spread}) * t_{asphalt})} \\
&= \frac{100.000}{2 * (0,220 + 2 * \tan(35°) * 0,140) * (0,220 + 2 * \tan(35°) * 0,140)} = 2,89 * 10^5 \text{ N/m}^2 \\
M &= \frac{1}{12}q a_{stiff}^2 = \frac{1}{12} * 2,89 * 10^5 * 0,125^2 = 376 \text{ Nm} \\
\sigma &= \frac{6M}{t^2} = \frac{6 * 376}{0,012^2} = 15,7 * 10^6 \text{ N/m}^2 = 15,7 \text{ MPa}
\end{aligned}
$$

(15.1)

The origin of the values that were filled in these equations can be found in table 4.2 and sections 11.3.7 and 11.4. The calculated stress is the component caused by bending in an ordinary situation. However, the presence of the support plate causes a stress concentration around it. The Eurocode therefore prescribes to multiply the calculated value by a factor: the SCF.

Two situations are distinguished: a deck without asphalt layer and with an asphalt layer of more than 50 mm thick. Although a 140 mm asphalt layer is used in this research, it is not explicitly modeled. For comparison of the analytical method to the finite element results, the SCF is therefore calculated as if no asphalt layer is present:

$$
\begin{aligned}
SCF &= 1,2975 - 0,00938t = 1,2975 - 0,00938 * 12 = 1,1875 \\
\sigma_{SCF} &= SCF * \sigma_{ord} = 1,1875 * 15,7 = 18,6 \text{ MPa}
\end{aligned}
$$

(15.2)

This value should be compared with the bending stresses found in the finite element model, caused by a single axle load. The values of table 15.3 cannot be used for this, as the maximum stress reversal is produced by the combined influence of multiple axes. The extrapolated stress peak for a single 100 kN axle was found to be equal to -25,4 MPa. However, this also contains a component of the normal force that is present due to the deck's role as crossbeam top flange.

Examination of the stresses in the deck plane at midplane revealed that this component was responsible for -7,9 MPa. The remaining bending stresses then account for $25,4 - 7,9 = 17,5$ MPa, which comes close to the analytical result. The latter is slightly conservative, as would be expected.

The second detail for which the Eurocode provides an analytical method is the trough-support plate connection (detail 2b). The bending stresses at this detail should then be calculated using the rotation of the trough at the support plate ϕ:

$$\sigma = \frac{1,5 * E * t_{supp} * \phi}{h} = \frac{1,5 * 210.000 * 13 * 0,00064}{250} = 10,5 \text{ MPa} \tag{15.3}$$

The value of ϕ was determined from the maximum rotation in the finite element model. For this, the difference in displacement between the trough at the support plate and at 150 mm from it was taken and divided by this distance. h is the distance from the bottom of the trough to the top flange of the crossbeam. This is equal to the height of the support plate (425 mm) minus the height of the trough (175 mm).

Similar to the previous detail, the bending stresses in the support plate were determined by subtracting the component from the normal force in the plate. This left a stress of 11,6 MPa, which is ten percent higher than the earlier calculated 10,5 MPa. Given the crudeness of the analytical method, the finite element result may again be called reliable.

15.4.5. Conclusion verification 3
The more detailed checks performed for the third found design alternative did not result in any violated constraints. The enlarged detail area increased the maximum stress reversal and damage in the trough splice, but remained just within the acceptable regions. The design is therefore labeled as feasible, albeit with little redundancy. More detailed analyses should confirm this conclusion. For now, extra checks using analytical methods validated the reliability of the finite element computations.

15.5. General conclusions from verifications
The additional checks in this chapter verify that the designs resulting from optimizations are feasible. The largest stress cycle at the fatigue details fell below the cut-off limit in almost all cases, meaning that mostly zero damage is expected for all three designs. Only the trough splice of the third design variant experiences a maximum stress reversal that is larger than the cut-off limit and is thus expected to experience fatigue damage.

This detail is also the only fatigue joint for which the stress cycle is not conservatively estimated by the approach of the optimization run. In all other instances, the simplified approach led to stress cycles that were slightly larger than those calculated in more detailed analyses. The deviation from this trend in the final design variant was caused by the larger increase in stresses when the accurately modeled area was enlarged. The reason for this may be the lower height and relatively larger bottom width of the troughs. This causes the neglect of the rounding of the troughs to result in a larger difference in the trough's stiffness than for the other designs.

Although the scaling of reference influence lines was almost always conservative, it was in general also very accurate. Differences were at most ten percent, but frequently much lower. The calculated stress for detail 2a in analysis 2 is the exception on this. It was mentioned that this could be improved by better estimation of the influence line when the wheel loads are placed on the trough span adjacent to the one the fatigue details are placed in. Besides this, it can be concluded that the proposed method for the reduction of the number of load cases performs very well.

The lateral weaves that should be applied according to the Eurocode load model were not used during the optimization and most of the verifications of this chapter. This is a conservative assumption, as all loads are thus placed at the expected worst position. It is, however, not expected that the mass of the decks can be reduced strongly when these would be taken into account. Chapter 13 already mentioned this conjecture, which is supported by tables 15.2 and 15.3. These show that only marginal exceedance of the cut-off limit is allowed for acceptable damages.

This is mainly due to the enormous amount of trucks (200 million) that is expected to pass the bridge during its lifetime. Stress reversals larger than the cut-off limit (which corresponds to a resistance of 100 million cycles) will therefore quickly lead to damages above one. For bridges where the expected number of trucks is smaller, including the weaves may be more beneficial.

An observation that was not explicitly mentioned in the prior checks, but could be relevant in future use concerns the origin of the largest stress reversals. For all details of all three designs, the third truck of table 4.2 was responsible for this. The three closely spaced and quite heavily loaded axles at the back of this truck reinforce the individual influence lines, leading to a stress cycle that is much larger than would be caused by the wheels separately.

III

Topology Optimization

16
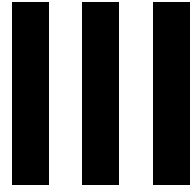
Exploratory study for layout optimization using the ground structure method

After the optimization of the conventional OSDs in the previous chapters, an effort was made to improve the design of steel bridge decks even further. The structural concept is loosened, meaning that the orthogonally placed troughs and crossbeams are no longer required. The new design will still consist of a stiffened plate, but the distribution of the reinforcing elements will be changed.

Inspiration for new forms was taken from applications in literature discussed in chapters 7 and 8. Two options are considered in this thesis. For the first, a topology optimization is made based on the ground structure method, making use of the method as presented by Bolbotowski et al. [22]. The second considers a design featuring curved crossbeams, which was inspired by the result found by Baandrup et al. [13]. The two options are treated in separate chapters. This chapter studies the first, while the second is discussed in chapter 17.

Here, the applicability of the ground structure method is shortly listed, after which the optimization problem is formulated and the studied situation is explained. This is followed by an illustration of the expected results, meant to clarify the choice for this method. Then, the actual results are shown and a conclusion is drawn.

16.1. Applicability
The ground structure method, discussed in section 7.2.1, searches for the optimal sizes of the members present in an initial design. As these sizes can approach zero, a new topology may be obtained by deleting members below a certain size. While the method is mainly used for the optimization of truss structures, Bolbotowski et al. [22] showed that the method can also be applied on plates to obtain the preferred orientation of stiffeners.

This may prove valuable for alternatives to the orthotropic bridge deck. The method is capable of automatically identifying the zones as analytically determined by Rozvany [95, 96], which prescribe the optimal orientation of stiffeners at any location in a plate structure (see section 5.4.1). Furthermore, Bolbotowski's method adds the determination of the members' cross section to the analytical approach.

On the other hand, the method makes two assumptions that may be questionable for use in steel bridge decks. The first concerns the linear relation between cross-sectional area and resistance. While this may be approximately true in truss structures, where the members are loaded axially, this is far from reality in beams loaded out of plane. Only when the height of these beams would be kept equal, the mentioned relation holds. This prevents, however, the formation of different orders of stiffeners often found in practical applications (e.g. main girder-crossbeam-trough in orthotropic decks). It may therefore be questioned whether solutions are truly optimal when the strong increase in resistance of higher of members is neglected.

Secondly, the torsional stiffness of all members is ignored. Recalling section 3.2.2, the increased torsional resistance of closed stiffeners was the main reason for adopting these. Changes in the force distribution could occur when the extra rigidity would be taken into account.

Still, it is thought that the topology optimization can give valuable insights into the optimal distribution of stiffeners. Even if a subdivision of stiffeners will not be found, it could still give an idea for an optimal distribution of higher orders of the stiffeners. Moreover, the torsional resistance of the crossbeams, often I-profiles, is also much smaller than their resistance in bending. This makes the second discussed assumption more valid when only the crossbeams are considered.

16.2. Problem formulation

The general form of the ground structure method (equation 7.2) can be kept intact when applied on plates, but the implementation of the components is somewhat different. First of all, the area of each beam can vary over its length to follow the non-equal moments at the end points. As normal forces in truss structures do not have this property, this would be irrelevant in these applications.

Secondly, the equilibrium matrix and force vector are adjusted to fit the new situation. Three forces can be applied at each node: a bending moment in both x- and y-direction, and a force in z-direction. The stress constraints are also changed to plastic moment constraints, but this only considers another interpretation. No changes in the problem's structure result from this.

Taking these changes into account, the problem is formulated as [22]:

$$
\begin{aligned}
\min_{\mathbf{a},\mathbf{q}} \quad & V = \mathbf{1}^T \mathbf{a} \\
\text{s.t.} \quad & \mathbf{B}\mathbf{q} = \mathbf{f} \\
& \mathbf{q} \geq -m^- \mathbf{a} \\
& \mathbf{q} \leq m^+ \mathbf{a} \\
& \mathbf{a} \geq \mathbf{0}
\end{aligned}
\tag{16.1}
$$

Where:

V = the structural volume

$\mathbf{1} = \left[\frac{1}{2}l_1, \frac{1}{2}l_1, ..., \frac{1}{2}l_m, \frac{1}{2}l_m\right]^T$ is a vector containing the length of the members

$\mathbf{a} = [a_{11}, a_{12}, ..., a_{m1}, a_{m2}]^T$ is a vector containing the cross-sectional area of the members

$\mathbf{q} = [q_{11}, q_{12}, ..., q_{m1}, q_{m2}]^T$ the vector containing the member forces

$\mathbf{B}$ = the equilibrium matrix, assembled from the individual member matrices that follow from 16.2

$\mathbf{f}$ = the vector containing the external forces, assembled from 16.3

m^- = the hogging bending moment resistance

m^+ = the sagging bending moment resistance

The addition of each member to the global stiffness matrix $\mathbf{B}$ is given by:

$$
\mathbf{B}_i =
\begin{bmatrix}
-\sin(\theta_i) & 0 \\
\cos(\theta_i) & 0 \\
\frac{1}{l_i} & -\frac{1}{l_i} \\
0 & -\sin(\theta_i) \\
0 & \cos(\theta_i) \\
-\frac{1}{l_i} & \frac{1}{l_i}
\end{bmatrix}
\tag{16.2}
$$

With θ_i being the angle of the member to the global x-axis and l_i representing the length of the member.

The global force vector is built from the local force vectors, given by:

$$\mathbf{f} = \begin{bmatrix} m_{1x} \\ m_{1y} \\ f_{1z} \\ m_{2x} \\ m_{2y} \\ f_{2z} \end{bmatrix} \tag{16.3}$$

Where m_{1x} represents the moment in x-direction applied at a node 1, while f_{1z} is the force at the same node in z-direction.

The presented formulation results in a linear programming problem (see section 6.1.1), which can be efficiently solved by many well-established algorithms. Its convex character makes that the results will not rely on initial conditions and the global optimum is guaranteed to be found. The script used for the implementation of this problem was based on the Python script provided by He et al. in [51].

16.3. Studied situation

The studied situation consists of five bridge sections like these would be found in the Van Brienenoord bridge. This comes down to a rectangular domain of 165x26 m, supported at the edges every 33 meters. A uniform load is applied to the complete domain. The value of this load and the resistances of the bending moments is chosen to be equal to 1. After all, only the orientation of the stiffeners is of interest. Their sizes can be determined by the parametric optimization to include effect of the (presumably governing) fatigue loads.

A joint cost of 0,1 is used. This constant value is added to each term of the length vector and therefore penalizes very short members. This does not affect the resulting orientation of the beams, but simplifies the result strongly by removing much of the very small elements [22, 50]. As only the orientation is of interest, this does not influence the desired result, while it does make it more workable.

16.4. Expected results

The choice for applying the ground structure method to find an improved layout for the stiffeners on an orthotropic bridge deck was partly based on the results presented in Bolbotowski et al. [22]. The case that comes the closest to the situation described in the previous subsection considers a rectangular plate that is clamped at its corners. The resulting topology is presented in in figure 16.1.
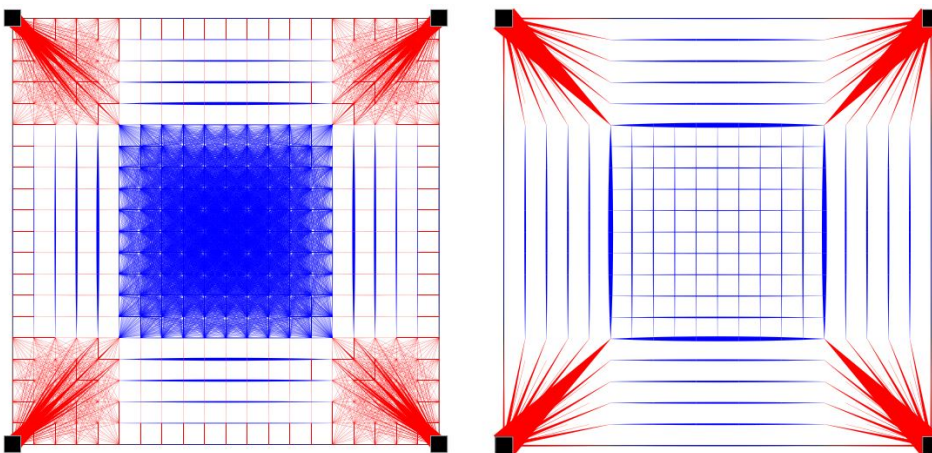

Figure 16.1: Optimal placement of stiffeners (or beams in a beam grid) for a rectangular, uniformly loaded domain, fully clamped at its corners, as presented by Bolbotowski et al. [22]. The right figure uses the same setup as the left except for a joint cost added to each member. The zones of figure 5.6 can be distinguished in the result. Red colored lines indicate hogging bending moments in stiffeners, while blue lines show sagging moments.

Extending this result to multiple bridge sections, it would be expected that multiple copies of this topology next to each other would be found. The major beams at the edges of the domain span in the direction of the supports and would therefore not be influenced by any beams in adjacent segments.

Figure 16.2 confirms this expectation. The figure presents the result of an optimization following the setup of the previous subsections applied on a domain of 99x26 m, corresponding to three bridge segments. The pattern in the result repeats itself three times and only differs slightly from the topology of 16.1 due to the non-square domain.
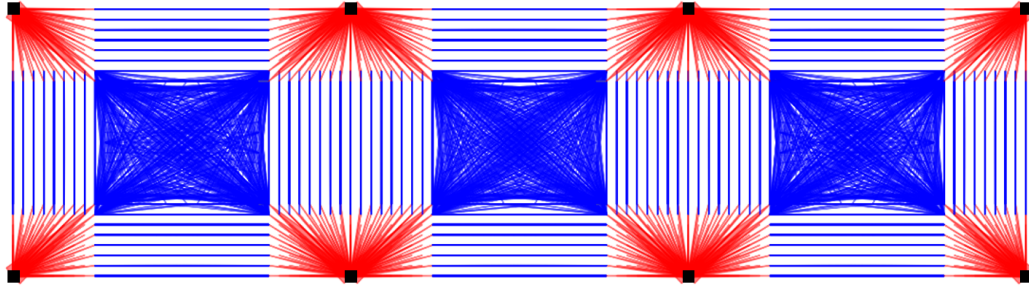

Figure 16.2: Optimal placement of stiffeners for a 99x26 m uniformly loaded rectangular domain. The black squares represent the clamped supports and are spaced at 33 m from each other. The similarity to figure 16.1 is clear.

However, the cable supports present in an arch bridge are not likely to provide much rotational support. The true behavior of these would likely be better approximated by simple supports. While it was expected that this would have an influence on the resulting layout, the differences were thought to be subtle.

16.5. Results of topology optimization

Figure 16.3 proves different. The simply supported deck does not feature the regions with a clear preference for longitudinal of transverse stiffeners and the fan-like pattern around the supports has disappeared. Instead, a pattern of orthogonal beams occurs between the supports, connected by parts that are densely filled with blue beams. Similar to figure 16.1, these regions correspond to the R^{++} zone derived by Rozvany (see figure 5.5). The orthogonal pattern represents an R^{+-} zone.
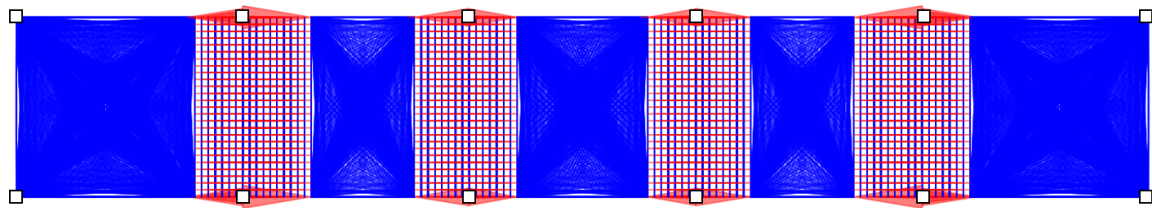

Figure 16.3: Optimal placement of stiffeners for a 165x26 m rectangular, corresponding to five bridge sections. The simple supports are indicated by the black outlined squares and placed at every 33 m. A uniform unity load was applied.

The large numbers of members in the blue colored regions are caused by the indeterminate optimal orientation of stiffeners in R^{++} and R^{--} regions, enabling many solutions to be equally optimal. The solver of the problem therefore tends to find a design that is a combination of all of these possibilities [22]. It is emphasized that while the latter is a consequence of the numerical method, the indeterminacy of the optimal orientation is not. This is also present in analytical results, as was demonstrated by Rozvany [95].

Adding a joint cost helped to simplify the resulting layout for the case of figure 16.1 in the cited paper. Unfortunately, this did not have the same effect on the layout of figure 16.3, even when larger joint costs were used.

16.6. Conclusion

The result of the topology optimization using the ground structure method was significantly different than expected. The eventual layout contains stiffeners placed in longitudinal and transverse direction between the supports, similar to to the traditional in orthotropic steel decks. These zones are connected by regions where the optimal orientation of stiffeners is arbitrary.

Taken this into account, the current layout of the orthotropic deck could be called optimal. However, this ignores the two questionable assumptions that have been made in the used method. The linear relation between the cross-sectional area and resistance, and the neglect of the members' torsional resistance are expected to influence the results considerably. To give above conclusion more credibility, an effort should be made to incorporate the non-linear relation between the moment capacity and height of members.

It is not expected that integration of costs into the objective function will lead to other results. Various values of the joint cost, which can include the additional cost of having many smaller members in a construction and should help in simplifying the found solution, were used without observing significant changes in the result. More detailed cost optimizations would again require the mentioned non-linear relation for useful results.

Adjustments in applied loading or constraints could give significant differences in the outcome of the optimization. It may be argued that (moving) point loads combined with constraints on the experienced stress range would be better suited for an OSD and research towards the implications of this change could therefore be of interest. In this new setup, however, the uniformly loaded deck would still be a relevant load case and the result of figure 16.3 would thus likely be part of the result.

Therefore, the method as presented in this chapter can currently not assist in finding innovative structural concepts. The orthogonal layout of the traditional design is to be preferred, at least until a non-linear relation between the cross-sectional area and moment resistance is implemented. Making the necessary adaptations was not achievable during the remaining available time in for this thesis. It was therefore decided to focus the attention of the remaining part of this thesis on the second option: the use of curved crossbeams. This concept is further explained in the next chapter.

17

Curved crossbeams

Following the parametric optimizations earlier in this thesis, two options were explored to find innovative designs that could improve steel bridge deck designs even further. The first was presented in the previous chapter and did not result in new design concepts on the short term. The second attempt was inspired by the highly detailed topology optimization made in Baandrup et al. [13] (see also section 8.2) and is discussed in this chapter.

The discussion will consist of an exploratory study towards the potential of the new structural concept. The level of detail will thus be less than the study performed during the parametric optimization. Two evaluations are performed to asses this potential: a mass optimization with fatigue constraints, similar to what was done in part 1 of this thesis, and a study of the general force transfer in the deck.

This chapter first discusses the new design and differences in the optimization setup. Due to some differences in the global design of the bridge, the results of Baandrup's study needed to be interpreted. The consequences of these differences on the applicability of the results is reviewed in the first section. The second section elaborates on the new structural design. The third section discusses the changes in the setup for the parametric optimization. The results of this optimization and the force transfer study is presented in the next two sections, followed by the conclusions that finalize this chapter.

17.1. Applicability

Baandrup's design featuring curved crossbeams was made for the Ozman Gazi bridge in Turkey, a suspension bridge with a main span of 1550 m. The deck is supported every 25 m and has a width of 36 m, which results in a significantly different length to width ratio compared to the 32,8 m long and 26 m wide[1] Van Brienenoord bridge.

The execution of the orthotropic deck concept forms a second difference. Opposed to the plate-like structure of the Van Brienoord bridge's deck, the deck of the Ozman Gazi bridge can be classified as a box girder that simultaneously functions as the main bridge girder (see figure 8.1). The crossbeams are therefore covered by steel plates on all sides and connect the top of the box to its bottom. The full height of the girder may thus be used for longitudinal load transfer, which is likely to make the deck much stiffer in longitudinal direction than the plate deck of the Van Brienenoord.

These two factors could decrease the optimality of the design concept when it is applied on the Van Brienenoord bridge. For a truly optimal design concept, the topology optimization should be repeated for the new deck design. As this would require a supercomputer, this is not possible for this thesis.

Still, the more direct transfer of loads of the curved crossbeams could also be beneficial in plate decks. The changed length to width ratio is furthermore not expected to cause a completely different optimal design. A change of number and shape of the crossbeams may then be more likely, but could be captured by the parametric optimization.

---

[1]measured on the inside of the main girders

17.2. Design

Figure 17.1 shows the new parametric finite element model in which the altered design can be seen. The crossbeams curve directly towards the supports (following a circular trajectory), therefore making the use of main girders redundant. Meanwhile, the length of some of the crossbeams is significantly increased. The use of the same cross-section as in the Van Brienenoord design would therefore greatly decrease the stiffness of the deck. On the other hand, the enlargement of all crossbeams equally would cause a significant overuse of material. Thus, the height of the web and width of the flanges are therefore enlarged by the same factor as the increase of their length. The choice for the width and height of the cross-section means that its stiffness is increased by the factor to the power three, which would counteract the effect of the larger length on the crossbeam stiffness when it would be seen as a simply supported beam subjected to a point load.
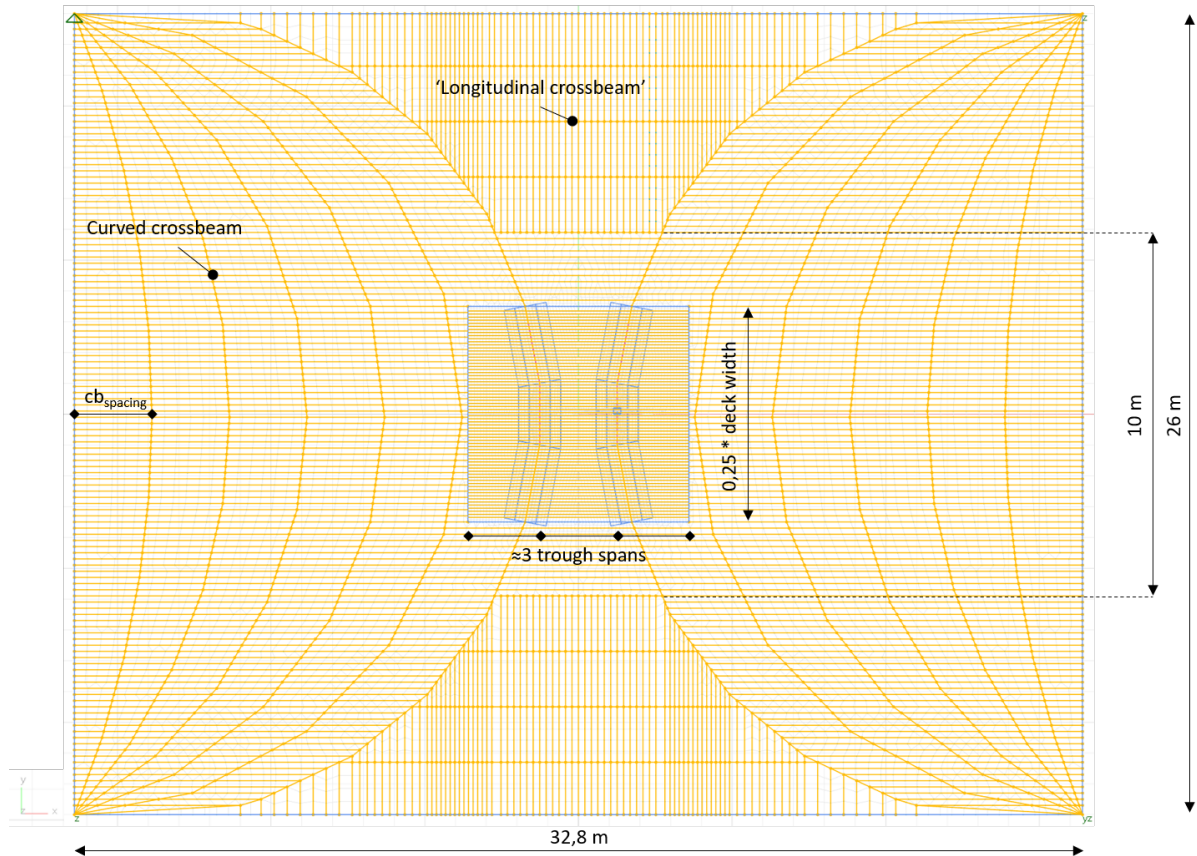

Figure 17.1: Top view of the finite element model made for the new deck design. The curved and longitudinal crossbeams are indicated. The restricted translations are labeled at the corners of the model.

Initially, it was tried to use the original cross-section of the Van Brienenoord bridge's crossbeams for all crossbeams in the new design. This, however, proved very detrimental for the fatigue performance of the deck. This is caused by the strongly increased influence length for the stresses at the fatigue details due to the lower stiffness of the crossbeams (see figure 17.2). Although the stresses there at itself do not increase tremendously, the increased influence length means that the various axle loads reinforce each other strongly. The resulting maximum stress reversal at the fatigue detail is therefore significantly enlarged.

17.2.1. Deck edges

The longitudinal orientation of the troughs in the middle of the deck is kept intact. At the edges of the deck, however, this would mean that the span of the troughs would increase tremendously. A traditionally sized stiffener is not able to span this distance. It was therefore decided to rotate the troughs 90 degrees in this area and add five 'longitudinal crossbeams' that span between the largest
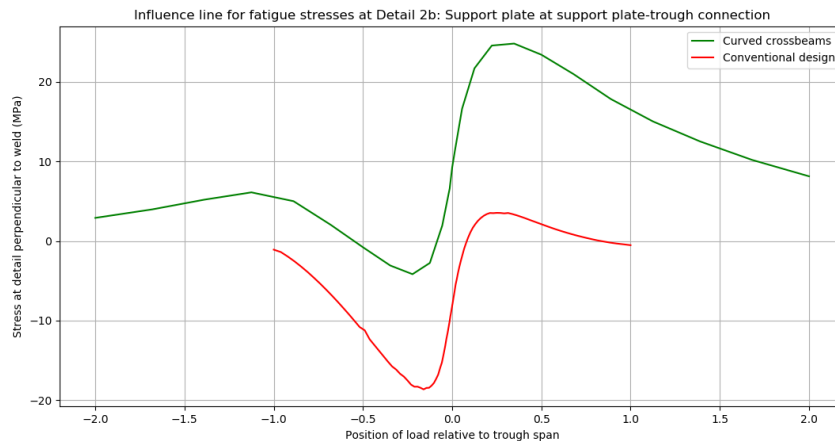
Figure 17.2: Comparison between the influence line for the fatigue stresses at detail 2b (the support plate at the trough-support plate connection) found for the conventional and new design with equal crossbeam cross-sections. Where the stresses in the conventional design are almost zero when the load is placed one trough span away, the stresses in the new design are still significant.

curved crossbeams on each side, starting five meters from the middle of the deck. These are given the the original cross-section from the Van Brienenoord bridge (see table 9.1). The dimensions of the troughs are determined by the design variables that apply to the regular troughs.

It can be seen in figure 17.1 that the troughs at the outskirts of the discussed area are not spaced equally to the regular troughs. This is caused by the decision to 'bend' the regular longitudinal troughs that reach the curved crossbeam and continue these to the edge of the deck. The creation of very small beam elements, which would lead to an ill-conditioned stiffness matrix, is prevented this way. The influence of the incorrect spacing on the considered results is expected to be small.

Some of the choices mentioned above are rather arbitrary. This is considered inevitable, as an innovative design is studied in a limited amount of time. The presented design is only a rough possibility and the precise implementation of this area is left for later studies.

17.3. Changes in optimization setup

The setup of the parametric optimization is kept intact as much as possible to reduce the time necessary for adaptations. This means that the considered fatigue details, detail categories, the artificial bee colony algorithm, and penalty function from chapter 10 apply to the new situation as well. The design variables and their constraints (table 10.1) are mostly copied as well. Only the crossbeam center-to-center distance is converted to the number of crossbeams in the considered bridge segment, as a non-repeatable or asymmetric placement of the curved crossbeams would be an illogical choice for the new design. Six to eighteen crossbeams are allowed to be placed in the deck by the algorithm, which comes down to a spacing in the middle of the deck between 1929 and 6560 mm. This is approximately equal to the allowed range in the previous parametric optimization. Uneven numbers of crossbeams are not used, as these do not accommodate a symmetric placement of the crossbeams.

Naturally, the expression for the mass of the deck needs to be adjusted for the new design. It was chosen to merely adjust the volume expression of the crossbeams (equation 10.4). The rotation of part of the troughs does not have a significant influence on the total mass of the deck and its expression is therefore maintained. The volume of the gaps in the support plate for the passage of the troughs is underestimated by holding on to the original expression, as the troughs cross the crossbeams at an angle in the new design. Given the fact that the volume of the gaps was already small in the original design, the difference is thought to be negligible.

The mass of the longitudinal crossbeams is not included in the objective function, but added manually after the optimization. The next section will show that this does not affect the results.

The new formula for the calculation of the normalized crossbeam volume is then given by:

$$ctc_{cb} = \frac{l_{cb}}{n_{cb} - 1} \tag{17.1}$$

$$r_{cb,arc}(d) = d + \frac{\frac{1}{4}w_{deck}^2 - d^2}{2d} \tag{17.2}$$

$$l_{cb,total} = w_{deck} + 2 * \sum_{i=1}^{\frac{1}{2}n_{cb}-1} r_{cb,arc}(d = i * ctc_{cb}) * \arccos\left(\frac{\frac{1}{4}w^2 - (i * ctc_{cb})^2}{\frac{1}{4}w^2 + (i * ctc_{cb})^2}\right) \tag{17.3}$$

$$V_{cb+sp} = \left(h_{sp} * t_{sp} + h_{cb,w} * t_{cb,w} + w_{cb,tf} * t_{cb,tf} + w_{cb,bf} * t_{cb,bf}\right) * \frac{l_{cb,total}}{w_{deck} * l_{deck}} \tag{17.4}$$

Where:

$r_{cb,arc}$ = the radius of the curved crossbeam

d = the horizontal distance between the supports and the crossbeam 'top'

w_{deck} = the width of the deck segment

l_{deck} = the length of the deck segment

$l_{cb,total}$ = the total length of the curved crossbeams.

n_{cb} = the number of curved crossbeams in the deck segment (including both on the edges).

The remaining symbols can be found in table 10.1. In the total length of the crossbeams, only one of the two crossbeams on the edges is considered. The other is attributed to the next bridge segment.

17.3.1. Finite element model
Figure 17.1 already showed that the three detail levels of modeling have remained. These use the same principles as chapter 11 described; meaning level 1 uses beam elements for the troughs and crossbeams, level 2 models everything in plate elements, and level 3 adds a finer mesh, trough roundings and thicker weld elements to this. The figure also revealed that the dimensions of these areas are mostly equal to those presented before. The level 2 area was only minimally shortened to prevent ill-shaped elements at its connection to the neighboring crossbeams.

The level 3 detail area was kept in the same location, meaning that the fatigue checks will be performed again at a trough located in the middle of the deck. It is acknowledged that it is uncertain if this is location is governing for the new design. Moreover, the larger trough spans and sharp crossing angles present at other locations would even suggest that this is unlikely to be the case.

However, determining the governing location and modifying the parametric model would require a significant amount of time, which was not available during this research. Furthermore, a precise determination of the fatigue lifetime of the deck is not intended in the evaluation of the new design, but rather a rough estimate of its potential. It is believed that a fatigue check in the middle of the deck is sufficient for this. Mitigating measures in problematic areas could then be investigated in further studies.

17.3.2. Loading
The altered design changes the load path and thus makes it likely that the position of the stress peak is shifted. A study similar to that presented in appendix C was therefore conducted. A model generated with the parameters from the best result of the parametric optimization was used for this. The resulting locations are summarized in table 17.1.

The table shows that the shift of the governing load positions is mostly relatively minor. Notable is that the stress peak at detail 1 is now obtained by placing the load above the trough leg instead of the trough middle. Besides, the most influential position of detail 2b now occurs at the other side of the crossbeam. This comes together with a change of the location of the stress, which now occurs at the top of the element. Both of these are on the inside of the curvature, present on the right of figure 17.1

Fatigue detail	Center position	Wheel type	Position
Detail 1	Above trough leg	A/B/C	0,00
Detail 2a	Above trough leg	A/C	-0,28
	Above trough leg	B	-0,28
Detail 2b	Above trough leg	A/C	+0,20
	Above trough leg	B	+0,28
Detail 3	Middle of trough	A/C	-0,16
	Middle of trough	B	-0,16

Table 17.1: Position of load relative to trough span causing the largest stress at each fatigue detail. A negative value indicates a placement before the trough-crossbeam connection of interest (to the left in figure 17.1), while a positive value prescribes a placement behind this.

17.4. Optimization results

The results of the mass optimization for the new design are given in table 17.2. Also presented are the Van Brienenoord bridge design and best result of chapter 14 as a reference. The normalized mass of the main girders was added to the earlier calculated mass of the deck itself to make a fair comparison with the new design. This can be calculated using the values of table 9.1 and comes down to an extra 98,9 kg/m^2. The mass of the longitudinal crossbeams was added to the calculated mass of the new designs and has a value of 17,7 kg/m^2.

run	t_d	ctc_{cb}	t_{sp}	h_{stiff}	a_{stiff}	b_{stiff}	t_{stiff}	mass (kg/m^2)
VBB PD	24	3645	16	325	300	105	8	438
Par. opt.	12	3500	13	175	125	110	8	379
1	17	2520	20	240	175	165	6	425
2	12	2520	17	295	110	110	5	416
3	20	2520	20	215	210	170	7	442

Table 17.2: Results from the optimizations of the new design featuring curved crossbeams. All values except mass are in mm. The Van Brienenoord design and best result of the parametric optimization are added as a reference. The normalized mass of the main girders are added to their mass to make a fair comparison. The number of crossbeams that resulted from the new design's optimization (14 in all cases) was converted to center-to center distance for better comparison.

The table shows that the new design cannot compete with the optimized form of the traditional orthotropic deck. The best performing new design has a mass that is 37 kg/m^2 (9,8 percent) higher than the 379 kg/m^2 that was found earlier. With 416 kg/m^2, the optimized form with curved crossbeams is still lighter than the Van Brienenoord design (438 kg/m^2).

The most important trends that were found in chapter 14 are again visible in the new design's leading result. The result features much narrower and more rectangular troughs, while the thickness of the deck plate has significantly decreased.

On the other hand, the new design significantly differs at other aspects. This is foremost visible in the strongly decreased crossbeam center-to-center distance and increased support plate thickness. The maximum number of crossbeams is used in the results of all three runs, reaching the minimum allowed crossbeam spacing. This even enabled the trough thickness to reach 5 mm in the second run. Both of these preferences were not observed in the previous optimizations.

An inspection of the complete set of design variants that were analyzed during the optimization reveals why these preferences are present: the performance of detail 2b, located in the support plate at the connection to the trough. Fatigue damages at this detail is present in almost all options and exceed the constraint for the majority of variants. The damages in no other detail show this trend, including those from the optimizations of chapter 14.

The poor performance of the support plate-trough connection causes all effort of the algorithm to be put into the search for alternatives that compensate this behavior. As a result, it was seen that the center-to-center distance of the crossbeams is strongly decreased, while the support plate thickness is significantly increased. The former reduces the rotation of the troughs and thus the bending moment at the support plate, while the latter increases the resistance of the detail to this bending.

The most obvious reason for the different behavior of this detail compared to its role in the conventional orthotropic deck lies in the changed stiffness of the crossbeams in- and out-of-plane. The lowered in-plane stiffness, which is explained in the next section, results in a larger rotations in the troughs. Meanwhile, the curved crossbeam, with the curved top flange in particular, stiffens the support plate at its bottom much stronger out-of-plane, hindering the mentioned trough rotation. These combined could lead to large bending moments in the support plate, giving large stresses at the problematic joint.

17.5. General structural behavior

The intention behind the curved crossbeams was to enable more direct load transfer towards the supports. Due to the differences with the box girder deck for which the design was originally obtained, it is not guaranteed that this is achieved within a plate girder deck as used in this thesis. The effect of the curved crossbeams on the overall stiffness of and force transfer within the new deck is discussed here.

17.5.1. Stiffness

The reaction of the deck on a uniformly distributed load is used to evaluate its general stiffness properties. Figure 17.3 shows a contour plot of the downwards displacement in reaction to a uniformly distributed load of 1 kN/m^2 applied to the complete deck plate. The maximum displacement in this situation was 15,8 mm. For comparison: the optimized conventional design resulting from chapter 14 had a deflection of only 6,0 mm in the same situation.
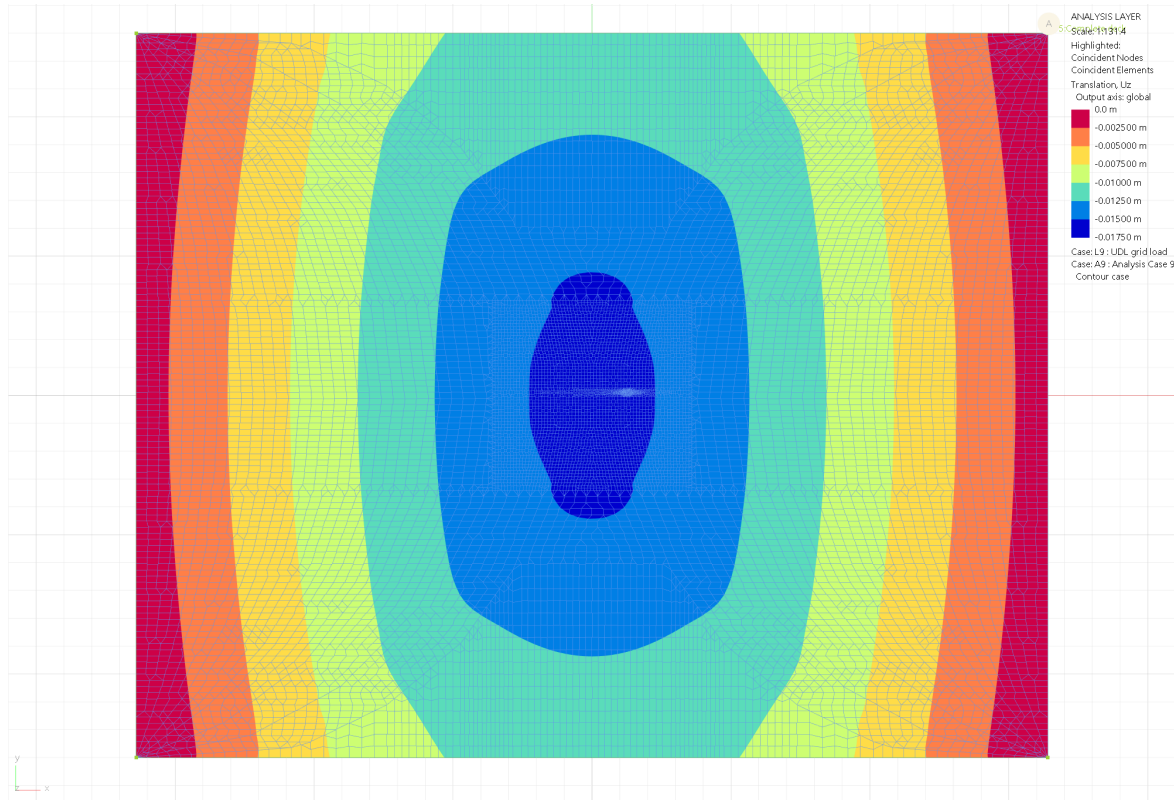

Figure 17.3: A contour plot of the displacement in global z-direction for the curved crossbeam design when loaded by a uniformly distributed load of 1 kN/m^2.

The contour plot in the figure displays that the deck structure mostly inclines from the left and right sides in the figure towards the middle. Combined with the relatively large displacements, this suggest that the stiffness in global x-direction is insufficient in the new design. The connection between the two largest curved crossbeams provided by the longitudinal crossbeams appears to be inadequate to support load transfer between them. Rotational rigidity at the supporting points is hardly added by the remaining crossbeams, even when adjacent bridge sections were modeled as well. This led to only a minimal reduction of the maximum vertical displacement.

Figure 17.4 further illustrates the rotation around the supports. It can be seen that the crossbeams rotate relatively freely, which gives large deformations in the middle of the bridge deck.
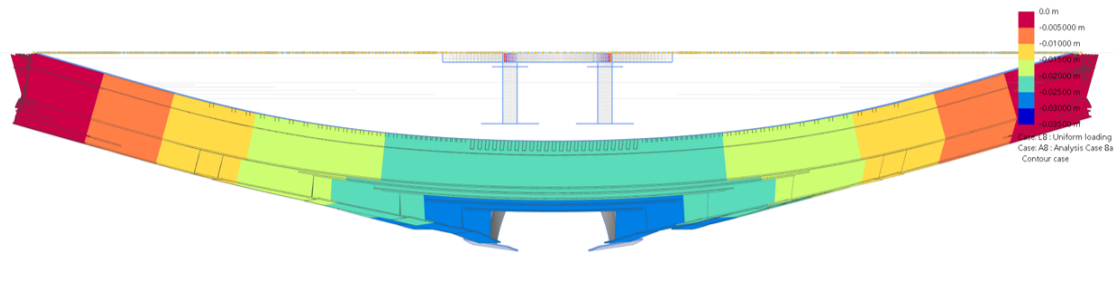

0

Figure 17.4: Side view of the deformed deck. The rotation of the crossbeams around the supports can be clearly seen. Deformations are exaggerated 120 times.

17.5.2. Force transfer

The left-right inclination and reliance on the longitudinal crossbeams for the bending moment resistance in x-direction is also clear from the moment distribution in figure 17.5. The plot in the figure shows large bending moments in the longitudinal and most inner curved crossbeams. The other curved crossbeams, on the other hand, appear to be much less loaded and experience smaller bending moments. Similar plots of the shear force distribution further reinforce this conjecture. Large shear forces are present in the inner curved crossbeams near the supports and at the ends of the shortest longitudinal crossbeams.
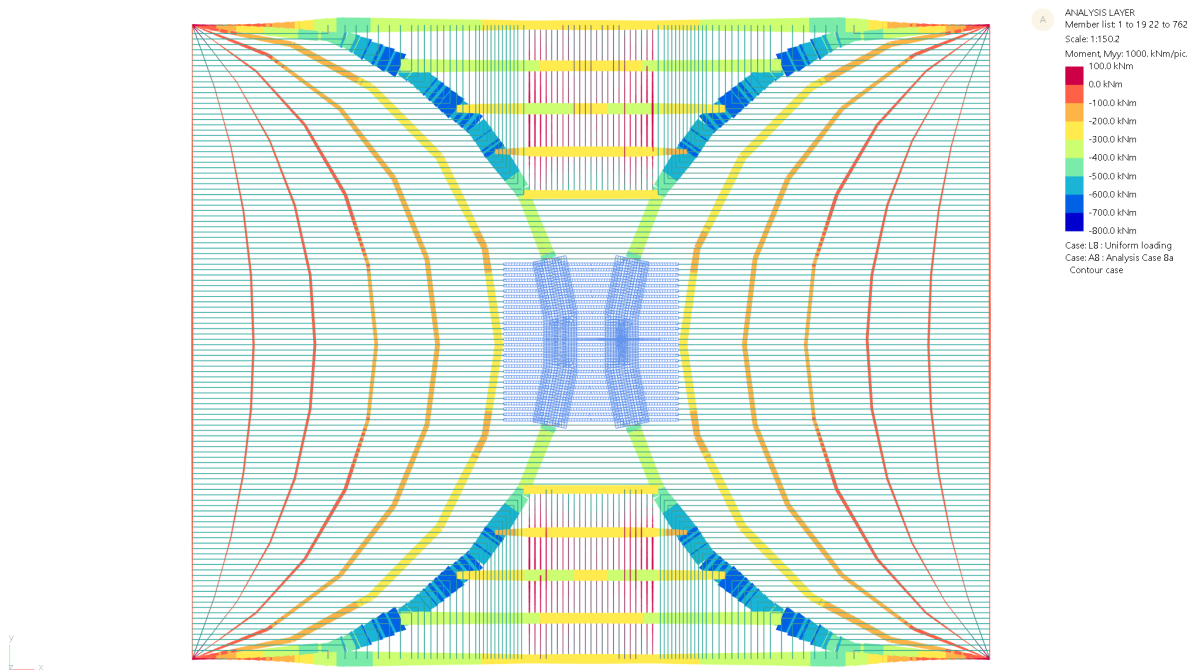

Figure 17.5: The bending moment distribution in the model's beam elements when the complete deck is loaded by a 1 kN/m^2 uniformly distributed load. The great burden that is put on the longest curved crossbeams and the longitudinal crossbeams is clearly visible.

17.5.3. Discussion

The short studies of the displacement of and force transfer within the deck both suggest that the intended flow of forces via the curved crossbeams directly to the supports is only partially achieved. The curved crossbeams do not directly connect the supports on the left and right side to each other. Therefore, they tend to rotate around the axis running through their supports. This can be prevented by the longitudinal crossbeams, troughs, deck plate, rotational stiffness at the supports, or a combination of

these. The longitudinal crossbeams appear to be leading in the current setup, but their effort is not sufficient to give the new deck design a stiffness that comes close to that of the conventional orthotropic deck concept.

Any effort for improvement of the new design should primarily aim to address the above issue. An obvious solution would be to increase the bending stiffness of the longitudinal crossbeams to enhance the rigidity of the connection between the two deck parts. This would, however, require a significant amount of extra material, while the normalized mass of the deck structure is already non-competitive to the conventional structural concept.

A more promising alternative could therefore be the increase of rotational stiffness at the supports. After all, the connection between the left and right supports would be unnecessary when the curved crossbeams are fixed at their ends. A quick check revealed that this would reduce the experienced deflection for the uniformly loaded deck to only 8,1 mm, which is just over half of the deflection for the simply supported case.

However, this gain in stiffness is not translated into lighter possible deck designs. An optimization as presented in section 17.4 was made again, but now with fixed supports. The lightest design variant that resulted from this had a mass that was higher than found for the simply supported case: 448 kg/m^2 against 442 kg/m^2.

Besides, it may be questioned whether this situation is interesting for practical purposes. The long-spanning bridges in which this type of steel deck is often used generally supports the deck using cables that, obviously, do not provide significant rotational resistance. Integral placement of the deck within other load-carrying structures (e.g. trusses) could give more fixation, but would likely also result in unwanted bending moments in elements therein. Moreover, their firmness must be considerable; the stiffness coming from adjacent bridge section already proved to be inadequate for this. It is then unlikely that truss members, mainly designed to take normal forces, can provide this rigidity.

Given the inability of the major structural components to connect the left and right side supports, it is also unlikely that the troughs or deck plate can achieve this with reasonable dimensions.

17.6. Conclusion

Based on the optimization results and structural behavior study in this chapter, it may be concluded that the use of curved crossbeams in orthotropic plate-like decks does not have the potential to further reduce the self-weight of the structure. The curved crossbeam alternatives resulting from the optimizations could not compete with the mass of the optimized conventional design. The best variant of the new concept had an almost ten percent higher mass, which cannot be expected to change with minor alterations to the setup or design.

Furthermore, it was shown that the overall stiffness of the new design is much lower than the conventional variant's. This difference can mainly be attributed to the rotation of the curved crossbeams around their supports, which cannot be prevented by the other structural members in the deck. Increasing their rigidity or fixation of the supports of the crossbeams would give an even heavier deck.

Here, the consequences of the different deck concept become clear. In the box girder concept, for which the curved crossbeam design was originally intended, the rotation of the crossbeams around the supports is prevented by the presence of the skin plates on the top and bottom of the girder. The significant distance separating these means that a considerable bending moment can be transferred, supporting the curved crossbeams and stiffening the deck as a whole.

Changes in the optimization method or case study are not expected to alter the above insights, as these would not remove the fundamental problem of the new design concept: the lacking stiffness of the deck in longitudinal direction. A different objective for the optimization, such as cost minimization, would bypass the intention of the new design concept and is therefore unlikely to give useful results. The curved crossbeams will lead to a large number of highly complex details that will likely increase the costs of both analysis and fabrication of the deck considerably.

IV

Conclusions and recommendations

18

Conclusions

This thesis demonstrated how structural optimization techniques can be used to improve the design of a real-world case: the Van Brienenoord bridge's new deck design. With this, it provides an example for future applications of these techniques on other complex practical design problems and gives valuable recommendations for lighter designs of orthotropic steel bridge decks.

To achieve these goals, the main research question was formulated as:

> What is an optimized topology for a steel bridge deck - as typically found within the larger bridges in the Netherlands - to minimize its weight while maintaining its fatigue service life?

The thesis was then split into two parts, with the first focusing on *parametric optimization*. Here, the orthotropic deck concept was left intact and a better ratio between the dimensions of certain structural members was sought. In the second, the focus was on *topology optimization*. The traditional orthogonal layout was no longer required and an effort was made to acquire even lighter steel bridge deck designs.

The findings of these two parts regarding the main research question can be summarized as:

1. A strongly decreased deck plate thickness, combined with the use of more, but narrower, lower, and more rectangular troughs, can provide a 17,4 percent lighter deck structure (280 instead of 339 kg/m^2) than was proposed in the Van Brienenoord bridge's preliminary design [8]. The apparent break with the general trend in orthotropic deck design (figure 18.2 and table 18.1) and the low number of influential global bridge parameters make it likely that similar changes can also give weight savings for orthotropic decks in comparably built bridges.

2. The two explored options for topology optimization considered in this thesis' second part - layout optimization using the ground structure method and the application of curved crossbeams in the deck design - could currently not assist in finding new structural concepts that would enable further weight reductions. For the ground structure method, this could change when future research would include a non-linear relation between cross-sectional area and resistance. Further studies of the curved crossbeam design, on the other hand, are unlikely to alter this conclusion for deck types other than the original box girder deck.

The remainder of this chapter discusses the conclusions from the parts more thoroughly in separate sections. This includes the answers to the subquestions that were given in the introduction. Recommendations for future research are given in the next chapter.

18.1. Part 1: Parametric optimization

In the first part of this thesis, a workflow was set up that enabled the parametric optimization of OSDs. An existing mathematical optimization solver (the artificial bee colony algorithm) was taken and coupled to a procedure that could evaluate the performance of a design. The artificial bee colony was discussed in section 6.2.3 and not changed in this thesis. The workflow for the evaluation of the OSD designs is summarized in figure 18.1.
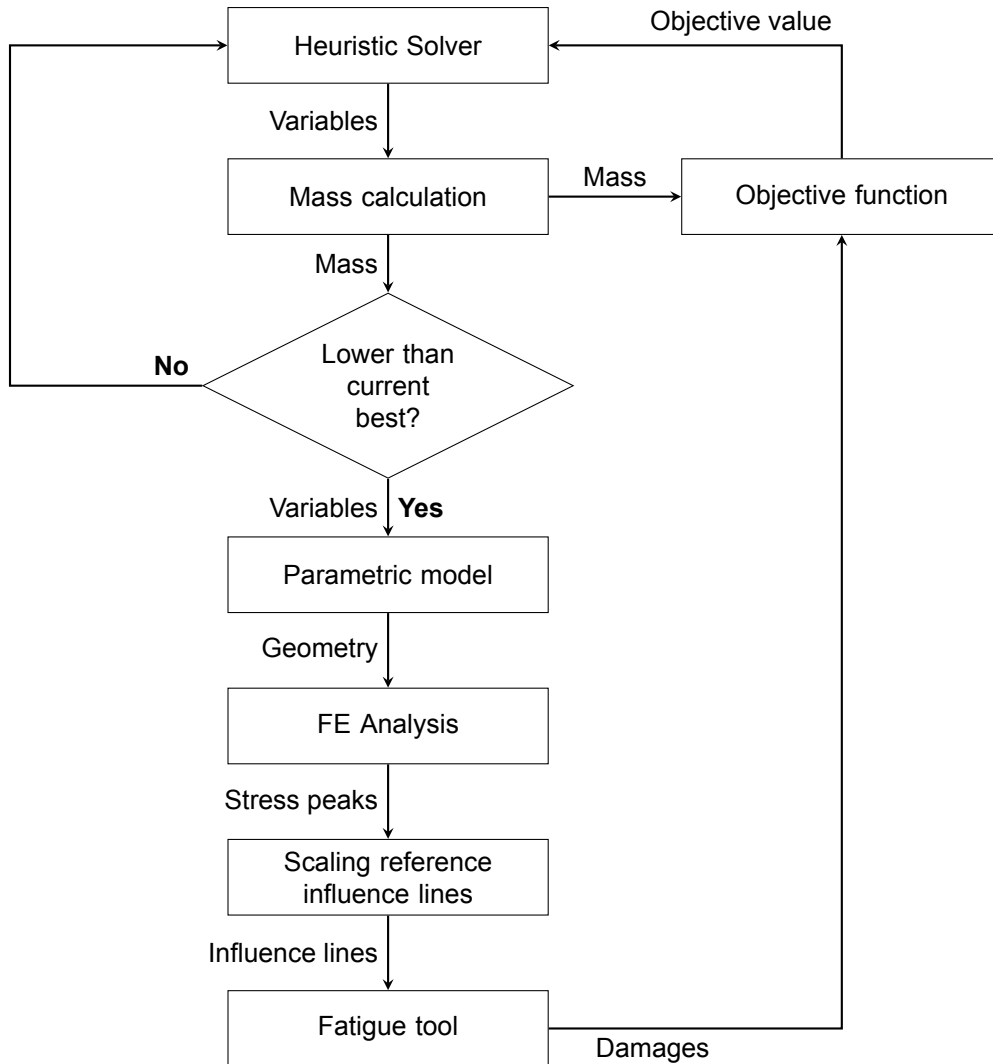

Figure 18.1: A visualization of the workflow that is used during the optimization to determine the performance of a generated design variant. The blocks describe certain processes, while the arrows indicate information that is shared between these. This figure is a copy of figure 13.1

As the figure shows, the process started with the optimization solver generating a set of seven variables that represented a collection of structural dimensions. These were then used by a Python script to create a finite element model in GSA (Arup's in-house FE-program) from which the stresses at four selected fatigue details for seven governing load cases were taken. The calculated stress peaks were utilized to scale a series of predetermined reference influence lines to obtain an estimation of the true influence line for that design variant. The estimated influence lines formed the input to a Python script (the fatigue tool) that translated these into expected fatigue damages for each detail. These damages were finally returned to the optimization solver, which used them to evaluate the performance of the respective design variant. Based on this information, the solver then continued its search for improved designs.

18.1.1. Heuristic solver

After a literature study and analysis of the optimization problem, it was chosen to only consider heuristic algorithms for the implementation of this solver. Their independence of gradients was decisive therein, as this makes them easy to integrate into the desired workflow and better suited to tackle the (proven) non-convex optimization problem.

Besides, the application of heuristics proved to give an answer to the **first two subquestions**:

- The evaluation of damage constraints can be included in the workflow by integration of a Python script that converts the full influence line of the stress at a detail into the fatigue damage. The extra time needed for this is small compared to the total time necessary for the finite element calculation. The heuristic's independence of gradients makes it untroubled by the non-linearity and discontinuity of the damage constraints.

- It was shown that a swarm-based heuristic, the artificial bee colony algorithm in this case, is capable of generating a set of optimized design alternatives parallel to the lightest solution. These alternatives significantly differ from the best variant, but can have competing mass and are generated without any extra computational effort.

The second point above mentions the chosen heuristic method: the artificial bee colony algorithm. This algorithm, inspired by the foraging behavior of honey bees, was again chosen after a literature study. Next to the successful generation of design variants, some other conclusions may be drawn from its performance as well:

- The algorithms *elitism* property, meaning that new variants are only remembered when they perform better than the currently remembered variant, can cut the run time required for the optimization significantly. Here, time savings of around 40 percent were observed.

- Despite the lack of gradients and high sensitivity of fatigue damage, the algorithm is capable of closely approaching the set constraints. In most analyses, the damage computed for the optimized variant was within five percent of at least one constraint.

18.1.2. Modeling simplifications

As was already stated in the introduction, a fully detailed finite element calculation is not feasible to perform more than a thousand times during the optimization. The **third subquestion** was aimed to tackle this problem. The answer to this question could be summarized as:

- The size of the finite element model can be effectively reduced by using different levels of detail, while the number of load cases can be limited by scaling known influence lines using governing load positions. Combining these, the time required for the analysis of the model remained manageable without significantly compromising its accuracy.

Besides these major tactics, some other conclusions can add to the answer for this subquestion:

- No satisfying simplifications for the implementation of the asphalt layer were found in literature. Fully modeling the layer with volume elements was also undesirable, as it would significantly increase the size of the FE model and experienced problems within the used finite element program. A conservative approach was therefore taken, assuming a 35° load dispersal through the asphalt layer. This deviates from the 45° spread currently prescribed by the Eurocode [4], which can be non-conservative at higher asphalt temperatures.

- To obtain feasible designs with reasonable dimensions and mass, it is necessary to model the welds with locally thicker elements. This moves the points of stress extraction away from the plate element intersections, reducing the eventual computed hot spot stress. Optimizations that did not include the weld modeling could not find any viable designs.

- Disregarding the lateral weaves leads to heavier decks resulting from the optimizations, but the difference is expected to be small. It was shown that the allowed exceedance of the cut-off limit is marginal due to the high number of trucks expected to cross the Van Brienenoord bridge's lifetime. Integration of the weaves would increase the allowed stress range only minimally.

18.1.3. Optimized designs

The partly random character of the heuristic algorithm causes a variance in the results of different runs. This hinders the formulation of general and definitive recommendations to answer the **fourth subquestion**, but two strong trends can still be identified:

- All optimized designs feature a much thinner deck plate than the 24 mm thick plate that was proposed in the Van Brienenoord bridge's preliminary design. The thinner deck plate is made possible by a strong decrease in the top width and spacing of the stiffeners. The best found design used a deck plate thickness of 12 mm and a trough top width of 125 mm.

- The cross-section of the optimized troughs is more rectangular than the trapezoidal cross-section used in the Van Brienenoord design. In many cases, the bottom width of the trough even approached its top width. The best result was one of these, having a bottom width of 110 mm compared to the 125 mm top width.

Eventually, this lowered the mass of the deck from 339 kg/m^2 down to 280 kg/m^2, a reduction of 17,4 percent. It must be noted that part of the reduction should be attributed to beneficial changes in recommendations for fatigue analysis. Figure 18.2 visualizes the differences between the Van Brienenoord design and optimized variant. Table 18.1 contains the full set of dimensions for both and compares them with other bridges having OSDs.

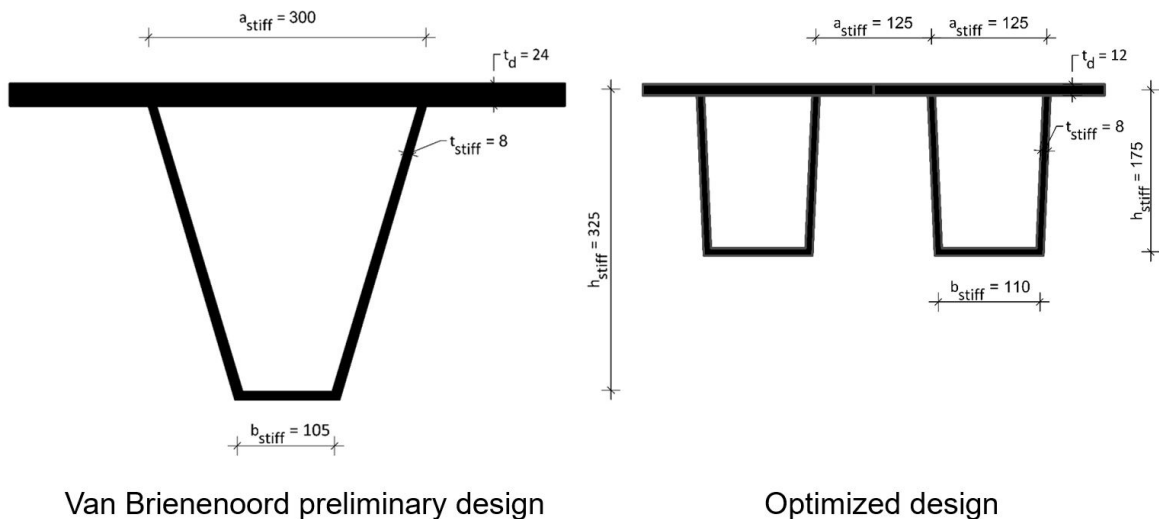Van Brienenoord preliminary design   Optimized design

Figure 18.2: Comparison of trough cross-sections used in the Van Brienenoord preliminary design and result of the parametric optimization made in this thesis. The use of a thinner deck plates and lower, narrower troughs is easily identified. This figure is a shortened copy of figure 14.3

Bridge	t_d	ctc_{cb}	t_{sp}	h_{stiff}	a_{stiff}	b_{stiff}	t_{stiff}
Ewijk	10	5000	10	350	302	105	6
1st GC	10	3333	10	250	300	110	6
2nd GC	10	3333	10	275	300	135	6
2nd VBB	12	3645	12	325	300	105	6
New SH	20	3100	12	300	300	180	7
New VBB	24	3645	16	325	300	105	8
Optimized	12	3530	13	175	125	110	8

Table 18.1: Comparison between the optimized result and the values used in the design of existing and future bridges. Bridge abbreviations: VBB = Van Brienenoord bridge, SH = Suurhoff, GC = Galecopper, Ewijk = Bridge near Ewijk. Figure 18.2 shows the definition of most of the other symbols. Other: ctc_{cb} = center-to-center distance crossbeams, t_{sp} = thickness support plate. This table is a shortened copy of table 14.15.

Although these results were obtained for the case study of the Van Brienenoord bridge, it is expected that similar optimized designs will be found for comparable bridges. Firstly, because the number of influential global bridge parameters is small. Only the width of the deck is believed to be significant for the obtained result, as it determines the span of the crossbeams. Further research should investigate its influence on the optimized results. The stiffness of the main girders had very little influence on the stresses at the fatigue details and is thus not expected to play a large role.

Secondly, because the findings break with the general trend for designing orthotropic steel decks. The 300 mm stiffener spacing (and trough top width) is most striking therein. This measure has been in use since the introduction of orthotropic decks in the 1950's (see e.g. figure 3.4) and is present in almost any bridge using an orthotropic deck (see e.g. table 18.1). When fatigue issues started to appear, it was generally decided to increase the deck plate thickness. The results in this thesis strongly suggest that decreasing the stiffener spacing and trough top width is the better option when material efficiency is considered.

The decreased stiffener spacing increases the number of welds present in the deck. A calculation based on two different sources was therefore performed to estimate the differences in costs. Depending on which source is considered, a 1,4 or 14,3 percent increase in costs was found compared to the suggested preliminary design (see tables 14.18 and 14.19). This, however, does not include potential reductions in weld troat dimensions and transport costs that could lower the price of the new design. Furthermore, the weight reductions are likely to enable lighter crossbeams, main girders, and super- and substructures to be used and can therefore still result in a cheaper design.

In future studies, it may be interesting to include the costs directly in the objective function. This may give designs that are better applicable in practice, where the price of a design is often governing. When costs are minimized, it is likely that the mass of the weld between the deck plate and stiffeners will be decreased, as it forms the largest component in the costs of the optimized design. This could lead to an increased stiffener spacing and thus result in a design that lies between the traditional design and the optimized design that was presented here. The result of the second optimization in chapter 14, however, showed that the low stiffener spacing combined with a small stiffener thickness could also give designs that are cheaper and lighter than the traditional one.

18.2. Part 2: Topology optimization

The second part of this thesis explored two leads that could improve the design of steel plate decks even further: a topology optimization by application of the ground structure method and the use of curved crossbeams for more direct load transfer to the supports. The resulting designs would remain a stiffened steel plate, but the orientation and size of stiffeners could vary.

18.2.1. Ground structure method

A topology optimization following the method of Bolbotowski et al. [22], made possible by the (modified) script of He et al. [51], was performed to determine the optimal distribution and orientation of stiffeners in the deck structure. The objective of the optimization was again minimization of self-weight, while the constraints were formed by limits on the bending moments occurring in the stiffeners. A uniformly distributed load was applied to rectangular domain representing five bridge sections. The corner points of these sections were simply supported.

The result (figure 18.3) contains two distinctive regions. Between the supports, an orthogonal grid of longitudinal and transverse stiffeners is found. These zones are enclosed by regions where the optimal orientation of the stiffeners is arbitrary (the dense blue areas in the figure). Based on this result, the conventional orthotropic deck could be labeled as optimal. Other solutions can be thought of as well, but would not be 'more optimal', while being harder to manufacture.

Before this conclusion can be seen as definitive, however, more research is needed. The derivation of the considered method contains two assumptions of which the applicability on bridge deck is questionable. The first assumption is to neglect the torsional resistance of the stiffeners. Given that closed stiffeners are specifically chosen in orthotropic decks for their increased torsional stiffness, it is likely that this assumption affects the optimality of the result.
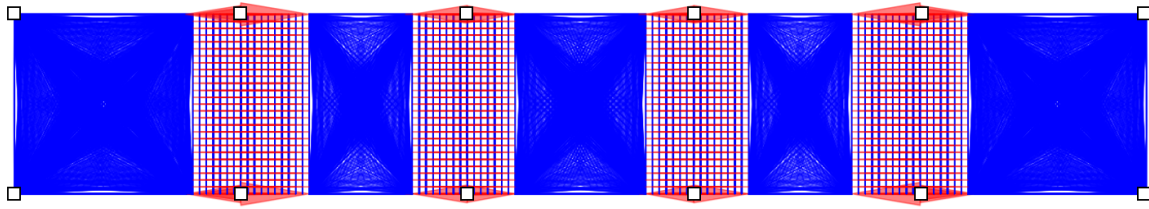
Figure 18.3: Optimal placement of stiffeners for a 165x26 m rectangular, uniformly loaded domain, corresponding to five bridge sections. Simple supports are placed at every 33 m (black outlined squares). This is a copy of figure 16.3.

Secondly, a linear relation between cross-sectional area and resistance is assumed. While this can be a valid assumption in certain cases, it prevents the formation of different order of stiffeners that are generally used in steel bridge decks. It is unlikely that the use of a single height for all members in the deck gives an optimal solution. Therefore, the conclusion of this study and answer to the **fifth subquestion** is formulated as:

- Based on a topology optimization using the ground structure method, the traditional orthogonal stiffener layout is preferred in a steel bridge deck regarding material efficiency. However, further research should implement a non-linear relation between the cross-sectional area and resistance in the method to confirm this conclusion.

The result of figure 18.3 and conclusions following from it apply, strictly speaking, only to the considered case. The support conditions of other bridge decks will, however, be very similar, while changes in dimensions or the number of considered segments did not alter the main characteristics of the result. It is therefore believed that the conclusions can be extended to steel plate girder decks in general.

Additionally, it is not expected that integration of costs into the objective function will lead to other conclusions. Various values of the joint cost, which can include the additional cost of having many smaller members in a construction and should help in simplifying the found solution, were used without observing significant changes in the result. More detailed cost optimizations would again require the mentioned non-linear relation for useful results.

Adjustments in applied loading or constraints could give significant differences in the outcome of the optimization. It may be argued that (moving) point loads combined with constraints on the experienced stress range would be better suited for an OSD and research towards the implications of this change could therefore be of interest. In this new setup, however, the uniformly loaded deck would still be a relevant load case and the result of figure 18.3 would thus likely be part of the result. Besides, the main conclusion of this substudy would still hold, as definitive conclusions would yet require the possibility for multiple orders of beams to form.

18.2.2. Curved crossbeams

Inspired by the result of Baandrup et al. [13], the straight crossbeams of the conventional design were exchanged for curved crossbeams that are directly connected to the supports. The main girders were therefore left out, while 'longitudinal crossbeams' spanned the space between the largest curved crossbeams (see figure 18.4).

The self-weight of the new design was optimized by the script developed in the first part of this thesis, again with constraints on the expected fatigue damages. This was followed by a short study of the force transfer within the new structural concept. This led to the following insights:

- The workflow developed in part 1 could be efficiently adapted to fit the new application. Only relatively minor adaptations in the parametric model were necessary, which shows the versatility of the proposed method.

- The use of curved crossbeams in a steel plate decks did not give an additional material reduction compared to the conventional optimized design. The lightest deck found had a mass of 416 kg/m^2, which is 9,8 percent higher than the 379 kg/m^2 found for the conventional design when the mass of the main girders is included.
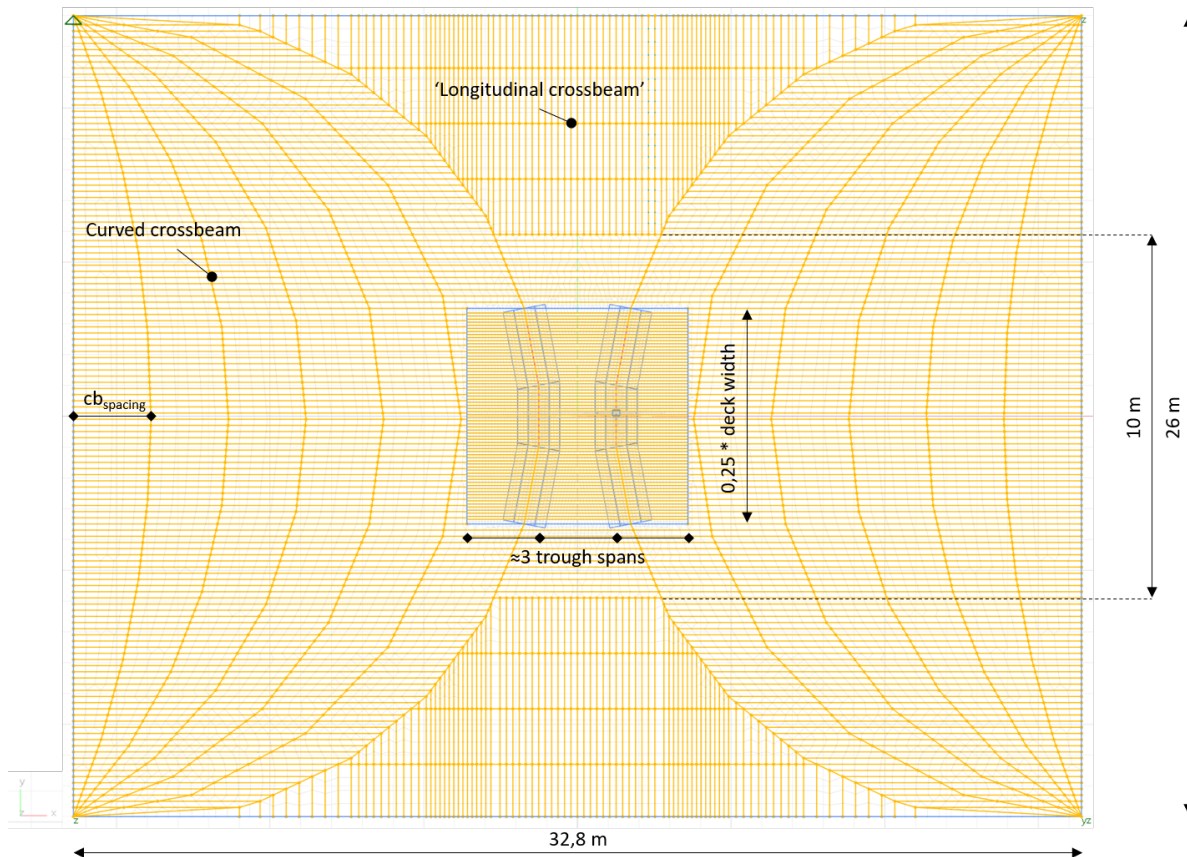
Figure 18.4: Top view of the finite element model made for the new deck design. The curved and longitudinal crossbeams are indicated. The restricted translations are labeled at the corners of the model. This figure is a copy of figure 17.1

- The overall stiffness of the deck is considerably lower than the stiffness of the conventional design concept. The curved crossbeams tend to rotate around their supports, which cannot be prevented by the other structural member in the deck. Increasing the rigidity of members in the deck or fixation of the supports was tried, but only resulted in an even heavier deck once optimized.

Changes in the optimization method or case study are not expected to alter the above insights, as these would not remove the fundamental problem of the new design concept: the lacking stiffness of the deck in longitudinal direction that causes the curved crossbeams to rotate around the supports. Any solution to this problem should be able to mimic the role of the closed cross-section present in the original application of a box girder deck.

A different objective for the optimization, such as cost minimization, would bypass the intention of the new design concept and is therefore unlikely to give useful results. The curved crossbeams will lead to a large number of highly complex details that will likely increase the costs of both analysis and fabrication of the deck considerably.

Thus, the final conclusion regarding this new design concept and answer to the **sixth subquestion** reads:

- The application of curved crossbeams on steel plate decks is not expected to enable further mass reductions than found for the conventional orthotropic concept. The translation from the original application of a box girder to a plate girder deck results in a fundamental problem in the force transfer and therefore stiffness of the structure, which is not expected to be solvable with a different optimization setup or minor changes in the deck layout. Combined with the expected difficulties in both analysis and manufacturing resulting from the complex design, any incentive for further investigations is considered to be lacking.

19

Recommendations

A set of recommendations will be given here that follows from the conclusions stated in the previous chapter. These are again split over the two parts that were considered in this thesis. Most of the recommendations consider future research, but the first part will start with a proposition for a different look on the design of orthotropic steel decks.

19.1. Part 1: Parametric optimization

Part 1 of this thesis found a 17,4 percent reduction of the deck's self-weight compared to the preliminary design for new the Van Brienenoord bridge [8]. This was achieved by halving the deck plate thickness and using a greater number of smaller stiffeners. Therefore, the suggestion towards designers of OSDs is given as:

- To increase the fatigue performance of traditional OSD designs, more closely spaced, smaller troughs should be favored over a thicker deck plate when material efficiency is of interest. The traditional stiffener spacing of 300 mm was developed based on static performance, not fatigue.

19.1.1. Verification

The limited time available for this research necessitated constraints on its scope. Two extensions of this should be made to increase the credibility of the conclusions and the recommendation given above:

- The feasibility of this thesis' best resulting design must be verified with more detailed checks. These should include loads by overtaking or in-convoy trucks, an asphalt layer modeled with 3D-elements and temperature-dependent stiffness, and the full set of fatigue details.

- The influence of global bridge parameters on the optimized result needs to be investigated. Most critical therein are the crossbeam stiffness and span (which is approximately equal to the bridge width). The main girder stiffness and span are of secondary interest.

Additionally, when the global bridge parameters would turn out to be of influence, more specific recommendations could be given for the design of future bridges. These could, for example, include guidelines for the crossbeam spacing related to the crossbeam span.

Alternatively, the dimensions determining the crossbeam stiffness could be included as variables in the optimization. This would not only reduce the workload of follow-up studies, but could also optimize the design even further.

19.1.2. Modeling simplifications

To enable the solving of the optimization problem in an acceptable amount of time, the computational size of the finite element model was significantly reduced. Two major tactics for this were the division into three modeling levels and the simplified approach to the asphalt layer's influence. For both, no satisfying guidelines or examples were found in literature. Therefore:

- Research needs to be done towards a proper simplified approach to include the effects of the asphalt layer in the finite element model. Essential therein is that the new approach accounts for the slip between the asphalt layers and the deck plate, as the assumption for a rigid connection would give unconservative results.

- Guidelines for the structural analysis of orthotropic steel decks should consider including recommendations for partial modeling of OSDs with beam elements. The results in this thesis have shown that this can generally be done conservatively and with little loss of accuracy. Further studies are necessary to provide improved justification of the detail levels' dimensions and investigate the influence of different deck designs.

Apart from the benefits these studies would have for optimizations as performed here, the results would also be useful for the conventional design process of OSDs. Derived recommendations would decrease the time required for FE analyses, making quicker manual checks possible as well.

19.1.3. Integration of costs
The optimization in this research has focused solely on finding the lightest possible design within the selected fatigue constraints. Minimization of self-weight has many advantages, such as the independence of price fluctuations and the largest expected savings in the superstructure. Furthermore, as mentioned in the introduction, it is often critical in the refurbishment or renovation of existing infrastructure.

In other situations, the minimization of costs may be of equal importance. The current tool could be used for this with a relatively small addition:

- An expression for the price of an OSD based on its general dimensions could extend the use of the current tool by enabling cost optimization. A future study could then include the non-material expenditures in the recommendations for future designs.

19.2. Part 2: Topology optimization
The exploration of the two topology optimization possibilities did not lead to further optimized designs. The first option, the ground structure method, still has potential to be useful in the future. For the second option, regarding the use of curved crossbeams in orthotropic plate decks, this is not the case. The recommendations for the further use of these methods are therefore formulated as:

- Future studies should try to include a non-linear relation between the cross-sectional area and resistance in the formulation of the ground structure method as proposed in Bolbotowski et al. [22]. This would enable the formation of different orders of plate stiffeners and could therefore increase the applicability on OSD design and similar practical design problems.

- The use of curved crossbeams, as found in Baandrup et al. [13], should not be extended to bridges with orthotropic plate girder decks. The differences with the box girder deck, for which the concept was developed, proved to be too detrimental for the stiffness and optimized mass of the new concept.

Bibliography

[1] NEN-EN 1993-2 + C1 - Eurocode 3: Design of steel structures - Part 2: Steel bridges, 2011.

[2] NEN-EN 1993-2 + C1 / NB - Eurocode 3: Design of steel structures - Part 2: Steel bridges, 2011.

[3] NEN-EN 1993-1-9 + C2 - Eurocode 3: Design of steel structures - Part 1-9: Fatigue, 2012.

[4] NEN-EN 1991-2 + C1 - Eurocode 1: Actions on structures - Part 2: Traffic loads on bridges, 2015.

[5] NEN-EN 1991-2 + C1 / NB - National Annex to NEN-EN 1991-2+C1: Eurocode 1: Actions on structures - Part 2: Traffic loads on bridges, 2019.

[6] AISC. *Design Manual for Orthotropic Steel Plate Deck Bridges*. 1963.

[7] Ryan Alberdi and Kapil Khandelwal. Comparison of robustness of metaheuristic algorithms for steel frame optimization. *Engineering Structures*, 102:40–60, 2015. ISSN 1873-7323. doi: 10.1016/j.engstruct.2015.08.012. URL http://dx.doi.org/10.1016/j.engstruct.2015.08.012.

[8] Arup. Van Brienenoordbrug West Arch Renovation: Appendix F; VO Deck Design, 2020.

[9] Arup. Oasys GSA - Theory, 2021. URL https://www.oasys-software.com/products/structural/gsa/.

[10] Mads Baandrup. *Innovative Design of Steel Girders in Cable-Supported Bridges By application of numerical optimization methods*. PhD thesis, Technical University of Denmark, 2019.

[11] Mads Baandrup, Peter Noe Poulsen, John Forbes Olesen, and Henrik Polk. Parametric Optimization of Orthotropic Girders in a Cable-Supported Bridge. *Journal of Bridge Engineering*, 24 (12):1–12, 2019. ISSN 10840702. doi: 10.1061/(ASCE)BE.1943-5592.0001499.

[12] Mads Baandrup, Peter Noe Poulsen, John Forbes Olesen, and Henrik Polk. Optimization of Truss Girders in Cable-Supported Bridges Including Stability. *Journal of Bridge Engineering*, 25 (11):04020099, 2020. ISSN 1084-0702. doi: 10.1061/(asce)be.1943-5592.0001632.

[13] Mads Baandrup, Ole Sigmund, Henrik Polk, and Niels Aage. Closing the gap towards super-long suspension bridges using computational morphogenesis. *Nature Communications*, 11(1): 1–7, 2020. ISSN 20411723. doi: 10.1038/s41467-020-16599-6. URL http://dx.doi.org/10.1038/s41467-020-16599-6.

[14] Claude Bathias and André Pineau. *Fatigue of Materials and Structures: Application to Design and Damage*. John Wiley & Sons, 2011. ISBN 9781118616512.

[15] R C Battista and M S Pfeil. Strengthening fatigue-cracked steel bridge decks. *Bridge Engineering*, 157(BE2):93–102, 2004.

[16] Lauren L. Beghini, Alessandro Beghini, Neil Katz, William F. Baker, and Glaucio H. Paulino. Connecting architecture and engineering through structural topology optimization. *Engineering Structures*, 59:716–726, 2014. ISSN 01410296. doi: 10.1016/j.engstruct.2013.10.032. URL http://dx.doi.org/10.1016/j.engstruct.2013.10.032.

[17] P Beld. Improvements for the prediction of the fatigue life of the deck plate in orthotropic steel decks, 2019. URL https://repository.tudelft.nl/islandora/object/uuid%3A8cb3eec9-0cce-469f-96e4-eada8df1d5f1?collection=education.

[18] Martin Philip Bendsoe and Noboru Kikuchi. Generating optimal topologies in structural design using a homogenization method. *Computer Methods in Applied Mechanics and Engineering*, 71: 197–224, 1988.

[19] Martin Philip Bendsoe and Ole Sigmund. *Topology Optimization: Theory, Methods and Applications*. Springer, Berlin, 2003. ISBN 3-540-42992-1.

[20] Lazlo Bleker. Hybrid truss layout optimization for generating multiple design alternatives, 2021. URL `https://repository.tudelft.nl/islandora/object/uuid%3A0aace575-f756-4a8b-8cfa-46f788b5a1c3?collection=education`.

[21] Klaus Block. The Interactive Method—Reliable and Reproducible S-N-Curves for Materials. In José A F O Correia, Abílio M P De Jesus, António Augusto Fernandes, and Rui Calçada, editors, *Mechanical Fatigue of Metals*, pages 197–204, Cham, 2019. Springer International Publishing. ISBN 978-3-030-13980-3. doi: 10.1007/978-3-030-13980-3{_}26.

[22] Karol Bolbotowski, Linwei He, and Matthew Gilbert. Design of optimum grillages using layout optimization. *Structural and Multidisciplinary Optimization*, 58(3):851–868, 2018. ISSN 16151488. doi: 10.1007/s00158-018-1930-6.

[23] B. Briseghella, L. Fenu, C. Lan, E. Mazzarolo, and T. Zordan. Application of topological optimization to bridge design. *Journal of Bridge Engineering*, 18(8):790–800, 2013. ISSN 10840702. doi: 10.1061/(ASCE)BE.1943-5592.0000416.

[24] David Broek. *Elementary Engineering Fracture Mechanics*. Martinus Nijhoff Publishers, The Hague, 1982. ISBN 9789401084253. doi: 10.1007/978-94-009-4333-9. URL `http://library1.nida.ac.th/termpaper6/sd/2554/19755.pdf`.

[25] Hongyou Cao, Xudong Qian, and Yunlai Zhou. Large-scale structural optimization using meta-heuristic algorithms with elitism and a filter strategy. *Structural and Multidisciplinary Optimization*, 57(2):799–814, 2018. ISSN 16151488. doi: 10.1007/s00158-017-1784-3.

[26] Marco Cavazzuti, Andrea Baldini, Enrico Bertocchi, Dario Costi, Enrico Torricelli, and Patrizio Moruzzi. High performance automotive chassis design: A topology optimization based approach. *Structural and Multidisciplinary Optimization*, 44(1):45–56, 2011. ISSN 1615147X. doi: 10.1007/s00158-010-0578-7.

[27] Razvan Cazacu. Comparison between the Performance of GA and PSO in Structural Optimization Problems. *American Journal of Engineering Research*, 5(11):268–272, 2016.

[28] Peter W. Christensen and Anders Klarbring. *An Introduction to Structural Optimization*. Springer, 2009. ISBN 9781402086656.

[29] Robert Connor, John Fisher, Walter Gatti, Vellore Gopalaratnam, Brian Kozy, Brian Leshko, David L. McQuaid, Ronald Medlock, Dennis Mertz, Thomas Murphy, Duncan Paterson, Ove Sorensen, and John Yadlosky. *Manual for Design, Construction, and Maintenance of Orthotropic Steel Deck Bridges*. 2012.

[30] Chuang Cui, Qinghua Zhang, Hong Hao, F Asce, Jun Li, and Yizhi Bu. Influence of Asphalt Pavement Conditions on Fatigue Damage of Orthotropic Steel Decks : Parametric Analysis. *Journal of Bridge Engineering*, 23(12):1–15, 2018. doi: 10.1061/(ASCE)BE.1943-5592.0001313.

[31] H. De Backer. Orthotropic steel decks. In *Innovative Bridge Design Handbook: Construction, Rehabilitation and Maintenance*, pages 597–613. Elsevier Inc., 2016. ISBN 9780128004876. doi: 10.1016/B978-0-12-800058-8.00022-0. URL `http://dx.doi.org/10.1016/B978-0-12-800058-8.00022-0`.

[32] W. De Corte. A review of alternatives for orthotropic bridge deck panels. *Bridge Structures*, 7 (2-3):95–102, 2011. ISSN 15732487. doi: 10.3233/BRS-2011-024.

[33] W. De Corte, V. Boel, P. Helincks, and G. De Schutter. Fatigue assessment of a lightweight steel-concrete bridge deck concept. *Bridge Structures*, 12(1-2):11–19, 2016. ISSN 17448999. doi: 10.3233/BRS-160100.

[34] De Groot Zwijndrecht N.V. Brug over de Waal bij Ewijk: Lasplan. Onderhoudsarchief kaart 1-069, bundel 3449, map 3B, 1971.

[35] A. Díaz and O. Sigmund. Checkerboard patterns in layout optimization. *Structural Optimization*, 10(1):40–45, 1995. ISSN 09344373. doi: 10.1007/BF01743693.

[36] Xiaohong Ding and Koetsu Yamazaki. Adaptive growth technique of stiffener layout pattern for plate and shell structures to achieve minimum compliance. *Engineering Optimization*, 37(3): 259–276, 2005. ISSN 0305215X. doi: 10.1080/0305215512331328231.

[37] Xiaohu Dong, Xiaohong Ding, Guojie Li, and Gareth Peter Lewis. Stiffener layout optimization of plate and shell structures for buckling problem by adaptive growth method. *Structural and Multidisciplinary Optimization*, 61(1):301–318, 2020. ISSN 16151488. doi: 10.1007/s00158-019-02361-0.

[38] W.S. Dorn, R.E. Gomory, and H.J. Greenberg. Automatic Design of Optimal Structures. *Journal de Mèchanique*, (3):25–52, 1964.

[39] ECCS publication N° 105. Good design practice - a guideline for fatigue design, 2000.

[40] European Steel Design Education Programme. Structural Systems: Bridges. Lecture 15B.3: Bridge Decks. URL http://fgg-web.fgg.uni-lj.si/~/pmoze/ESDEP/master/wg15b/l0300.htm.

[41] M. Feldmann, G. Sedlacek, and A. Geßler. A system of steel-elastomer sandwich plates for strengthening orthotropic bridge decks. *Mechanics of Composite Materials*, 43(2):183–190, 2007. ISSN 01915665. doi: 10.1007/s11029-007-0018-y.

[42] Abdullah Fettahoglu. Assessment on Web Slope of Trapezoidal Rib in Orthotropic Decks Using Fem. *Journal of Engineering and Natural Sciences*, 32(1):52–59, 2014. ISSN 13047191. URL http://search.ebscohost.com/login.aspx?direct=true&db=a9h&AN=94993237&lang=es&site=ehost-live.

[43] Abdullah Fettahoglu. Optimizing rib width to height and rib spacing to deck plate thickness ratios in orthotropic decks. *Cogent Engineering*, 3(1), 2016. ISSN 23311916. doi: 10.1080/23311916.2016.1154703. URL http://dx.doi.org/10.1080/23311916.2016.1154703.

[44] P. C. Fourie and A. A. Groenwold. The particle swarm optimization algorithm in size and shape optimization. *Structural and Multidisciplinary Optimization*, 23(4):259–267, 2002. ISSN 1615147X. doi: 10.1007/s00158-002-0188-0.

[45] Matthew Gilbert and Andrew Tyas. Layout optimization of large-scale pin-jointed frames. *Engineering Computations (Swansea, Wales)*, 20(7-8):1044–1064, 2003. ISSN 02644401. doi: 10.1108/02644400310503017.

[46] Global Alliance for Buildings and Construction, International Energy Agency, and The United Nations Environment Programme. 2019 Global Status report: Towards a zero-emissions, efficient and resilient buildings and construction sector. Technical report, 2019. URL https://www.worldgbc.org/sites/default/files/UNEP188_GABC_en(web).pdf.

[47] Google Maps. Van Brienenoordbrug, 2021. URL https://www.google.com/maps/place/Van+Brienenoordbrug/@51.904524,4.534405,14.83z/data=!4m5!3m4!1s0x47c432f1df9975fd:0x1ad62782ed0e125a!8m2!3d51.9044812!4d4.5423371.

[48] Ravi Shankar Gupta. Prediction of Fatigue Crack Propagation in Orthotropic Steel Decks using XFEM based on LEFM and VCCT, 2019.

[49] Warren Hare, Julie Nutini, and Solomon Tesfamariam. Advances in Engineering Software A survey of non-gradient optimization methods in structural engineering. *Advances in Engineering Software*, 59:19–28, 2013. ISSN 0965-9978. doi: 10.1016/j.advengsoft.2013.03.001. URL `http://dx.doi.org/10.1016/j.advengsoft.2013.03.001`.

[50] L. He and M. Gilbert. Rationalization of trusses generated via layout optimization. *Structural and Multidisciplinary Optimization*, 52(4):677–694, 2015. ISSN 16151488. doi: 10.1007/s00158-015-1260-x.

[51] Linwei He, Matthew Gilbert, and Xingyi Song. A Python script for adaptive layout optimization of trusses. *Structural and Multidisciplinary Optimization*, 60(2):835–847, 2019. ISSN 16151488. doi: 10.1007/s00158-019-02226-6.

[52] A. F. Hobbacher. *Recommendations for Fatigue Design of Welded Joints and Components*. Springer, 2019. ISBN 9781855733152. doi: 10.1007/978-3-319-23757-2{_}8.

[53] Hollandia N.V. Brug over de Waal bij Ewijk. Vloersectie Merk 71A. Technical Drawing. REGnr: A65887, 1973.

[54] P.C.J. Hoogenboom. The sectio aurea of structural engineers. *Heron's fountain*, 57(1):69–72, 2012.

[55] Wei Huang, Minshan Pei, Xiaodong Liu, Chuang Yan, and Ya Wei. Nonlinear Optimization of Orthotropic Steel Deck System Based on Response Surface Methodology. *Research*, 2020: 1–22, 2020. ISSN 2639-5274. doi: 10.34133/2020/1303672.

[56] X. Huang and Y.M. Xie. *Evolutionary Topology Optimization of Continuum Structures: Methods and Applications*. Wiley, 2010. ISBN 978-0-470-74653-0.

[57] M. Ito. Super long span cable-suspended bridges in Japan. In *15th Cong. IABSE*, pages 1009–1018, 1996.

[58] F. B. P. de Jong and M. H. Kolstein. Strengthening a Bridge Deck With High Performance Concrete. In *2004 Orthotropic Bridge Conference*, pages 328–345, 2004.

[59] A Rezaee Jordehi. A review on constraint handling strategies in particle swarm optimisation. *Neural Computing and Applications*, pages 1265–1275, 2015. ISSN 0941-0643. doi: 10.1007/s00521-014-1808-5. URL `http://dx.doi.org/10.1007/s00521-014-1808-5`.

[60] A. Kallassy and J. L. Marcelin. Optimization of stiffened plates by genetic search. *Structural Optimization*, 13(2-3):134–141, 1997. ISSN 09344373. doi: 10.1007/BF01199232.

[61] Dervis Karaboga and Bahriye Basturk. An artificial bee colony (ABC) algorithm for numeric function optimization. In *Proceedings of the IEEE swarm intelligence symposium*, Indianapolis, IN, USA, 2005.

[62] Dervis Karaboga and Bahriye Basturk. A powerful and efficient algorithm for numerical function optimization: Artificial bee colony (ABC) algorithm. *Journal of Global Optimization*, 39(3):459–471, 2007. ISSN 09255001. doi: 10.1007/s10898-007-9149-x.

[63] A. Kaveh and A. Zolghadr. Comparison of nine meta-heuristic algorithms for optimal design of truss structures with frequency constraints. *Advances in Engineering Software*, 76:9–30, 2014. ISSN 18735339. doi: 10.1016/j.advengsoft.2014.05.012. URL `http://dx.doi.org/10.1016/j.advengsoft.2014.05.012`.

[64] Uri Kirsh. *Structural Optimization: Fundamentals and Applications*. Springer-Verlag, 1993. ISBN 9783540559191. doi: 10.1007/978-3-642-84845-2. URL `https://link-springer-com.ezproxy.lib.monash.edu.au/content/pdf/10.1007%2F978-3-642-84845-2.pdf`.

[65] M. H. Kolstein. Fatigue; Lectures Steel Structures Part 1, 2007.

[66] M. H. Kolstein. *Fatigue classification of welded joints in orthotropic steel bridge decks*. PhD thesis, 2007.

[67] J.S. Leendertz. *Fatigue Behaviour of Closed Stiffener to Crossbeam Connections in Orthotropic Steel Bridge Decks*. PhD thesis, TU Delft, 2008. URL `https://repository.tudelft.nl/islandora/object/uuid%3Afd2f2137-d89c-4bda-8187-cc591ffc8f07`.

[68] Ming Li, Kunitaro Hashimoto, and Kunitomo Sugiura. Influence of Asphalt Surfacing on Fatigue Evaluation of Rib-to-Deck Joints in Orthotropic Steel Bridge Decks. *Journal of Bridge Engineering*, 19(10):1–14, 2014. doi: 10.1061/(ASCE)BE.1943-5592.0000610.

[69] Lokilech. Pedalarm Bruch, 2007. URL `https://commons.wikimedia.org/w/index.php?curid=2239906`.

[70] Vijini Mallawaarachchi. Introduction to Genetic Algorithms - Including Example Code, 2017. URL `https://towardsdatascience.com/introduction-to-genetic-algorithms-including-example-code-e396e98d8bf3`.

[71] Arek Mazurek. Michell cantilever, . URL `https://en.wikipedia.org/wiki/File:MichellCantilever.jpg`.

[72] Arek Mazurek. Michell's solution for A single force F applied at C centered between supports at points A and B, . URL `https://en.wikipedia.org/wiki/File:Michell_centrally_loaded_in_half_space.jpg`.

[73] J. Corey McMillan. Fatigue Crack Propagation under Programmed and Random Loads. Technical report, Solid State Physics Laboratory, Seattle, 1966.

[74] A.G.M Michell. Limits of Economy of Material in Frame-Structures. *Philosophical Magazine*, 8 (47):589–597, 1904.

[75] Eric J. Mittemeijer. Failure by Fatigue. In *Fundamentals of Materials Science*, pages 567–573. 2010. ISBN 9783642104992. doi: 10.1201/b15858-11.

[76] Jun Murakoshi, Shi-ichi Hirano, and Hideaki Harada. Effect of Deck Plate Thickness of Orthotropic Steel Deck on Fatigue Durability. URL `https://www.pwri.go.jp/eng/ujnr/tc/g/pdf/29/29-5-4_murakoshi.pdf`.

[77] Wim Nagy, Marco Diversi, Philippe van Bogaert, and Hans De Backer. Improved Fatigue Assessment Techniques of Connecting. *Eurosteel 2014*, pages 1–8, 2014.

[78] Nederlandse Bruggenstichting. Grootste bruggen in Nederland. URL `http://www.bruggenstichting.nl/informatief/grootste-bruggen-in-nederland`.

[79] Erkki Niemi, Wolfgang Fricke, and Stephen J. Maddox. *The Structural Hot-Spot Stress Approach to Fatigue Analysis*. Springer, 2018. ISBN 9789811055676. doi: 10.1007/978-981-10-5568-3{_}2.

[80] OECD. Road traffic, vehicles and networks. *Environment at Glance 2015: OECD Indicators*, pages 66–69, 2015. doi: 10.1787/9789264235199-17-en. URL `https://doi.org/10.1787/9789264235199-17-en`.

[81] W. Pelikan. Leichtfahrbahnen. In *Deutscher Ausschuss für Stahlbau, 1908-58*, pages 117–126. Stahlbau Verlag, Köln, 1958.

[82] Cristian Perea, Julian Alcala, Victor Yepes, Fernando Gonzalez-Vidosa, and Antonio Hospitaler. Design of reinforced concrete bridge frames by heuristic optimization. *Advances in Engineering Software*, 39(8):676–688, 2008. ISSN 09659978. doi: 10.1016/j.advengsoft.2007.07.007.

[83] Nestor Perez. Fatigue Crack Growth. In *Fracture Mechanics*, pages 1–418. 2017. ISBN 9783319249995. doi: 10.1007/978-3-319-24999-5.

[84] Ruben E Perez and Kamran Behdinan. Particle Swarm Optimization in Structural Design. In *Swarm Intelligence: Focus on Ant and Swarm Optimization*. Itech Education and Publishing, Vienna, 2007. ISBN 9783902613097.

[85] André Pineau and Claude Bathias. *Fatigue of Materials and Structures Fundamentals*. John Wiley & Sons, 2010. ISBN 9781848210516.

[86] William Prager and R.T. Shield. A General Theory of Optimal Plastic Design. *Journal of Applied Mechanics*, 34(1):184–186, 1968. doi: https://doi.org/10.1115/1.3607621.

[87] Rijkswaterstaat. A16: vernieuwen Van Brienenoordbrug, . URL https://www.rijkswaterstaat.nl/wegen/projectenoverzicht/a16-renovatie-van-brienenoordbrug/index.aspx.

[88] Rijkswaterstaat. ROK 2.0 - Vermoeiing van orthotrope rijvloeren (WIP), .

[89] Rijkswaterstaat. Richtlijnen Ontwerp Kunstwerken 1.4, 2017. URL http://publicaties.minienm.nl/download-bijlage/97120/rtd1001-rok1-4-april2017.pdf.

[90] Rijkswaterstaat Directie Bruggen. Overbrugging in A'dam Rijkanaal in RW12 - 2e Nieuwe Galecopperbrug (Noord): Vloersecties 2-3-4-5-6-13-16-4'-5'-6'en 16'. Technical Drawing. REGnr: A51658.

[91] Rijkswaterstaat Directie Bruggen. Overbrugging A'dam Rijnkanaal in RW12 (Nieuwe Galecopperbrug): Dwarsdragers. Technical Drawing. REGnr: A41038, 1968.

[92] Rijkswaterstaat Directie Bruggen. Bricor RW16 Verbreding westzijde brug over de Nieuwe Maas bij Van Brienenoord: Normale Vloersecties. Technical Drawing. REGnr: A90199, 1986.

[93] A Romeijn. Steel Bridges; Dictaat deel I, 2006.

[94] Royal HaskoningDHV. Alkmaar opent grootste beweegbare verkeersbrug van composiet, 2016. URL https://www.royalhaskoningdhv.com/nl-nl/nederland/nieuws/nieuwsberichten/alkmaar-opent-grootste-beweegbare-verkeersbrug-van-composiet/358.

[95] G.I.N. Rozvany. Grillages of maximum strength and maximum stiffness. *International Journal of Mechanical Sciences*, 14(10):651–666, 1972. ISSN 00207403. doi: 10.1016/0020-7403(72)90023-9.

[96] G.I.N. Rozvany. Optimal load transmission by flexure. *Computer Methods in Applied Mechanics and Engineering*, 1(3):253–263, 1972. ISSN 00457825. doi: 10.1016/0045-7825(72)90007-2.

[97] G.I.N. Rozvany. A critical review of established methods of structural topology optimization. *Structural and Multidisciplinary Optimization*, 37(3):217–237, 2009. ISSN 1615147X. doi: 10.1007/s00158-007-0217-0.

[98] RWS West-Nederland Zuid. Tijdelijke verbinding Suurhoffbrug. DO stalen brug: Materiaalspecificatie. Technical drawing. Teknr. SHB-000158. Versie 3.0, 2020.

[99] J. Schijve. Fatigue of structures and materials in the 20th century and the state of the art. *Fiziko-Khimicheskaya Mekhanika Materialov*, 39(3):7–28, 2003. ISSN 04306252.

[100] Jaap Schijve. *Fatigue of Structures and Materials*. Springer, Dordrecht, 2009. ISBN 978-1-4020-6808-9. doi: https://doi-org.tudelft.idm.oclc.org/10.1007/978-1-4020-6808-9.

[101] L A Schmit. Structural Design by Systematic Synthesis. *Proceedings, 2nd Conference on Electronic Computation, ASCE*, pages 105–122, 1960.

[102] A. J. G. Schoofs. Structural Optimization History and State-of-the-Art. *Topics in Applied Mechanics*, pages 339–345, 1993. doi: 10.1007/978-94-011-2090-6{_}37.

[103] G. Sedlacek, M. Paschen, M. Feldman, A. Geßler, S. Möller, B. Steinauer, and K. Scharnigg. *Instandsetzung und Verstärkung von Stahlbrücken unter Berücksichtigung des Belagssystems*. Bundesanstalt für Straßenwesen, Bergisch Gladbach, 2011. ISBN 9783865098719.

[104] O. Sigmund and J. Petersson. Numerical instabilities in topology optimization: A survey on procedures dealing with checkerboards, mesh-dependencies and local minima. *Structural Optimization*, 16(1):68–75, 1998. ISSN 09344373. doi: 10.1007/BF01214002.

[105] Ole Sigmund. On the usefulness of non-gradient approaches in topology optimization. *Structural and Multidisciplinary Optimization*, 43(5):589–596, 2011. ISSN 1615147X. doi: 10.1007/s00158-011-0638-7.

[106] Ole Sigmund and Kurt Maute. Topology optimization approaches: A comparative review. *Structural and Multidisciplinary Optimization*, 48(6):1031–1055, 2013. ISSN 1615147X. doi: 10.1007/s00158-013-0978-6.

[107] Mustafa Sonmez. Performance Comparison of Metaheuristic Algorithms for the Optimal Design of Space Trusses. *Arabian Journal for Science and Engineering*, 43(10):5265–5281, 2018. ISSN 21914281. doi: 10.1007/s13369-018-3080-y. URL https://doi.org/10.1007/s13369-018-3080-y.

[108] Mathias Stolpe. Truss optimization with discrete design variables: a critical review. *Structural and Multidisciplinary Optimization*, 53(2):349–374, 2016. ISSN 16151488. doi: 10.1007/s00158-015-1333-x.

[109] Jan Swinnen. Modelling the mechanical performance of bolted deck-to-girder connections in FRP-steel hybrid bridges, 2020. URL https://repository.tudelft.nl/islandora/object/uuid%3A07a2c6fd-7bfe-46ac-b9b6-a3cd253caa72?collection=education.

[110] Hamdy A. Taha. *Operations Research: An Introduction*. Pearson, 2017. ISBN 978-1-292-16554-7.

[111] Niels van den Berg. Effects of residual stresses on the fatigue crack propagation of an orthotropic steel bridge deck, 2020. URL http://resolver.tudelft.nl/uuid:753e6f58-8dcd-431e-b20b-f32820d18ad8.

[112] Gaoxin Wang, Youliang Ding, Zhijun Liu, and Jingshu Shao. Method of Calculating Life-Cycle Fatigue Damage of Orthotropic Steel Bridge Decks under the Combined Actions of Vehicle Loads and Pavement Temperature. *Hindawi*, 2020, 2020.

[113] Qiudong Wang, Bohai Ji, Junyuan Xia, and Zhongqiu Fu. Fatigue assessment of rib-deck welds in orthotropic steel decks integrating the effect of load dispersal through asphalt surfacing. *Structures*, 28(April):1701–1712, 2020. ISSN 2352-0124. doi: 10.1016/j.istruc.2020.10.017. URL https://doi.org/10.1016/j.istruc.2020.10.017.

[114] Garth N. Wells. The finite element method: An introduction, 2009.

[115] Roman Wolchuk. Lessons from Weld Cracks in Orthotropic Decks on Three European Bridges. *Journal of Structural Engineering*, 116(1):75–84, 1990.

[116] Roman Wolchuk. Steel orthotropic decks: developments in the 1990s. *Transportation Research Record*, (1688):30–37, 1999. ISSN 03611981. doi: 10.3141/1688-04.

[117] Weijian Wu, Henk Kolstein, and M. Veljkovic. Fatigue resistance of rib-to-deck welded joint in OSDs, analyzed by fracture mechanics. *Journal of Constructional Steel Research*, 162, 2019. ISSN 0143974X. doi: 10.1016/j.jcsr.2019.105700.

[118] Y.M. Xie and G.P. Steven. Shape and layout optimization via an evolutionary procedure. In *Proceedings of the International Conference of Computational Engineering*, Hong Kong, 1992.

[119] Fei Yan, Weizhen Chen, and Zhibin Lin. Prediction of fatigue life of welded details in cable-stayed orthotropic steel deck bridges. *Engineering Structures*, 127:344–358, 2016. ISSN 18737323. doi: 10.1016/j.engstruct.2016.08.055. URL http://dx.doi.org/10.1016/j.engstruct.2016.08.055.

[120] R. J. Yang and A. I. Chahande. Automotive applications of topology optimization. *Structural Optimization*, 9(3-4):245–249, 1995. ISSN 09344373. doi: 10.1007/BF01743977.

[121] Ji Hong Zhu, Wei Hong Zhang, and Liang Xia. Topology Optimization in Aircraft and Aerospace Structures Design. *Archives of Computational Methods in Engineering*, 23(4):595–622, 2016. ISSN 18861784. doi: 10.1007/s11831-015-9151-2. URL http://dx.doi.org/10.1007/s11831-015-9151-2.

[122] Meiling Zhuang, Changqing Miao, and Rongfeng Chen. Analysis for Stress Characteristics and Structural Parameters Optimization in Orthotropic Steel Box Girders based on Fatigue Performance. *KSCE Journal of Civil Engineering*, 23:2598–2607, 2019. ISSN 19763808. doi: 10.1007/s12205-019-1618-5.

V

Appendix

A
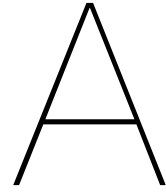
Load spread from asphalt layers

Eurocode 1 part 2 [4] prescribes to spread loads for local checks over a 45° angle through any asphalt layers that lie on top of the deck plate. However, literature [15, 30] as well as experience at Arup suggests that this spread is often not achieved. Especially at higher asphalt temperatures the load dispersal provided by the wearing course may be limited. This is also represented by the newer version of the ROK [88], which dictates that the asphalt layers should be modeled by volume elements with a temperature dependent stiffness (see section 4.3).

The use of volume elements during the intended optimization is undesirable, however. Firstly, because the implementation of 3D elements in GSA is still in development. The element type can be used, but meshing needs to be done manually. This poses a problem to the intended workflow, where structural members are defined and meshed automatically by GSA. Writing a script that generates the complete mesh of the structure is possible, but is deemed to be too time-consuming for doing this during this research.

Secondly, the addition of 3D elements to the finite element model would greatly increase its computational demand. The low thickness of an asphalt layer (70 mm) would require a small element size, while the width and length of layer would need to be large enough to properly account for the load spread. An asphalt model as used in section A.1 would double the amount of elements when added to the orthotropic deck model as presented in the chapter 11.

Therefore, an attempt is made to find a more conservative estimate for the load spread provided by the asphalt layers on top of the deck plate than is given by the current Eurocode. In a first step, the deck will be assumed as infinitely rigid, enabling a separation between the model of the deck and that of the asphalt. A connection between the two models is made in the second step, which will be used to investigate the consequences of the finite stiffness of the deck. This is done to verify the results of the first step.

It should be noted that finding an accurate, generally applicable load spread is beyond the scope of this thesis. Accordingly, only linear elastic analyses are performed, and making some simplifications is deemed to be inevitable.

A.1. Analysis 1: Rigidly supported asphalt

The first analyzed model consists of two stacked rectangular cuboids, representing the top ZOAB layer and bottom mastic asphalt layer respectively. The thickness of both layers is set to 70 mm, following the current practice in the Netherlands. The two layers are only connected in global z-direction. As mentioned in section 4.3, membranes between the layers are often present, causing cooperation between the layers to be minimal. The displacement of the bottom layer is only restricted in z-direction for the same reason.

The loading in the model has dimensions of 320 x 220 mm, following wheel type A of EN 1991-2 [4]. A unit pressure of 1 MPa is applied to ease the interpretation of the results. The expected best and worst
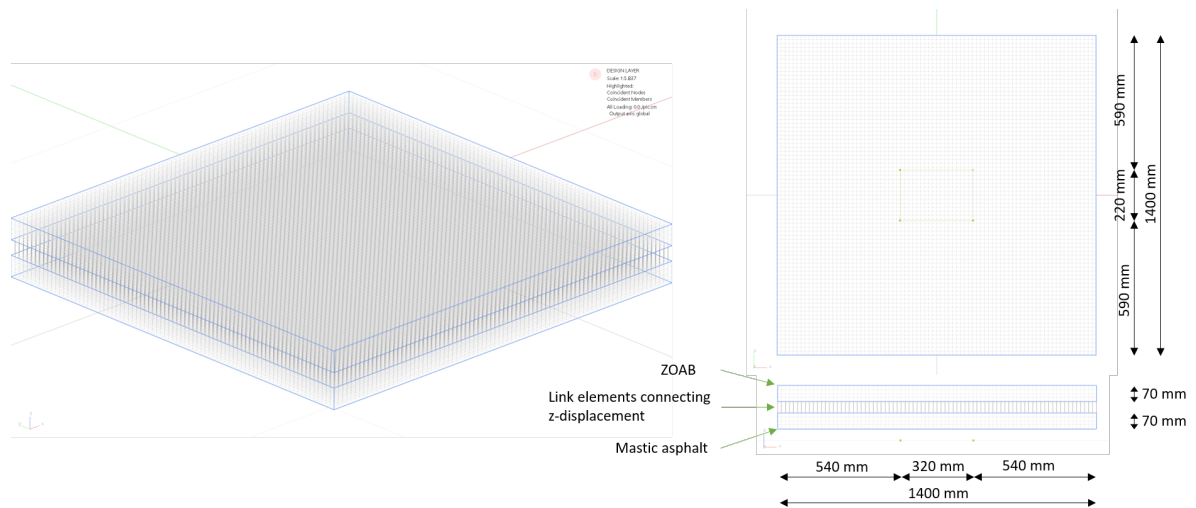
Figure A.1: Overview of the first model. An isometric, top, and side views are given. Dimensions as used in the model are given and members are labeled. The footprint of the load is visible in green on the top view.

case scenarios are investigated, where the asphalt temperatures are equal to 0 and 27,5° respectively. This corresponds to a Young's modulus of 8850 MPa for the ZOAB and 16650 MPa for the mastic asphalt layer at 0°C and 1350 MPa and 1900 MPa at 27,5°C.

A.1.1. Results
The resulting vertical stress at the bottom of the mastic asphalt layer resembles a three dimensional bell, as can be seen in figure A.2. Figure A.3 shows the distribution of the stress in the longitudinal and transverse direction. The points of zero pressure that are indicated in the figure can be seen as the edges of the influence zone of the load. Outside this zone, only a very small tensile force is present. It is assumed this force is negligible.
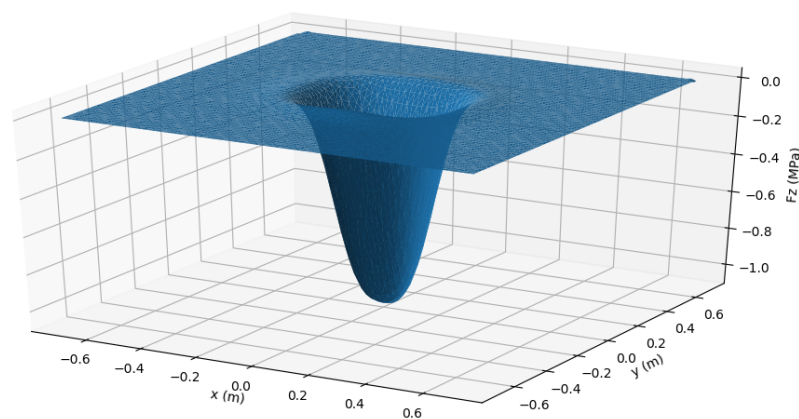
Figure A.2: The surface formed by the vertical stress at the bottom of the mastic asphalt layer in the rigidly supported model at T = 27,5°C.

When this influence zone is seen as equal to the load spread, the angle under which this occurs at a temperature of 0°C can be estimated by:

Vertical stress at bottom of asphalt layers when rigidly supported
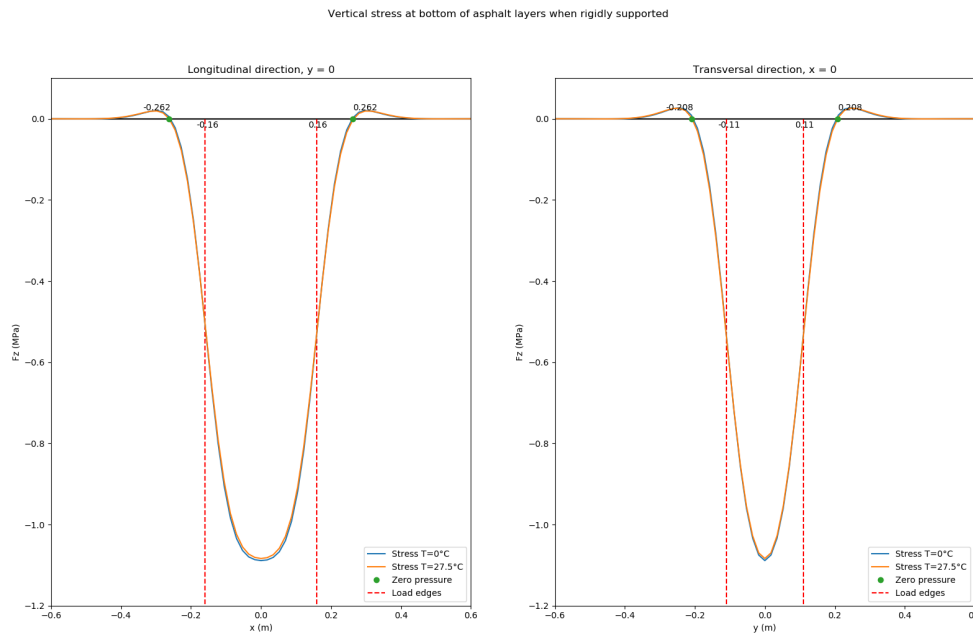
Figure A.3: Vertical stress at the bottom of the rigidly supported mastic asphalt layer along the longitudinal en transverse axes. Points of zero stress and the outer edges of the applied load are indicated. The applied loading is equal to 1 MPa.

$$\theta_x = \arctan\left(\frac{0,262 - 0,16}{t_{ZOAB} + t_{mastic}}\right) = \arctan\left(\frac{0,102}{0,14}\right) = 36,1° \tag{A.1}$$

$$\theta_y = \arctan\left(\frac{0,208 - 0,11}{t_{ZOAB} + t_{mastic}}\right) = \arctan\left(\frac{0,098}{0,14}\right) = 35,0° \tag{A.2}$$

Which confirms that a spread of 45° does occur not in the asphalt layers when the support of the deck is considered as rigid. Assuming such a spread may thus give non-conservative results.

A.2. Analysis 2: Asphalt on orthotropic deck model

It may, however, be doubted if the deck structure can be modeled as a rigid support for the asphalt layers. A simple hand calculation reveals that the deck plate is only twice as stiff in bending as the two asphalt layers combined at a temperature of 27,5°C. At lower temperatures, the asphalt layers even have a higher bending stiffness than the deck plate itself.

Therefore, a second analysis is made, where the asphalt is supported by a modified version of the orthotropic deck model that was presented in section 11. The limitations for the meshing of volume elements in GSA required some workarounds to properly connect the 2D elements of the deck plate to the 3D elements of the asphalt layer.

First of all, the detail area as described in section 11.3.4 was left out. Secondly, only one crossbeam and one trough are (partly) modeled with plate elements. The low spread and small thickness of the asphalt layers suggest that their influence will be very local.

Furthermore, some dimensions are slightly modified compared to the original values of the case study. The top width of the trough is modified from 300 mm to 350 mm and the bottom width from 105 mm to 350 mm. The crossbeam spacing has been decreased from 3645 mm to 3500 mm. By choosing the dimensions to be divisions or multiplications of the asphalt thickness, a predictable mesh is generated when the mesh size is chosen wisely. This enables the mesh of the 3D elements of the asphalt to be connected to the 2D elements of the deck plate properly.

Figure A.4 and figure A.5 visualize the used model and its dimensions. Also shown are the placement of the loads on the model. Five load cases are considered, placing the load in the middle of the trough, above the trough leg, and in between two troughs. The loads in the middle of the trough and above the trough leg are both considered at the crossbeam and in the middle of two crossbeams. The load in between two troughs is only placed at the crossbeam.

Although the modified dimensions may have a small effect on the results, this is considered to be irrelevant for the intended goal. Only a verification of the load dispersal as given in the Eurocode is sought, as a full study seeking for a simplification of the load spread trough the asphalt lies outside of the scope of this thesis.
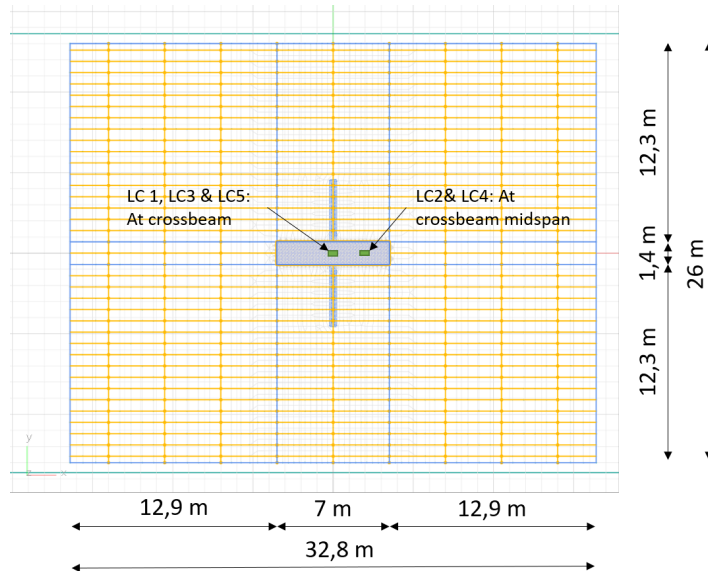
Figure A.4: Top view of the model that was used to verify the load spread by the asphalt layers when it is placed on the orthotropic deck model. The area where the asphalt is modeled is visible in the middle. The longitudinal location of the load cases is indicated.
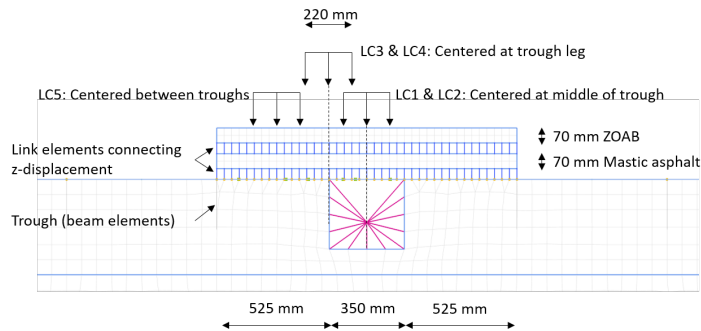
Figure A.5: Side view of the model that was used to verify the load spread by the asphalt layers when it is placed on the orthotropic deck model. The asphalt layers and their connectivity is labeled. The transverse placement of the load cases is shown.

A.2.1. Results
Figure A.6 shows the vertical stress at the bottom of the mastic asphalt layer. The shape of the stress distribution graph is similar to that of figure A.2, but the extreme value has significantly decreased.

Figure A.7 shows the distribution of vertical stress at the bottom of the asphalt layers along the x and y-axes for load case 1. Using the found points of zero pressure of figure A.7, a new estimation for the angle of load spread can be made:

$$\theta_x = \arctan\left(\frac{0,257 - 0,16}{t_{ZOAB} + t_{mastic}}\right) = \arctan\left(\frac{0,097}{0,14}\right) = 34,7° \tag{A.3}$$
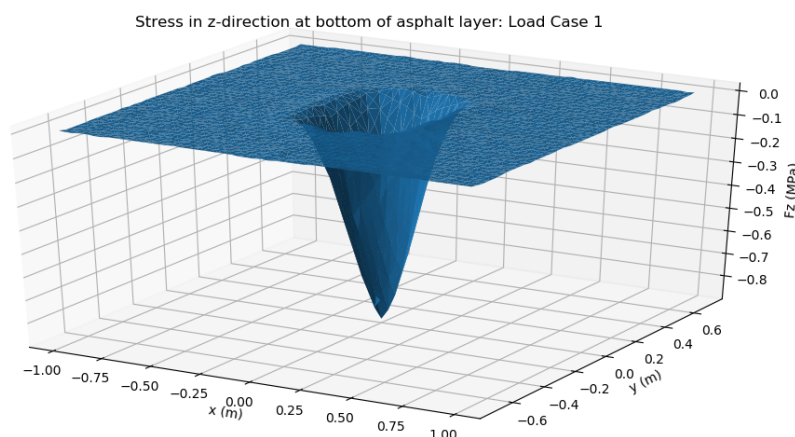
Figure A.6: Vertical stress at the bottom of the asphalt layer for load case 1, where the load is placed in the middle of the trough at the crossbeam-trough intersection. The stiffness of the asphalt layers corresponds to a temperature of 27,5°C

$$\theta_y = \arctan\left(\frac{0{,}226 - 0{,}11}{t_{ZOAB} + t_{mastic}}\right) = \arctan\left(\frac{0{,}116}{0{,}14}\right) = 39{,}6° \tag{A.4}$$

The finite rigidity of the deck thus has a small positive influence on the resulting load dispersal in transverse direction. For the longitudinal direction, the dispersion angle has slightly decreased. Thus, when only these angles are considered, the assumption of a rigid support as in analysis 1 seems to be justified.

However, the distribution of the vertical stress within the influenced area shows some strong deviations. The effect of the trough legs is the most evident herein. The vertical stress increases greatly (in absolute sense) just next to these for the 0°C case, while for the 27,5°C case, the stress in between them seems to be more evenly distributed than for the rigidly supported asphalt from analysis 1.

These differences between the results for the two asphalt temperatures are also worth noting. The stiffer asphalt at 0°C appears to transfer the loads more directly towards the more rigid parts of the deck structure. That way, the unsupported part of the deck plate experiences much less loading, while the force at the crossbeam-trough connection is larger.

Similar trends are found in the results from the other load cases. The area influenced by the load comes close to that found in analysis 1, but stress concentrations are found at the stiffer deck parts formed by trough legs and crossbeam webs. These can even be found at a greater distance from the load than is to be expected based on the angle of dispersal that was calculated above. At lower temperatures, the load is generally more directly transferred to the stiffer parts of the deck, and the influenced area is larger.

This is best visible in the load cases 3 and 4, where the load is placed above the trough leg. Figure A.8 shows a strong stress concentration at the loaded trough leg for both temperatures. However, at 0°C, the opposite trough leg also carries a significant part of the load. The warmer asphalt only transfers a small part of the load towards this location.

The transverse stress profiles of figure A.7 figure A.8 at lower temperatures cannot be properly modeled by a single patch load. Although the dispersion angle at lower temperatures is not strongly increased, the resulting stress profile is significantly different.

The plots containing the results from the remaining load cases can be found at the end of this chapter.
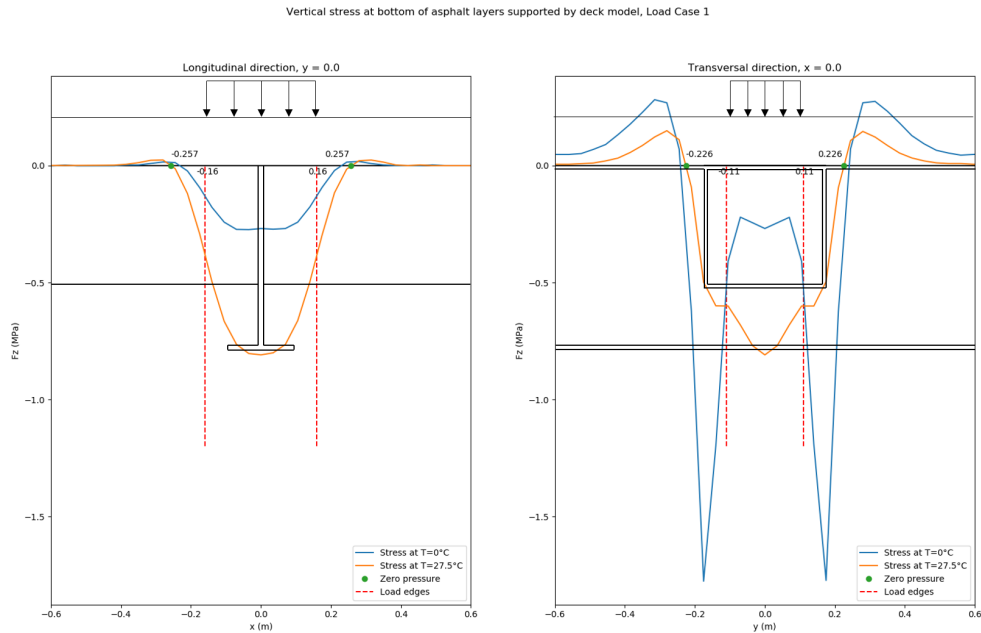
Figure A.7: Vertical stress at the bottom of the asphalt layers along the x and y-axes. Load case 1 is considered, where the load is placed at the middle of a trough at a crossbeam-trough intersection. The stress distributions at 0 and 27,5°C are plotted, the edges of the applied load are shown, and the most inner point of zero stress is indicated for the stress at 0°C. A sketch of the structure is provided in the graph to make the situation more clear.

A.3. Literature verification and additional research

As the two presented analyses contradict the recommendations found in the Eurocode and cannot give a definitive solution for the integration of the asphalt layer, a more thorough literature analysis was done.

First of all, this was done to verify the results from analyses 1 and 2. Cui [30] also reports an equivalent dispersal angle below 45° when the asphalt temperature drops below 22,5°C. The stress profiles as shown by Li [68] show good agreement with the results found in analysis 2 of this appendix.

Secondly, an attempt was made to find a proper simplification to model the asphalt layer without 3D elements. The mentioned paper by Cui tries to do this by using an equivalent load spread and assigning the deck plate an equivalent thickness that also accounts for the bending stiffness of the asphalt layers. However, the assumption is made that the deck plate and any layers on top are rigidly connected, and act fully compositely. As discussed before, this assumption is expected to be non-conservative. Li suggests to disregard the stress dispersal completely, as it supposedly has a very small influence on the stresses at fatigue details, but makes the same assumption.

Something both Cui and Li, and also Wang [113] and Wang [112] report is the great negative effect of higher asphalt temperatures on the fatigue life of orthotropic steel decks. Cui calculates that the damage at 27,5°C may be 12 times as high as at 0°C, and Li shows that the fatigue lifetime of details may decrease tenfold when effects of higher temperatures are considered. Wang and Wang both describe a quadratic relation between temperature and stress at fatigue details. As stress is used to the power three or five to calculate fatigue damage, this can greatly enlarge the effect of a temperature increase.

Again, these papers all assume a rigid connection between deck plate and asphalt layers. The effect on the stresses when this assumption is not made will be smaller, but these results still suggest the a strong negative impact of higher asphalt temperatures. Studies applying more conservative assumptions were not found.
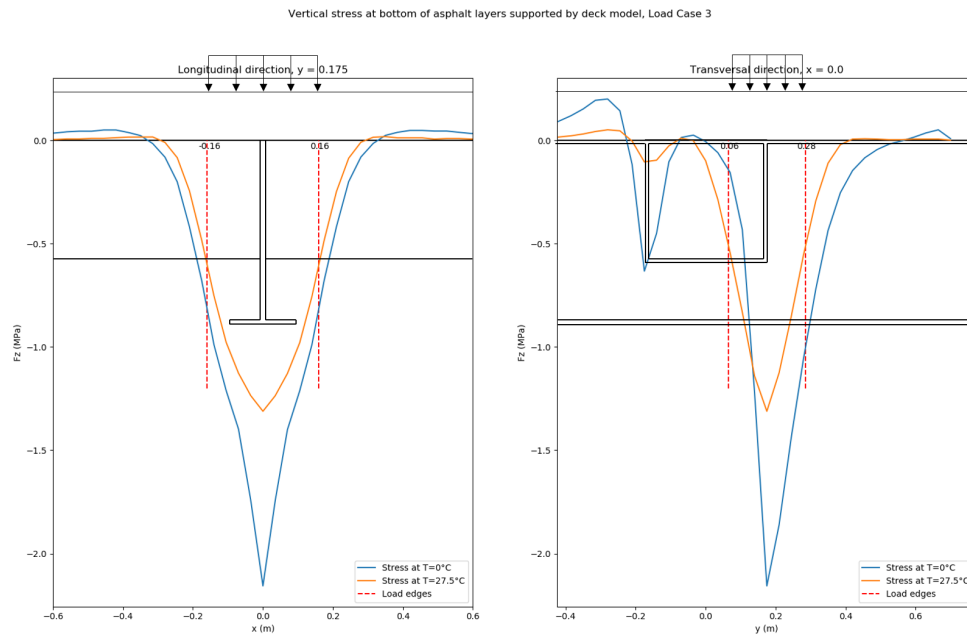
Figure A.8: Vertical stress at the bottom of the asphalt layer supported by the deck model of section A.2 for load case 3: above trough leg at crossbeam-trough intersection. The stress distributions at 0 and 27,5°C are plotted and the edges of the applied load are shown.

A.4. Conclusion

The results from both analysis 1 and analysis 2 confirm the questioning of the 45 degree spread of wheel loads as suggested by Eurocode 1 part 2 [4]. In neither of the considered cases, this dispersion rate was properly reached for an asphalt stiffness corresponding to a temperature of 27,5°C.

At lower temperatures, this spread can be achieved in some situations. However, assuming a single, uniformly distributed load patch is a strong simplification. The stiffer asphalt layers transfer loads more directly towards the rigid parts of the deck structure, but also strongly increase the maximum stress that is transferred to the deck plate. Still, the larger spread provided by the colder asphalt is expected to have beneficial effects on the stresses at the fatigue detail, as structural members weak in bending are loaded less. This hypothesis is strengthened by literature that has investigated the influence of the asphalt temperature on the fatigue life [112, 113].

Suggestions have been made in literature to simplify the role of the asphalt [30] or disregard the effect of load dispersal [68], but these all consider the asphalt and deck to be rigidly connected. It can be strongly questioned whether this is an appropriate assumption, especially when membranes are used between the deck plate and the asphalt layers. It is therefore recognized that there is a need of more research towards the simplification of the load dispersal provided by the asphalt layer.

It is considered too time-consuming to do this within the scope of this thesis. Providing proper guidelines to accurately yet conservatively model the influence of the asphalt layer deserves a research on its own. Therefore, a conservative assumption of 35° will be made for the angle of load dispersion through the asphalt. This has been the (rounded) lower bound of the dispersion angles found in the two analyses that were presented in this appendix.

As using 3D elements is currently not a viable option in the intended workflow and methods to properly integrate the effect of temperature in the load dispersal of the asphalt are lacking, it is decided to disregard the effects of asphalt temperature in this research for now. The assumption of a single angle of stress dispersal is considered conservative, and may decrease the optimality of the structure. This could be improved in future studies once one of the two mentioned obstacles has been resolved. On the other hand, indications are present that a (very) large part of the total fatigue damage in an orthotropic

deck occurs at higher temperatures, when the influence of the asphalt is lower [30, 68, 112]. This could reduce the differences with more accurate analyses that do integrate the effect of asphalt temperature.
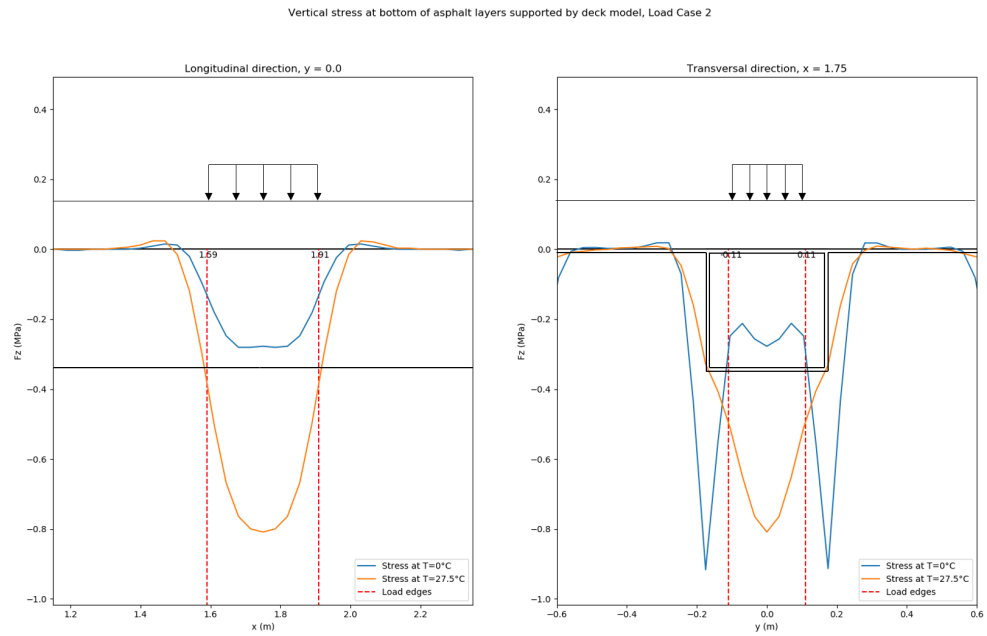

Figure A.9: Vertical stress at the bottom of the asphalt layer supported by the deck model of section A.2 for load case 2: middle of trough at midspan.
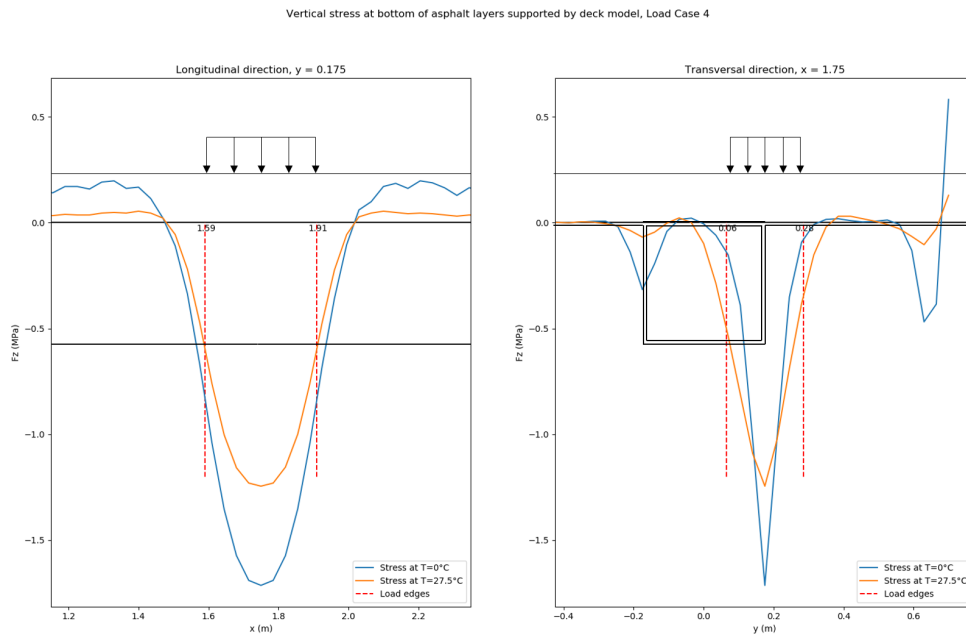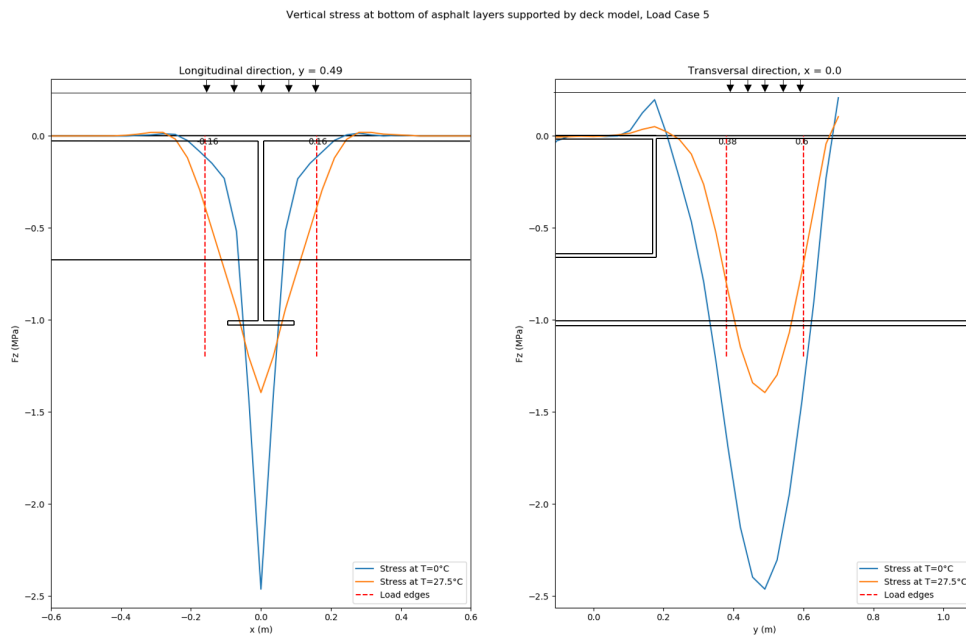
Figure A.10: Vertical stress at the bottom of the asphalt layer supported by the deck model of section A.2 for load case 4: above trough leg at midspan.

Figure A.11: Vertical stress at the bottom of the asphalt layer supported by the deck model of section A.2 for load case 5: at crossbeam in between troughs.

<div align="right">

B

</div>

Preferred position of trough splice

This appendix covers the short analysis that was done to determine the best location of the trough splice in the deck. This was done by calculating the maximum stress ranges that occur in the deck at the bottom of the trough at various positions from the crossbeam. The model of chapter 11 was used for this with some minor alterations.

First, the used method will be further elaborated, after which the results will be presented. The appendix finalizes with a conclusion about the best possible location of the trough splice.

B.1. Methods

The trough splice is generally located at some distance from the crossbeams, and is therefore less prone to strong stress concentrations. As such, extrapolations using the hot-spot stress method (see section 2.3.2 are not needed, and the ordinary nominal stress may be used for the calculation of fatigue damage. Stresses extracted from elements can thus be directly used for the decisive stress at the respective location.

This also makes the the use of the detailed area as presented in chapter 11 unnecessary. It was therefore left out to generate a regular mesh with an approximate size equal to the width at the bottom of troughs. This width, and all other dimensions, are taken from the preliminary design of the case study. An overview of these is visible in table 9.1.

The load on the model corresponded to wheel type A of table 4.3, dispersed under an angle of 35° through the 140 mm thick asphalt layers as suggested in appendix A. This results in a loaded area of 516 by 416 mm, that was centered once at the middle of the trough, and once at the trough leg. The former would turn out to be governing in all cases, and will therefore solely be treated in the remaining of this appendix. The load traveled over three crossbeam bays in the deck in 51 equally spaced intervals. As only relative results are of interest in this study, the magnitude of the load was set to 1 MPa.

The stresses were extracted from the center of each element present in the bottom of the troughs. As cracks are expected to start at the bottom of the detail [88], the results from the bottom layer of the shell elements were used.

B.2. Results

The stress in each element resulting from the traveling load gives a set of influence lines that is plotted in figure B.1. Notable in the figure is the gradual transition in the nature of the influence line when the splice is placed closer to the crossbeam. A splice placed at midspan will only experience one large stress reversal, which is exclusively tensile. Once the splice is moved more towards the crossbeam, the occuring compressive stress increases, while the maximum tensile stress reduces. This is caused by the clamping effect of the continuous trough.

Also visible in the figure is that splices that are placed closer to the trough are influenced more by loads at adjacent spans. For the locations closest to the crossbeam, this gives a second stress reversal which is (almost) as large as the primary stress range from the traveling load.
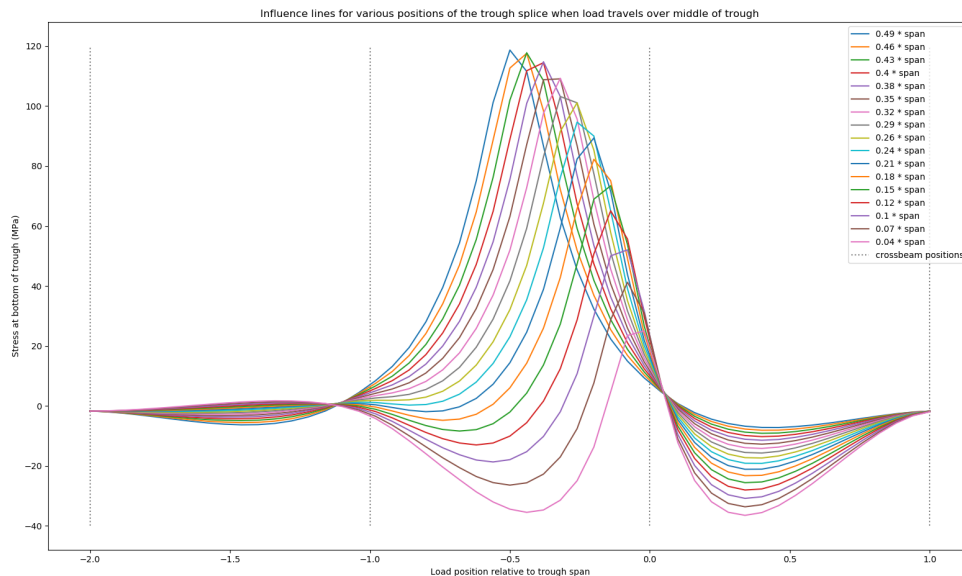

Figure B.1: The influence lines resulting from the traveling load for various possible trough splice locations. The load position is converted to be relative to the trough span, with x = 0 at an intersection with a crossbeam. The legend indicates the relative position of the splice location each graph belongs to.

When the maximum and minimum values of each graph in figure B.1 are subtracted and plotted against the location from which they are extracted, figure B.2 is obtained. Evident is the strong decrease in the experienced stress range for locations closer to the crossbeam. Where the magnitude of the stress reversal does not greatly differ for the area between a third and half of the span, it decreases rapidly for each step that is taken closer to the crossbeam.

As mentioned, this comes at the cost of a second stress reversal. However, as the expected stress range appears to the power 5 in the calculation of damage, two smaller cycles are generally preferred over a single larger cycle.

B.3. Conclusion

From the presented results, it is clear that the trough splice should be placed as close as possible to the crossbeam. This drastically reduces the occurring stress range in the joint, with the stress range at $1/25^{th}$ of the span being approximately half of that at midspan. The fact that two stress reversals occur at locations closer to the crossbeam is of less importance, as the stress range appears to the power 5 in the damage calculation.

However, the joint is also subject to constraints regarding manufacturability. The new guidelines by Rijkswaterstaat [88] therefore prescribe that the first weld of the adapter (see figure B.3) should be at least 300 mm from the crossbeam, and the length of the adapter itself should be at least 300 mm as well. As the stress range is larger further from the crossbeam, the second weld at 600 mm from the crossbeam will be governing. This measure will therefore be used for the location of detail 3 described in chapter 11.
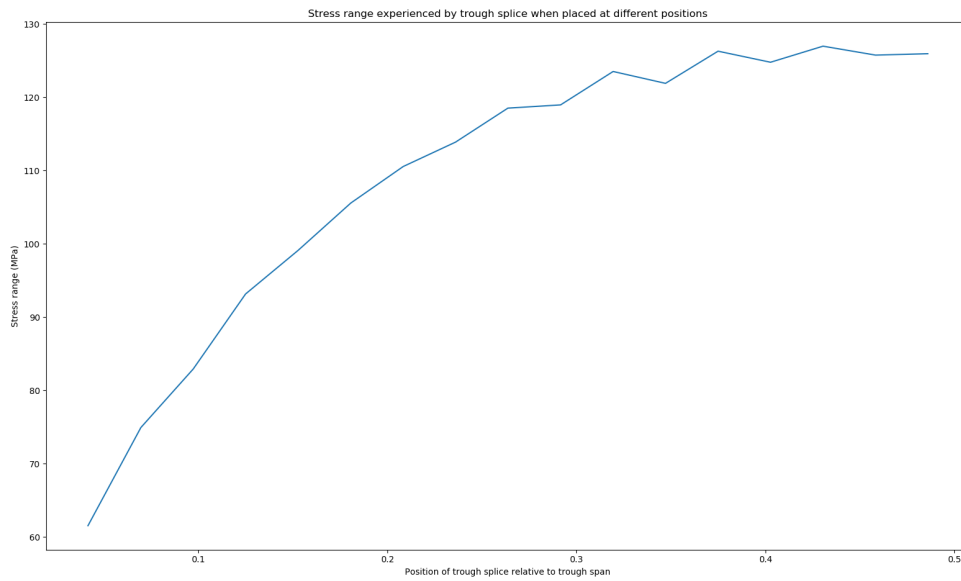
Figure B.2: The occurring stress range plotted against the trough splice location. The trough splice location is relative to the trough span, with x = 0 at a crossbeam.
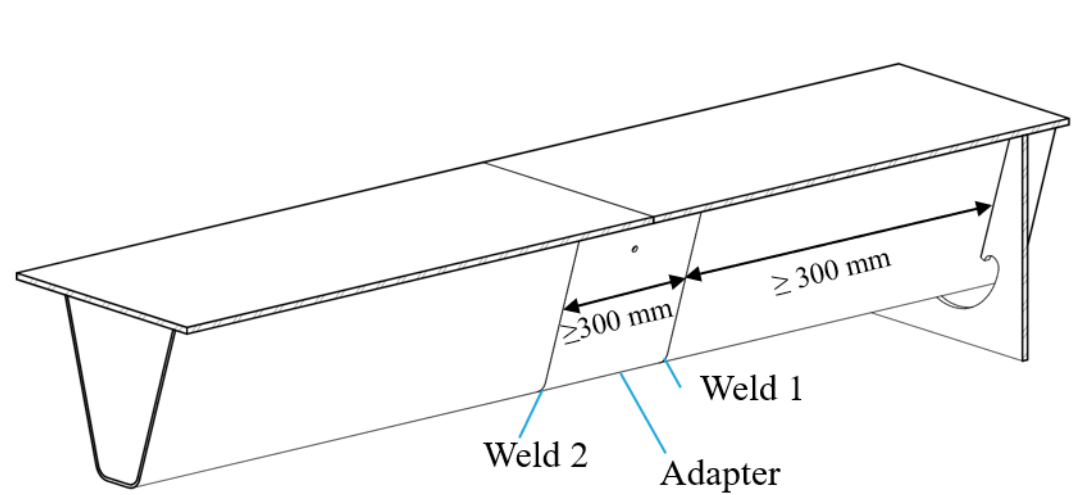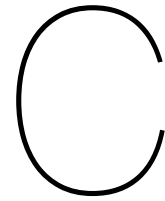

Figure B.3: Schematic drawing of the trough splice, the adapter, and their minimal dimensions. Source: Arup/Royal Haskoning DHV. (2018). Renovation design Van Brienenoordbrug: Drawings trough splices.

C

Determination of load placement

To limit the time needed for the analysis of the finite element model, it is essential use as little load cases as possible. However, as the the fatigue damage is very sensitive to changes in stresses, obtaining the true stress peak in the influence line is of equal importance. This appendix investigates where the stress peaks in the influence line are expected and what load spacing should be used to capture these within an acceptable amount of load cases. Two proposals for a load placements are given, in which the first tries to capture the rough profile of the influence line, while the second only aims to determine the absolute maximum. The latter can be used to scale a known influence line for a variant of interest.

The methods used are first explained, followed by the obtained results, and the appendix is closed with a conclusion.

C.1. Methods

As the detailed hot spot stress profiles are needed for proper judgment of the influence lines, the full parametric model as presented in chapter 11 is used for the current analysis. The used dimensions for the model are taken from the preliminary design of the Van Brienenoord bridge, which can be found in table 9.1.

The three wheel types of EN 1991-2 [4] (see table 4.3) were each centered once above the middle of the trough and once above the trough leg. The loads all traveled over two trough spans in 51 intervals, resulting in a total of 306 load cases. The spacing of the intervals was obtained by squaring an equally spaced array of numbers from -1 to 1, apart from the sign, such that more load cases are present near the fatigue details. Multiplying the squared array with the used center-to-center distance of the crossbeams finally gives the used load positions. The loads were dispersed through the 140 mm thick asphalt under the 35° angle that was obtained in appendix A.

A unit load of 1 MPa was used for wheel type A. As the wheel types each have a different contact area, the loads for type B and C were adjusted to make a proper comparison possible. This results in a load of 0,565 MPa for wheel type B and 0,892 MPa for wheel type C. The dispersal of the load was included in the calculation of these modified loads.

C.2. Results

The results of the analysis will be discussed per detail in this section.

C.2.1. Detail 1: Deck plate at crossbeam-trough intersection

The influence line for the stress at the first detail likely has the most predictable form, visible in figure C.1. Its minimum is obtained when the load is exactly above the crossbeam, and the remainder of the graph is symmetric in that point. Stresses only start to increase rapidly once the load has approached to approximately 0.15*span, and are relatively low outside this area.

Interesting to note is also the ratio between the extreme value of the stress for different wheel types when centered at the middle of the trough. This turns out to be very close to the ratio between the area of the different wheel types, and is thus likely to be caused by the correction that was applied to the loads.

Figure C.2 confirms this suggestion. The difference in minimum stress value for the three wheel types lies within 0,5 MPa and can be considered practically equal. This likely means that only the load placed in between the trough legs is of interest for the stress peak, which would make it possible to estimate the peak value for the other two wheel types fairly accurately once the stress peaks for one wheel types is known.
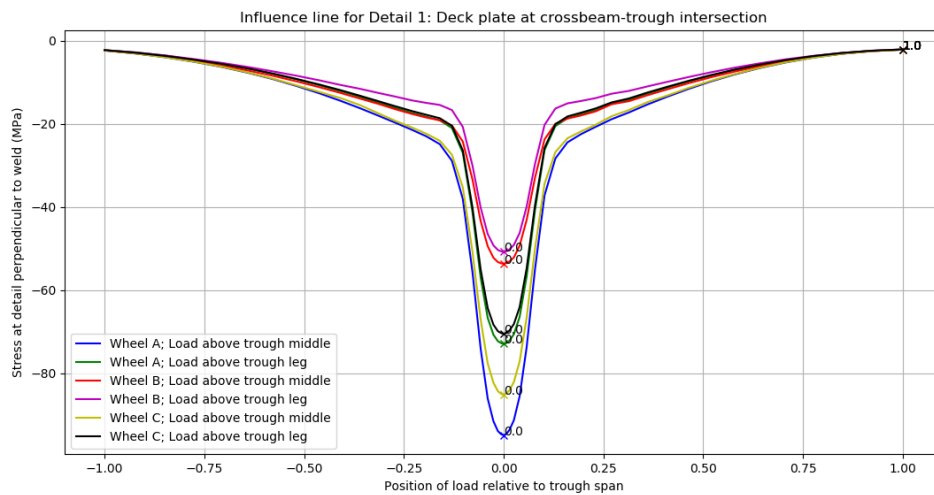

Figure C.1: Influence line for the hot spot stress in the deck plate at the crossbeam-trough intersection. Three different traveling wheel types were centered at two different locations: in the middle of the trough and above the trough leg. The relative position of the load at the extreme values is indicated in the graph.
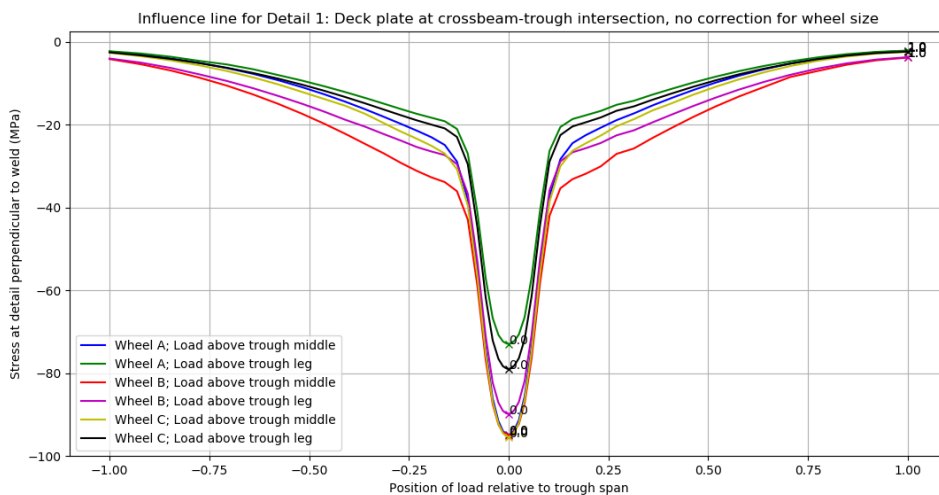

Figure C.2: Influence line for the hot spot stress in the deck plate at the crossbeam-trough intersection. The same as figure C.1, but now without correction factor that takes the area of the applied load into account. The minima for three wheel types turn out to differ by less than 0,5 MPa when centered in the middle of the trough.

C.2.2. Detail 2a: Trough at support plate- trough connection

The influence lines for the stresses at detail 2a have a more complex profile. Three different result groups seem to occur: wheel A and C at the trough leg, wheel A and C at the middle of the trough, and wheel type B, of which its placement only slightly affects the results. For wheel type A and C, the stress profiles are very similar, and for both the maximum value is obtained when the load is placed above the trough leg. The maximum value of the stress found for the smaller A type is slightly larger.

Peaks in the graphs are present around a quarter and a sixth of the trough span. Furthermore, a sharp deviation in the graph is present around 0,05*span. A point in this region should be included for a fairly accurate representation of the stresses. The remaining parts of the graphs could be reasonably linearized.
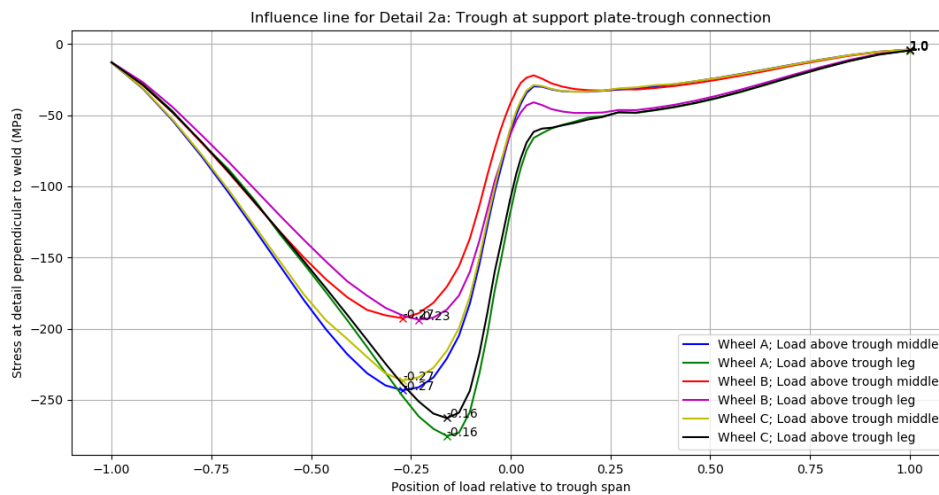

Figure C.3: Influence line for the hot spot stress in the trough at the support plate-trough intersection. Three different traveling wheel types were centered at two different locations: in the middle of the trough and above the trough leg. The relative position of the load at the extreme values is indicated in the graph.

C.2.3. Detail 2b: Support plate at support plate-trough connection

Figure C.4 shows the influence line for detail 2b. Visible is the change of sign in the stress once the load travels further in the second trough span, leading to a second peak. Just like detail 2a, the wheel types A and C show very similar results, while the graphs from wheel type B significantly differ. The maximum value is obtained when wheel type A is placed above the trough leg, also just like detail 2a.

The extreme values for the compressive stress are more distributed than was the case for the previous two details. The largest stress occurs at 0,13*span when the load is above the trough leg, while it occurs at 0,23*span when centered in the middle of the trough. Wheel type B gives maximum values at 0,19 and 0,27 times the span, of which the former gives the largest stress.

For the tensile stresses, the peaks lie between a 0,22 and 0,36 times the span. Notable is the lower gradient of the graph in this domain compared to the other peaks. This decreases the error that is made when the peak is not precisely obtained, and can thus be beneficial for the limitation of load cases.

C.2.4. Detail 3: Trough splice

The final detail, the trough splice, shows very similar influence lines for all considered cases (see figure C.5 . Only the magnitude of the extreme values that are found differ, while the shape of the graphs and position of the extremes is equal.

The largest stress occurs when wheel A is placed in the middle of the trough at a sixth of the span. The differences with wheel C are negligible, while wheel type B results in a significantly lower value. This is likely due to the spread towards other troughs that is possible for the much wider B type.

The maximum value occurs when the load is at a sixth of the span, which is very close to the position
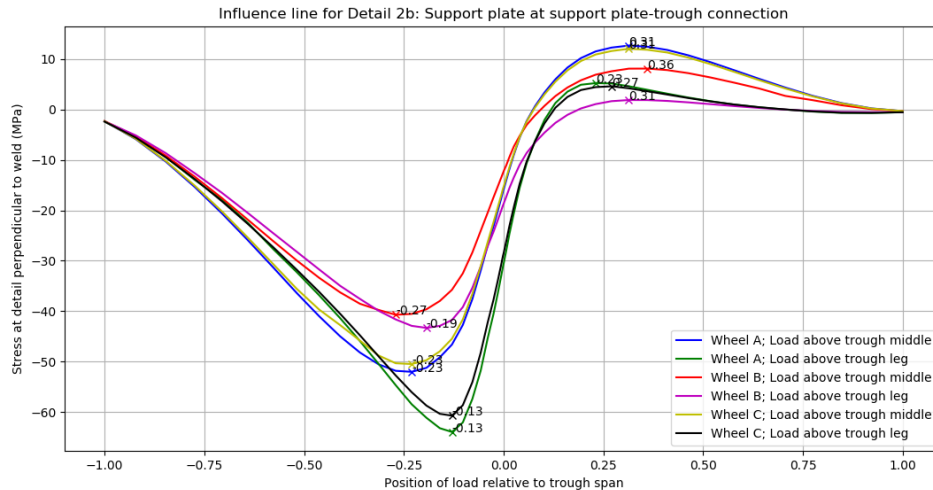
Figure C.4: Influence line for the hot spot stress in the support plate at the support plate-trough intersection. Three different traveling wheel types were centered at two different locations: in the middle of the trough and above the trough leg. The relative position of the load at the extreme values is indicated in the graph.

of the detail itself for the used parameters. It is therefore deemed very likely that the maximum value is obtained when the load is placed directly above the splice location. The minimum stress is obtained around 0,36*span, and shows a more gradual progress of the stress. A small error in the location of the load will thus not lead to large deviations in the obtained stress.
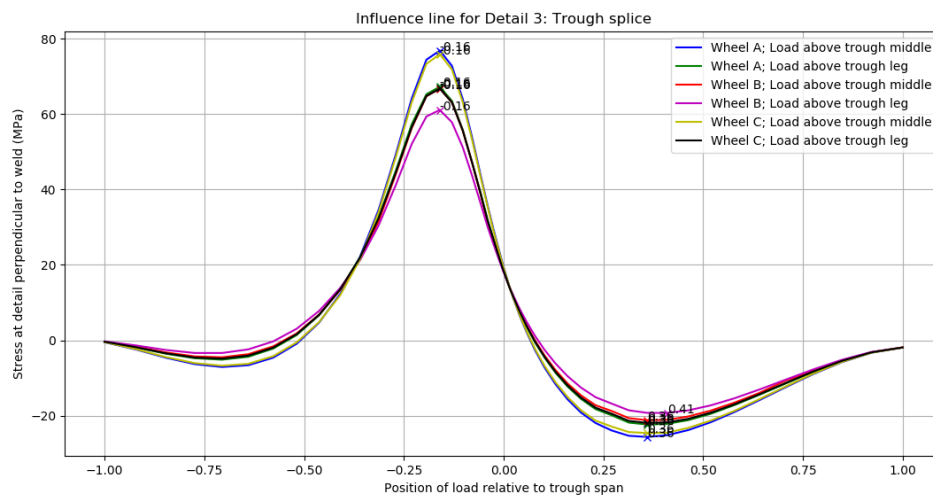

Figure C.5: Influence line for the nominal stress at the trough splice. Three different traveling wheel types were centered at two different locations: in the middle of the trough and above the trough leg. The relative position of the load at the extreme values is indicated in the graph.

C.3. Conclusion

With the results presented in this appendix, a first proposal for the placement of the load can be given. With this proposal, it is intended to capture the extreme values of the influence lines, while minimizing the amount of needed load cases. A first step to do this is to disregard wheel type C. It is clear from the graphs in this appendix that the difference between wheel type A and C is very small for most details, and predictable for detail 1.

A second step may be to use the symmetry of the situation to decrease the amount of weave positions from five to three when the load is centered in the middle of the trough. For the load centered at the trough leg, this is unfortunately not possible, and the full five weaves need to be considered.

When considering the expected location of the extreme values, a minimum requirement for the placement of the loads was made and presented in table C.1. These values are chosen such that the rough shape of the influence line is kept, with the extreme values being accurately captured. The motivation for the values is given in the previous section.

Center position	Wheel type	Positions relative to trough span	Other positions
Middle of trough	A/C	-0,16; 0,00; 0,16; 0,38	Above trough splice
	B	0,00; 0,38	Above trough splice
Trough leg	A/C	-0,16; -0,13; 0,05; 0,25	
	B	-0,23; -0,19; 0,05; 0,30	

Table C.1: First proposal of load positions to use, ordered per load position and wheel type. The load positions in this proposal aim to capture the rough profile of the influence lines.

However, a quick calculation taking the needed weave positions into consideration reveals that even these minimal amount of load positions would already result in 64 load cases. A small test with the current parametric model needed almost 5 minutes to run with this amount of load cases. With the expectation of over a thousand iterations needed for the optimization, the feasibility of this is doubtful.

It may therefore be necessary to limit the amount of load cases further. Investigating the option of only using the expected worst position of each truck could be useful for this, but even then the amount of load cases can become large. With five trucks, four details and thus four worst positions, and three or five weave positions, 80 load cases would be necessary for a full analysis. Research towards the influence of truck types and weave positions will then still be required to decrease the computational demand.

Another option worth investigating is the scaling of a known influence line based on only the stress peak of a variant of interest. In that case, only the expected worst position of wheel type for a fatigue detail would be needed. This would lead to seven load cases without weaves (two wheel loads per fatigue detail, except for the detail 1 where one wheel load is sufficient), or 32 when weaves are considered. The former is for now preferred. Table C.2 shows an overview of the placements of the loads for this proposal.

Fatigue detail	Center position	Wheel type	Position relative to trough span
Detail 1	Middle of trough	A/B/C	0,0
Detail 2a	Above trough leg	A/C	0,16
	Above trough leg	B	0,23
Detail 2b	Above trough leg	A/C	0,13
	Above trough leg	B	0,19
Detail 3	Middle of trough	A/C	Above trough splice
	Middle of trough	B	Above trough splice

Table C.2: Second proposal for load positions to use, ordered per corresponding fatigue detail and wheel type. These positions can be used when scaling of a known influence line is to be used. Multiple wheel types in the same row would be possible to predict using a single load.

D
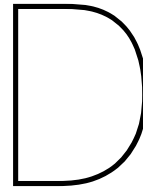
Determination of detail level dimensions

This chapter presents the analyses that were done to calibrate the dimensions of the detail levels that were introduced in chapter 11. This step is deemed crucial, as both the accuracy and the speed of the optimization can highly depend on these dimensions. Choosing the accurately modeled regions too small will undermine the precision of the analysis, leading to worthless results, while on the other hand overly accurate modeling may lead to unnecessary long run times of the optimization.

It is recognized that the short analysis in this appendix is not sufficient to provide comprehensive guidelines for the simplification of orthotropic deck modeling. The applicability on decks with different dimensions should also be checked, which will be done in the verification step in this thesis. Still, a better alternative was not found in literature. Recommendations regarding modeling simplifications for orthotropic bridge decks could therefore be a valuable subject of further research, and could be valuable for both the applicability of structural optimization and conventional practice.

Similar to the previous appendices, the used methods, results and a conclusion will be discussed consecutively. The conclusion will give the definitive dimensions of the detail levels that will be used in the optimization procedure.

D.1. Methods
The full parametric model of chapter 11 is again used in the current analysis, with the dimensions of the preliminary design of the case study (see table 9.1). Figure 11.3 is repeated in figure D.1 to show the positions of the detail levels, this time with the terms used to describe the dimensions of detail level 2.

In the first analysis, the relative dimensions of detail level 2 will be determined. This will be limited to a a ratio of the deck width for the transverse direction, and number of trough spans for the longitudinal direction. During the determination of the width ratio, the number of trough spans will be kept equal to 5. The width ratio will be equal to 1/4 during the investigation regarding the number of trough spans. The length and width of detail level 3 is set to 0,6 times the center-to-center distance of the troughs.

The second analysis will be aimed at detail level 3. The width and length of this part will be expressed as a ratio of the trough top width. A width ratio of 1/4 and 3 trough spans will be used for the dimensions of detail level 2 in this analysis.

Wheel type A was chosen for the load on the model, as it resulted in the largest stress peak in all influence lines investigated in appendix C. The other two wheel types were not used, as only the qualitative influence of the detail area's dimensions is sought. The load travels in 51 equal steps over the two trough spans adjacent to the fatigue details to capture the full stress influence line. This proved to be sufficient in the analysis of the mentioned appendix for the identification of extreme values. The larger computational demand compared to the load placement determined in the same appendix is deemed of less of importance for the one-time analysis that is made here for each case.
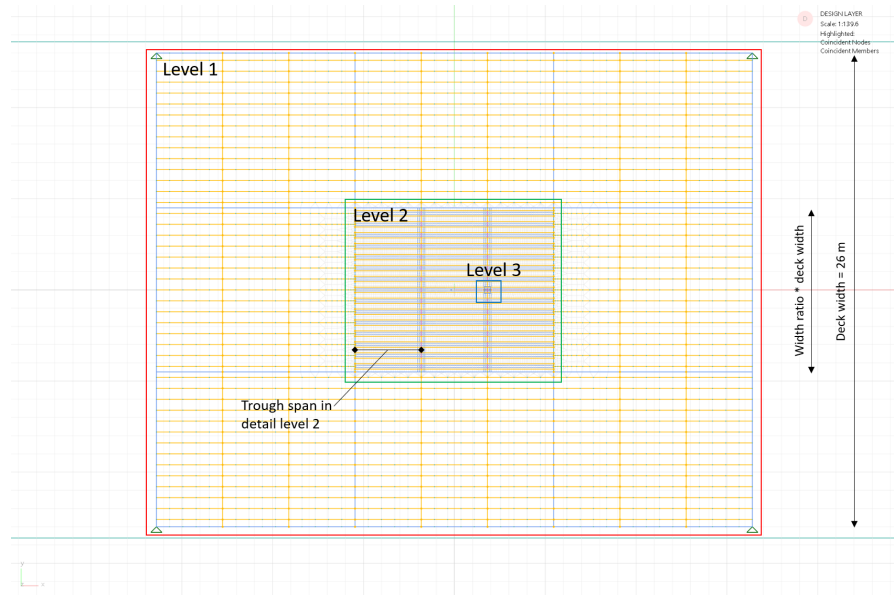
Figure D.1: Location of detail levels within the deck with the used terms for the dimensions of detail level 2.

D.2. Results

The results of the analysis will be presented in this section. The results for the width ratio and number of trough spans for detail level 2 are first presented, followed by the results for the dimensions of detail level 3.

D.2.1. Analysis 1a: Width ratio detail level 2

For a single wheel traveling over the deck, the stress range that occurs at the fatigue detail is most important. Figure D.2 therefore shows the stress range obtained from finite element models using different width ratios. It is clear that in most cases a smaller width ratio will lead to an overestimation of the stresses. Apart from the local minima around a width ratio of 0,2, the error appears to steadily increase. It could be that the beam elements of the troughs, which have open cross-section and thus lower torsional stability, decrease the transverse load spread.
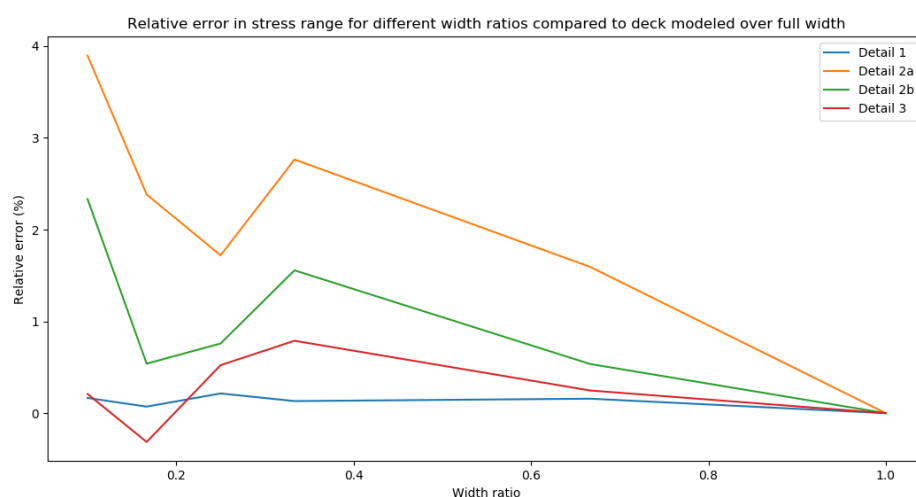

Figure D.2: Relative error in the experienced stress range at the fatigue details for different width ratios. The deck modeled by shell elements over the full width corresponds to a width ratio of 1. Visible is that a smaller width ratio mostly causes larger stress ranges to occur at the fatigue details.

For some instances however, a proper estimate of the stress peak can be more important. This can be the case when multiple wheel loads are placed closer together, or when only the stress peak is used to approximate the influence line based on earlier determined values. The relative error of the stress peak for different width ratios is therefore plotted in figure D.3. Detail 2a and 2b show a similar course as for the stress range, but the error in detail 3 deviates significantly. The decrease of the graph for lower width ratios is not present, and the sign of the error has changed. This means that the estimation of the stress peak is not conservative when the width ratio is chosen smaller. This should be taken into consideration when these are still applied.
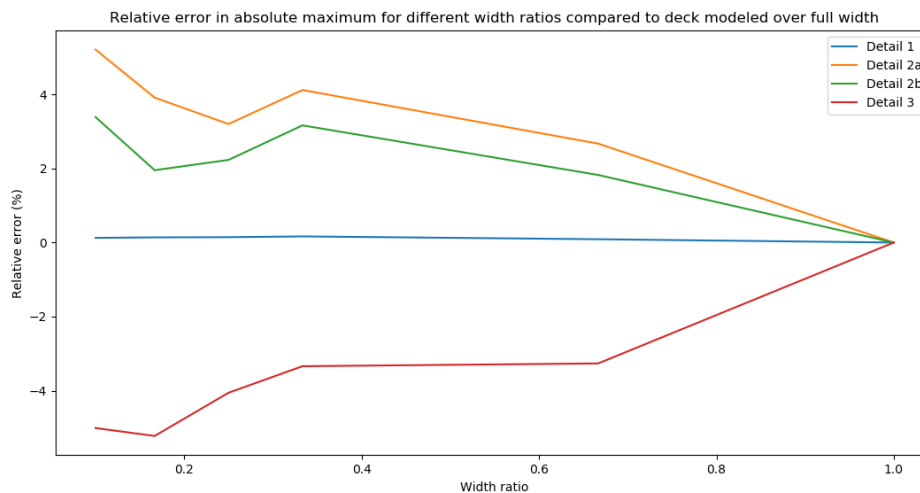

Figure D.3: Relative error in the maximum stress (in absolute sense) at the fatigue details. The deck modeled by shell elements over the full width corresponds to a width ratio of 1. Visible is the overestimation of the maximum value of the stresses for detail 2a and b, while the peak stress at detail 3 is underestimated. The stress at detail 1 is completely independent of the used width ratio.

Both figure D.2 and figure D.3 show that the extreme values of the stresses at fatigue detail 1 are completely independent of the used width ratio. This is in line with the results of appendix C, where it already became clear that the stress at detail 1 is only influenced by very local factors.

D.2.2. Analysis 1b: Number of trough spans in detail level 2

Similar to the analysis in the previous subsection, figure D.4 shows the relative error in stress range resulting from modeling a limited amount of trough spans with plate elements compared to using plate elements over the full length of the deck. The error appears to be small for most considered cases. Only the stress range of detail 3 becomes significantly larger with a decreased amount of spans modeled by plates. Closer inspection reveals that this is caused by an underestimation of the negative stress in the end part of the influence line (see figure C.5). It could be that the adjacent crossbeam, which is modeled by beam elements, provides a stiffer support and thus carries more of the load. The trough span in which the splice lies is then loaded less.

When only the absolute maxima are taken from the influence lines, the inaccuracy caused by limited modeling becomes even smaller. Figure D.5 displays that the difference between three and nine modeled spans is less than one percent for all details. The error for detail 2a and 2b has a peculiar profile, where modeling five spans with plate elements appears to be less accurate than three. When the trough is seen as a continuous beam over multiple supports, this can possibly be explained by the support from crossbeams. Changing the stiffness of different crossbeams may then have opposite effects on the stress at the fatigue detail.

Contrary to the stress range, the extreme value of the stress found at detail 3 is hardly influenced by the number of plate element spans. The same is valid for detail 1.
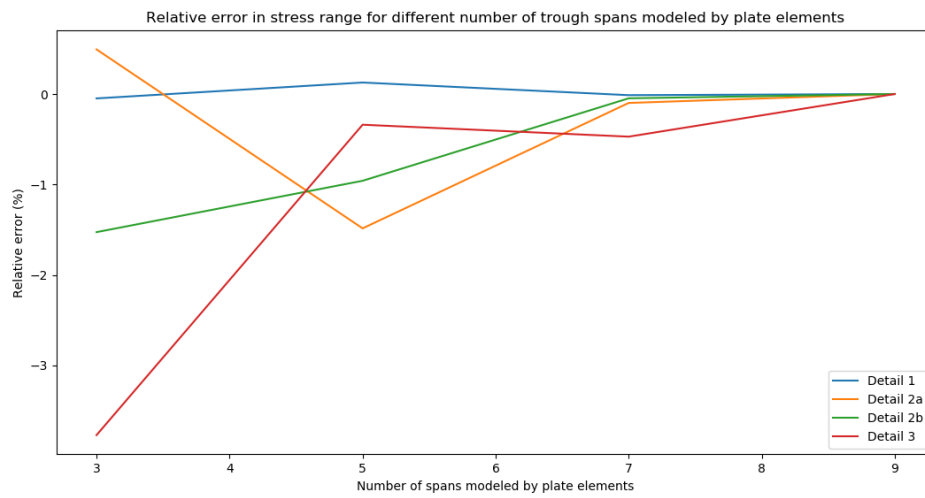
Figure D.4: Relative error in the experienced stress range at the fatigue details for different numbers of trough spans modeled by plate elements. All trough spans modeled by plate elements was used as a reference case, which corresponds to nine trough spans.
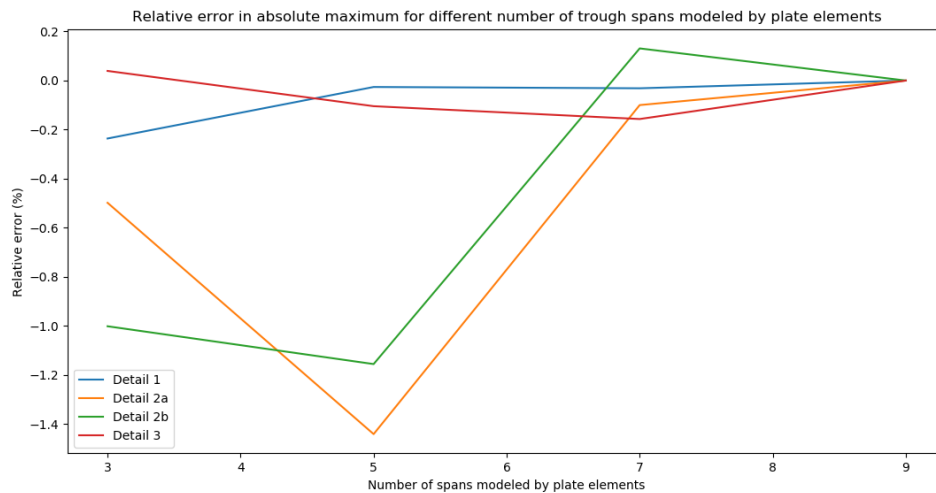

Figure D.5: Relative error in the maximum stress (in absolute sense) at the fatigue details for different numbers of trough spans modeled by plate elements. All trough spans modeled by plate elements was used as a reference case, which corresponds to 9 trough spans.

D.2.3. Analysis 2: Transverse dimension detail level 3

Figure D.6 and figure D.7 show the effects of varying the width of detail level 3 on the stresses. In most cases, the error that is made increases when the width of the detail area is chosen smaller. The made inaccuracy is small, however, and mostly on the conservative side. Like in the earlier analyses, only the estimation of the stress at fatigue detail 3 may be underestimated, but with a maximum deviation of approximately 1,5 percent, it is deemed to be acceptable.
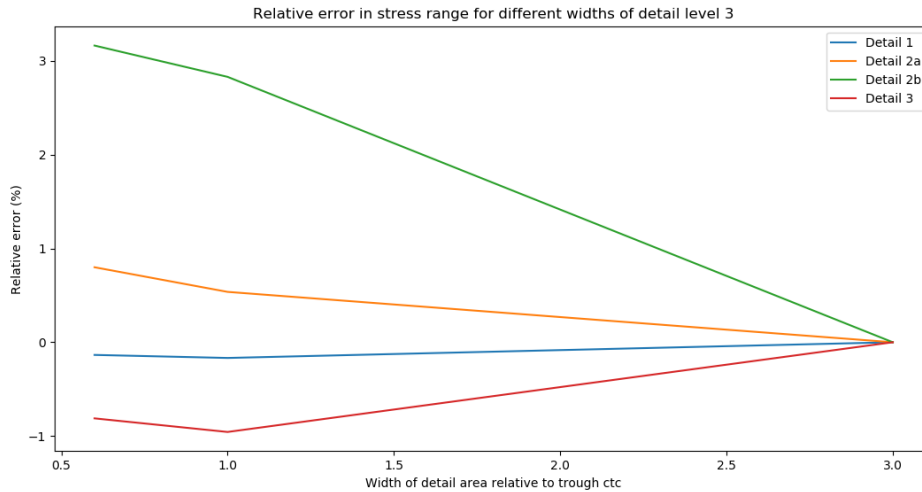

Figure D.6: Relative error in the experienced stress range at the fatigue details for different widths of detail level 3. The reference case is a width equal to three times the center-to-center distance of the troughs.

Figure D.7: Relative error in the maximum stress (in absolute sense) at the fatigue details for different widths of detail level 3. The reference case is a width equal to three times the center-to-center distance of the troughs.
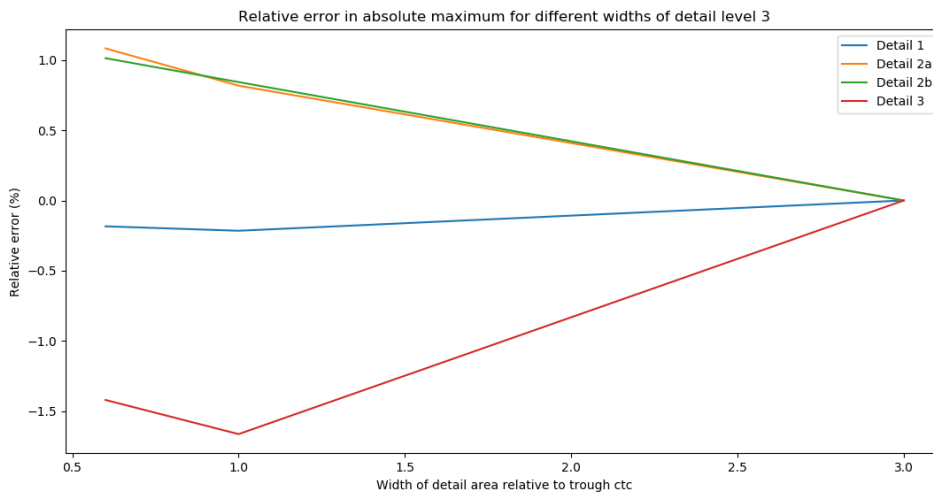
D.2.4. Analysis 2: Longitudinal dimension detail level 3

Similar to the previous subsections, figure D.8 and figure D.9 show the relative differences in stress range and the absolute stress peak for various lengths of detail level 3. Both graphs show that the influence of this dimension is significantly higher than the previously studied quantities. When the length of the detail area is chosen smaller than five times the center-to-center distance of the troughs, the error for detail 2b and 3 increases strongly. The stresses at detail 1 and 2a appear to be less affected by the choice of a detail length.
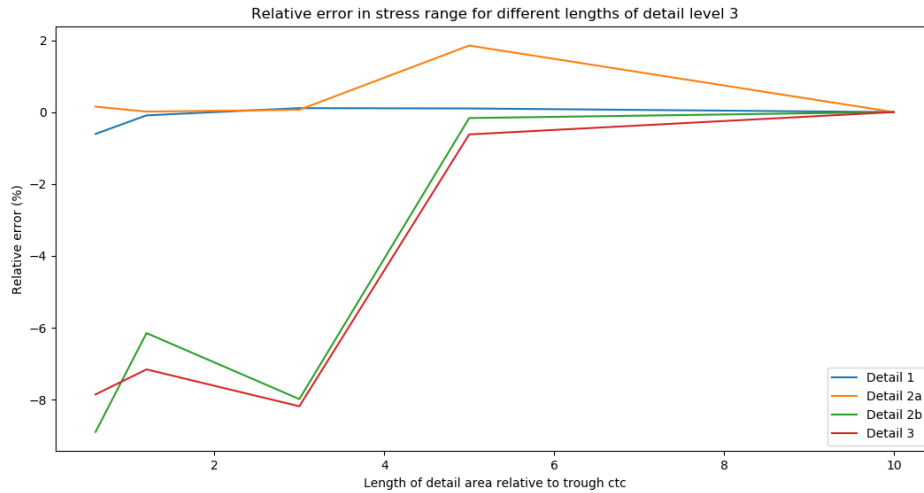
Figure D.8: Relative error in the experienced stress range at the fatigue details for different lengths of detail level 3. The reference case is a length equal to ten times the center-to-center distance of the troughs, which corresponds to approximately two trough spans being modeled in detail.
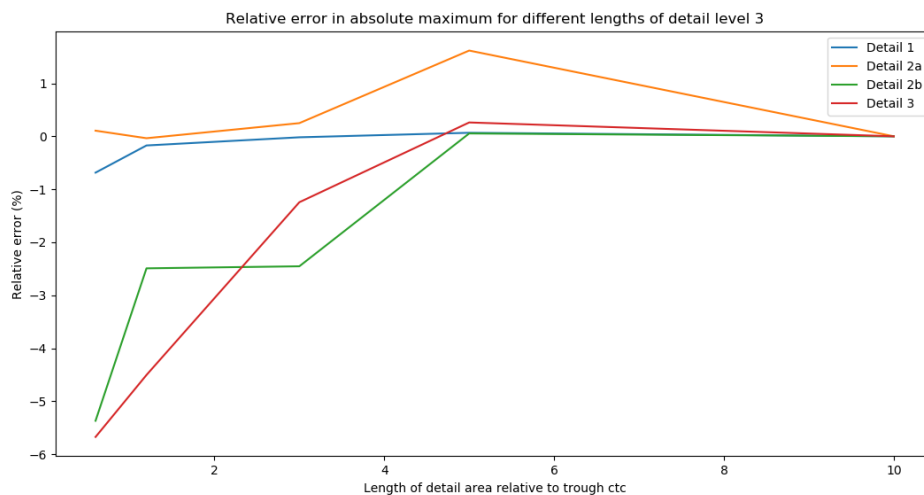

Figure D.9: Relative error in the maximum stress (in absolute sense) at the fatigue details for different widths of detail level 3. The reference case is a length equal to ten times the center-to-center distance of the troughs, which corresponds to approximately two trough spans being modeled in detail.

The lower stress at the mentioned details could be caused by the slightly lower stiffness of the trough when its rounding is incorporated. This effect could be strengthened by the small mesh size that is used in a larger part of the trough when the detail length is increased. The stresses at detail 2a appear to be governed by bending of the plate (based on the differences in stresses between the middle and bottom of the element). As this is a more local effect, it could explain why the stresses at the detail are less sensitive to the chosen dimension. The indifference of the stresses at detail 1 are unsurprising given the earlier analyses that found that the influence area of this detail is only very local.

The results of the analysis for lengths of five or ten center-to-center distances are very similar. This suggests that in the reference case the dimensions are chosen large enough, and reasonably accurate estimations of the expected error are made.

D.3. Conclusion

D.3.1. Analysis 1: Dimensions of modeling level 2

Based on analyses 1a and 1b, it is chosen to use a width ratio of 1/4 and 3 trough spans as the dimensions for detail level 2. The width ratio of 1/4 resulted in a relative error in the absolute stress peak of less than four percent for all fatigue details and an acceptable run time. It gives a conservative estimate for the stress range at all fatigue details, but the stress peak at fatigue detail 3 may be underestimated. This should be accounted for when only extreme values are considered.

The three trough spans modeled by plate elements should be sufficient to accurately obtain the absolute maximum of the influence line. In the analysis that was done, the differences with troughs modeled by plate elements over the full length was less than one percent for all fatigue details. This is considered negligible compared to other inaccuracies present in the analysis. When the full stress range is important though, deviations at fatigue detail 3 should be considered.

For completion, it can be useful to note that a model using plate elements over either the full width or length is not a viable option in the intended optimization. Both reference cases in analysis 1 needed over 30 minutes to run, mainly because the memory of the used computer was insufficient for an analysis of that size (which was approaching one million degrees of freedom). An analysis with both the length and width fully modeled in plate elements failed multiple times. When this would be absolutely necessary, the use of specialized soft- and hardware is advised. Based on the made analyses in this appendix, this research will assume the approximation of partial use of beam elements is acceptable.

## D.3.2. Analysis 2: Dimensions of modeling level 3

Based on analyses 2a and 2b, it is chosen to use a width of 0,6 and a length of 1,2 for modeling level 3. Section D.2.3 showed that the influence of the width of this area is very minor. The smallest investigated dimension is therefore chosen to reduce the number of needed elements in the model as much as possible. The found error of approximately one percent is assumed to be negligible.

The length of the detailed area did turn out to be of significant influence, however. Faults in the obtained stress range of over eight percent were observed, while the stresses at details 2b and 3 were underestimated by over five percent for the case with the smallest detail length. A minimum of five times the center-to-center distance of the troughs would need to be modeled in detail to limit the error in the stresses to two percent.

Unfortunately, this would also come at great computational cost. The model with a detailed area with a length of five times the center-to-center distance of the troughs has approximately three times as many elements as that using 1,2 times this dimension. The analysis time of the former was found to be unfeasible and thus a smaller value was chosen. The value of 1,2 was chosen over 0,6 as the underestimation of the stresses at detail 2b was much smaller in this case.

The non-conservative error for the stresses at detail 3 is added to the underestimation due to the limited area modeled in plate elements. In total, the absolute maximum of the stress at this detail would be underestimated by approximately ten percent due to the modeling simplifications made here. The fatigue damage at joints is related to stress to the power three or five. Using an average of four, the true damage would be 46 percent higher than computed using the current model. A damage of 0,68 would then be acceptable during the optimization. To be on the save side, a value of 0,65 will be used as a damage constraint for detail 3. The expected error for the other details is, net, approximately equal to zero and will not be accounted for in the damage constraint.

Note: The width of the detailed area was later increased to twice the top width of the troughs because of practical reasons (see section 11.2).
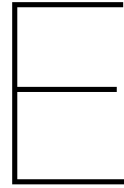
Verification of element size at detail 2a

The influence lines shown in appendix C show that the stresses at fatigue detail 2a are significantly larger than at the other details. As this detail is located in the thinnest member in the deck structure, its needed element size was chosen for the whole level 3 modeling area (see section 11.3.4). This also means that the elements that are used for stress extraction are directly adjacent to the respective joint. For the other details, an additional element is present in between.

This modeling choice at detail 2a does not correspond to the recommendations as named in section 4.6. The future version of the ROK [88] prescribes to use two elements between the intersection and the point of stress extraction, while Niemi [79] advises to use quadratic elements when the element of interest are placed adjacent to the plate intersection.

Visual inspection of contour plots of stresses at the detail (see figure E.1) also show that the stresses increase only very close to the intersection between the trough and support plate. This raised the suspicion that the high maximum stress value is caused by the improper modeling of the elements. It could be that the the singularity that is present at the plate intersection is now included, while the used hot-spot stress method should avoid this peak. If this is not achieved, a strong overestimation of the stress would be obtained, which would drastically decrease the optimality of the eventual result of this thesis. A short analysis was therefore done to investigate the influence of the mesh size on the stress found for this detail.
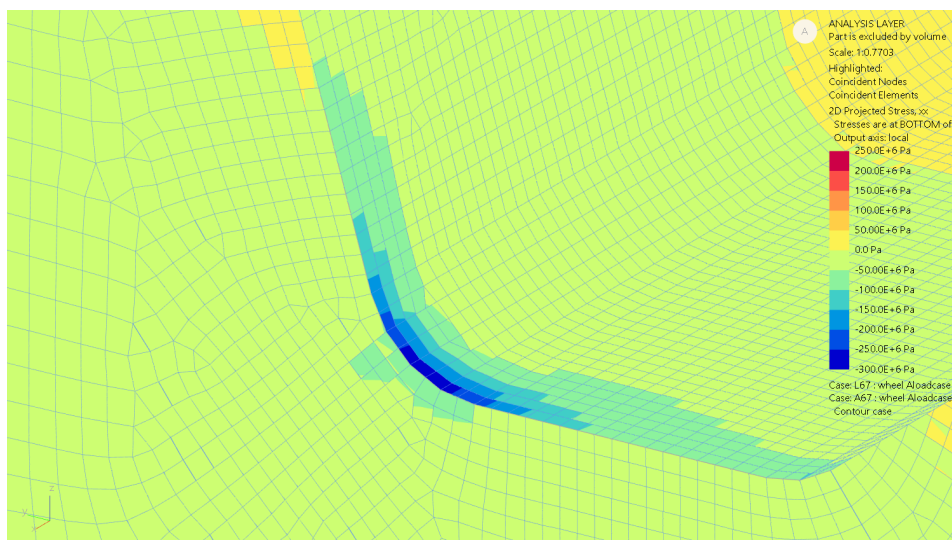

Figure E.1: Contour plot of the stresses at the bottom of the elements in local x direction, which is perpendicular to the plate intersection. The first point of stress extraction is indicated by the pink point. Visible is the strong increase of the stress close to this.

E.1. Methods

The parametric model as presented in chapter 11 was again used for this analysis. The used dimensions were taken from the preliminary design of the Van Brienenoord bridge (see table 9.1). The original mesh size of 8 mm (equal to the thickness of the trough) was halved twice to get a mesh size of 4 mm and 2 mm. This smaller mesh was only applied in the troughs. A fourth analysis kept the mesh size intact, but used eight-noded quadratic elements instead of the four-noded linear elements that are used elsewhere in this research.

As the hot-spot stress method prescribes, the stress at 0,5 and 1,5 times the thickness of the troughs were extracted. For the reference case and the fourth analysis with quadratic elements, this is at the middle of an element. The halving of this element in the other cases places a node at the extraction location which prohibits this. For these cases, the stresses at the respective node for the four connected elements are averaged.

E.2. Results

The results of the analysis are presented in table E.1. The differences between the stresses found for different mesh sizes are small. Only the largest linear elements show an increase that can be considered significant, but not enough to be considered a singularity. The differences between the smallest used mesh sizes can be seen as negligible, indicating that further refinement of the mesh would not substantially affect the results.

Element type	Mesh size	$\sigma_{xx;0,5t}$	$\sigma_{xx;1,5t}$	$\sigma_{xx;extrapolated}$
Linear	t_{stiff}	-218	-96	-279
	$0,5 * t_{stiff}$	-208	-94	-265
	$0,25 * t_{stiff}$	-208	-96	-264
Quadratic	t_{stiff}	-211	-98	-268

Table E.1: Maximum stresses (in absolute sense) at detail 2a in local x-direction (perpendicular to the joint) for different mesh choices. The stresses at the three extraction locations are given: at $0,5 * t_{stiff}$, $1,5 * t_{stiff}$, and the extrapolated value at the weld. All values are in MPa.

Something not reported in the table, but visible in the contour plots of the model is the maximum value of the stresses near the detail. Contrary to the mentioned results, these did significantly increase for smaller mesh sizes. The plate intersection for the model with the smallest mesh size showed stresses of over -400 MPa, while a value of -250 MPa was not reached for the linear model with the largest elements.

E.3. Conclusion

The results presented in table E.1 show that the decrease in stresses for smaller element sizes is minor. The relative error compared to smaller mesh sizes was approximately five percent on the conservative side. Differences between linear and quadratic elements were even smaller. The negligible changes between mesh sizes of $0,5 * t_{stiff}$ and $0,25 * t_{stiff}$ suggest that further refinement will not have any effects on the observed values.

The strong increase in maximum stress value found in the model shows that the singularity is present, especially with smaller elements. The location of stress extraction, however, appears to be adequate to mitigate this. The original choice for linear elements with an approximate mesh size of the thickness of the troughs will therefore be maintained.

Note: the stress at the detail treated in this appendix proved much higher than expected based on other considered designs. It was therefore decided to model the welds by a row of one or two elements with an increased thickness. The extrapolation of the stresses is then performed towards the edge of the thicker elements. This drastically decreases the found fatigue stresses and explains the difference between the numerical values of the stresses presented in this appendix and elsewhere in this thesis.

$$\mathsf{F}$$
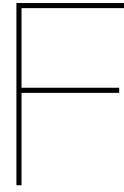
Preliminary runs

This appendix analyzes the results from some preliminary optimization runs, which aim to find suitable parameters and setup choices. The influence of the penalty function, limit, and maximum number of function evaluations will be explored. This was done in four runs, here presented after each other. More accurate checks of the results of these runs did not lead to feasible variants, hence their classification of 'preliminary'.

Besides, an error in the input for the fatigue calculation was made, causing all calculated damages to be a factor 100 too large. The found results are therefore not representative for the correct outcome of a run. However, the exploration of the parameter influence is still thought to be valuable and the runs do show the process that came to the eventual setup of the optimization.

Each section of the appendix treats a performed run, presented in chronological order.

F.1. Run 1

The values of table F.1 were used in this run:

Penalty function	ϵ	Population size	Limit	Max evaluations	Parameter type
$\left(\sum_{i=1}^{4} \delta_i\right)^{\epsilon}$	$1 \to 3$	30	10	1000	Continuous

Table F.1: Optimization setup choices for the first preliminary run. δ_i is the damage at detail i and ϵ increases linearly from 1 to 3 during the optimization.

The result of this optimization are presented in table F.2. Most striking is the resulting value of the top width of the troughs, which has adopted the lowest possible value. This enables a thinner deck plate of 15,5 mm, giving a total mass of 280 kg/m^2. This would mean a weight reduction of more than seventeen percent. Other significant changes are the relatively high bottom width of the trough (compared to the top width) and larger crossbeam spacing.

t_d	ctc_{cb}	t_{sp}	h_{stiff}	a_{stiff}	b_{stiff}	t_{stiff}	mass (kg)
15,5	4300	14,1	147	140	127	8,49	280

Table F.2: Optimized results from the first run. All values except mass are in mm. All values are rounded to have 3 significant digits.

Although no fatigue damage was found in the estimated analysis during the optimization, the full fatigue analysis of this design variant did result in unacceptable damages. The fatigue life of detail 2a eventually turned out to be inadequate. The cause of the higher peak stress did not lie in the improper extraction of the stress peak, but turned out to be in the divergent path of the influence line for the detail. When the wheel loads are placed at the adjacent trough span, the reference influence lines from the Van Brienenoord design give a small compressive stress at the details. For the optimized variant however,

a significantly larger value is obtained. This leads to a higher peak stress when the three closely spaced wheels under the trailer of the third truck of load model 4a (figure 4.2) pass the detail. The increase in the stress peak appears to be enough to exceed the cut-off limit and fatigue damage occurs.
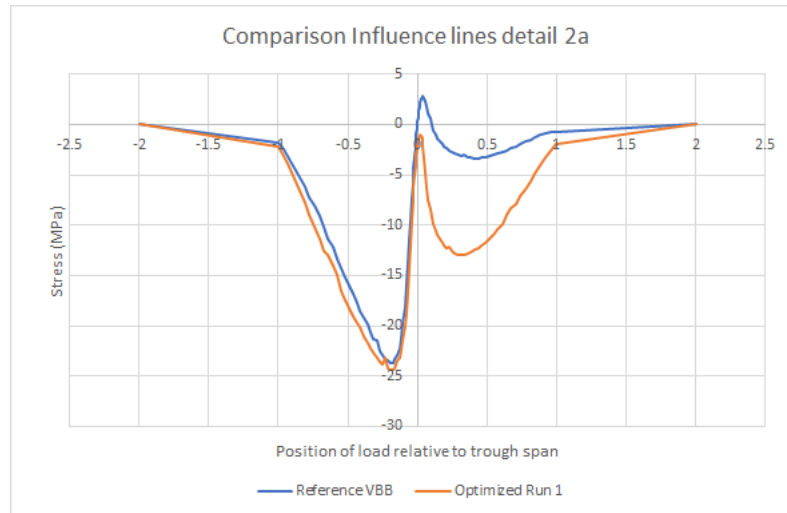

Figure F.1: Comparison between the influence lines of detail 2a for the reference case (the preliminary design of the Van Brienenoord bridge) and the optimized variant. Visible is the divergent path when the load is placed at the adjacent trough span.

To prevent such non-conservative estimations in future runs, the influence lines from this variant will be used as reference for the next runs. The shift towards the compressive side will always lead to equal or higher stresses when scaling influence lines, which could prevent underestimation of peak stresses. Furthermore, it is likely that future optimized decks will be more similar to the result from this run than to the preliminary design of the Van Brienenoord. Although the former gave unacceptable damages, these were relatively limited. Minor changes in the design parameters could give a very light deck with a proper fatigue life.

Secondly, the data from this run showed that a variant similar to the eventual result was very quickly found, but only little improvement was made from then on. Inspection of the best result per food source also showed that only five of the fifteen had discovered a feasible variant. These two observations combined, this may suggest that the algorithm converges too quickly into a local minimum. The strong penalty of variants with high damages leads to them getting very little attention from employed bees and thus less chance of finding feasible variants. The increase of ϵ in the penalty function may even hinder them completely from adopting new variants. Even if these have less damage, the penalty function may still turn out higher.

F.2. Run 2

The values of table F.3 were used in this run:

Penalty function	ϵ	Population size	Limit	Max evaluations	Parameter type
$\sum_{i=1}^{4} \delta_i$	-	30	10	600	Continuous

Table F.3: Optimization setup choices for the second preliminary run. δ_i is the damage at detail i. ϵ was removed from the penalty function of run 1 to give more room for the search of the design space.

Visible is the removal of the ϵ power to enable more search of the search space. It is tried to give more attention towards food sources with initially higher objective function values to drive them towards feasible solutions as well. The maximum number of evaluations was lowered to 600, as the result of run 1 was obtained much earlier than the 1000 evaluations that were made. For the exploration now made, the gained speed with 600 evaluations is more important than the possible decrease in precision.

The result of this second run is shown in table F.4. Again, the the top width of the stiffness reaches the lower bound of 140 mm and a significantly thinner deck plate is obtained. The reached mass is

somewhat higher than for the previous run, which could be caused by the different influence lines used as reference.

t_d	ctc_{cb}	t_{sp}	h_{stiff}	a_{stiff}	b_{stiff}	t_{stiff}	mass (kg)
17,1	3840	13,5	253	140	122	6,55	297

Table F.4: Optimized results from the second run. All values except mass are in mm. All values are rounded to have 3 significant digits.

Further investigation of the results showed that some problems occurred in the parametric model for high values of b_{stiff}. The width of the detail area was increased from $1,2 * a_{stiff}$ to $2 * a_{stiff}$ to prevent this for future cases. This did have a slight effect on the stresses at fatigue detail 2b for the optimized case of run 2, leading to a calculated damage of 122 in its 100-year life time. Future runs will use the new value to prevent problems and give a more accurate estimation of the stresses.

The change in the penalty function did lead to some improvement regarding the number of food sources with useful results. Run 2 had seven food sources with useful results while less evaluations were made during it. The random nature of the used algorithm makes definitive conclusions not possible, but it does hint on an improvement compared to the previous setup.

F.3. Run 3

Run 3 used the values of table F.5:

Penalty function	ϵ	Population size	Limit	Max evaluations	Parameter type
$\left(\sum_{i=1}^{4} \delta_i\right)^{\epsilon}$	$0,5 \rightarrow 1,5$	30	10	600	Continuous

Table F.5: Optimization setup choices for the first preliminary run. δ_i is the damage at detail i and ϵ increases linearly from 0,5 to 1,5 during the optimization.

The table shows that the power ϵ returned in the penalty function. Its starting value of 0,5 is a final try to get more food sources to be working towards a feasible solution. Damages are now significantly less punished in early stages, such that onlooker bees are distributed more evenly in early stages. It is expected that this may lead to slower convergence, but more thorough search of the design space.

Unfortunately, this was not achieved during this run. The applied penalty function turned out to be too soft for variants with damage in early stages. This meant that very light decks with moderate damages were preferred at the beginning of the optimization, as the low value of ϵ made sure that the value of the objective function would remain low despite the exceedance of constraints. Decks without any damages could not compete with these found 'solutions' meaning that the results of this run are not of practical interest.

F.4. Run 4

Run 4 used the values of table F.6:

Penalty function	ϵ	Population size	Limit	Max evaluations	Parameter type
$\sum_{i=1}^{4} \delta_i$	-	30	30	600	Continuous

Table F.6: Optimization setup choices for the first preliminary run. δ_i is the damage at detail i.

Due to the unsuccessful attempt of run 3 with a lower initial ϵ, the penalty function of run 2 returns in run 4. The limit is increased to 30 to enable intenser search of the neighborhood of variants. The previous runs suggested that the algorithm converged fast and abandoned variants rather quickly. The current setup aims to enable wide search of the design space in early stages and enough room to find local optima around promising alternatives.

Table F.7 shows that the best found alternative again uses narrower troughs and a thinner deck plate, but the lower bound of 140 mm is not reached this time. A large center-to-center distance of the

crossbeams is obtained combined with higher and thicker troughs. The minimal mass is with 300 kg higher than in previous runs.

t_d	ctc_{cb}	t_{sp}	h_{stiff}	a_{stiff}	b_{stiff}	t_{stiff}	mass (kg)
15,9	5110	16,9	304	173	81,2	7,42	300

Table F.7: Optimized results from the fourth run. All values except mass are in mm. All values are rounded to have 3 significant digits.

Inspection of the results per cycle reveals that the eventual solution is significantly later achieved than in previous runs. The reported value was reached in the seventeenth iteration and it may therefore be that improvement was still possible. Furthermore, the number of food sources that found at least one feasible result was nine in this run, which is a considerable improvement compared to the five in the first run.

Again, a model with an increased number of load cases was analyzed to check whether the scaled influence line approximates the true line close enough. Figure F.2 shows the two lines for wheel type A and C. It can be seen that the influence line obtained with the complete number of load cases is shifted to the left and gives a significantly higher tensile stress when the load is placed at the adjacent trough span. Although the largest stress peak is very accurately predicted by the scaled influence line, this gives a larger stress range for the full analysis. The increase is just enough to surpass the cut-off limit, resulting in a damage of 122.
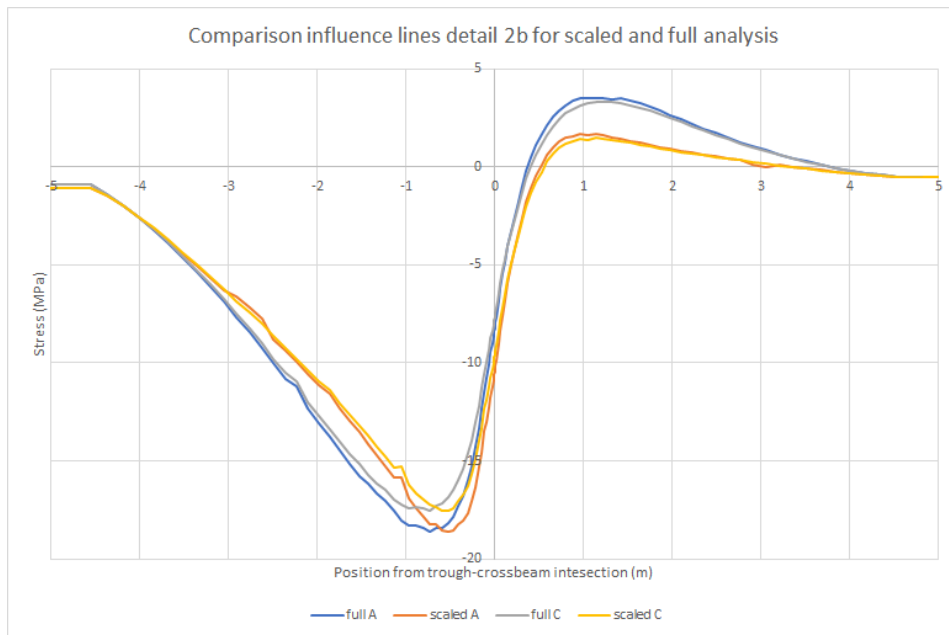

Figure F.2: Comparison between the scaled influence line used during the optimization and the influence line which was later obtained with a high number of load cases. The results for wheel type A and wheel type C are plotted. Visible is the underestimation of the tensile stress when the load is placed at the adjacent trough span.

Figure F.2 shows that the reference influence line for the support plate detail obtained in run 1 is not conservative for all cases. The influence line for the full case as presented in the figure is therefore adopted as the new reference for this detail in future runs.

G

Proof of non-convex design space

The conclusion of chapter 14 hypothesized that one of the reasons for the great spread in the outcome of the optimizations could be the strong non-convexity of the design space. To give this statement more credibility, this appendix will prove the non-convex (or *concave*) character of the design space.

G.1. Method

Section 6.1 explained the general concept of convexity. In summary, a domain may be called convex when every point on the line between two arbitrary points in the domain is also part of the domain. Equation 6.1 expressed this mathematically.

Applied on the optimization problem studied here, a point should be interpreted as a design variant. Points on the line between two variants represent designs that have structural dimensions in between those. For the domain to be convex, any design lying between two known feasible designs should thus also be feasible. Furthermore, the objective function may not acquire any local minima in the studied range.

The applicability of these two requirements are tested for the optimization problem by using the preliminary design of the Van Brienenoord bridge and the best resulting designs from the made analyses. These variants are known to be feasible and, at least for the optimization results, expected to lie in or close to (local) optima. As the result of analysis 3 was the lightest design variant found, it is used as the reference case. Its design variables are then step-wise changed to one of the other variant's dimensions.

Thus, the intermediate design's variables are computed by:

$$\mathbf{x}_{intermediate} = \lambda \mathbf{x}_i + (1 - \lambda) \mathbf{x}_{analysis3} \tag{G.1}$$

Where $\mathbf{x}_i$ represents the vector containing the design variables of one of the other known feasible designs. The vectors $\mathbf{x}_j$ are thus formed by:

$$\mathbf{x}_j = \begin{bmatrix} t_{d,j} \\ ctc_{cb,j} \\ t_{sp,j} \\ h_{stiff,j} \\ a_{stiff,j} \\ b_{stiff,j} \\ t_{stiff,j} \end{bmatrix} \tag{G.2}$$

187

G.2. Results

The objective function values that result from the described approach are plotted in figure G.1. Variants for which the computed damage at any detail exceeds the constraint of table 10.2 are marked with red dots. This violation causes a penalty function to be added to the normalized mass to compute the objective function value, explaining the deviation of the graphs from the expected path. The result of analysis 3 also slightly violated the constraint at detail 3 (see table 14.11), hence the slight dip in the graphs to analysis 1 and the Van Brienenoord preliminary design. During the verification of the result, the violation was no longer present, thus making the design feasible. Its mass was still lower than other variants computed here.
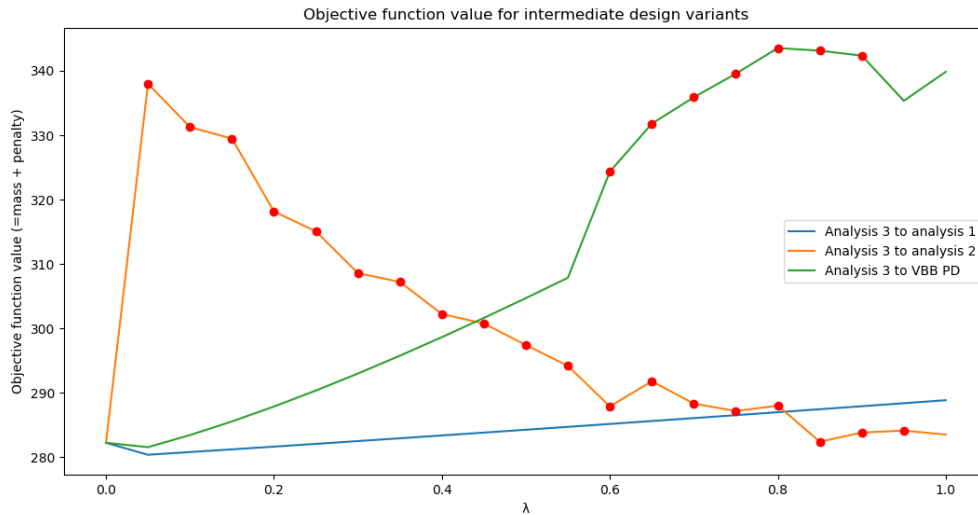

Figure G.1: The computed value of the objective function (=mass + penalty for constraint violation) for various intermediate designs that were determined by equation G.1. A lambda value of zero corresponds to the design that was obtained from analysis 3 of chapter 14, while a lambda value of 1 corresponds to the other variant named in the legend. Red dots indicate a computed infeasible design variant. (VBB PD = Van Brienenoord Preliminary Design).

The graph clearly shows the concave character of the design space between the result of analysis 3 on the one hand and the Van Brienenoord preliminary design and the outcome of analysis 2 on the other. Between these, multiple infeasible variants and a local optimum were found. Both violate the condition for convexity, thus proving the hypothesis of chapter 10.

However, the line between analysis 1 and 3 suggests that this cannot be named as the sole reason for the varying results of the artificial bee colony algorithm. The objective function does not have any local optima that would hinder the algorithm in finding better solutions in the proximity of the result. In this regard, it should be recalled that the setup of analysis 1 did not allow for any damages to occur. The design space then does become non-convex, although lighter solutions still could have been found.

G.3. Discussion

The large differences between the three graphs may be remarkable, they are also well-explainable. When figure 14.3 is considered, the similarity in the designs of analyses 1 and 3 is clear. The gradual course of the graph connecting these two is therefore reasonable. It is plausible that the two designs are present in the same section of the design space and the result of analysis 1 was unable to adopt the more optimal design of analysis 3. After all, analysis 1 used stricter constraints than later analyses.

The differences between the design of analysis 3 and that of analysis 2 and the Van Brienenoord are much larger. Unsurprisingly, this also gives a much more irregular graph profile. Both variants experience a decrease in trough height during the transition to the result of analysis 3, which could lead to higher stresses in detail 2a, 2b, and 3, while the necessary force redistribution only occurs at a later stage. Furthermore, the significant changes in this process could have a large influence on the

stress concentrations around the joints. These are notoriously hard to predict and it is probable that these also change during the transitioning.

Detail 2a and 2b may be mentioned explicitly in this. The Van Brienenoord PD and analysis 2 result both have a relatively shallow bottom width of the trough compared to the analysis 3 design. During the transitioning, the length of the rounded part of the trough therefore changes significantly. The two mentioned details are situated in the rounding and are thus almost certainly influenced by this. Inspection of the intermediate results confirms this.

Finally, the numerous infeasible designs in between the design of analyses 2 and 3 can be justified as well. The optimized designs will generally approach a constraint that hinders further reduction of the mass. With a non-linear constraint, it can occur that the results of the analyses are limited by the same constraint on different sides (figure G.2). Any design that lies between these results then falls outside of the feasible domain.
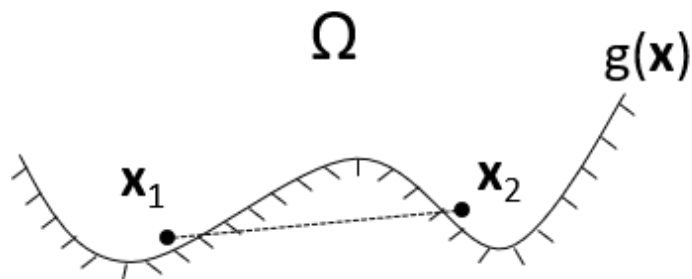

Figure G.2: Graphical interpretation of the line connecting the designs of analyses 2 and 3 relative to the constraints. x_1 and x_2 represent the designs, g(x) the constraint, and Ω the side of the feasible domain. When designs between x_1 and x_2 are considered, these will almost all be unfeasible.